Université catholique de Louvain
Faculté des Bioingénieurs
Earth and Life Institute

Assessing 29 years of global land cover dynamics from satellite Earth Observation

---

Doctoral dissertation presented by

Céline Lamarche

in fulfillment of the requirements for the degree of

Doctor in Agronomical Sciences and Biological Engineering

Thesis committee:

Prof. Pierre Defourny (Supervisor)	UCLouvain, Belgium
Prof. Patrick Bogaert (Secretary)	UCLouvain, Belgium
Dr. Gregory Duveiller	Max Planck Institute for Biochemistry, Germany
Dr. Martin Stefan Brandt	University of Copenhagen, Denmark
Prof. Emmanuel Hanert (President)	UCLouvain, Belgium

Louvain-la-Neuve, May 2024

Abstract

Land use and land cover change contribute significantly to anthropogenic CO_2 emissions and biodiversity loss. However, current inventory-based statistics miss year-to-year land changes, preventing a comprehensive global understanding. Earth observation by satellite provides valuable information for mapping global annual changes at the pixel level. Yet, consistency is crucial to capture change signals among variability from natural surface fluctuations or evolving satellite mission capabilities. In this thesis, we co-develop and evaluate the very first global annual land cover change time series at 300 m from 1992 to 2020, maintaining consistency across space, time and satellite missions. This dataset, currently used for Intergovernmental Panel on Climate Change (IPCC) climate modeling and Intergovernmental Science-Policy Platform on Biodiversity and Ecosystem Services (IPBES) analysis, enables us to quantify and analyze the global dynamics of land cover change over the last 30 years. This research also contributes to enhancing the qualification of land cover datasets. While validation guidelines are well-established for individual product assessment, we introduced a stratified random sampling method for product benchmarking, tailored to areas prone to discrepancies between products, to highlight the satellite product strengths and weaknesses. To improve climate and land surface, we enabled the conversion of land cover categories to plant functional types (PFT) composition per pixel. This was made possible thanks to the development of a globally applicable framework to seamlessly integrate multiple high-resolution datasets that might otherwise not be compatible. Finally, we investigate the impact of uncertainty in Earth observation surface reflectance measurement on the categorical land cover classification process. Building on a Monte Carlo simulation, we quantify errors and propose a classification ensemble approach to effectively mitigate them. This work contributes to more informed land accounting in the context of rapid anthropogenic change and climate evolution, supporting the assessment of the Food and Agriculture Organization (FAO) and Organization for Economic Co-operation and Development (OECD) environmental-economic accounting systems.

Remerciements

Ce qui devait être un simple passage de quelques mois au laboratoire de géomatique s'est finalement transformé en une traversée de plus d'une décennie. Et... ironie du sort, moi qui pensais suivre une route bien balisée, j'ai fini par emprunter des chemins de traverse, la thèse que je pensais éviter m'a finalement rattrapée.

À l'heure où se clôture ce chapitre doctoral, j'aimerais exprimer ma gratitude envers tous ceux et celles qui ont croisé ma route et m'ont aidé à atteindre cette destination.

Mes premiers remerciements vont naturellement à Pierre, qui m'a offert l'opportunité de m'impliquer dans des projets en accord avec mes convictions, comme le projet ESA CCI LC qui est à l'origine de cette thèse. Son énergie inépuisable m'a encouragé à donner le meilleur pour atteindre les objectifs fixés (et au-delà), espérant ainsi que notre travail ait un impact réel sur la société. Je lui suis également reconnaissante pour sa patience lors de mes moments de dispersion et de doute (pour employer un euphémisme). Sa compréhension face à mes éventuelles gaffes, dont je préfère taire les détails ici, a été grandement appréciée. Travailler avec des experts aux quatre coins de l'Europe a été un réel plaisir (un merci particulier à Catherine, Andy et Philippe).

Je tiens également à exprimer ma gratitude envers Patrick, dont la collaboration pour rédiger un article m'a démontré à quel point cela peut être efficace. Je remercie également Grégory pour son exigence ; même si elle n'a pas toujours été facile à recevoir, elle m'a permis de progresser. Le retrouver dans mon jury de thèse après qu'il ait été présent dans celui de mon mémoire, c'est boucler la boucle ! Thanks also to Martin B. for agreeing to be on the thesis jury and for your invaluable advice on the next improvements to be made to maps, notably in China.

Mon parcours ici n'aurait probablement pas été aussi long si nous n'avions pas cultivé les liens entre les ENGEs. Continuons à faire tinter la cloche!

Je tiens à exprimer ma sincère gratitude envers les Enges pour leur contribution à cette ambiance stimulante et pour leur amitié précieuse. Aux GlobCroppers, merci pour votre capacité à mélanger travail sérieux et moments festifs, montrant ainsi que l'engagement professionnel peut être audacieux ! Un merci spécial à Sophie, qui m'a initié aux défis des projets exigeants et m'a guidé dans mes débuts. Julien, gardien des traditions, ta loyauté sans faille et ta précision (exactitude ?) garantit la qualité technique du labo. Même si j'ai souvent mis du temps à saisir ta logique, tu m'as (très) souvent prêté main forte ! Les experts en informatique, Éric, Thomas et Benjamin, que serions-nous sans vous ? Sans votre expertise, aucune carte n'aurait vu le jour opérationnellement! À Astrid et Raphaël, je comprends désormais pleinement ce que signifie faire une thèse. J'aurais dû faire ça en même temps que vous ! Mathieu, à travers tes échanges philosophiques et tes débats, tu as toujours su nous pousser à nous interroger et à clarifier nos convictions. Jean, merci pour les cafés partagés, ton écoute active et tes conseils. Je te souhaite le meilleur à Rome. Un merci spécial à Quentin D. qui a contribué à réduire les incertitudes au propre comme au figuré! Et merci Maxime pour ta répartie pleine d'esprit!

Passer des années dans un labo, c'est comme faire un GR, en passant de refuges en refuges.

J'ai commencé l'aventure par le paysager tropical avec Quentin, Yodit et JPK aka "le Président". Notre refrain était simple: 'Wapi Jean-Paul ? ... en réunion. Jean-Paul qui, sur un coup de poker, m'a envoyé donner une formation à Kinshasa. Un bluff avoué huit ans plus tard ! Tu nous as poussés, déstabilisés, testés dans notre capacité d'adaptation, un vrai défi mais une aventure dont je ne regrette rien ! Intense, oui, mais tellement enrichissante ! Maïté, ma complice de cette épopée africaine, qui a évité que cette aventure ne tourne au fiasco ! Merci pour ton écoute attentive en toutes circonstances, c'est toujours un plaisir de partager avec toi ce qui me tient à coeur et nos passions communes. Et vivement nos prochaines escapades en montagne. Quentin, ta qualité de facilitateur, parmi tes autres talents, a permis que notre retour à Kin se fasse comme sur des roulettes. Ça a été un plaisir de travailler avec toi!

Un merci tout particulier à mes compagnons de bocal, Nico B et Nico D. Quel plaisir de partager avec vous ce lieu stratégique, un poste de sentinelles bien avant l'ère des satellites. À la "nouvelle génération des ENGEs", vous avez le code dans le sang et vous servez d'exemples à suivre pour une approche

collaborative de la recherche ! Un merci tout particulier à Barbara, Thibauld, Audric et Boris. Votre bienveillance, votre enthousiasme communicatif, votre résistance au stress et votre calme efficacité font du C301 the place to be. Thibauld, et ce costume au bureau alors ? Je ne serais pas là où j'en suis si je n'avais pas eu la chance d'être bien entourée en dehors du labo ! Margaux, nos retrouvailles à Esperanzah sont l'exemple même de ces heureuses coïncidences. Ton soutien, tangible, authentique, est d'un réconfort inestimable. Ta porte est toujours ouverte et pour cela, je te suis reconnaissante! Un merci tout particulier à Anne-Marie, pour ton attention discrète mais bien présente.

Catherine, un immense merci aussi pour ton soutien indéfectible. Notre randonnée belge rocambolesque, des sentiers de randonnée aux balades en kayak, jusqu'au festival improbable et nuit à la scoute, restera gravée dans ma mémoire. Nos discussions et nos échanges intellectuels sont tout aussi enrichissants. Tu sais à quel point ces derniers mois ont été difficiles pour moi, et ta présence a été plus que réconfortante. Merci. Johanne et Bénédicte, que de souvenirs dans ces refuges! La nage irrépressible de Béné dans les eaux glacées des lacs, et Johanne, impossible à suivre dans les montées ! Aux Castors, Adri, Nat, Thib, Anton et Nicolas, quel bonheur de partager ma passion pour la nature avec vous ! À quand notre prochaine escapade matinale pour un affût ? A quand une soirée à refaire le monde autour d'une bibiche bien méritée?

Un grand merci à mes parents, dont l'exigence m'a donné la ténacité nécessaire pour toujours continuer, même dans les moments difficiles. Et un merci tout particulier à ma grand-mère qui, du haut de ses 100 ans, a toujours cru en moi, parfois même plus que moi-même.

Je conclus en exprimant ma profonde gratitude envers Antoine. C'est grâce à toi que j'ai trouvé l'élan nécessaire pour entamer cette thèse. Merci de m'avoir fait grandir et de m'avoir permis de me faire enfin confiance.

Contents

Abstract iii

Remerciements v

Contents ix

List of Figures xv

List of Tables xxiii

List of acronyms and abbreviations xxvii

Introduction 1
A planet under threat . . . 1
Recognizing Land Cover as an Essential Climate Variable . . . 2
Satellites, a powerful tool for global Land Cover mapping . . . 4
Land cover from a remote sensing perspective . . . 5
Crafting Land Cover data for climate model integration . . . 6
Land Cover map validation and uncertainty . . . 7
Objectives . . . 8
Outline . . . 10

Author contribution 13

1 Uncovering 29 Years of Global Land Cover Transformations through Harmonized Satellite Streams 15
1.1 Introduction . . . 17
1.2 Material and Methods . . . 18
1.2.1 Harmonized pre-processing of multi-sensor radiance to 7-day global composites . . . 19
1.2.2 Decoupling the LULC mapping from the LCC detection 20
1.2.3 LULC change analysis at various scales . . . 23
1.2.4 Land cover change validation . . . 24
1.3 Results and discussion . . . 25

1.3.1 Global land use changes . . . 25
1.3.2 Spatial repartition of land use changes . . . 33
1.3.3 Validation . . . 37

2 A Stratified Random Sampling Approach for Binary Product Comparison 43
2.1 Introduction . . . 45
2.2 Material . . . 49
2.2.1 Potential products to build the CCI global map of open water bodies . . . 49
2.2.2 Auxiliary datasets . . . 49
2.3 Method . . . 50
2.3.1 Qualitative assessment of input water body maps . . . 50
2.3.2 Generating a global map of open water bodies and ocean at 150m . . . 52
Combination of water body products . . . 52
Consolidation . . . 52
Spatial resampling . . . 52
Differentiation of inland/ocean Water . . . 52
User tool . . . 53
2.3.3 Quantitative thematic assessment . . . 53
Sampling scheme . . . 53
Generation of the validation database . . . 54
Accuracy assessment . . . 55
2.4 Results . . . 56
2.4.1 The CCI global map of open water bodies . . . 56
2.4.2 Accuracy assessment . . . 58
2.4.3 Assessing total water surface . . . 62
2.5 Discussion . . . 63
2.5.1 Comparing the capacity of sampling schemes to sample correct and incorrect pixels . . . 64
2.5.2 Comparison with the global 3 arc-second water body map 65
2.5.3 Permanent versus temporary water bodies . . . 66
2.6 Conclusion . . . 67

3 Quantifying Global Plant Functional Type Composition at the Pixel Level for Climate Models 69
3.1 Introduction . . . 71
3.2 Input data . . . 72
3.2.1 CCI MR LC products (150–300 m) . . . 72
3.2.2 High-resolution auxiliary datasets . . . 73
Surface water product (30 m) . . . 73
Tree canopy cover product (30 m) . . . 74
Tree canopy height product (30 m) . . . 74

Built-up product (38 m) 74
3.2.3 Zonation products 74
3.3 PFT dataset development 75
3.3.1 Static pixels 75
General considerations induced by the FAO LCCS and the LC legend 76
Water fraction 79
Tree cover classes 79
Cropland classes 81
Sparse vegetation classes 82
Shrubland classes 83
Urban class 83
Water body class 84
Bare area classes 84
Permanent snow and ice class 85
Tree fraction leaf type and leaf phenology 85
Assigning PFT fraction to the global extent 86
3.3.2 Pixels experiencing LC change 86
3.4 The CCI PFT dataset 87
3.5 Discussion 92
3.5.1 Comparison between the CCI PFT dataset fractions (PFT_{local}) and the global CWT table approach (PFT_{global}) 92
Tree cover 92
Shrub cover 94
Natural and managed grasses 95
Water 96
Bare 96
Built fraction 97
Permanent snow and ice 97
3.5.2 Evaluation of a land surface model using the CCI PFT dataset 97
3.6 Conclusion and perspectives 98

4 Pilot Study on Land Cover Categorical Uncertainty 105
4.1 Introduction 107
4.2 Study sites and data 109
4.2.1 Study sites 109
4.2.2 Satellite imagery 109
4.2.3 Reference data for the LC classification 110
4.3 Methods 111
4.3.1 Preprocessing scheme 112
Monte Carlo simulations 113
Seasonal compositing 113

4.3.2 LC classification scheme 118
Reference dataset preparation 118
Classifier description 118
4.3.3 Uncertainty in the classification scheme 119
Non-spatially explicit LC maps uncertainty 120
RF contribution to uncertainty 120
Pixel-wise LC uncertainty and ensemble most probable LC map 120
4.4 Results and discussion 122
4.4.1 Seasonal compositing strategy impact on reflectance uncertainty 122
4.4.2 Non-spatially-explicit LC uncertainty 124
4.4.3 RF uncertainty contribution to LC map uncertainty . . 126
4.4.4 LC map* and pixel-wise uncertainty indicators 128
4.4.5 Pixel-wise uncertainty indicators 132
4.4.6 Comparison against LC maps of majority 133
4.5 Conclusions 137

Conclusions and perspectives **139**
Summary of the principal contributions 139
What do harmonized satellite data streams tell us about the global LC transformations over the past 30 years? 140
Sampling design tailored to compare and select the best available LC products 141
How can we provide a spatially explicit quantification of PFT composition using harmonized datasets at multiple scales? 142
Pilot study on LC uncertainty 143
Perspectives 144

5 Appendix **149**
A The CCI MR LC processing chain 151
A.1 Data 151
A multisensor archive 151
Auxiliary data 152
A.2 Pre-processing: from L1b to seasonal composites 152
A.3 Land cover and land cover change legends 153
B Complementary information about the CCI PFT dataset description 157
Tree fraction leaf type and leaf phenology 157
C Supplementary materials to Ch4. LC uncertainty 167
C.1 Uncertainty analysis 167
Uncertainty analysis diagrams 167
Monte Carlo simulations 169
C.2 Methodology for retrieving preprocessing uncertainty . 169

Auxiliary data for the preprocessing 169
Sentinel-3 OLCI L1B uncertainty 170
Aerosol optical depth uncertainty 173
Cloud detection uncertainty 173
Atmospheric correction 177
C.3 Complementary results to land cover uncertainty 178
The most probable land cover map and pixel-wise uncertainty indicators 178
Comparison to the maximum frequency uncertainty . . 179

Bibliography **187**

List of publications **219**

List of Figures

1 The overall research approach articulating the four objectives of this thesis. 10

1.1 Schematic representation of the methodology developed to derive global annual LC maps from the baseline global LC map and the LCC, detected and delineated at 1 km and 300 m, respectively. . . 19
1.2 EO long-term time series built on the entire archive of five different space missions. 20
1.3 Cumulative area of land changing from one IPCC land category to another between 1992 and 2020, as mapped from satellites at the global scale and including areas changing several times over the period (i.e. less than 0.5% of the changed area). 27
1.4 Cumulative areas of losses and gains (Mkm^2) in IPCC land categories estimated at each annual time step between 1992 and 2020. The left-hand column represents the total area of all observed losses (8.4 Mkm^2) cumulated on a yearly time step from 1992 to 2020 and the corresponding percentage of each concerned IPCC land category. The right-hand column represents the total area of all observed gains across all IPCC land categories over the same period. Each stream connecting the blocks from left to right represents the area converted from one category to another, considering all years of the period 1992-2020. The width of the streams indicates the relative importance of the conversion from one land category to another. 30
1.5 Per-year evolution of net change per IPCC land category at the global scale (in Mkm^2) highlights the significant increase of anthropogenic land use land cover conversions at the expense of all the (semi)-natural land cover types. This summarizes the fast increase and then the stabilization of cropland extent, the steady urban expansion and the slight grassland increase while forest and shrubland are the most impacted land cover. 32

1.6 Cumulative annual evolution of the share of (semi-)natural vegetated areas eroded by anthropogenic land use land cover change processes according to nature conservation status on a global scale. Only the land change detected after the year of the protected area establishment as reported by (UNEP-WCMC, 2019) is considered for the green curve. 34
1.7 Global distribution of anthropogenic LULC changes as observed by satellite during the 29 years. The cropland and settlement expansion can be observed respectively in South America, East Asia and Europe (top) while the forest loss is more widely distributed around the world and the cropland loss is much related to urban development (bottom). Regional trajectories of land conversion depict very contrasting land dynamics for six different regions delineated by a white polygon. The left-hand column represents the cumulative area and proportion of all observed losses by IPCC land category in each year from 1992 to 2020. The right-hand column represents the cumulative area of all observed gains per IPCC land category per year over the same period. Each stream connecting the blocks from left to right represents the cumulative area converted from one category to another, considering all annual transitions over the period 1992-2020. The width of the streams indicates the relative importance of the conversion to another category and the colour legend is the same as in Figure 1.4. 35
1.8 Four types of country or region profiles can be distinguished from the relationship between the net LCC associated with anthropogenic processes and population change in their population between 1992 and 2020. The respective geographical aggregation of countries into the 26 regions was defined after Stehfest et al. (2014). The semi-natural reservoir fraction per inhabitant is computed as the ratio between the proportion of remaining (semi-)natural vegetated areas for a given region and the number of inhabitants of this region. 36
1.9 The global LU LC map 2020 describes the world's landscape into 22 global classes with a spatial resolution of 300 m and the seasonality of 3 land surface variables weekly: the vegetation greenness, the snow cover and the burned areas (`https://maps.elie.ucl.ac.be/CCI/viewer/`). 41

2.1 Flowchart outlining the compilation of the CCI global map of open water bodies and the quantitative thematic assessment of this study. 48
2.2 The CCI global map of open water bodies. 57

2.3 Examples illustrating the complementarity of selected input data sources to the CCI global map of open water bodies: (**a**) the lack of continuity in the GIW v1.0 river network was complemented by the GFC-datamask; (**b**) the lack of continuity in the GFC-datamask river network was complemented by the GIW v1.0; (**c**) artifacts from the Scan Line Corrector-off issue in Landsat ETM+ in the GFC-datamask were compensated with inclusion of water from the GIW v1.0. (**d**); GIW v1.0 unprocessed or atmospherically-contaminated areas were filled with the GFC-datamask; (**e**) detections in the SAR-WBI in areas north of 68°N, not included in other water body products; (**f**) map updating with the SAR-WBI for more recent water bodies. 58
2.4 Effects of consolidation of input water bodies: (**a**) removal of commission errors in the GIW v1.0 dataset due to seasonal water events; (**b**) removal of commission errors due to black lava detected as water in the Landsat-based products; (**c**) replacement of the GIW v1.0 dataset with the SRTM-SWBD in case of incomplete characterization of islands; (**d**) removal of water commission over glaciers with the RGI dataset. 59
2.5 Location of the 2110 samples (area of 150 m × 150 m) selected for the validation of the water body products. For each sample, the Level-2 stratum is specified (land agreement, water agreement and discrepancies). 60

3.1 Flowchart depicting the creation of the PFT map series for stable and dynamic pixels from the CCI MRLC map series, ensuring legend harmonization, and using high-resolution auxiliary datasets to provide PFT fractions. Large solid colored squares illustrate 300m pixels described by the FAO LCCS categorical legend. Squares on the right-hand side represent the resulting PFT composition per pixel. 76
3.2 Implementation of the FAO land cover classification system to the description of the PFT fractions. 79
3.3 Synoptic view of the decision rules applied to derive pixel-level functional type composition by LC class by combining auxiliary datasets and the FAO LCCS used to describe the CCI MR LC classes. For each LC class, a systematic sequence of steps is applied to derive the fraction composition of each pixel from the water % to the snow/ice %. The dashes represent subtractions. See Table 3.1 for more comprehensive class descriptions. 80

3.4 For each year within the period, the CCI MRLC map categories (a) ensure both spatial and temporal consistency of the (b) 14 PFT fractions generated (one for each of the 14 PFTs). Data values at a resolution of 300 meters indicate the percentage cover (ranging from 0% to 100%) of the PFT for the given year. 88
3.5 (a–h) Percentage cover in 2010 for the 14 PFTs included in the PFT_{local} data product at a spatial resolution of 0.25° × 0.25°. . . . 89
3.5 (a–h) Percentage cover in 2010 for the 14 PFTs included in the PFT_{local} data product at a spatial resolution of 0.25° × 0.25°. . . . 90
3.6 (a) Area distribution, in million km^2, for each PFT of the 2010 PFT_{local} dataset and corresponding proportions (%). (b) Proportion of aggregated PFT types of the 2010 PFT_{local} dataset and the distribution of subtypes. 91
3.7 Percentage cover in 2010 for the built, total tree, grass, and inland water PFTs in Amsterdam, the Netherlands, in the PFT_{local} product. 92
3.8 Percent difference in areal fraction between PFT_{local} and PFT_{global}. Positive values indicate an increase in the areal fraction of PFT_{local} compared to the global fraction. 93
3.9 PFT with the largest increase (a) and largest loss (c) in coverage within 0.25° x 0.25° pixels in the PFT_{local} dataset compared to the PFT_{global} and corresponding fractions gained (b) and lost (d). White areas remained stable in both PFT datasets. 93
3.10 Distribution of the tree cover fraction (%) in the rainfed cropland class pixels over (a) Africa, (b) Ibadan (Nigeria), and (c) Kisangani (DRC). Gray pixels belong to other LC classes. 94
3.11 Comparison of reduced shrub fraction in the PFT_{local} product, constrained to the shrubland class, against the PFT_{global} fraction. . . . 95
3.12 Comparison of JULES PFT distributions to both the CWT (PFT_{global}) and PFT (PFT_{local}) products for major vegetation types. Rows show each major surface type (Tree, Shrub, Grass, Bare), whilst rows show (a) JULES vegetation distribution compared to the global CWT, (b) the same compared to new $PFTl_{ocal}$ distributions, (c) the difference between (a) and (b), where green (pink) indicates positive or negative anomalies evaluate closer to 0 (further away from 0) using new PFT_{local} distributions, (d) absolute latitudinal average fractions for each major vegetation type from CWT, PFT, and JULES. 98

4.1 (a) Spatial distribution and extents of the 3 study sites. Sentinel-3 OLCI false-color composites for the sites in (a) Europe–EU, (b) Africa–AF, and (c) South America–SA. These are typical infrared false-color composites with 885 nm Near-Infrared (NIR) band in the red channel, 665 nm Red band in the green channel, and 560 nm green band in the blue channel. Composites dates correspond to the first period (see Table 4.1). 110
4.2 Overview of the workflow for the error identification and uncertainty propagation considered in the processing chain split into preprocessing and classification. 111
4.3 Monte Carlo simulations applied to the preprocessing stage, which converts TOA reflectance to surface directional reflectance. Simulations involve randomizing reflectance measurements, cloud detection, and atmospheric correction. 114
4.4 Example of twelve Monte Carlo variants of 490 nm surface reflectance (SR) for the African site (52 week composite). Colours indicate the deviation of a variant from the pixel-wise ensemble mean (Quast et al., 2024 *in preparation*). 116
4.5 Example of Monte Carlo variants of 885 nm surface reflectance (SR) for the African site (52 week composite). Colours indicate the deviation of a variant from the pixel-wise ensemble mean (Quast et al., 2024 *in preparation*). 117
4.6 Uncertainty retrieval at the classification stage. Variability in OA and class areas among variants serve as non-spatially explicit uncertainty indicators. Pixel-wise uncertainty indicators (ERP*, MaxP*, and Std*) are derived from the mean class membership probability vector of the ensemble. The most probable LC map in the ensemble is derived from MaxP*. 119
4.7 Quantification of the RF classifier contribution to the LC accuracy calculated from 30 repeated classifications per MSC variant. . . . 121
4.8 (a) Box plot depicting the relative uncertainty distribution of seasonal land surface reflectance across sites for the 52-week MSC duration. (b) Box plot of the relative uncertainty distribution of seasonal land surface reflectance across wavebands for Africa, according to the season duration (weeks). (c) OLCI mean revisit time with two satellites: 2 days at the equator (red) and less than 0.5 days at high latitudes (blue) (`https://sentinels.copernicus.eu/web/sentinel/user-guides/sentinel-3-olci`). (d) Bar plots expressing the reduction in uncertainty as a percentage, per band, as the composite period changes from 7 weeks for the Africa site and 13 weeks for the Europe and South America sites to 52 weeks. 123

4.9 Per-site relationship between class area uncertainty (CV) and (a) the mean edge density per class, and (b) the class area dominance. (c) Relationship between class area uncertainty and class dominance per LC categories. 126
4.10 (a) Probability density functions of OA per site, combining the Monte Carlo randomization process and RF contribution to uncertainty. Each distribution represents 100 x 30 classifications. (b) Box plot comparing OA with and without mitigating the RF contribution to uncertainty. The lower and upper boundaries of the box represent the 25th and 75th percentiles, respectively, with the line inside being the median. Error lines depict the 10th and 90th percentiles, while diamonds highlight data outside this range. . . 127
4.11 (a) EU, (b) AF, and (c) SA. From top to bottom: most probable LC map of the Monte Carlo ensemble (LC map*) determined by the LC class with the maximum probability (legend in Table A.3), the maximum probability (MaxP*), standard deviation (Std*), and the equivalent reference probability (ERP*). All variables are derived from the average vector of class membership probabilities of the Monte Carlo ensemble. 129
4.12 EU site. More detailed illustration of the spatially explicit uncertainty LC map*, MaxP*, and ERP* indicators. 130
4.13 Zoomed-in section of the EU site illustrates (a) Salt-and-pepper effect of a randomly selected LC variant compared to (b) the more compact class patches in the LC map*. (c) Comparison of connectivity value distributions between LC map variants and LC map* across EU, AF, and SA sites. (d) Percentage difference in average frequency of connectivity values between LC map* and all variants across sites. Negative values indicate lower average frequency in LC map*. 131
4.14 (a) Connectivity index maps per site, where a value of 1 denotes an isolated pixel of a class, while 9 indicates a pixel entirely surrounded by pixels of the same class. (b) Boxplot displaying the distribution of MaxP*, ERP* and Std* values per connectivity value. 134
4.15 EU site. Distribution of ERP*, MaxP* and Std* indicators across LC classes. nat. veg.: natural vegetation, TC: tree cover, Br: broadleaved, De: deciduous, Ne: needleleaved, Ev: evergreen, c. to o.: close to open, herb.: herbaceous cover. 135
4.16 EU site. Illustration of a most probable LC map (top) derived from the maximum frequency of LC variants (bottom). 136

B.1 (a–h) Absolute differences (percentage of pixel) between the 2010 PFT_{local} dataset and corresponding PFT_{global} maps (i.e., applying the global cross-walking scheme) for the 14 PFT types. The spatial resolution is 0.25 x 0.25 degrees. 158

B.1 (a–h) Absolute differences (percentage of pixel) between the 2010 PFT_{local} dataset and corresponding PFT_{global} maps (i.e., applying the global cross-walking scheme) for the 14 PFT types. The spatial resolution is 0.25 x 0.25 degrees. 159
C.1 Uncertainty analysis diagram template 168
C.2 Uncertainty analysis diagram for the processing from TOA reflectance ρ^{t} to surface directional reflectance ρ. Dashed lines indicate minor sources of error not considered in this study. 169
C.3 Monte Carlo processing of TOA reflectance to surface directional reflectance (SDR) randomizing reflectance measurements, cloud detection, and atmospheric correction. 170
C.4 Monte Carlo atmospheric correction randomizing estimates of aerosol optical depth (AOD). 171
C.5 Example of Monte Carlo variants of 885 nm TOA reflectance for the African site. The colour indicates the deviation from the ensemble mean TOA reflectances. (Based on Sentinel-3A OLCI L1B EFR granule 2020-05-28; cycle 058, relative orbit 363, frame 2700). 174
C.6 Examples of Monte Carlo variants of total aerosol optical depth (AOD) for the African site. (Based on CAMS total aerosol optical depth data; co-registered with Sentinel-3A OLCI L1B EFR granule 2020-05-28; cycle 058, relative orbit 363, frame 2700). 175
C.7 Examples of Monte Carlo variants of total aerosol optical depth (AOD) for the African site. The colour indicates the deviation from the ensemble mean AOD. (Based on CAMS total aerosol optical depth data; co-registered with Sentinel-3A OLCI L1B EFR granule 2020-05-28; cycle 058, relative orbit 363, frame 2700). 176
C.8 Probabilities of false cloud omission and false cloud discovery over land surface as a function of the threshold value t^{c}. The graph of the probability distribution of the threshold value (green) refers to the axis on the right-hand side. 177
C.9 Examples of Monte Carlo variants of 490 nm surface directional reflectance (SDR) for the African site. The colour indicates the deviation from the ensemble mean SDR. (Based on Sentinel-3A OLCI L1B EFR granule 2020-05-28; cycle 058, relative orbit 363, frame 2700). 179
C.10 Examples of Monte Carlo variants of 885 nm surface directional reflectance (SDR) for the African site. The colour indicates the deviation from the ensemble mean SDR. (Based on Sentinel-3A OLCI L1B EFR granule 2020-05-28; cycle 058, relative orbit 363, frame 2700). 180
C.11 AF site. More detailed illustration of the spatially explicit uncertainty LC map*, PMax*, and ERP* indicators. 181
C.12 SA site. More detailed illustration of the spatially explicit uncertainty LC map*, PMax*, and ERP* indicators. 182

C.13 AF site. Illustration of spatially explicit uncertainty indicators derived from the frequency of LC variants. 185
C.14 SA site. Illustration of spatially explicit uncertainty indicators derived from the frequency of LC variants. 186

List of Tables

1 Products and requirements for LC ECV (GCOS, 2022) 3

1.1 Land area (in Mkm²) corresponding to persistence, loss, gain, total, net and swap change between IPCC categories from 1992 to 2020 as estimated by pixel counting adjusted for pixel-area latitudinal variation. Persistence indicates pixels where no change in classification is observed. Gains and losses represent the cumulative increase and decrease in land cover, respectively, over the 29-year period. Formally, swapping is defined as twice the minimum of the gain and loss. This occurs when a land cover class transitions to another class in one location, while a gain of similar area in the same land cover class compensates for this loss (Pontius et al., 2004). 26
1.2 Global legend of the 22 LC classes, based on the UN LCCS and their corresponding area as observed by satellite (Mkm² and percentage of the global ice-free land area including inland water bodies) considering the varying area of each pixel on the globe. 28
1.3 Relative percentages of IPCC category area changes compared to their corresponding areas in 1992. Fraction of swap change concerns the gross change of the class. 31

2.1 Available global and near-global EO-derived product of permanent inland water bodies with their references, extent, source, pixel resolution, and thematic validation 46
2.2 Characteristics of the water body data products selected to compile the CCI global map of open water bodies. 50
2.4 Set of options included in the user tool. 53
2.6 Input water body maps and CCI water body map with their accuracy estimates in percent (%) based on an evaluation of 2110 samples. 61
2.7 Accuracy results, in percent (%), for the error-prone Stratum 3 (1030 samples). 62
2.8 Probability, in percent (%), to sample correctly and incorrectly classified pixels depending on the sampling scheme. 65
2.9 G3WBM accuracy values for the global and error-prone area samples (Stratum 3), in percent (%). 66

3.1 Non-zero PFTs fractions permitted per CCI MR LC classes. 77
3.2 Global areal cover (1000 km²) of each PFT by LC class for 2010 in the PFT_{local} product. 100
3.3 Percentage PFT composition by class for 2010 calculated as an area-weighted mean over all pixels of the class globally. 102

4.1 Seasons selected for seasonal compositing 115
4.2 Mean overall accuracy (percentage) computed from 100 land cover maps obtained for each study site using a RF applied on the 100 variants of mean seasonal composites. The standard deviation indicates the impact of the processing chain set-up of 100 classifications on land cover map uncertainty. 125
4.3 Mean overall accuracy (percentage) computed from an ensemble of 30 RF applied on 100 land cover maps obtained for each study site using 100 variants of mean seasonal composites. The standard deviation indicates the impact of the entire processing chain made of 3000 classifications on land cover map uncertainty. 127
4.4 Mean overall accuracy (percentage) computed from an ensemble of 30 RF applied on 100 land cover maps obtained for each study site using 100 variants of mean seasonal composites. The contribution of the RF random component to uncertainty is expressed in comparison to OA std across the entire processing chain (see Table 4.3). 128

A.1 Types of LCC detected at 1km. Note that changes in the settlement class are detected in a separate processing chain. 154
A.3 LCCS legend of the CCI MR LC product 155
A.4 Correspondence between LCCS codes of the CCI LC class aggregation used to assess thematic discrepancies between the classifications of the seasonal composite ensemble mean and realizations. See table A.3 for the labels associated with the LCCS codes. 156
B.1 Global areal cover (1000 km²) of each PFT by land cover class for 2010 based on the most recent version of the global CWT applied to v2.0.8 of the CCI MR LC map. 160
B.2 Percentage PFT composition by class based on the most recent update to the global cross-walking table. 162
B.3 Default land cover to plant functional type cross-walking table from (Poulter et al., 2015). 164
C.1 Relative standard uncertainty of pixel-wise seasonal land surface reflectance. The table lists the interquartile ranges $(Q1, Q3)$ of pixel-wise relative standard uncertainties (Quast et al., 2024 *in preparation*). 167

C.2 EU site. RF model accuracy per site and per class, with f1-score, precision, recall, and support as mean ± std, for the 100 variants of mean seasonal composites. 183
C.3 AF site. RF model accuracy per site and per class, with f1-score, precision, recall, and support as mean ± std, for the 100 variants of mean seasonal composites. 183
C.4 SA site. RF model accuracy per site and per class, with f1-score, precision, recall, and support as mean ± std, for the 100 variants of mean seasonal composites. 183
C.5 Matrice of overall agreement between LC map* and LC map Maj . 184

List of acronyms and abbreviations

(A)ATSR	(Advanced) Along Track Scanning Radiometer
ADD	Antarctic Digital Database
AF	Africa
AFOLU	Agriculture, Forestry and Other Land Use
AGB	Above Ground Biomass
AOD	Aerosol Optical Depth
API	Application Programming Interface
ARD	Analysis Ready Data
ASAR	Advanced Synthetic Aperture Radar
ATBD	Algorithm Theoretical Basis Document
AVHRR	Advanced Very High Resolution Radiometer
BC	Brockmann-Consult
BD	Broadleaved Deciduous
BE	Broadleaved Evergreen
BIPM	Bureau International des Poids et Mesures
BRDF	Bidirectional Reflectance Distribution Function
CCI	Climate Change Initiative
CCI-LC	Climate Change Initiative Land Cover
CDR	Climate Data Record
CEOS	Committee on Earth Observation Satellites
CMC	Climate Modelling Community
CMIP	Coupled Model Intercomparison Project
CRS	Coordinate Reference System
CV	Coefficient of variation
CWT	Cross Walking table
DMA	Defense Mapping Agency
DTE	Digital Twin Earth
ECMWF	European Centre for Medium-Range Weather Forecasts
ECV	Essential Climate Variable
Envisat	Environmental Satellite
EO	Earth Observation
EODC	Earth Observation Data Cubes
ERP	Equivalent Reference Probability

ESA European Space Agency
ESM Earth System Models
EU Europe
EUMETSAT European Organisation for the Exploitation of Meteorological Satellites
FAO Food and Agriculture Organization
FR Full Resolution
G3WBM Global 3 Arc-Second Water Body Map
GCOS Global Climate Observing System
GCS Global Coordinate System
GDAL Geospatial Data Abstraction Library
GEDI Global Ecosystem Dynamics Investigation
GFC Global Forest Change
GHGs GreenHouse Gases
GHSL Global Human Settlement Layer
GIW Global Inland Water
GLIMS Global Land Ice Measurements from Space
GLOWABO Global Water Bodies database
GLWD Global Lakes and Wetlands Database
GMST Global Mean Surface Temperature
GPP Gross Primary Productivity
GSHHS Global Self-consistent, Hierarchical, High-resolution Shoreline
GTOS Global Terrestrial Observing System
GUF Global Urban Footprint
GUM Guide to the expression of uncertainty in measurement
HMM Hidden Markov Model
HR High Resolution
IPBES Intergovernmental Science-Policy Platform on Biodiversity and Ecosystem Services
IPCC Intergovernmental Panel on Climate Change
ISO International Organization for Standardization
ISODATA Iterative Self-Organizing Data Analysis Technique
JCGM Joint Committee for Guides in Metrology
Landsat Land remote sensing Satellite
LC Land Cover
LCC Land Cover Change
LCCS Land Cover Classification System
LPV Land Product Validation
LS Land Surface
LSM Land Surface Model
LTDR Long-Term Data Record
LULC Land Use and Land Cover
MC Mean Compositing

MERIS	Medium Resolution Imaging Spectrometer
MOD44W	MODIS/Terra Land Water Mask
MODIS	Moderate Resolution Imaging Spectroradiometer
MR	Medium Resolution
MRLC	Multi-Resolution Land Characteristics
MSC	Mean Seasonal Composite
ND	Needleleaved Deciduous
NDVI	Normalized Difference Vegetation Index
NE	Needleleaved Evergreen
NIR	Near InfraRed
NLCD	National Land Cover Database
NOAA	National Oceanic and Atmospheric Administration
OA	Overall Accuracy
OECD	Organization for Economic Co-operation and Development
OLCI	Ocean and Land Colour Instrument
PA	Producer Accuracy
PFT	Plant Functional Types
PROBA-V	Project for On-Board Autonomy-Vegetation
PSF	Point spread Function
PUG	Product User Guide
QA	Quality Assurance
RF	Random Forest
RGI	Randolph Glacier Inventory
RMS	Root Mean Square
RR	Reduced Resolution
S1	Sentinel-1
S2	Sentinel-2
S3	Sentinel-3
SA	South America
SAR	Synthetic Aperture Radar
SCAR	Scientific Committee on Antarctic Research
SPOT-VGT	Satellite Pour l'Observation de la Terre - Vegetation
SR	Surface Reflectance
SRTM	Shuttle Radar Topography Mission
SWBD	SRTM Water Body Database
TOA	Top Of Atmosphere
UA	User Accuracy
UCLouvain	Université catholique de Louvain
UN	United Nations
UNEP	United Nations Environment Programme
UNFCCC	United Nations Framework Convention on Climate Change
VIIRS	Visible Infrared Imaging Radiometer Suite
WB	Water Body

WBI	Water Body Indicator
WCMC	World Conservation Monitoring Centre
WDPA	World Protected Areas Database
WGCV	Working Group on Calibration and Validation
WGS84	World Geodetic System 84
WVS	World Vector Shorelines

Introduction

A planet under threat

Already in the 1930s, the close link between the increase in temperature of the Earth's surface and the concentration of CO_2 was established and observed in terrestrial stations (Callendar, 1938). In the late 80's, as the Earth's surface continued to warm, the signal of temperature increased and emerged from the noise of natural variability (Mann et al., 1999, 2004; Hawkins et al., 2020). It was not until the 2000s that the convergence of evidence led to the conclusion that warming of the climate system is unequivocal (Solomon et al., 2007). The average temperature from 2006 to 2015 has increased by 0.87°C [0.75-0.99°C] at the surface of the Earth since the pre-industrial period (1850-1900). But on the land, the average temperature has increased twice as much (Arneth et al., 2019). Assuming a similar rate of increase of 0.2°C per decade, the global average temperature rise is likely to reach 1.5°C by 2030-2054 (Masson-Delmotte et al., 2022). The temperature increase is clearly attributable to anthropogenic emissions caused by economic and population growth (Bindoff et al., 2014; Pachauri and Meyer, 2014).

The consequences of climate change are societal and environmental (Foley et al., 2005; Díaz et al., 2019; van der Geest et al., 2019). Land provides the basis for human livelihoods and well-being through the supply of food, fresh water, settlements and other ecosystem services (Arneth et al., 2019). Terrestrial biomes play key roles in water, energy and carbon balances through a complex interplay at different nested scales (Bonan, 2008). But it is observed that climate change shifts the climate zones towards the poles and higher elevations leading to changes in the abundance and seasonal activities of wildlife and vegetation (e.g., earlier arrival of spring) (Rosenzweig et al., 2008; Urban, 2015; Parmesan and Yohe, 2003). A warmer climate and earlier spring also increase the conditions for wildfire initiation and maintenance (Richardson et al., 2022; Bradstock et al., 2009; Westerling A L et al., 2006) and risk of frost damage (Unterberger et al., 2018; Augspurger, 2013). Continued mass loss of terrestrial glaciers and decreasing duration and the persistence of snow cover, particularly in spring, have been documented (Pörtner et al., 2019; Derksen and Brown, 2012; Chen et al., 2015b). Extreme weather events such as heat-

waves, droughts and, conversely, heavy precipitation have increased in frequency and severity since the 1950s worldwide, with spatial variations (IPCC, 2014, 2021). Longer and more intense droughts imply a deficit in soil moisture. Increased evapotranspiration enhances plant stress and survival and reduces crop yields (Seleiman et al., 2021; Lobell et al., 2011).

Recognizing Land Cover as an Essential Climate Variable

Alarming assessments on the causes and consequences of climate change called for action. In 2015, the Paris Agreement defined the objective of capping the global average temperature at well below 2°C compared to pre-industrial levels and called for continuing efforts to limit it to 1.5°C. Human activities are undoubtedly the source of the problem but can play a key role in reducing climate change (Fyson and Jeffery, 2019), providing opportunities for mitigation, adaptation (Nabuurs et al., 2022; Pongratz et al., 2021), and meeting the sustainable development goals (Herold, 2009; Latham et al., 2014). To achieve the long-term climate goals, which include greenhouse gas reduction, climate mitigation and adaptation, as established in the United Nations Framework Convention on Climate Change (UNFCCC) Paris Agreement (UNFCCC, 2015), it is necessary to strengthen scientific knowledge through research and systematic observation of the climate system (Article 7).

In this context, the Global Climate Observing System (GCOS) has identified 54 Essential Climate Variables (ECVs). These ECVs are technically observable variables that make a significant contribution to our understanding of global climate conditions, enabling more accurate predictions of climate change and attribution of underlying causes (GCOS, 2022). Recognizing the importance of Land Cover (LC) in this framework, it was designated as an ECV by the GCOS (GCOS, 2006; Bojinski et al., 2014).

"LC" is defined as the observed biophysical cover of the Earth's surface (Di Gregorio and Jansen, 2005; Turner et al., 1993). Previously considered as a local environmental issue, Land Use (LU) LC Change (LCC) is increasingly affecting the Earth system (Foley et al., 2005; Houghton and Nassikas, 2017; Venter et al., 2016). LCC affects greenhouse gas emissions, surface energy balance, induced by modified albedo, evapotranspiration, and roughness (Pielke et al., 2011; Mahmood et al., 2014; Pielke, 2005; Brovkin et al., 2006; Dale, 1997; Liu et al., 2017). LCC also causes habitat loss and fragmentation, two major drivers of the global biodiversity crisis (Pouzols et al., 2014). LCC is the second-largest source of anthropogenic CO_2 emissions to the atmosphere (3.8 ± 0.6 GtC yr−1 in the 2011–2020 decade) (Friedlingstein et al., 2022). LULCC and forestry, of which deforestation is the main driver, accounts for about (45%) of total net CO_2 emissions, or 5.9 ± 4.1 $GtCO_2$-eq yr-1 (IPCC, 2022). It is also the most uncertain source with uncertainties ranging from 34.3% up to 50% (Smith et al., 2014; Perugini et al., 2021). Contributions to

this uncertainty are manifold from the representation of the global vegetation or processes implemented in models (Bastos et al., 2020; Houghton et al., 2012; Pitman et al., 2009; McGlynn et al., 2022), flux definitions (Pongratz et al., 2014), land management practices (Houghton et al., 2012), biomass density estimates (Houghton, 2005), and estimations of LC and rates of change (Houghton et al., 2012; Bastos et al., 2020, 2021).

GCOS experts, guided by valuable input from a diverse user community, have established distinct levels of requirements for each ECV that are found essential for advancing regional and global climate modelling. To meet these requirements, LC ECV products must have a minimum spatial resolution of 300 meters and cover a period from 10 to 50 years, enabling the assessment of historical changes. An annual update frequency is imperative to effectively detect inter-annual variations. Accuracy levels per class must be greater than or equal to a threshold of 80%, with an even higher expectation for the overall accuracy. Temporal stability, i.e. the persistence of accuracy over time, is a key parameter. It can be assessed through an independent assessment of accuracy carried out at several dates (Table 1). Given the primary objective of assessing changes in LC and capturing long-term trends, the emphasis on the stability of ECV products covering several dates is more important than meeting overall accuracy standards (GCOS, 2022).

Table 1: Products and requirements for LC ECV (GCOS, 2022)

Products	*	Unit	Values
Horizontal Resolution	G	m	100-300
	B		300-1 km
	T		1 km
Temporal Resolution	G	month	1
	B		12
	T		60
Timeliness	G	month	3
	B		12
	T		60
Time span	G	year	50
	B		10-50
	T		0 (once)

Continued on next page

Table 1: Products and requirements for LC ECV (GCOS, 2022) (Continued)

Uncertainty (2-sigma)	G	% for accuracy and errors of omission and commission and hectares for area estimates incl. 95 %confidence intervals	5
	B		20
	T		35
Stability	G	% for accuracy and errors of omission and commission and hectares for area estimates incl. 95 %confidence intervals	5
	B		15
	T		25

⋆ Goal (G) is the optimal requirement, while Breakthrough (B) is an intermediate level that, when achieved, significantly improves the targeted application, possibly enabling specific uses within climate monitoring. Different breakthrough values may be appropriate for varying applications. Threshold (T) is the minimum requirement to ensure data usefulness.

Satellites, a powerful tool to meet global Land Cover mapping requirements

Satellite instruments have been systematically collecting comprehensive Earth Observation (EO) data from the global land surface for decades. This space-based EO infrastructure represents a valuable tool for acquiring consistent observations of ECVs, aligning with the criteria set by the GCOS. These observations play a crucial role in diminishing uncertainties, thus supporting the effective implementation of initiatives like the Paris Agreement (GCOS, 2006; Hegglin et al., 2022).

Early attempts at repeated global LC mapping with multiple categories using highly automated processing chains relied on independent yearly classifications of EO data at 300 m into categorical LC classes (Defourny et al., 2007; Arino et al., 2008), followed by a series of annual LC classifications at 500~m (Friedl et al., 2010). Intercomparing classifications in time revealed large differences because of spurious year-to-year variability due to LC natural variations of the surface, misclassifications between thematically close LC classes, and the impact of classes with low accuracy (Friedl et al., 2010; Bontemps et al., 2012; Herold et al., 2008). To address this, researchers have used Hidden Markov Chain models to statistically determine the most likely change (Sulla-Menashe and Friedl, 2018; Bogaert et al., 2022). Alternative approaches rely on expert-based reconstruction models. Such methods incorporate data sources of different characteristics and resolutions assuming integrating them results in more consistent information (Winkler et al., 2021). More recent multi-class mapping initiatives yielded global annual map series spanning shorter periods (e.g. 5 years) using a single sensor with slightly higher spatial resolutions (PROBA-V at 100 m) (Buchhorn et al., 2020b).

The opening of the Landsat archive in 2008 (Woodcock et al., 2008) paved the way towards global High Resolution (HR) LC mapping at 30 m but the recent availability of Sentinel-2 (S2) A (2015) and S2 B (2017) at 10 m spatial resolution and 5 days frequency offers an unprecedented opportunity to characterize the land surface in even greater details. Multiclass LC products at 10 m or 30 m cover periods of 2 to 3 years (Zanaga et al., 2021, 2022; Gong et al., 2013, 2019). A larger variety of long-term time series exist but for single classes only like water bodies (Pekel et al., 2016), urban areas (Pesaresi et al., 2016) or tree cover (Hansen et al., 2013b). The longest map series currently available refers to consistent successive maps at a coarse resolution of 0.05° for a limited number of vegetation fractions of trees, short vegetation and bare soil (Song et al., 2018a) or LC classes (cropland, forest, grassland, shrubland, tundra, barren land, and snow/ice) (Liu et al., 2020). A step towards mapping the anthropogenic pressure on the land is the global LC land use map 2019 at 30 m (Hansen et al., 2022). Here, the map is described by a mix of LC categories (inland water, cropland, and permanent ice), continuous fractions (bare ground, built-up, wetlands), change (tree loss and gain), and vegetation parameters like tree height. Despite considerable effort, recently produced LC maps at 30 and 10 m do not fully meet the global requirements of the climate modelling community. These requirements include the provision of a global LC map series with annual updates, long-term coverage, consistency, accuracy and operational usability while maintaining a high spatial and thematic granularity, as prescribed by GCOS. In addition, there is often a lack of thorough documentation regarding LC typology, which hinders the validation and appropriate use and comparison of the respective datasets.

Land cover from a remote sensing perspective

In the context of the ever-increasing frequency of EO acquisitions, the common definition of LC, the observed biophysical cover of the Earth's surface, remains vague. In fact, there could be as many LC maps as there are observation time intervals under consideration. This concept has been explored in the Dynamic World solution developed by Google, the National Geographic Society, and the World Resource Institute (Brown et al., 2022). This solution produces diverse LC maps based on user-defined time intervals. Interestingly, Dynamic World assumes that one LC typology fits all users' needs, despite the observation time interval varying from any single observation to the entire satellite archive. This variable LC concept significantly impacts the interpretation of LCC and appears somewhat disconnected from the scientific literature.

To meet GCOS requirements, the needs of scientific communities engaged in climate research, global carbon budget analysis, and international reporting are frequently surveyed. Given the paramount importance placed on long-term consistency by these communities, a crucial improvement was identified—explicitly incorporating the time dimension into the definition of LC

across three interrelated aspects (Defourny and Bontemps, 2012). The term "LC" is defined as the commonly understood concept referring to its stable component. This stable component comprises the set of land surface features that remain constant over time, defining the LC independently of any sources of temporary or natural variability (e.g., trees). When there is a permanent modification of the intrinsic nature of the LC, such as a transition between two LCs (e.g., from forest to cropland), it is termed a "LCC"—the second component. The third dimension refers to changes that do not permanently alter its nature but disrupt its appearance or surface temporarily and, possibly occurring recurrently over the years. Vegetation phenology, snow cover, or burned areas fall into this category, representing land surface processes with pronounced seasonal variability often based on annual cycles.

The lack of a clear definition for LC classes in a map's legend results in thematic uncertainty (Defourny et al., 2012a). To allow creating a common understanding of the LC nomenclatures to produce datasets that can be reconciled at different scales, levels of detail and geographic locations, the United Nations (UN) Food and Agriculture Organization (FAO) developed a Land Cover Classification System (LCCS) (Di Gregorio and Jansen, 2005; Gregorio, 2016). This system ensures unambiguous and consistent LC class definitions, avoids overlaps between class boundaries and defines relationships between classes (Herold and Di Gregorio, 2012). It can be seen as a tool for creating exhaustive standardized LC nomenclatures based on a hierarchy of quantitative and qualitative criteria, using biotic and abiotic factors known as "classifiers" (Di Gregorio and Jansen, 2005; Gregorio, 2016). The framework's unique aspect is that it shifts the emphasis from describing a legend to using classifiers as building blocks to construct complex classes that are suitable for various classification systems, like the Plant Functional Type (PFT) scheme used in Chapter 3. This systematic yet flexible classification framework is independent of scale, level of detail of the landscape, and sensor-agnostic, thus meeting many user needs. In contrast, a typology (or legend) is the application of a classification system at a specific scale, over specific landscapes, using specific input data and classification methodologies (Di Gregorio and Jansen, 2005). The UN LCCS, recognized as an ISO standard, has gained widespread acceptance as it has been adopted by international programs like the IGBP (McConnell et al., 2002), GOFC-GOLD (Herold et al., 2009), and GCOS (GCOS, 2022).

Crafting global Land Cover information for climate model integration

LC maps serve as input to land surface models (LSM), playing a significant role in quantifying the historical and present-day land use and LCC impacts on climate (Fisher and Koven, 2020). In the field of LSMs, the global vegetation is typically represented using a simplified set of similarly behaving plant

types known as PFTs. These PFTs incorporate attributes related to plant characteristics such as physiognomy, phenology, climate preferences, which define the geographical regions where a plant type can naturally grow and reproduce (Box, 1981), and physiological traits, including photosynthetic pathways like C_3/C_4 (Box, 1996).

To effectively run LSMs, detailed information about the distribution of each PFT within model grid cells is essential and is typically expressed as a fraction of the total cell area. The parameterization of global vegetation processes, encompassing vital functions like photosynthesis and evapotranspiration, relies on assigning fixed values to each PFT (Hartley et al., 2017). Consequently, LC often serves as a surrogate for PFTs through a process known as cross-walking, which translates the LC class legend into PFTs specifically tailored for a model (Jung et al., 2006; Poulter et al., 2011). However, uncertainties in the distribution of these PFTs contribute to uncertainties in carbon budgets (Jeong et al., 2012; Ballantyne et al., 2015; Hartley et al., 2017). These uncertainties can stem from the definition of LC classes or the cross-walking procedure itself, which relies on expert knowledge and auxiliary data sources (Poulter et al., 2011, 2015). Notably, when modelling gross primary production, evapotranspiration, and albedo, research has highlighted that greater uncertainty is often associated with PFT fraction estimates attributed to the choice of cross-walking procedure compared to uncertainties related to LC (Hartley et al., 2017).

Global LC map validation and uncertainty retrieval

An essential component of the map production process is map validation, which is defined as the "process of independently assessing the quality of data products derived from system outputs" (CEOS, 2024). The CEOS Land Product Validation (LPV) subgroup has established general guidelines for the global validation of categorical LC products (Strahler et al., 2006a). Typically, the validation procedure involves defining the sampling design, response design, and accuracy analysis (Congalton and Green, 2009; Stehman, 2009). These assessment findings are often presented in the form of a confusion matrix, from which various statistics are derived, including overall accuracies and per-class accuracy metrics, such as user and producer accuracies, and F1-scores. International validation standards are currently being updated, notably to address the specificities of validating LCC. The existence of multiple global LC products generated for the same purpose raises the question of map comparison. Benchmarking activities are commonly employed for this purpose, where different map products are thematically compared, resulting in a comparison matrix that highlights discrepancies between them. However, this method does not necessarily indicate accuracy since maps can agree and still be incorrect. In benchmarking exercises, the question of determining which map is the most accurate remains unanswered.

Objectives

This thesis aims to contribute to the global long-term monitoring of LC by providing a comprehensive description of land dynamics in the context of increasing anthropogenic impacts and climate change. **The overall objective of this research is to develop methods for globally mapping land cover consistently in time and characterize its associated uncertainty. It is achieved by taking advantage of multiple satellite missions and integrating various Earth Observation products.**

More specifically, four complementary objectives have been defined in the context of collaborative research to develop a major dataset that meets the Land Cover Essential Climate Variable requirements for the climate modeling community.

The first specific objective will attempt to answer the following question: **to what extent does a long-term consistent land cover map series, built from harmonized satellite observations, improve our understanding of global land cover change patterns?** Using a 29-year time series of surface reflectance from five harmonized satellite streams, this objective aims to demonstrate, assess, and analyze LC maps to advance our understanding of long-term global LC dynamics. Beyond the climate community, this long-term observational series is valuable for various land-related domains, as evidenced by its extensive use in describing global land dynamics. LULC statistics based on inventories, such as those compiled by FAOSTAT, rely on sampling designs to estimate annual land change areas at various administrative levels, with confidence intervals varying by LC classes and reporting countries. Here we show that spatially explicit year-to-year LC change detection reveals not only net changes but also gross changes and other ecologically important land indicators, such as LC conversion and persistence.

Recently, several global EO-derived products targeting individual LC classes have been published. While these datasets are valuable for training or integrating into long-term LC observation series, selecting the optimal dataset remains challenging. Conventional benchmarking approaches, which compare products on a pixel-by-pixel basis, highlight their differences and identify areas that are difficult to map but do not assess product quality since no reference data is involved. Consequently, the second research question is: **can we compare several global datasets in a statistically sound manner to select the most performant one for integration into our global land dynamics analysis?** To address this, the second objective is to develop a statistical benchmarking approach involving a stratified random sampling design to compare and identify the best available products. This approach, initially tested on water body datasets, has facilitated the creation of a new global

land mask, now adopted as the common layer for all European Space Agency (ESA) Climate Change Initiative (CCI) ECVs.

As Earth system and land surface models translate LC classes into model-appropriate PFTs to characterize land surface-atmosphere interactions, the third research question arises: **to what extent can harmonized high-resolution datasets be integrated into a long-term consistent time series to describe PFT distribution at the pixel level globally?** The current translation of LC into PFTs often relies on generic cross-walking tables that assign standard PFT compositions to each LC class globally, without accounting for spatial variability.

To address this challenge, the third specific objective is to design and demonstrate a scientifically sound framework that allows the integration of multiple high-resolution datasets, which may not be compatible with the LC observational time series, into a spatially explicit series of annual maps of PFT fractional composition at 300m resolution for the period 1992-2020.

Spatio-temporal consistency is essential for ensuring the stability of annual land cover classifications, enabling effective detection of land cover change. The long-term series of both LC and plant functional type maps rely on interpreting surface reflectance data collected by observing systems from five distinct satellite missions, assuming compatibility across sensors. The final research question addresses this issue: **is it possible to quantify the uncertainty at the pixel level throughout the entire workflow, from radiance measurement to LC class map?** In close collaboration with the team responsible for pre-processing harmonization, the fourth specific objective is to design and test an end-to-end uncertainty propagation scheme from radiance measurement to LC class maps. While guidelines are well established for quantitative continuous variables, the uncertainty of categorical variables resulting from the complete LC processing chain has not yet been investigated. This objective examines the impact and propagation of error from radiance measurements to seasonal composites on LC uncertainty, using Monte Carlo simulations. It aims to incorporate a broad range of potential surface reflectance values into a multiple classification protocol, obtaining both non-spatial and pixel-level uncertainty indicators, including the classifier's contribution to land cover uncertainty.

The articulation of these four objectives is illustrated in Figure 1.

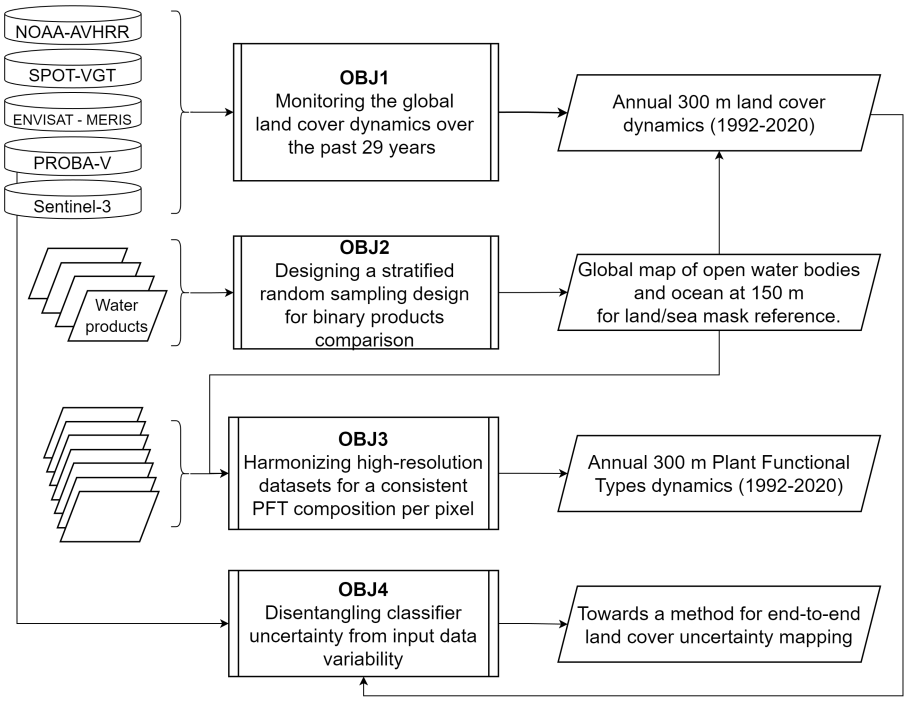

Figure 1: The overall research approach articulating the four objectives of this thesis.

Outline

This document is organized into 4 chapters corresponding to the objectives outlined in the previous section. The first three chapters have each been published, as a first or second author. These chapters have been revised to enhance readability and improve the overall coherence of the thesis.

Chapter 1 studies in detail the global LC and LU changes at the medium spatial resolution over the past ~30 years. Various variables such as net, gross, permutation and total LCC are derived from the CCI MR LC maps and analyzed to provide a globally richer representation than the net changes often detailed in inventory databases such as the one from FAOSTAT.

In **Chapter 2**, we propose a modified stratified random sampling scheme usually implemented as part of a validation, designed with variations in strata definitions to assist users in selecting the best available products from a set mapping the same binary class. This sampling method is applied in a case of comparative evaluation of three global waterbody datasets. A new global land/inland water/ocean, developed as a result of this study, is also presented.

Chapter 3 addresses the need to reduce uncertainty on the representation of PFTs in the context of climate modelling. Taking advantage of the availability of multiple HR datasets, a hierarchical fusion method is proposed to combine the high spatial and thematic accuracy of binary LC products with the thematic richness and spatial consistency of CCI MR LC maps to produce a time series of ready-to-use PFTs in the Earth System and land surface models. The resulting dataset consists of an annual PFT map series with pixel values indicating the percentage cover (0-100%) for each of the 14 PFTs.

Chapter 4 is a pilot study about the retrieval of uncertainty for categorical variables in the context of end-to-end uncertainty budget. This approach not only allows us to introduce detailed uncertainty indicators at the non-spatial and pixel levels, but also highlights the role of the classifier in influencing land cover uncertainty.

The conclusions and perspectives are summarized and discussed in the last section.

Author contribution

Chapter 1

Céline Lamarche (CL) contributed to the methodology, actively participating in the development of the research approach with Pierre Defourny (PDY). CL was involved in the investigation phase, participating in the research and data collection process. CL took on the responsibility of data curation, managed all research data, developed the data analysis code and produced all the LU LCC statistics. CL designed and provided all the published figures and tables. CL contributed to the writing of the original paper draft especially for the method section and reviewed the paper. She contributed to the design of the online visualization interface with TDM. Along with several other authors (SB, TDM, EVB, IM, JR, CB, MB, GK), CL provided essential input material to the study, contributing to the generation of the LC maps, the change algorithm integration and the generation of the land surface seasonality variables. CL conducted the validation of the land cover change and revised the manuscript under the supervision of PDY. More recently, she has been actively involved in funding acquisition alongside PDY and has taken on the role of project manager.

Chapter 2

CL carried out the study under the supervision of PDY. MS provided the SAR-WBI product and guided the writing. CL, SB, JR, and RD contributed to the quantitative quality assessment. CL wrote the original draft and MS thoroughly revised the document. CB conducted the work of the distinction inland water/ocean and developed the user tool that adapts the water body product for climate and land cover applications. JW realized the inland water/ocean delineation. SB, OA, and PDY coordinated the research in the framework of ESA CCI MR LC project. CL completed the peer review.

Chapter 3

PDY conceived the idea and supervised the research effort with contributions from PP. CL coordinated the research study and supervised KLH, who tested the methodology with the contribution of CL. KLH developed the code to generate the CCI PFT dataset 2010. AH, PP, CO, VB, RSM, and SIB designed the modeling experiments and analyzed the results. GK, MB, RS, and CB designed and developed the user tool. GK and RS managed and produced the CCI PFT dataset 2010 metadata. KLH wrote the original draft with contributions from CL, AH, SIB, PP, and CO. All co-authors reviewed the manuscript. CL handled the interactive discussion and completed the peer review.

Chapter 4

CL conceived the idea under the supervision of PDY. RQ et al. developed the method for handling pre-processing uncertainty, upon which CL expanded in this chapter. CL designed the method for obtaining categorical uncertainty indicators, wrote the code, generated the results and conducted their analysis. CL and RQ drafted the original content for the classification and preprocessing sections, respectively. PDY reviewed and provided input for this chapter, which was finalized by CL.

Chapter 1

Uncovering 29 Years of Global Land Cover Transformations through Harmonized Satellite Streams

This chapter is based on the following article:

Defourny, P., **Lamarche, C.**, Brockmann, C., Boettcher, M., Bontemps, S., De Maet, T., Duveiller, G., Hartley, A., Kirches, G., Moreau, I., Peylin, P., Ottlé, C., Radoux, J., Van Bogaert, E., Ramoino, F., Albergel, C., Arino, O. 29 years of consistent land use land cover observation from harmonized satellite streams reveal annual changes for every pixel on Earth.*Under revision.*

Abstract

Land Use Land Cover Change (LULCC) is the second-largest source of anthropogenic CO_2 emissions and a major driver of biodiversity loss. While satellite EO has the capacity to describe land surface properties across the globe, the complexity of having to deal with different satellite missions to reach a long-term data record has so far complicated the establishment of an adequate and consistent quantification of land change over a long period. Here we present a novel series of global annual maps at 300 m using a harmonized processing of five different EO missions spanning the period from 1992 to 2020. Built-in long-term consistency is ensured by decoupling LC change detection and LC mapping. From this dataset, we show that LU and LC changes annually observed in such a spatially-explicit manner reached more than six percent (8.4 Mkm^2) of the global ice-free land surface from 1992 to 2020. The cumulative change trajectories over the whole period and the annual transitions at the pixel level highlight very dynamic land conversions three times higher than the net change usually reported by inventory-based statistics. On the contrary, the persistence of stable LC classes during the entire observational period (consisting of 94% of the land) indicates where the land has potentially had the chance to develop into more stable and biodiverse ecosystems following ecological succession. Anthropogenic LU changes, such as cropland and urban expansion, drive highly contrasting conversions of (semi)-natural LC, influenced by available green capital and population growth. Conversely, fast-increasing protected areas enforcing nature conservation significantly reduce these processes by more than half at the global scale. Such a unique multi-decade observational dataset supports long-term land trajectory reconstruction for climate modelling improvement and impact assessment as well as policy indicators based on green capital evolution.

1.1 Introduction

LCC is the second-largest source of anthropogenic CO_2 emissions to the atmosphere (3.8 ± 0.6 GtC yr−1 in 2011–2020 decade) (Friedlingstein et al., 2022). Habitat loss and fragmentation are major drivers of the global biodiversity crisis (Pouzols et al., 2014). Land provides the basis for human livelihoods and well-being through the supply of food, fresh water, settlements and other ecosystem services (Arneth et al., 2019). Previously considered a local environmental issue, LU change is increasingly affecting the Earth system (Foley et al., 2005; Houghton and Nassikas, 2017; Venter et al., 2016). The impacted terrestrial biomes play key roles in water, energy and carbon balances through a complex interplay at different nested scales (Bonan, 2008). Land-use change is both a driver and a consequence of global environmental change.

Monitoring land dynamics in the long term is of paramount importance to address today's societal challenges. Until recently, the scientific community primarily assessed land surface changes through inventory-based statistics, which consists of a bottom-up accounting based on the statistical compilation of activity data usually reported by countries (FAO, 2021a). This method typically describes only the net change observed during the survey period. The most recent synthesis dedicated to global land change from the Intergovernmental Panel on Climate Change (IPCC) (Arneth et al., 2019) referred to land studies primarily based on such inventory-based datasets (Luyssaert et al., 2014; Erb et al., 2007; Venter et al., 2016), claiming that the year 2000 was the year in which available data sets are most reconciled amongst each other. Recent estimates of carbon fluxes from LU and LCC also relied on net rates of LCC as derived from such datasets (Houghton and Nassikas, 2017; Fuchs et al., 2016). Even in the latest IPCC report (IPCC, 2022), global LU change could only be reported at 0.05° in terms of long-term trends of simplified classes (proportions of the tree canopy, short vegetation and bare soil) due to the lack of global land synthesis. FAO statistics are widely used in the literature and are based on questionnaire surveys taken every five years (FAO, 2021b) or on national samplings to estimate LC areas over time. Net change can then be quantified only as the area difference between two endpoints of a given period and for a given spatial aggregation. Due to the marginal nature of land changes, gross change estimation based on surveys requires the sampling scheme to be either very dense or very targeted.

EO systems, such as satellites, play a key role in surpassing the collection of statistics from individual countries. Instead, they facilitate the systematic and repetitive mapping of the entire Earth's surface. Global LC mapping was first achieved owing to international collaborative initiatives using one year of 1-km satellite observation (Loveland and Belward, 1997; Bartholomé and Belward, 2005) then followed by the rather intensive processing chains that ingest 500 m, 300 m, 100 m, 30 m and even 10 m annual surface reflectance time

series, respectively, using either selected training datasets (Friedl et al., 2010; Buchhorn et al., 2020a; Hansen et al., 2022; Chen et al., 2015a; Venter et al., 2022) or building on a large set of outdated but precise maps (Defourny et al., 2007). Unfortunately, because these global LC maps were created separately for specific years, they could not be combined for LCC assessment due to significant disagreements related to irreconcilable typologies, geometric discrepancies, year-to-year meteorological variability and uneven map quality (Hua et al., 2018; Bontemps et al., 2012; Fritz and See, 2008). Some researchers addressed the discrepancies between independent annual LC maps using Hidden Markov Chain models to statistically estimate the most probable change (Sulla-Menashe and Friedl, 2018; Bogaert et al., 2022). Alternatively, the discrepancies are managed by an expert-based reconstruction model mixing various datasets from very different sources, nature and resolution (satellite observation, statistics and models), assuming that their combination provides more consistent information (Winkler et al., 2021). Single satellite missions provide much more consistent datasets to directly assess major land change at a global scale but generally only for single terrestrial features, like tree cover (Hansen et al., 2013b), surface water (Pekel et al., 2016), or urban areas (Pesaresi et al., 2016). These approaches successfully map the changes at 30 m resolution but do not provide any information about the land conversion nor about the interplay between land surface dynamics. The only satellite-based study quantifying multi-dimensional global land change based on a consistent approach for a long-term observation time series refers to vegetation fractions for trees, short vegetation and bare soil at a coarse resolution of 0.5° (Song et al., 2018b). There has been a crucial gap in global LCC mapping whereby the untapped potential of using multiple streams of global satellite archives together has not been fully exploited.

Driven by the GCOS support for climate science and recognition of LC as a key terrestrial ECV (GCOS, 2022), we present a satellite-based approach that decouples LC mapping and the LCC detection to produce the longest time series of annual LC maps. Unlike previous global mapping efforts that relied on a single satellite (Loveland and Belward, 1997; Friedl et al., 2010; Song et al., 2018b; Buchhorn et al., 2020a) this time series was produced by harmonizing and combining the full archives of five different satellite missions. The resulting LC map series highlights the major transformations that our planet's LC has experienced over the 29 past years at a global scale with a granulometry as fine as 300 m.

1.2 Material and Methods

Maintaining long-term consistency in the map series was identified as a key requirement by the climate modelling community (Bontemps et al., 2012; GCOS, 2022). This is reflected in the LC map series processing chain (Figure

1.1). A long-term period of nearly 30 years required the use of global daily surface reflectance from five different observing systems. Innovative methods were developed accordingly to preprocess the multi-mission surface reflectance and exploit the resulting time series. The spatiotemporal consistency of the annual LC maps is ensured by decoupling tailored LC mapping, driven by spectro-temporal signatures, from the annual detection of LCC. A comprehensive typology definition based on the LCCS ISO standards supports such an approach (Defourny and Bontemps, 2012).

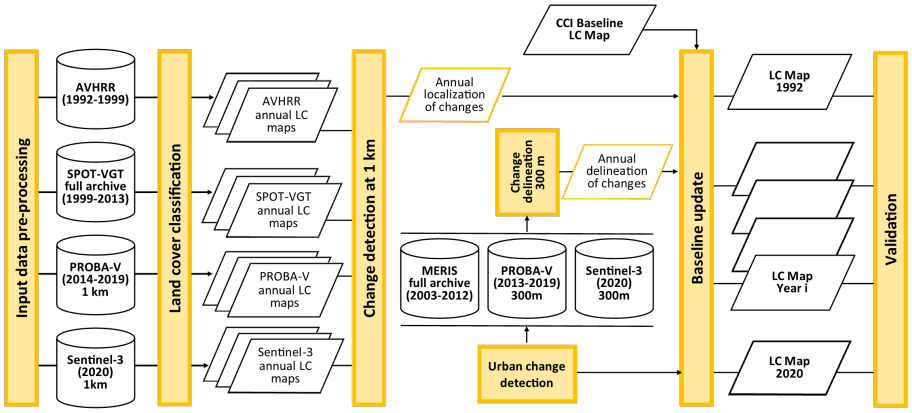

Figure 1.1: Schematic representation of the methodology developed to derive global annual LC maps from the baseline global LC map and the LCC, detected and delineated at 1 km and 300 m, respectively.

1.2.1 Harmonized pre-processing of multi-sensor radiance to 7-day global composites

Global consistent 7-day multispectral composites at 300 m and 1 km from 1992 to 2020 were generated from the L1 radiances of the complete archives of five types of sensors (Figure 1.2).

The harmonized pre-processing workflow included state-of-the-art radiometric calibration, geometric and atmospheric corrections, normalizing reflectances, and screening for clouds and cloud shadows. The geometric correction of the 300 m Medium Resolution Imaging Spectrometer (MERIS) Full Resolution (FR) image archive ensures that the geolocation root-mean-square errors remain better than 80 m. State-of-the-art spectral and radiometric calibrations provided by data suppliers were applied to different mission archives. No dedicated data harmonization was applied but all methods used were made as consistent as possible across sensors. Each resulting dataset was validated for radiometric and geometric accuracy, pixel identification and

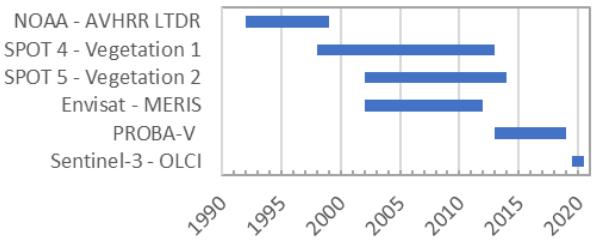

Figure 1.2: EO long-term time series built on the entire archive of five different space missions.

atmospheric correction, including aerosol retrieval aspects, to ensure consistency.

The consistency of the resulting top-of-atmosphere reflectance values has been assessed over the CEOS LandNet sites (Burini et al., 2010) and other stable areas, while anomalous Advanced Very High-Resolution Radiometer (AVHRR) products were discarded. A unified pixel state classification module was implemented to estimate, using instrument-specific methods, similar sets of features combined to obtain the final pixel states. The atmospheric correction includes the correction for the absorbing and scattering effects of atmospheric gases, in particular ozone, oxygen and water vapour, of the scattering of air molecules and the correction of absorption and scattering due to aerosol particles. Atmospheric gas concentrations were obtained from various meteorological data sets (Simmons et al., 2016), e.g. European Centre for Medium-Range Weather Forecasts (ECMWF) atmospheric reanalysis data, ERA-Interim data set (Dee et al., 2011) and ECMWF ERA5 (Hersbach et al., 2020). Furthermore, the atmospheric correction calculates the aerosol properties and the actual correction of the reflectance (Leonard et al., 2013). The resulting atmospherically-corrected daily reflectances were finally composited to a global 7-day composite using the mean compositing method (Vancutsem et al., 2007). A complete description of the LC generation methodology is available in (Defourny et al., 2017b).

1.2.2 Decoupling the LULC mapping from the LCC detection

The two-fold challenge of global LC monitoring is to classify the whole land diversity represented by every ecosystem into a few discrete categories, and do so consistently in space and time whilst satellite observations vary continuously according to ecoclimatic and anthropogenic gradients. Three principles were established to tackle this challenge: (i) stratifying the planet in equal-reasoning areas to take into account the regional peculiarities while running the same processing chain; (ii) decoupling the LULC mapping from

the LULC monitoring to tailor the input dataset accordingly and to disentangle the LULC mapping error from LULC change detection; and (iii) relying on the most precise multiyear dataset to establish a consolidated multiyear LC baseline, fully recognizing that annual LCC is still marginal at global scale compared to the sheer land area of the planet.

Unlike most other global mapping efforts (Friedl et al., 2002; Hansen et al., 2013b; Pekel et al., 2016), an equal-reasoning stratification was designed to combine the genericity and specificity of the algorithms. A set of 22 strata, including polar areas, were delineated to tailor the input dataset to each stratum according to their vegetation seasonality, ecoclimatic gradients, observation sun angles and frequency of cloud-free observation. Such a stratification strategy capitalizes on the GlobCover experience (Defourny et al., 2009; Bontemps et al., 2011; Arino et al., 2008), which successfully demonstrated for 2005 and 2009 the performance of fully automated global LC mapping thanks to regionally-tuned input datasets.

A baseline LULC map was established from the 10-year MERIS archive (2003–2012) thanks to the 15 narrow spectral bands at 300 m resolution. Stratum-specific seasonal composites were specified in terms of number, timing and duration to enhance the discrimination of LC classes according to the ecoclimatic context and the conditions of observations, i.e. sun and satellite viewing angle distributions and cloud coverage probabilities.

Seasonal composites were classified with independent unsupervised and machine learning classifiers subsequently merged into one global baseline LC map. The Iterative Self-Organizing Data Analysis Technique (ISODATA) unsupervised classifier gathers pixels into clusters according to their similarity in the spectro-temporal space and was found quite efficient for the most frequent LC classes. The machine learning algorithm corresponds to an automatically trained maximum likelihood classifier with performances fine-tuned thanks to adjusted locally training data within a moving and possibly growing window (Radoux et al., 2014). This classifier was specifically targeting the identification of marginal classes such as water or flooded vegetation. Decision rules then attribute a unique LC label to each cluster based on the histogram of class frequency derived from the spatial correspondence between clusters and the 20 m reference database compiled from more than fifty regional and global LC products selected for being the most accurate, thematically rich, as recent as possible. The LC typology was defined using the ISO 19144 LCCS developed by the UN FAO to describe the different land categories unambiguously and to be compatible with the IPCC land classes. The global legend counts 22 globally consistent classes at the scale of the entire world (Table 1.2). The frequent daily observations provided by sensors with medium spatial resolution allow for the characterization of vegetation leaf phenology, unlike legends found in higher spatial resolution products, which typically comprise around 10 classes (Chen et al., 2015a; Gong et al.,

2019; Zanaga et al., 2022). The LC maps also include a more detailed legend, a so-called regional legend including a more precise definition of 37 classes, only mapped where the available information allows reaching this higher level of detail in the legend (Defourny et al., 2017a). Some specific classes like "flooded tree cover by saline water", "urban areas", "water bodies" and "permanent snow and ice" were directly derived from higher-resolution binary products, i.e. the global mangrove atlas (Giri et al., 2011), the Global Human Settlement Layer (GHSL) (Pesaresi et al., 2016) and the Global Urban Footprint (GUF) (Esch et al., 2017), the ESA CCI global map of open water bodies v4.0 (Lamarche et al., 2017) and the Randolph Glaciers Inventory (Pfeffer et al., 2014), respectively.

Since actual LCC is a rare event on a global scale (Congalton and Green, 2019), comparing annual LC maps contaminated by errors for LCC leads thus to significant change overestimates (Friedl et al., 2010; Bontemps et al., 2012). Independent year-to-year classifications are known to suffer from spurious changes due to a combination of inter-annual phenology variability and poor discrimination between spectrally-close LC classes. Therefore, this particular approach to LCC detection was developed independently of the baseline LC map production and involved two distinct steps: initially identifying change hotspots through the analysis of multiple-sensor daily 1 km time series, followed by consolidating and delineating LCC using a separate multiple-sensor time series at 300m. Such an annual change detection requires EO data with the highest frequency, such as daily global observation, to record enough cloud-free surface reflectance measurements within each year for most regions to disentangle seasonal inter-annual variability from actual LCC. Multispectral sensors with a higher frequency of acquisitions have a spatial resolution of 1 km, i.e. AVHRR (1992–1999), SPOT-VGT (1999–2013), while PROBA-V (2014–2019), and Sentinel-3 OLCI (2020) were also processed at 1 km for the sake of consistency. We assume that the standard pre-processing ensures consistent surface reflectance across different sensors and that the annual LC classifications have achieved a high level of accuracy, enabling a comparison of LC labels over a time series. The impact of preprocessing noise on the classification will be quantified in Chapter 4.

A per-pixel trajectory-based approach analyzing annual LC classifications over the time series successfully identified a total of thirteen types of abrupt yearly LCC during the 1992 –2020 period. The 22 CCI-LC classes were grouped into the main IPCC land categories, i.e. cropland, forest, grassland, shrubland, sparse vegetation, bare areas, wetland, water, and settlement. The suite of annual classifications was scanned on a per-pixel basis within a 14-year moving window to detect potential change hotspots according to stratum-specific decision rules of LC class occurrences and transitions in time (Defourny et al., 2017b). Any potential change needs to be further confirmed for at least two years to conclude an actual LCC hotspot, except for

changes with an unambiguous signal (forest to cropland, cropland to forest and water loss). The LCC hotspot module identifies the year of change within 12 types of change, excluding urban expansion, which corresponds to gains and losses in the IPCC land categories (Table A.1). The sliding nature of the window allows identifying up to 7 LCC during the period and straightforwardly extending the map series yearly (Moreau, 2016). The limited quality of the 1992-1999 AVHRR LC classifications hindered the detection of LCC types, restricting it only to forest and water losses and gains.

For each LCC pixel detected as a change hotspot, less frequent but more detailed MERIS, PROBA-V, and Sentinel-3 OLCI composites were classified to confirm and delineate the actual LCCs at 300 m within a 5x5 km window centred on the detected LCC hotspot. A locally adjusted maximum likelihood classifier was applied to take advantage of its performance over small areas.

The consolidated LCC, precisely delineated at a resolution of 300 m since 2003 and 1 km before that, provides information on specific locations, the year of change and the types of LC transitions. In the final stage of the process, this information is used to update or backdate the reference LC map, providing a detailed and consistent representation of LC and its dynamics from 1992 to 2020.

Mapping urban expansion precisely requires a specific approach because of the mismatch between the urban land process and the spatial resolution of the harmonized surface reflectance time series. Before 2003, the 1 km spatial resolution brought by AVHRR and SPOT-VGT did not allow for accurate urban change detection. Between 1992 and 1999 and between 2000 and 2003 the urban footprint corresponds to the GHSL 1990 and GHSL 2000 derived from 30m Landsat imagery (Pesaresi et al., 2016). From 2003 onwards, urban change detection relied on a series of annual machine-learning spectral classifications at 300 m trained by the GHSL and GUF (Esch et al., 2017). A gap-filling procedure aims to overcome high-resolution data intervals. The ESA CCI LC maps are generated globally using the World Geodetic System 1984 (WGS84) geographic Coordinate Reference System (CRS) (EPSG:4326). This CRS is not an equal-area projection, and pixel area is distorted as a function of latitude. The area of each pixel is based on its latitudinal position, treating it as a trapezoid, with the base lengths calculated according to the Vincenty method.

1.2.3 LULC change analysis at various scales

Thanks to the consistency built into the LCC method, the LULC change is studied from pixel level to global scale. The pixel-based analysis allows assessing the number of pixels experiencing multiple changes over the period and quantifying the LC persistence and swapping dynamic in addition to their classical gross, net, gain and loss estimates. The persistence corresponds to

pixels for which no change in classification is observed in the map series over the full period, i.e. 29 years and gives some insights about the stability and, for some LC classes like wetland or forests, the potential ecological succession. Swapping corresponds to the transition of a given LC class to another in a given location, while in another location, a gain of a similar area of this given LC class compensates for this loss.

The global land area, referring to the ice-free land area, including inland water bodies, is estimated at 132.34 Mkm². The land mask produced in Chapter 2 was split into 26 regions reconstructed after the IMAGE 3.0 framework region classification (Stehfest et al., 2014) and used to derive regional LCC statistics. We delineated terrestrial protected areas using the UN Environment Programme's (UNEP) World Conservation Monitoring Centre's (WCMC) World Protected Areas Database (WDPA) (UNEP-WCMC, 2019). All references to (semi-)natural vegetated areas include the CCI IPCC-like classes forest, grassland, wetland, shrubland, and sparse vegetation. All reported areas have been calculated by considering the actual area of each pixel based on its latitudinal position.

1.2.4 Land cover change validation

To complement the LC assessment over stable areas, we independently validated significant LCC processes using a distinct reference sample. Given the hotspot LCC detection scale of 1 km, we used a window of 3x3 MERIS pixels (300 m) as our sampling unit. The sampling region covers the mapped area below 60°N, documenting LC transitions between 1992 and 2020 defined with the IPCC legend. We used a stratified random sampling design for allocating sample units, with strata aiming to target distinct processes of gains and losses across the LC class spectrum, from densely vegetated terrestrial to abiotic types. These strata included forest extents divided into subregions inside and outside the tropics, cropland, water bodies, and bare areas. About 150 samples, with a specific emphasis on the most anthropogenic LULC processes, were randomly selected for each IPCC land conversion ensuring at least 30 samples per change direction after availability and quality check of the Landsat imagery. A team of three EO experts visually interpreted 29 years of dataset of the USGS Landsat 4-9 combined Collection 2, Tier 1 using the GEE time series explorer extension with the support of publicly available very high-resolution imagery. A sample was labelled as change when an IPCC class conversion was observed for at least one MERIS pixel of the sample unit. Confidence in the high-resolution satellite data visual interpretation was scored in percent and samples with less than 60% confidence were systematically discussed and resolved by the team. For product validation, we translated both the map and reference data into a binary legend indicating change or no change between 1992 to 2020. Consequently, the map accuracy metrics

reflect the user accuracy of LCC process, representing the commission errors within the map series. The presented accuracy figures are calculated based on sample counts.

1.3 Results and discussion

1.3.1 Global land use changes

Here we report a spatially explicit evolution of LULC for the entire planet over the last three decades, providing a comprehensive overview of major anthropogenic LU changes. For the first time, land observation from five different EO satellite missions was exploited in a harmonized way using a new land change detection method to consistently map the terrestrial surface of the Earth on an annual basis for each pixel of 300 m for the last 29 years. The gross rate of LCC, as observed annually from global scale daily observations, depicts a planet almost three times more dynamic than the net change suggested by national statistics compiled at the global scale. More than 5.88% (7.78 Mkm^2 over 29 years) of the global ice-free land surface experienced LCC once between 1992 and 2020. An additional 0.47% of this global area experienced multiple conversions over the period, bringing the cumulative land change to 6.35% (8.4 Mkm^2), which is roughly the size of Brazil or twice the size of the European Union.

A comparison to inventory-based approaches helps to illustrate the added value provided by this novel dataset. Using the CCI LC dataset as in an inventory-based approach based on a confrontation between the LC areas in 1992 and 2020 at the global scale would lead to a net change of only 2.18% (2.88 Mkm^2) of the global ice-free land surface. FAO and national inventory-based statistics describing LULC rely on a sampling design to estimate the area of land classes at a given administrative level with a given confidence interval. Such an approach does not capture the dynamics of permutation between land classes (so-called swapping) within each administrative unit, but only estimates the area of land per class for that unit. The inventory-based rate of change is an estimate of net change at the level of interest, which is often the national scale, masking swapping-change dynamics.

Net change estimates illustrate the apparent stability of the respective fraction of LU categories over the decades, showing only a very slight evolution of LU proportions (Table 1.1).

By 2020, about 20% of the world's land area was intensively used for cropland (18.64%) and urban settlements (0.61%) (Table 1.2). Assuming that most of the natural grasslands are grazed through various forage-livestock and transhumance systems, it is reasonable to consider that one-third of the global land area is used for food production, one-third is occupied by natural and managed forests, and the last third is equally divided between low/sparse

Table 1.1: Land area (in Mkm²) corresponding to persistence, loss, gain, total, net and swap change between IPCC categories from 1992 to 2020 as estimated by pixel counting adjusted for pixel-area latitudinal variation. Persistence indicates pixels where no change in classification is observed. Gains and losses represent the cumulative increase and decrease in land cover, respectively, over the 29-year period. Formally, swapping is defined as twice the minimum of the gain and loss. This occurs when a land cover class transitions to another class in one location, while a gain of similar area in the same land cover class compensates for this loss (Pontius et al., 2004).

IPCC Class	Persistence	Loss	Gain	Gross change	Net change	Swap change
Forest	41.65	2.63	2.16	4.79	-0.47	4.31
Cropland	22.80	1.34	1.96	3.30	0.62	2.68
Bare areas	18.84	0.66	0.29	0.95	-0.36	0.59
Grassland	13.61	0.91	1.26	2.17	0.35	1.82
Shrubland	12.61	1.02	0.67	1.68	-0.35	1.33
Sparse vegetation	9.66	0.88	0.72	1.60	-0.16	1.43
Water	3.20	0.14	0.16	0.30	0.01	0.29
Wetland	1.74	0.30	0.21	0.51	-0.09	0.42
Settlement	0.35	0.00	0.46	0.46	0.46	0.00

vegetation and rather less productive bare areas. Our estimations differ from the IPCC estimate (Arneth et al., 2019), which considers that three-quarters of the global land area is affected by human use based on less harmonized sources, summing the areas of cropland, inhabited areas, grasslands and all forests reach only two-thirds (64%) of the global terrestrial surface. This last figure is very close to the 67% obtained by the FAOSTAT for 2019 (FAO, 2021b). At first glance, this proportion of LUs seems fairly stable over the last three decades, as also reported by FAO (FAO, 2021b). However, a steady increase in gross LULC change area is observed from 1992 to 2020 based on the annual global observation time series (Figure 1.3). The average gross rate of change (considering all changes at the 300 m pixel level from one year to another and averaged over the period) is as high as 0.22% per year, while the average annual net rate is only 0.075% (2.18% / 29–the length of the map series). Up to 7.4% of this changing area corresponds to two or more changes in the same location over 29 years.

Such a spatially explicit land change detection method allows the description of the trajectory of each 300 m pixel on an annual basis and the quantification of the land conversion processes. Figure 1.4 highlights the respective IPCC land categories transition in terms of loss (left side) and gain (right side). One-third of the global change area corresponds to forest conversion mainly into cropland, grassland and shrubland. The second major loss (17%) concerns cropland conversion to forests, grassland or urban areas. The first two of these transitions are typically associated with shifting cultivation, fallow practices or land abandonment. Urban expansion at the expense of agricultural land corresponds to a significant artificialization process of currently

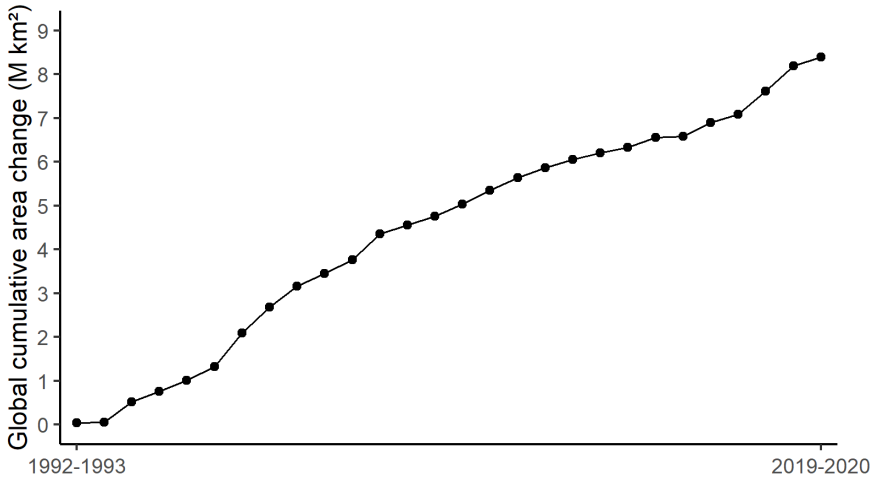

Figure 1.3: Cumulative area of land changing from one IPCC land category to another between 1992 and 2020, as mapped from satellites at the global scale and including areas changing several times over the period (i.e. less than 0.5% of the changed area).

productive soils. Grassland represents another very dynamic LC that is converted into any of the other classes depending on the region. A striking outcome is the wetland loss largely due to forest expansion. The cumulative LCC area observed since 1992 (8.4 Mkm^2) is as high as a quarter of the current estimate of all surfaces that have been converted by humankind (31.5 Mkm^2), as compiled by Arneth et al. (2019).

Table 1.2: Global legend of the 22 LC classes, based on the UN LCCS and their corresponding area as observed by satellite (Mkm² and percentage of the global ice-free land area including inland water bodies) considering the varying area of each pixel on the globe.

IPCC classes	CCI Land Cover classes		2020 area		
			(Mkm²)	(%)	(%)
Cropland	10	Rainfed cropland	15.32	11.53	30.43
	20	Irrigated cropland	2.42	1.82	
	30	Mosaic cropland (50%) / natural vegetation (50%)	3.42	2.58	
	40	Mosaic natural vegetation (50%) / cropland (50%)	3.60	2.71	
Settlement	190	Urban area	0.81	0.61	
Grassland	110	Mosaic herbaceous cover (50%) / tree and shrub (50%)	1.11	0.83	
	130	Grassland	13.76	10.36	
Forest	50	Tree cover, broadleaved, evergreen, closed to open (15%)	12.68	9.55	32.97
	60	Tree cover, broadleaved, deciduous, closed to open (15%)	10.41	7.84	
	70	Tree cover, needleleaved, evergreen, closed to open (15%)	8.77	6.60	
	80	Tree cover, needleleaved, deciduous, closed to open (15%)	4.98	3.75	
	90	Tree cover, mixed leaf type (broadleaved and needleleaved)	2.14	1.61	
	100	Mosaic tree and shrub (50%) / herbaceous cover (50%)	3.72	2.80	
	160	Tree cover, flooded, fresh or brackish water	0.88	0.66	
	170	Tree cover, flooded, saline water	0.21	0.16	

Continued on next page

Table 1.2: (Continued)

IPCC classes	CCI Land Cover classes		2020 area (Mkm²)	2020 area (%)	(%)
Wetland	180	Shrub or herbaceous cover, flooded, fresh-saline or brackish water	1.95	1.47	
Shrubland	120	Shrubland	13.28	9.99	
Sparse vegetation	140	Lichens and mosses	1.49	1.12	33.68
	150	Sparse vegetation	8.89	6.69	
Bare areas	200	Bare areas	19.14	14.41	
Water	210	Water	3.36	2.53	2.92
Glaciers	220	Snow and ice	0.51	0.39	

In contrast to the inventory-based approach, change detection based on a wall-to-wall mapping approach allows the quantification of several aspects: (1) the LC persistence defined as the unchanged land areas over the entire time series; (2) the area losses and gains needed to estimate gross and net change; and (3) the swap change (Pontius et al., 2004). This last metric captures the intensity of land conversions at the pixel level on a year-to-year basis, which is not reflected by the net balance of losses and gains. Such analysis is made possible thanks to the built-in consistency of the overall methodology. Table 1.1 clearly shows that the area of swap change is often an order of magnitude higher than the net change, highlighting the very active dynamics of LU change on our planet. For instance, the similar net change values for forest and settlement hide the ten times larger forest dynamic explicitly quantified by its swap change. The wall-to-wall mapping approach allows for highlighting the persistent areas and the swap change areas which can be interpreted in terms of ecological impacts. A striking example of this is related to forest conversion - an increase in forest area can balance an equivalent forest loss in terms of area but certainly not in terms of ecological functioning, biodiversity, ecosystem complexity and resilience. While the lost forest may concern an old-growth natural forest, the forest gain is necessarily due to afforestation or natural regeneration, which both might evolve very slowly towards a complex structure of a biological community. Quantifying areas of LC persistence is therefore of primary importance to identify and map zones that have effectively remained stable over the decades, thereby delineating ecosystems that have been preserved over a long term and which have potentially developed higher levels of biodiversity and resilience. The global network of protected

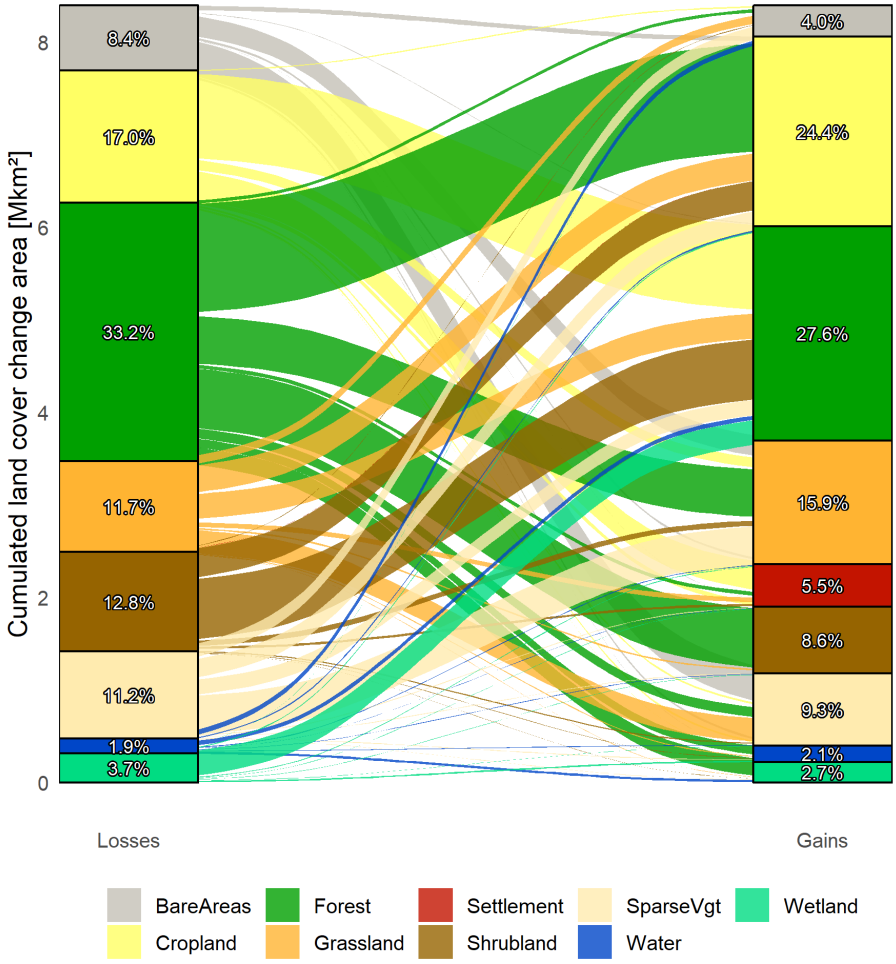

Figure 1.4: Cumulative areas of losses and gains (Mkm²) in IPCC land categories estimated at each annual time step between 1992 and 2020. The left-hand column represents the total area of all observed losses (8.4 Mkm²) cumulated on a yearly time step from 1992 to 2020 and the corresponding percentage of each concerned IPCC land category. The right-hand column represents the total area of all observed gains across all IPCC land categories over the same period. Each stream connecting the blocks from left to right represents the area converted from one category to another, considering all years of the period 1992-2020. The width of the streams indicates the relative importance of the conversion from one land category to another.

Table 1.3: Relative percentages of IPCC category area changes compared to their corresponding areas in 1992. Fraction of swap change concerns the gross change of the class.

IPCC Class	Fraction of persistence	Relative gross change	Fraction of swap change	Relative net change
Forest	94.06	10.81	90.15	-1.07
Cropland	94.44	13.67	81.3	2.56
BareAreas	96.63	4.87	61.62	-1.87
Grassland	93.72	14.96	83.99	2.39
Shrubland	92.53	12.35	79.05	-2.59
SparseVgt	91.67	15.14	89.95	-1.52
Water	95.7	8.98	95.67	0.39
Wetland	85.28	25	82.21	-4.45
Settlement	100	133.36	0	133.36

areas accounts for a significant share of this persistence area, demonstrating their relative effectiveness.

The only land categories undergoing expansion correspond to human LUs, namely cropland, settlements and grasslands. These gains add up to more than 1.43 Mkm^2 (0.62, 0.46 and 0.35 Mkm^2, respectively), which corresponds to the combined area of France, Germany and Spain. The land classes related to natural covers are generally decreasing in extent. The most pervasive anthropogenic land changes are driven by agriculture and urban expansion. Cropland extent increased by only 2.56% over the 29 years, but the systematic analysis of annual transitions reveals that almost 14% of cropland area has changed over the period, highlighting a much more active landscape than indicated by the net change (Table 1.3). While urban growth is responsible for 23% of the cropland loss, the swapping between cropland and forest is responsible for about 60% of both cropland gain and loss. A second significant agricultural dynamic corresponds to the large grassland expansion mainly by forest cutting, while one-third of grassland loss is due to cropland expansion. Interestingly, the cropland area starts to increase drastically in the late nineties, probably due to the emergence of a globalized market (Krausmann and Langthaler, 2019), while the grassland only starts to expand from the 2000s onwards.

In only three decades, the urban extent has more than doubled (an increase of 133%, corresponding to the area of Spain), artificializing the terrestrial surface by built-up made of settlements and infrastructures. Three-quarters of this urban expansion occurred at the expense of the cultivated lands (66% cropland and 11% grassland), highlighting the intricate nature of land dynamics once reported in a spatially explicit manner using comprehensive transition matrices. Only 10% of the urban expansion is converted directly from forested areas. Unlike the cropland expansion slowing down

from 2005, urban growth appears to have steadily increased since 2000 (Figure 1.5).

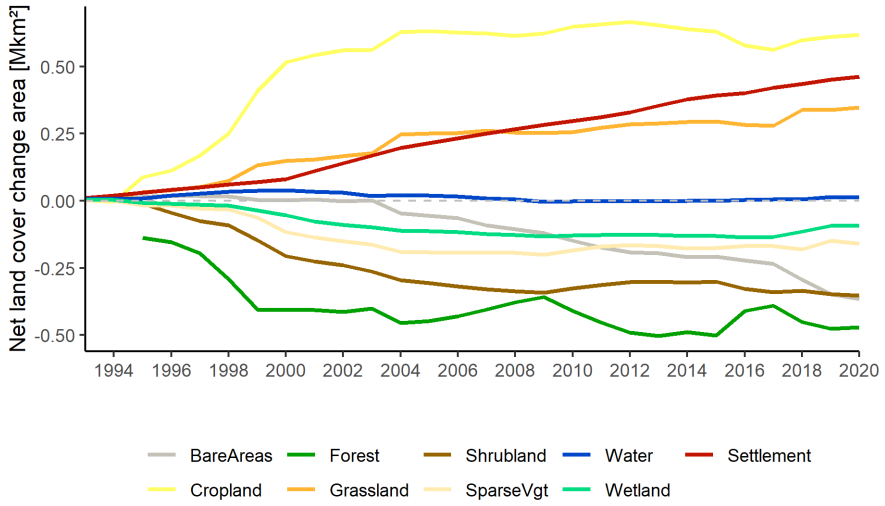

Figure 1.5: Per-year evolution of net change per IPCC land category at the global scale (in Mkm²) highlights the significant increase of anthropogenic land use land cover conversions at the expense of all the (semi)-natural land cover types. This summarizes the fast increase and then the stabilization of cropland extent, the steady urban expansion and the slight grassland increase while forest and shrubland are the most impacted land cover.

Almost 7% of the (semi-)natural vegetated ecosystems, here considered as the green capital, have been affected by land changes, either due to anthropogenic LU conversions or due to various secondary ecological successions. Such an area is larger than half of the USA. Low persistence and a high swapping fraction (Table 1.1), as observed for most (semi-)natural categories correspond to significant degradation processes. Indeed, while balancing gain and loss through swapping may create the illusion of landscape stability, it does not preserve the biological diversity and associated resilience of natural ecosystems, such as forests and wetlands, which rely on persistence over time for their development and sustainability. For instance, 6% of the global forest area was impacted by LCCs over the period, and 60% of the observed forest loss was due to agricultural conversion, which could in some cases return to forest after a few years but will take many decades to be restored as complex forest ecosystems. On the other hand, progressive ecological successions towards forest and grasslands dominate the shrubland and sparse vegetation transformation, respectively. These natural processes, which partly balance out anthropogenic vegetation degradation, are also essential to quantify. It

is worth mentioning that natural disruptive processes enhanced by climate change stress, like unusual forest fire impact or pest outbreaks can also induce LCC, albeit often more regionally or locally (van Lierop et al., 2015; Raffa et al., 2008).

Wetlands are the natural LC shrinking the most since 1992 (- 4%) and they are also the most perturbed, as a quarter of current wetland was either lost or slightly expanding. Even though they are often the richest natural ecosystem in most regions, they show the lowest persistence fraction. Almost 15% of the 1992 wetland area was converted by 2020, mainly into forests (85%), cropland (4%) and water bodies (5%). Land conversion was recognized as one leading driver of wetland degradation (Millennium Assessment Ecosystem, 2005; Galatowitsch, 2018). Cropland expansion often requires additional water management involving drainage and clearing of wetland (Van Asselen et al., 2013). The afforestation dynamic appears quite similar across continents, such as in Europe and North America, while wetland seem also significantly transformed into water bodies in Brazil, North Africa and West Africa. Fortunately, the overall conversion rate seems to be slowing down since 2005 (Figure 1.5), which could hopefully be linked to the 50 years of international efforts under the Convention on Wetlands of International Importance (Ramsar, 1971), the oldest of the modern intergovernmental environmental agreements.

In contrast, the most stable LC is, as expected, the bare area. It still shows a swap change probably partly explained by the development and the abandonment of large irrigated projects due to water shortage, soil salinity or silting up, and possibly by the intrinsic variability of the arid and semi-arid climates. The open inland waters show a very balanced dynamic over the whole period but with a significant expansion of open waters observed from the late 1990s onwards. Due to the construction of large dams, the annual expansion of inland water bodies (5410 km^2/year) matches the figure obtained from the Landsat archive analysis from 1984 to 2015 (5750 km^2/year Pekel et al. (2016)).

Expanding LU for biodiversity conservation through the establishment of the legal status of protected areas has become a top priority for many governments, resulting in an increase to over 14% of terrestrial land over the past three decades. Interestingly this global land change analysis highlights the impact of such legal protection status on the anthropogenic LC conversion, which is reduced by half in 2020 (Figure 1.6). More importantly, the overall trend shows a steady decrease in the slope for the designated areas compared to the non-protected areas.

1.3.2 Spatial repartition of land use changes

Overall, LCC of the terrestrial surface is located almost 40% in Asia, a second 40% split equally in South America and Africa and the last 20% occurs in the

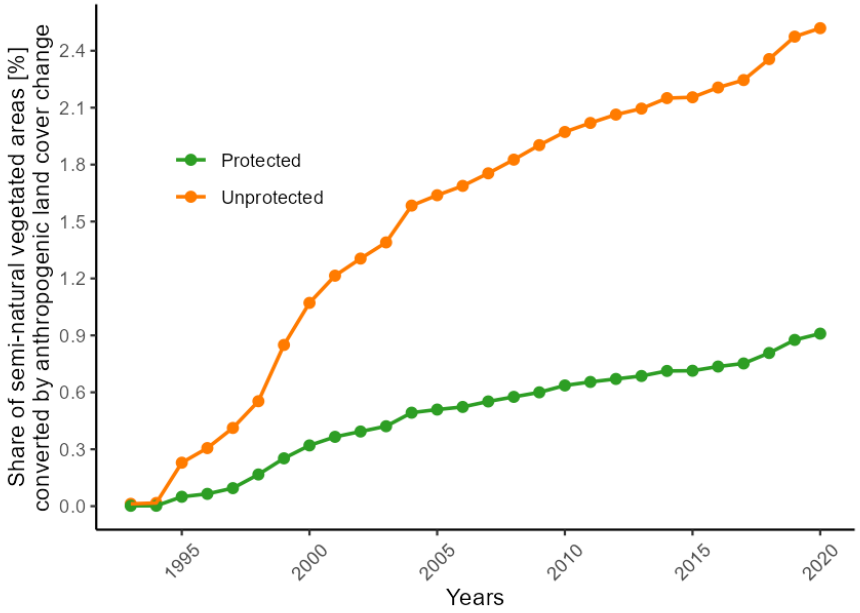

Figure 1.6: Cumulative annual evolution of the share of (semi-)natural vegetated areas eroded by anthropogenic land use land cover change processes according to nature conservation status on a global scale. Only the land change detected after the year of the protected area establishment as reported by (UNEP-WCMC, 2019) is considered for the green curve.

rest of the world (Australia, Oceania, North America and Europe) (Figure 1.7). This spatial distribution is driven by landmass repartition, population distribution and historical trajectories of socio-economic development, balancing land conversion and LU intensification. More specifically, the cropland dynamics appear widely distributed over all the inhabited regions, the forest changes predominantly located in the tropical and boreal zones and the urban growth in East Asia, Europe and North America. These overall patterns enhance the already existing LULC distribution as they are predominantly related to the biomes. These maps also highlight regional patterns, such as cropland conversion into settlements and infrastructures in Northern China and Central and Eastern Europe, or cropland expansion at the expense of forests in South America.

Reporting the net LULC change related to anthropogenic processes like urban and cropland conversion as a function of population change highlights quite contrasted processes for the different regions of the world (Figure 1.8). Four distinct quadrants depict very different LU change trajectories. The most significant anthropogenic LU changes (upper left quarter) tend to be propor-

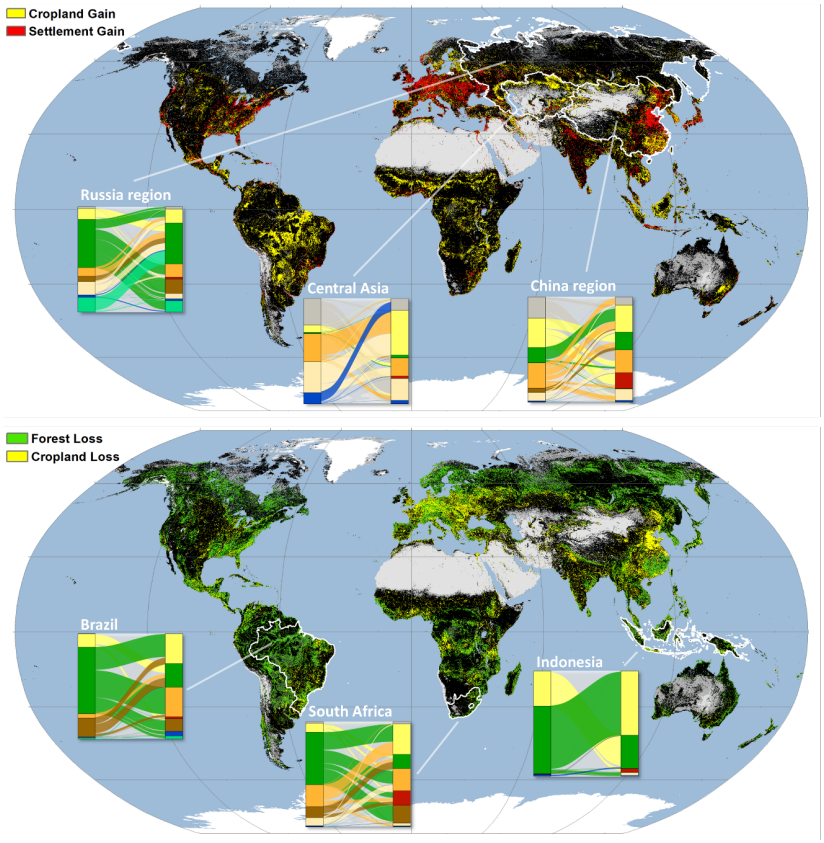

Figure 1.7: Global distribution of anthropogenic LULC changes as observed by satellite during the 29 years. The cropland and settlement expansion can be observed respectively in South America, East Asia and Europe (top) while the forest loss is more widely distributed around the world and the cropland loss is much related to urban development (bottom). Regional trajectories of land conversion depict very contrasting land dynamics for six different regions delineated by a white polygon. The left-hand column represents the cumulative area and proportion of all observed losses by IPCC land category in each year from 1992 to 2020. The right-hand column represents the cumulative area of all observed gains per IPCC land category per year over the same period. Each stream connecting the blocks from left to right represents the cumulative area converted from one category to another, considering all annual transitions over the period 1992-2020. The width of the streams indicates the relative importance of the conversion to another category and the colour legend is the same as in Figure 1.4.

tionally inverse to the population increase but also linked to the share of remaining (semi-)natural vegetated areas per inhabitant. Except for some parts of Indonesia, these regions primarily consist of countries with a relatively low population density and with LU change probably driven by economic drivers. The upper right quadrat includes China and West Africa experiencing both large areas of LULC change and high population growth over the 29 years on territories that are already quite intensively exploited (as indicated by the very limited share of (semi-)natural reservoir per inhabitant). These trajectories seem quite different from India, Eastern Africa and the Rest of South Asia (lower right quadrat), where the population growth does not seem to impact the remaining (semi-)natural LC, probably because of their scarcity and their legal protection status. In the lower-left quadrat, many regions were quite often industrialized before the study period, corresponding to low population increase and low but still increasing anthropogenic LU conversion. Finally, it is worth mentioning that the only two regions that reported a decrease in population during the considered period have also experienced an expansion of (semi-)natural vegetated land, as could be expected.

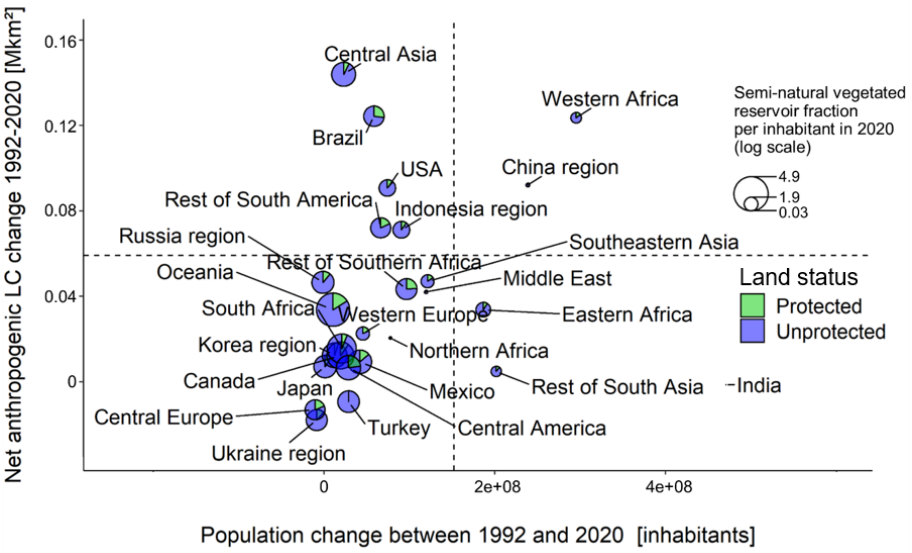

Figure 1.8: Four types of country or region profiles can be distinguished from the relationship between the net LCC associated with anthropogenic processes and population change in their population between 1992 and 2020. The respective geographical aggregation of countries into the 26 regions was defined after Stehfest et al. (2014). The semi-natural reservoir fraction per inhabitant is computed as the ratio between the proportion of remaining (semi-)natural vegetated areas for a given region and the number of inhabitants of this region.

Different patterns of LULC transition according to geographies are illustrated in Figure 1.7. For instance, the well-documented deforestation trend in Brazil (Silva Junior et al., 2021) is reported as a major conversion to grassland and cropland. The regions of Russia, South Africa and Indonesia are also dominated by forest conversion to a lesser extent, but they follow different patterns. Indonesia shows the simplest landscape transformation involving the interplay of only two major classes, forest and cropland. South Africa and China are much impacted by urban expansion in relative terms. Most striking is the conversion of water into bare soil in Central Asia, mainly due to the spectacular and continuous shrinking of the Aral Sea for irrigation purposes (Micklin, 2010; Cai et al., 2003).

1.3.3 Validation

The resulting series of consistent 300 m annual LULC maps from 1992 to 2020 is delivered with an uncertainty value at the pixel level, indicating the confidence that an LC class was assigned for each pixel. According to international standards, these products were also assessed globally, using a fully independent validation dataset to produce a confusion matrix and derive an overall accuracy estimation. Strict independence of the validation process was ensured by using only EO data sources not used in the processing calibration and relying on a dozen internationally recognized LC experts providing information for their respective regions of expertise. A unique object-based validation database of 2600 primary sampling units randomly selected on a regular 0.5° degree grid (FAO et al., 2009) was completed by a panel of widely distributed international LC experts using very-high-resolution imagery and Normalized Difference Vegetation Index (NDVI) temporal profiles (Defourny et al., 2012a). Using all samples interpreted as "certain" by the experts and "homogeneous at 90% (i.e. made of a single LC class) for the 22 LC typology, the overall accuracy was found to be 70.46% for the 2020 map (Defourny et al., 2021). The highest F1 scores were found for the classes of rainfed cropland (82%), irrigated cropland (93%), broadleaved/needleleaved evergreen forest (87%/80%), urban areas (75%), and water bodies (97%). Conversely, mosaic classes with a majority of herbaceous cover, either natural or cultivated, sparse vegetation and flooded natural vegetation were associated with low user accuracy values.
These figures are of the same order of magnitude as other 500m global LC products (Sulla-Menashe et al., 2019). Several global LC products mapping at 30 m a smaller number of LULC classes reported an overall accuracy of 77% with 7 classes for North America only (Friedl et al., 2022), 78.35% for 12 classes globally (Hansen et al., 2022), and 80.33% for 9 classes respectively (Chen et al., 2015b). Interestingly, the higher spatial resolution of Landsat seems to reduce but does not resolve, the impact of frequent mixed-class pixels as relatively few pixels are actually uniform at 30m resolution (Friedl et al.,

2022; Potapov et al., 2022). The quite variable density of valid cloud-free Landsat observation is another challenge, particularly in regions with year-to-year phenology variation (Friedl et al., 2022; Zhang et al., 2022). Furthermore, the overall accuracy of the initial version of the ESA CCI LC products was also estimated by independent studies at a global scale (Tsendbazar et al., 2016) and over specific regions (e.g. over China (Yang et al., 2017)), which can give valuable insights for specific applications.

Since these global annual LULC maps are produced for the EU Copernicus Climate Change Service, the annual accuracy assessments vary from 70.5% to 71.1% based on the annual update of the object-based validation database. Such a regular update of the validation database captured some LULCC events (8.05% of the reference samples between 2010 and 2020) but is not relevant to assess the LULCC detection accuracy because of the marginal occurrence and the spatial autocorrelation of LULCC.

Limitations

Despite the innovative methodology combining five different satellite missions, the consistency of this time series is hindered by the lack of global satellite observation at 300 m in the 1990s. The persistent LULC pixels are backdated at 300 m until the hotspot LULCC detection is triggered by the 1 km time series analysis and the change mapped at 1 km. The limited AVHRR data quality allows us to map only forest cover loss and water loss between 1992 and 1999 (except in 1994 due to missing AVHRR data). The urban expansion is mapped from 1992 thanks ancillary dataset as previously explained. The change in snow and ice class could not be mapped consistently over the period across the globe using the 300m satellite data. Forthcoming high-resolution data sources, such as the Sentinel constellation, are expected to improve this fine monitoring as such capabilities have become more feasible in recent years.

The 22 LULC classes typology was found very appropriate for supporting many applications like dynamic global vegetation modelling or biodiversity assessment. The change detection however needs to reduce the possible land conversion to 13 types which are remapped at 300 m resolution according to the 22 classes typology in the second step. The mosaic classes were found appropriate for accurately capturing various fragmented landscapes and natural gradients at a resolution of 300 meters. However, due to the challenges encountered in their delineation and validation, mosaic classes were not accounted for in the reported overall accuracy (Defourny et al., 2017a). This is particularly true for irrigated croplands, where the diversity of irrigation patterns, equipment, and irrigation intensities contributes to the complexity of classification. The high number of LULC classes in the legend hinders the

computation of weighted overall accuracy due to the limited number of reference sampling units for some of them.

Most of these issues will be addressed in the near future to improve not only the global long-term multi-mission LULC time series but also its LULCC validation for recent years. This is facilitated by the increasing availability of high and very high-resolution imagery at the global scale and the recent developments in data fusion from multiple sources.

Conclusions and perspectives

This paper provides for the first time a thorough analysis of LCC at the pixel level of a pivotal global land data record. By doing so, it demonstrates essential characteristics of what global monitoring of LC transitions should entail going beyond the observation of land change areas. The dataset underlying this analysis is temporally consistent by design, spatially explicit at the finest pixel level, and covers a sustained and long archive period. By capitalizing on the initial 2005 GlobCover experience combined with long-term research, the approach has today turned into an operational Copernicus service, serving as ECV for various applications. Some studies have already demonstrated the value of such data records based on the initial version of part of this global map time series (first delivered in 2017). Analyses of land change trajectories have been published and have reported alternative figures for various reasons. For instance, coarser results were obtained by spatial aggregation of the dataset to a 0.5° x 0.5° grid cell (Liu et al., 2018; Li et al., 2018) combined with user clustering of classes or conversion of classes to PFT distribution based on a cross-walking table designed for Earth system models. LCC assessed as landscape dissimilarity at the 9 x 9 km² tile level was as high as 22% of the landmass (Nowosad et al., 2019). Others (Haščič and Mackie, 2018; Iannini et al., 2016; Mousivand and Arsanjani, 2019) considered net change only or derived area estimates by simply multiplying the number of pixels by their area without considering their variable size by latitude. Looking at the urban impact, van Vliet (2019) focused on single land conversion. In parallel, FAO (2017) converted the LCCS typology of this map time series to its System of Environmental-Economic Accounting Central Framework to provide country estimates with its proper legend. This initial uptake by key stakeholders provides encouraging prospects for this finalized product as a whole, while the detailed and unprecedented analysis presented in this paper should open its use to a wider audience.

There are considerable perspectives to go beyond LC transitions with this unique and harmonized dataset. First, it will be adapted to satisfy the precise descriptions of PFTs distribution that are much needed to parametrize how climate models represent land-atmosphere interactions, and specifically the fluxes of water, energy, and carbon (Hartley et al., 2017; Feddema et al., 2005;

Hibbard et al., 2010). This 300 m long-term time series is the cornerstone to fuse various existing higher-resolution observational datasets to provide a spatially-explicit description of the PFT distribution to support the climate change modelling. In this context, monitoring LC transitions as illustrated here has a critical role in better estimating both land-based greenhouse gas emissions and surface-to-atmosphere fluxes, especially during this period of transient climate.

The findings reported here illustrate the significant contribution of such built-in temporal consistency to monitor land surface dynamics at the pixel level. Such longitudinal analysis is of critical interest for policy impact assessments and contributes to international transparency in the context of multilateral agreements for a more sustainable planet such as the Paris Agreement.

In addition to the interannual change over decades, the 22 LC types are further described by their local seasonal dynamics provided at 1 km resolution. Weekly dynamics of the vegetation cycle, the fire regime and the snow occurrence characterized each square kilometre of the LC. The annual vegetation greenness cycle is depicted every week by a vegetation index time series averaged from the 13 years of daily observations. Similarly, the probability of fire and snow is reported weekly for each 500m grid cell and can be interactively displayed on the online visualization interface (Figure 1.9). Combining interannual LCC and seasonal dynamics paves the way for a new ontology for land surface characterization. LULC is observed along a continuum, and the characterization of LULC lacks a universally accepted standard granularity for space (e.g., pixel size) or time (e.g., frequency) because it depends on the specific objectives of the observation. This ontology introduces a multidimensional time dimension to characterize the various facets of the land surface, thus paving the way for the development of an integrated definition of LC that can adapt to different spatial and temporal scales.

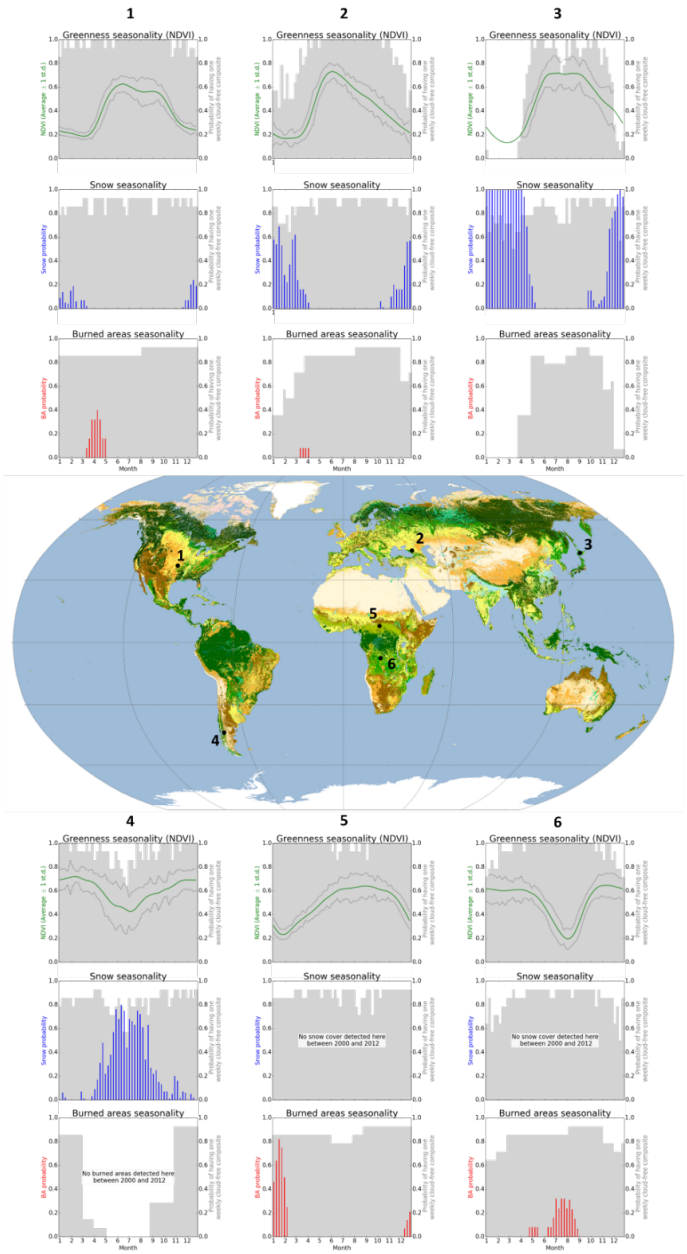

Figure 1.9: The global LU LC map 2020 describes the world's landscape into 22 global classes with a spatial resolution of 300 m and the seasonality of 3 land surface variables weekly: the vegetation greenness, the snow cover and the burned areas (`https://maps.elie.ucl.ac.be/CCI/viewer/`).

Chapter 2

A Stratified Random Sampling Approach for Binary Product Comparison

This chapter is based on the following article:

Lamarche, C., Santoro, M., Bontemps, S., d'Andrimont, R., Radoux, J., Giustarini, L., Brockmann, C., Wevers, J., Defourny, P. & Arino, O. (2017). Compilation and validation of SAR and optical data products for a complete and global map of inland/ocean water tailored to the climate modeling community. *Remote Sensing*, 9(1), 36.

Abstract

Accurate land cover mapping relies significantly on integrating various Earth observation-derived products, especially those with high spatial resolutions, for training and compilation. This integration approach is fundamental to the methodology developed for generating global land cover maps, as described in Chapter 1. However, with few guidelines provided by the Committee on Earth Observation Satellites-Land Product Validation for product comparison, assessing the relative quality of available binary map products that characterize the same class, especially on a global scale, poses a significant challenge. This chapter aims to address this issue by focusing on the validation of three global inland water products using a reference database created from 2110 photo-interpreted samples. Here we show that a stratified random sampling approach, tailored to areas prone to disagreement between the maps and using the same reference dataset allows for highlighting the respective advantages or drawbacks of the different products. The overall accuracy, assessed across all sample units, was exceptionally high for all products, ranging from 98% to 100%. However, when focusing solely on sample units targeting error-prone areas, the accuracy substantially decreased for all products. This resulted in significant differences between products, with overall accuracies in the error-prone stratum ranging from 74% to 89%. In addition to illustrating the significance of this customized sampling design for product benchmarking, this study enabled the compilation of a new global land mask. This mask has been adopted for the processing of several European Space Agency Climate Change Initiative Essential Climate Variables.

2.1 Introduction

Fresh surface water is one of the most precious resources on Earth, fulfilling social, economic and environmental services (Connor, 2015; GEO, 2013). Reliable assessment of the world water resources is of paramount importance for decision-making, governance and mitigation (Bates et al., 2008). Maps of open water bodies allow for retrieving key climate variables, such as evaporation, water/land surface temperature, energy balance, selecting appropriate aerosol algorithms and sharing a common coastline map between processes.

Numerous products that describe surface water features are accessible. Among global databases, the Global Lakes and Wetlands Database (GLWD) (Lehner and Döll, 2004) compiles worldwide and regional sources concerning lakes, reservoirs, and wetlands whose area is greater than 0.1 km^2, prior to 2000. The Global Insight Plus database comprises drainage features represented as lines/polylines at a 1:1M scale, with a horizontal accuracy of 2,048 m or less (Europa-Technologies, 2014).

However, remote sensing is regarded as the primary tool to provide accurate, detailed and up-to-date characterization of inland water bodies on a systematic basis for any location on Earth. Various methods and datasets have been developed to map open water bodies using active radar and passive optical satellite observations with different spatial resolutions (30 m to 1,000km), as shown in Table 2.1.

The first wall-to-wall map of water bodies for large parts of the globe was obtained with Synthetic Aperture Radar (SAR) data acquired during the Shuttle Radar Topography Mission (SRTM). The SRTM Water Body Dataset (SRTM-SWBD) (Farr et al., 2007) is a by-product of the digital elevation model of all land masses imaged by the SAR. The SRTM-SWBD map represents the water extent between 11 and 21 February 2000 between 60°N and 54°S at a spatial resolution of 90 m, is void-free, with river continuity being ensured by a thorough post-processing of the initial classification (Slater et al., 2006). The SAR-based Water Body Indicator (SAR-WBI) is a nearly global dataset of permanent open water bodies which covers land masses between 84°N and 60°S and has a spatial resolution of 150 m, except in areas with predominant coarse resolution Advanced Synthetic Aperture Radar (ASAR) data (1000 m) (Santoro and Wegmuller, 2014). It is derived from the exploitation of Multi-temporal SAR metrics derived from Envisat ASAR data acquired between 2005 and 2012. It was found to accurately characterize the spatial distribution of water bodies, primarily in the northern latitudes. The major caveat of the SAR-WBI is the omission of water along shorelines and the absence of water features being smaller than twice the pixel size.

Table 2.1: Available global and near-global EO-derived product of permanent inland water bodies with their references, extent, source, pixel resolution, and thematic validation

Products	Extent	Source	Pixel size	Accuracy assessment
SRTM WBD (Farr et al., 2007)	60°N–54°S	SAR (SRTM)	90m	not reported
SAR-WBI (Santoro and Wegmuller, 2014)	84°N–60°S	SAR (ASAR)	150m, 1000m	product-to-product benchmark
MOD44W (Carroll et al., 2009)	global	SAR (SRTM) + Optical (MODIS)	250m	not reported
GFC-datamask (Hansen et al., 2013a)	80°N–57°S	Optical (Landsat)	30m	not reported
GIW v1.0 (Feng et al., 2016)	90°N–60°S	Optical (Landsat)	30m	not reported
G3WBM (Yamazaki et al., 2015)	global	Optical (Landsat)	30m	not reported

The first water bodies dataset based on optical remote sensing data is the Global Raster Water Mask at 250-m resolution (MOD44W) (Carroll et al., 2009). It builds on the SRTM-SWBD, by filling gaps with MODIS optical data available for years 2000 and 2001. To achieve a truly global extent, it was complemented with water detections from the MODIS data north of 60°N and with a mosaic of Antarctica land masses (Snow et al., 2005) south of 60°S (Carroll et al., 2009). In regions where water was detected using MODIS data, water bodies smaller than 2–3 pixels may have been missed (Carroll et al., 2009). MODIS data at 250- and 500-m resolution were also used in the Global Water Pack methodology to derive the daily temporal dynamics of water (Klein et al., 2015), but no product has been released so far. PROBA-V acquisitions from January 2014 to the present at a spatial resolution of 1000 m are used to generate the Copernicus Global Land Service Collection 2 (Copernicus WB) dataset, consisting of water body maps every 10 days between 80°N and 60°S (Lacaze et al., 2015).

HR (30 m) Landsat time series were intensively exploited in the last few years to detect water surfaces and monitor water dynamics. The Global Forest Change (GFC) product depicts forest extent and change from 2000–2012

(Hansen et al., 2013a). The sub-dataset "datamask" (hereafter, GFC-datamask) includes the class "permanent water bodies" covering all land masses between 80°N and 57°S. The 30-m Landsat Global Land Survey (GLS) data acquired for the 2000 epoch were used to generate an inland surface water classification between 90°N and 60°S referred to as the Global Inland Water (GIW) v1.0 product (Feng et al., 2016). Using multi-temporal GLS images from 1990–2010, Yamazaki et al. (2015) produced a map of permanent and seasonal water bodies referred to as the Global 3 Arc-Second Water Body Map (G3WBM). The data product spans 90°N and 60°S and has a spatial resolution of 90 m. Pan-sharpened Landsat 7 (14.25 m spatial resolution) imagery circa 2000 was used to generate the Global Water Bodies database (GLOWABO), including all lakes larger than 0.002 km^2 (Verpoorter et al., 2014b). The Deltares Aqua Monitor (Donchyts et al., 2016) and the Landsat-based 30-year global surface water dynamics (Pekel et al., 2016) are also available at a spatial resolution of 30 m.

The process of validation is essential to ensure the reliability and appropriate use of any cartographic product. The LPV subgroup of the CEOS WGCV has established comprehensive guidelines for the global validation of categorical LC products, one class of which is inland water bodies (Strahler et al., 2006a; Olofsson et al., 2013).

Various strategies have been used to validate the above-mentioned water body products. Some, including the SRTM-SWBD, GFC-datamask, Copernicus WB, and Global Insight Plus were not thematically validated. Accuracy assessments of other products such as MOD44W, GIW v1.0, GLWD, GLOWABO, and G3WBM relied on the comparison of total water bodies area with existing products, without providing specific information about disagreements between products or validating results against reference data. The SAR-WBI was validated over limited areas by comparison against independent maps. Santoro and Wegmuller (2014) reported confusion matrices with the OA, Producer Accuracy (PA), User Accuracy (UA) and Kappa indices. However, the variety of validation approaches makes it challenging to compare the strengths and weaknesses of available water body products. Furthermore, reference validation datasets cover limited areas and are only used to validate a particular product, without making performance comparisons with other existing products.

In the framework of the ESA CCI, the climate and remote sensing communities expressed the need for a global (90° N–90° S and 180° W–180° E), spatially-complete, accurate (maximum 10% error) mask of the open water body product with a MR of a minimum of 300 m (Herold et al., 2010). The distinction between inland water and oceans was requested as an extra feature.

One of the objectives of this study is to generate the CCI global map of open water bodies at 150 m that fulfills all criteria of the climate modelling

community. The moderate spatial resolution was found adequate for contemporary global circulation, regional and emerging convection-permitting models that run at a current horizontal spatial resolution coarser than 150 m (IPCC; Flato et al., 2013; Prein et al., 2015). Rather than developing new classification schemes, we focused on the synergistic combination of multiple individual datasets.

This chapter also aims to address validation issues while allowing the comparison of binary map products where one class is marginally distributed, as is the case for inland water products. We use a stratified random sampling approach with strata corresponding to error-prone areas in water body mapping and compare its effectiveness to other sampling methods such as simple random sampling or class-based stratified random sampling. A reference database created from 2110 photo-interpreted samples of very HR imagery was created for this purpose. The CCI WBv4.0 and its constitutive inputs were the selected products for this testing process. The methodological flowchart is illustrated in Figure 2.1.

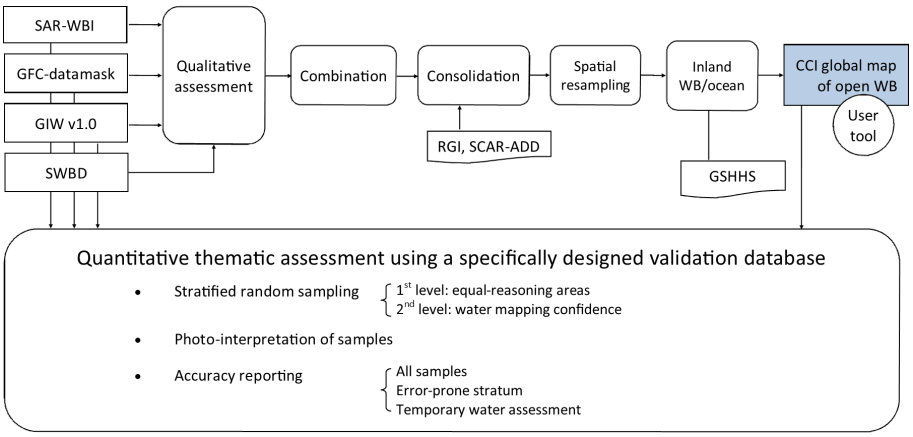

Figure 2.1: Flowchart outlining the compilation of the CCI global map of open water bodies and the quantitative thematic assessment of this study.

The selection of water body and auxiliary datasets relevant to our objective is first presented (Section 2.3.3). Then, the methodology adopted to combine and consolidate the selected input products is described along with the stratified random sampling design (Section 2.3). The CCI global map of open water bodies and its assessment are presented in Section 2.4 and discussed in Section 2.5. Finally, a set of conclusions and future outlooks is included in Section 2.6.

2.2 Material

2.2.1 Potential products to build the CCI global map of open water bodies

With reference to the water body products listed in the Introduction, the GLWD, the Global Insight Plus and the Copernicus WB were discarded a priori because they did not fulfill the target requirement of a spatial resolution of less than 300 m. Furthermore, the MOD44W data product was not considered due to the MODIS high view zenith angle that implies that individual observations regularly cover several adjacent grid cells (Duveiller et al., 2011). This effect can significantly increase the actual observation footprint and reduce the effective spatial resolution. The GLOWABO database (Verpoorter et al., 2014a), the G3WBM (Yamazaki et al., 2015), the Deltares Aqua Monitor (Donchyts et al., 2016) and the product from (Pekel et al., 2016) were not available at the time of this study.

As a consequence, only the SWBD, the SAR-WBI, the GFC-datamask and the GIW v1.0 dataset were retained as candidate inputs to build the CCI global map of open water bodies. The SWBD captured the actual water state of 10 days in February 2000 from the orthorectified SRTM radar image (Farr et al., 2007). Permanent water pixels of the GFC-datamask were selected as having a fraction of water-flagged observations for all non-cloudy observations greater or equal to 50% of the Landsat image time series selected during the growing season (Potapov et al., 2012). A thresholding algorithm was applied to multi-temporal SAR metrics to map water bodies of the SAR-WBI (Santoro and Wegmuller, 2014). In the GIW v1.0, water pixels were the ones with the highest water/non-water probability calculated on each Landsat scene of the GLS 2000 collection (Feng et al., 2016). Product characteristics are presented in Table 2.2.

2.2.2 Auxiliary datasets

Each of the selected datasets presents local errors related to the imperfect delineation of glaciers. These were corrected with the Randolph Glacier Inventory v3.2 (RGI) (Pfeffer et al., 2014; GLIMS). The RGI compiles glacier outlines as a complement to the Global Land Ice Measurements from Space (GLIMS) initiative. The RGI was selected for its wall-to-wall coverage of glaciers and frequent outline improvements.

To fill the data gap that would occur south of 60° S when combining the input water body datasets, the Scientific Committee on Antarctic Research Antarctic Digital Database (SCAR ADD) (Fox et al.) was selected. The SCAR ADD is a seamless compilation of coastline and topographic data for the continent of Antarctica. The aim of SCAR ADD is to provide the best currently available data over Antarctica with a maximum offset of 1000 m with respect to the true coastline (Fox et al.).

The distinction between inland and ocean water relied on the Global Self-consistent, Hierarchical, HR Shoreline (GSHHS) dataset (Wessel and Smith, 1996). The GSHHS combines the World Vector Shorelines (WVS) and the CIA World Data Bank II (Wessel and Smith, 1996). The WVS is the basis for shorelines with a working scale of approximately 1:100,000. The GSHHS database considers rivers as inland water bodies limited by a straight line located inland at no more than 1.85 km from the river mouth (US DMA, 1991). The GSHHS dataset was selected because of its global coverage and the accurate delineation of coastlines (Wessel and Smith, 1996).

Table 2.2: Characteristics of the water body data products selected to compile the CCI global map of open water bodies.

	SWBD	**SAR-WBI**	**GFC-Datamask**	**GIW v1.0**
Sensor/ mission	Shuttle Radar Topography Mission	Envisat ASAR	Landsat	Landsat
Data source	Interferometric C- and X-band observations	Multi-temporal SAR backscatter observations	Landsat time series	Global Land Survey 2000, collection of Landsat images
Spatial resolution	90 m (public release)	150 m or 1000 m depending on ASAR acquisition mode	30 m	30 m
Time frame of EO data	11–22 February 2000	2005–2012	2000–2012	1999–2002
Legend	3 classes: water, non-water, no data	3 classes: potential WB, land, no data	3 classes: no data, mapped land surface, permanent water bodies	6 classes: no data, land, water, snow/ice, cloud shadow and cloud
Spatial extent	60° N/56° S	84° N/60° S	80° N/57° S	90° N/60° S

2.3 Method

2.3.1 Qualitative assessment of input water body maps

The qualitative assessment of the SAR-WBI, the GFC-datamask, the GIW v1.0 and the SWBD was guided by the following user requirements: completeness, quality and spatial resolution. None of these products fulfilled the requirements on global extent and inland/ocean water delineation.

The completeness of each product was assessed by calculating the percentage and location of no data values or thematic classes different from land or water. The GIW v1.0 included the highest proportion of invalid data (9%), spread over land masses. Invalid data belong to classes 'no data', 'snow/ice', 'cloud shadows' and 'clouds'. Invalid data in the SAR-WBI and GFC-datamask were localized in contiguous areas and summed up to 3% and 7% of the total number of land pixels, respectively. None of the three products include Antarctica, and only ocean water close to the coast was explicitly mapped. Islands in the North of Canada, Greenland, Svalbard, Northern Russia and the islands in the Pacific Ocean were not included in the GFC-datamask. The northernmost latitudes and Svalbard were not included in the GIW v1.0 dataset. No classification could be obtained in the SAR-WBI for south Panama, north Australia and several isolated islands due to a lack of ASAR observations. In addition, a 1-degree longitudinal belt between 84° N and 83° N was removed because of permanent sea ice, systematically classified as land. The classification was not undertaken for the Greenland ice sheet because permanent water bodies are not included (Santoro and Wegmuller, 2014). The SWBD was complete between 54° S and 60° N. As a result of this investigation, missing information was not systematically located over the same areas among all products so that their fusion could contribute to achieving completeness.

The quality of the products was assessed in terms of errors and their location. Errors were related to misclassifications of temporary water events as permanent water (e.g., snow or ice melt, floods), incorrect coastline delineation, icebergs classified as land, confusion between water and dark landscape features, such as black lava or shadows in mountainous terrain, classification of wetlands or irrigated fields as permanent water, processing-induced artifacts (e.g., seams), and defective sensors.

With regard to the spatial resolution, the best characterization of water bodies was observed in the GFC-datamask and GIW v1.0 products. The 30-m resolution indeed better-ensured river connectivity and delineation of small water bodies, such as thermokarst lakes and narrow tributaries. The analysis of these two products furthermore revealed their complementarity in the sense that errors and omissions were not systematic in both (Section 2.4.1). Despite the coarser spatial resolution, the spatial distribution of water bodies in the SWBD and the GFC-datamask was similar. The added value of the SWBD in this context is the presence of islands, which were not included elsewhere. Because of the coarser resolution (150 m), the delineation of water bodies in the SAR-WBI was less accurate compared to the 30-m data products. Nevertheless, the very high density of observations by ASAR (Santoro et al., 2015b) resulted in a more precise characterization of coastlines, lakes and river systems. In addition, some artificial lakes created during the last decade were detected in the SAR-WBI only.

2.3.2 Generating a global map of open water bodies and ocean at 150m

Combination of water body products

The GFC-datamask was selected as the primary source of information due to the 30-m resolution, the high quality of the water body delineations and the tendency to map the minimum water extent. The GFC-datamask was supplemented with the GIW v1.0 water class, which brought additional spatial details to the water characterization and increased spatial completeness. The SWBD was used to replace the water in correspondence to islands missing in the GFC-datamask and the GIW v1.0 datasets. Finally, the water and land classes from the SAR-WBI resampled at 30 m, filled the remaining voids north of 68° N.

Consolidation

Consolidation of the combined product obtained with the procedure outlined in Section 2.3.2 served to improve it in terms of completeness and accuracy. The SCAR ADD Antarctica layer was added to extend the data product to 90° S. The RGI was used to fill gaps on glaciers and correct for water commission errors. At this stage, the data product presented voids only over oceans, which were manually corrected to water to reach completeness.

Macroscopic errors due to imperfections in each of the input products were finally corrected. To this end, the land surface was divided into a regular grid of cells of 1×1 degree inside which the individual datasets were compared. Hotspots of disagreement were furthermore cross-checked with high spatial resolution imagery from Bing Maps and Google Earth. Confirmed errors were manually delimited and removed. To correct for water omissions, the SAR-WBI was introduced south of 68° N.

Spatial resampling

The nearest neighbor algorithm was chosen for resampling the combined data product to the final spatial resolution of 150 m. The 150-m spatial resolution was chosen as the final spatial resolution as this is the lowest resolution of the data layers used to generate the CCI water body product. This choice will be discussed in Section 2.5.

Differentiation of inland/ocean Water

The main constraint in defining the land/water boundary was to maintain the detailed coastline from the input water bodies while including the rivers flowing into the ocean in the inland water class.

Around river mouths, the GSHHS was used to define the limit between the inland section of the rivers and the ocean. Due to discrepancies between

the coastline of the input water bodies and the one defined by the GSHHS database, a positive buffer of 0.033 degrees (~3.6 km at the Equator) was applied to ensure extracting rivers from oceans without affecting the coastlines of the global map of open water bodies. Since the GSHHS database considered rivers as inland water bodies limited by a straight line located inland at no more than 1.85 km from the river mouth, the resulting rivers are represented as inland water bodies limited by a straight line located inland at no more than ~5.45 km from the river mouth. Elsewhere, the coastline is defined by the water detection implemented in the input water body products.

User tool

The CCI global map of open water bodies is delivered at 150-m spatial resolution in a Plate-Carrée projection. To support a wide range of communities requesting a different spatial resolution and/or projection, a stand-alone software tool was developed to allow sub-setting, re-scaling and re-projection (Table 2.4). Re-scaling generates the fractional area of each class in the target cell and the class value with the largest fractional area.

Table 2.4: Set of options included in the user tool.

Sub-Setting	Predefined regional subset
	Free specification of regional subset (4 corner coordinates)
Re-Scaling	Original resolution
	0.250, 0.500, 1.000, 1.875 degree
Re-Projection	Original projection (Plate-Carrée)
	Gaussian grid

2.3.3 Quantitative thematic assessment

Sampling scheme

Differently than traditional accuracy assessments relying on simple random sampling, a two-fold stratified random sampling was used to avoid undersampling rarely occurring map classes, as is the case for the "water" class (Congalton, 1988).

The first level of stratification was geographic in order to exclude open oceans and polar areas. It generated 21 "Level-1" strata defined by bioclimatic and remote sensing criteria (Defourny et al., 2012b). The number of samples per Level-1 strata was proportional to their area. Good practices of accuracy assessment suggest that class-based stratification reduces standard

errors of class-specific accuracy estimates (Olofsson et al., 2014a). However, because inland water corresponds to a marginal class concerning global LC, using water and land as strata would be beneficial for user accuracy, but could result in optimistic producer accuracy results due to the reduced probability of sampling water omissions. The second level of stratification was therefore developed based on the a priori confidence of correctly representing map classes. This confidence-based stratification was categorized into three Level-2 strata: high confidence in correctly mapping the land class (Stratum 1), high confidence in correctly mapping the water class (Stratum 2) and error-prone areas (Stratum 3). The combination of the MOD44W (Carroll et al., 2009), the GLWD (Lehner and Döll, 2004) and the Global Insight Plus water layer (Europa-Technologies, 2014) were used to obtain the three strata. Stratum 1 corresponded to land agreement between the three maps, Stratum 2 to water agreement and Stratum 3 to discrepancies between at least two of the three maps. The surface of Stratum 3, i.e., error-prone areas, corresponded to 76% of the total surface of inland water.

The sample size, N, was optimized according to the expected accuracy of the CCI global map of open water bodies, and the confidence interval was derived according to the binomial distribution (Stadelman, 1994):

$$N = \frac{p \times (1-p)}{(\frac{E}{Z_\alpha})^2} \tag{2.1}$$

where E is the allowable error in the sample (half of the confidence interval), Z_α is the critical value drawn from the normal distribution for a given level of confidence and p is the targeted accuracy of the product. A confidence interval of 4% with a confidence level of 95% ($Z_\alpha = 1.96$) was chosen.

We assume that the accuracy of water classification is lower where different maps disagree, while water bodies are usually classified with high to very high OA in areas of agreement. The targeted accuracy was therefore set to be at least 85% in the error-prone area, which corresponds to approximately 1200 samples. An additional 1200 samples were distributed equally to the other two strata, where the targeted accuracy was at least 93%.

Generation of the validation database

The sampling unit was the pixel materialized with a footprint of 150 m × 150 m. These samples were visually interpreted independently from the product using HR Google Earth imagery. Careful attention was paid to interpreting and recording the permanent, as well as the temporary character of snow and water evenly across the globe by extensive use of historical imagery. According to the photo-interpretation practices building on the convergence of evidence (Estes and Simonett, 1975; Teng et al., 1997), it was possible to identify

water presence at the time of imaging, but also surfaces that can be seasonally flooded. In particular, these surfaces concern dry river beds, flood-prone areas, irrigated agriculture, mangroves/inundated forests, ephemeral streams, salt pans and snow packs. Samples were labelled as water when at least half of the sample was covered with open surface water. Samples showing temporary snow or water were labelled as land, but the temporal aspect was also recorded. For all samples, the date of the HR imagery was recorded. In addition, wetlands and swamps were also recorded.

Accuracy assessment

The CCI global map of open water bodies, the SAR-WBI, the GIW v1.0 dataset and the GFC-datamask were each validated against the reference samples of the validation database, assuming that these represent the true Earth surface state. The SRTM-SWBD was not validated given its minor contribution to the CCI global map of open WB (0.69% of the total inland water surface). Here, accuracy was assessed at three levels. One assessment included all samples and took into account all strata. A second assessment exclusively focused on the error-prone stratum of Level-2. A third assessment focused on the samples recorded as temporary water to evaluate whether seasonal water bodies affect the water body product.

The assessment was quantified in terms of confusion matrices built by comparing each class of the map (n_i) to the reference sample classes (n_j). Each confusion matrix reported the OA, UA, PA (Strahler et al., 2006b), and the F1-score.

OA represents the proportion of all cases correctly classified (Equation (2.2)) with n being the total number of samples and q the total number of classes (water and non-water). Because the sampling probability was different among the three Level-2 strata, global index values were weighted according to the sampling probability.

$$OA = \sum_{s=1}^{3} w_s \sum_{k=1}^{q} \frac{n_{kks}}{n_s} \tag{2.2}$$

In Equation (2.2), w_s is the weight of the stratum, which is inversely proportional to the sampling effort. The weights are computed for each stratum based on Equation (2.3).

$$w_s = \frac{S_s/n_s}{\sum_{s=1}^{3} S_s/n_s} \tag{2.3}$$

where S_s is the area of the stratum and n_s is the number of sample points in the stratum.

UA corresponds to the probability that a randomly-selected pixel from the map is classified as correct in the reference sample. PA corresponds to the probability that a reference sample is correctly classified in the map. Therefore, UA is related to the commission error while PA informs about the omission error. They are calculated following Equations (2.4) and (2.5) inside each stratum and thereafter weighted using the same method as for the global OA.

$$UA_i = \frac{n_{ii}}{n_{i+}} \tag{2.4}$$

$$PA_j = \frac{n_{jj}}{n_{+j}} \tag{2.5}$$

The F1-score (Equation 2.6) represents for a class k the harmonic mean of the user and producer accuracies and ranges between 0 and 1.

$$F1 - score = 2 * \frac{UA_k * PA_k}{UA_k + PA_k} \tag{2.6}$$

As the same reference samples were used to assess each map, the samples are not independent, a McNemar test (McNemar, 1947) was applied to evaluate if the difference in the disagreements reported in the confusion matrix between the reference and each individual product were significantly different (Foody, 2004). The McNemar test is non-parametric and is based on 2 x 2 confusion matrices that focus on the binary distinction between correct and incorrect class allocations. A 5 % level of significance was selected for the tests.

2.4 Results

2.4.1 The CCI global map of open water bodies

The CCI global map of open water bodies is illustrated in Figure 2.2. This global, void-free dataset consists of two separate layers: an inland water/ocean repartition at 150-m spatial resolution and an inland water fraction, in percent of the 150-m grid cell. The total inland water area is 3.41 million km^2.

The complementarity of the GFC-datamask and the GIW v1.0 products was key to obtaining an exhaustive detection and delineation of water bodies. Figure 2.3 illustrates the increase of river continuity brought by the GIW v1.0 (a, b), compensations for water body omissions present in the GFC-datamask (c) and "no data" filling by the GFC-datamask (d). The SAR-WBI contributed significantly north of 68°N (Figure 2.3e). In addition, it contributed to updating the classification based on the Landsat data in areas with more recent

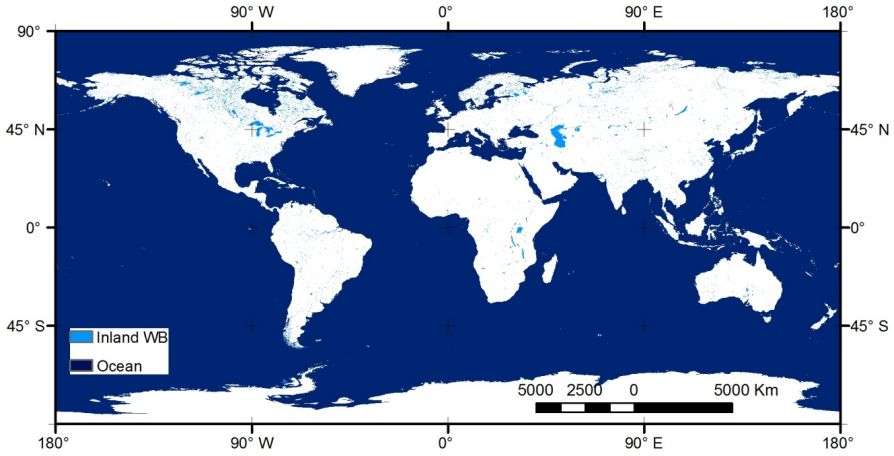

Figure 2.2: The CCI global map of open water bodies.

artificial basins. Figure 2.3f illustrates the Indira Sagar Dam commissioned on May 2005, where neither was included in GIW v1.0, nor in the GFC-datamask.

Excluding Greenland, Antarctica and islands south of 60°S, the consolidation affected 29% of the inland water class. Figure 2.4 illustrates a few examples of a posteriori consolidation aided by the auxiliary datasets and manual corrections of macroscopic errors. Macroscopic commission errors along the Ob River in the GIW v1.0 dataset were manually removed and replaced with the classification of the GFC-datamask (Figure 2.4a). Black lava in Saudi Arabia was misclassified by both the GIW v1.0 and the GFC-datamask; the manual correction was applied here (Figure 2.4b). Land contamination and incompleteness in the GIW v1.0 dataset could be corrected with the aid of the SRTM-SWBD (Figure 2.4c). Water commission over glaciers was corrected with the aid of the RGI dataset (Figure 2.4d).

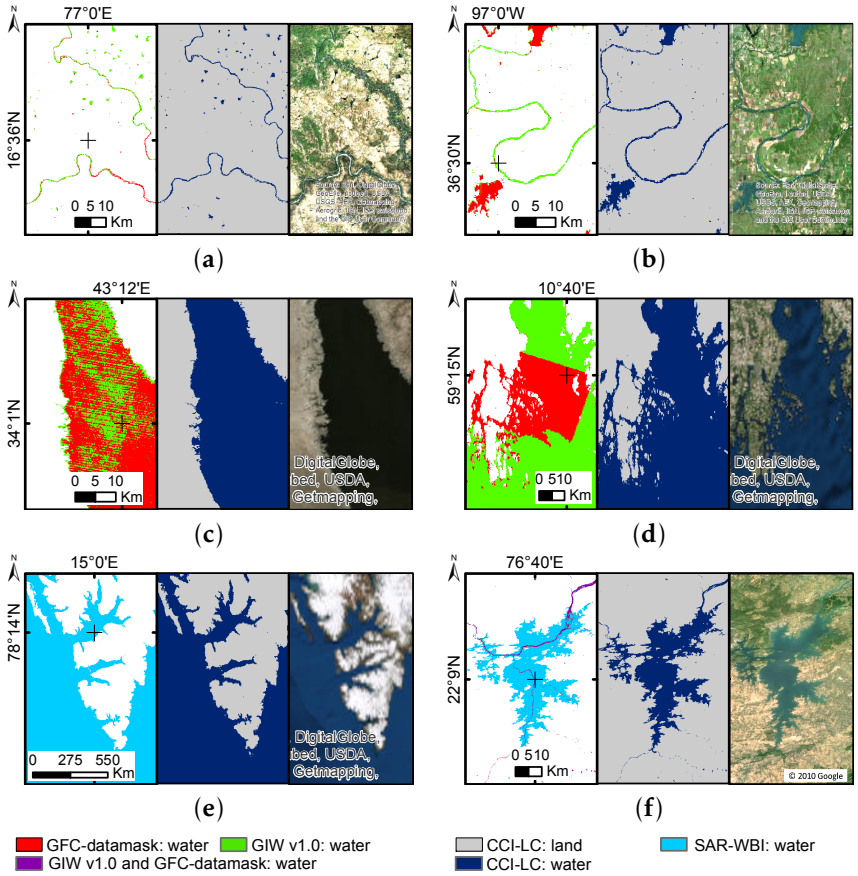

Figure 2.3: Examples illustrating the complementarity of selected input data sources to the CCI global map of open water bodies: (**a**) the lack of continuity in the GIW v1.0 river network was complemented by the GFC-datamask; (**b**) the lack of continuity in the GFC-datamask river network was complemented by the GIW v1.0; (**c**) artifacts from the Scan Line Corrector-off issue in Landsat ETM+ in the GFC-datamask were compensated with inclusion of water from the GIW v1.0. (**d**); GIW v1.0 unprocessed or atmospherically-contaminated areas were filled with the GFC-datamask; (**e**) detections in the SAR-WBI in areas north of 68°N, not included in other water body products; (**f**) map updating with the SAR-WBI for more recent water bodies.

2.4.2 Accuracy assessment

The reference database included 2400 samples spread over land masses with the exclusion of polar areas (Figure 2.5). Of these, 2121 corresponded to valid data in each of the datasets used to generate the CCI water body product. Eleven samples were further discarded either because of cumbersome inter-

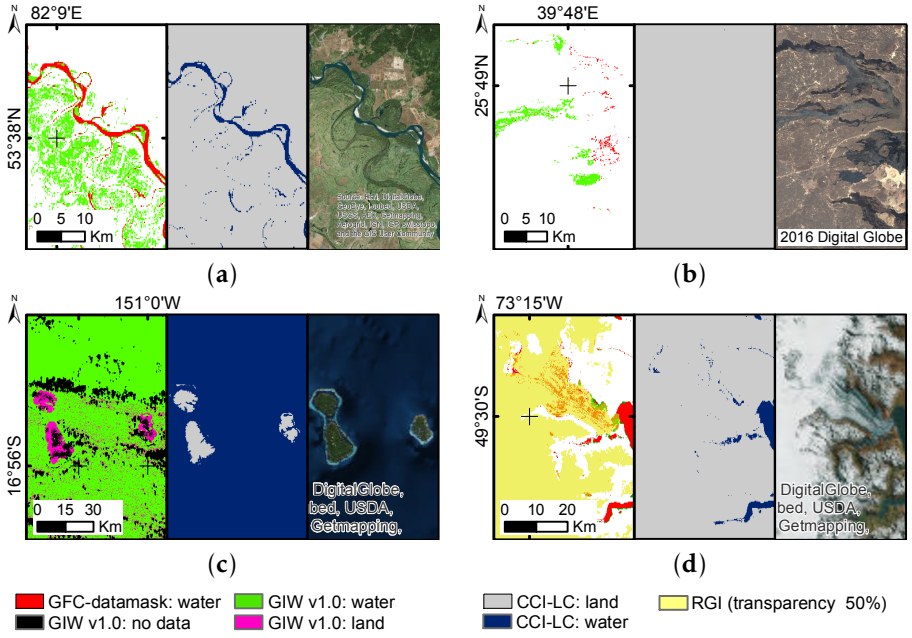

Figure 2.4: Effects of consolidation of input water bodies: (**a**) removal of commission errors in the GIW v1.0 dataset due to seasonal water events; (**b**) removal of commission errors due to black lava detected as water in the Landsat-based products; (**c**) replacement of the GIW v1.0 dataset with the SRTM-SWBD in case of incomplete characterization of islands; (**d**) removal of water commission over glaciers with the RGI dataset.

pretation of the Google Earth imagery due to cloud coverage, unavailability of images or uncertain interpretation. Of the 2110 samples, 1030 samples were included in the error-prone stratum of Level-2, and 234 corresponded to temporary water bodies like ephemeral streams, beaches, irrigated cultures and salty lakes.

The OA of all three products (the SAR-WBI, the GIW v1.0 and the GFC-datamask) was always very high, between 98 and 100% (Table 2.6). This was a consequence of the overwhelming proportion of the land class at the global scale compared to the marginal water class. Yet, water surfaces were not identified with high accuracy in any of the input datasets (Table 2.6). The PAs of water were always lower compared to the values obtained for the CCI water body map, with considerable differences among the individual input datasets. The PA of the CCI global map of open water bodies (92%) outperformed the best PA of the input datasets by 13%. On the contrary, the UA of the GFC-datamask was higher (97%) compared to the UA of the CCI global map of open water bodies (86%). The CCI global map of open water bodies overestimated

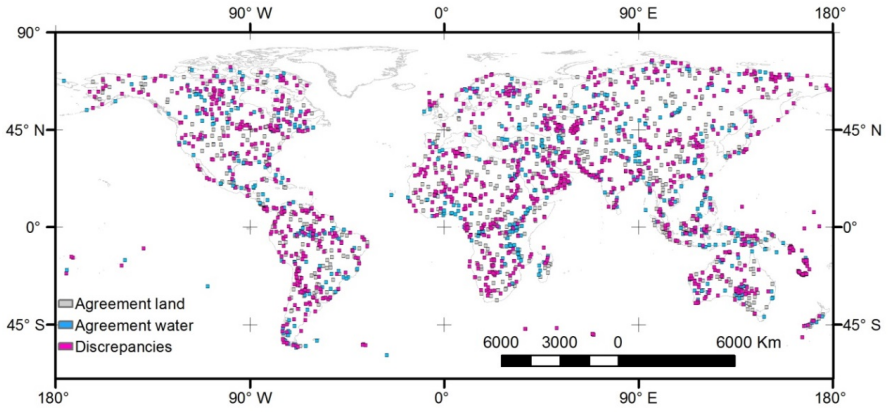

Figure 2.5: Location of the 2110 samples (area of 150 m × 150 m) selected for the validation of the water body products. For each sample, the Level-2 stratum is specified (land agreement, water agreement and discrepancies).

water, while the GFC-datamask underestimated it. The underestimation of water in the GFC-datamask was also a result of the qualitative assessment and justified the introduction of the class water from the GIW v1.0 in the consolidation. The GFC-datamask water omissions were found typically along lake banks, shallow water and dams. The GFC-datamask minimum water extent is probably due to its definition of water using a strict threshold greater or equal to 50% of water detections in the Landsat image in the time series (Potapov et al., 2012). Commission errors are marginal and occur along some lakes and over black lava rocks (e.g. Ethiopia).

Table 2.6: Input water body maps and CCI water body map with their accuracy estimates in percent (%) based on an evaluation of 2110 samples.

Products	Extent (LAT)	OA	Non-Water			Water		
			PA	UA	F1	PA	UA	F1
		(%)	(%)	(%)	(%)	(%)	(%)	(%)
SAR-WBI*	84°N–60°S	98	99	99	99	62	84	71
GIW v1.0*	90°N–60°S	98	99	99	99	78	77	77
GFC-datamask*	80°N–57°S	99	100	99	100	79	97	87
CCI WB v4.0	90°N–90°S	99	99	100	100	92	86	89

* Sources with a limited completeness: SAR-WBI: 97%; GIW v1.0: 91%; GFC-datamask: 93%

The F1-score of the CCI global map of open water bodies (89%) was significantly higher than the value obtained for the GFC-datamask. The F1-score of the SAR-WBI was the lowest of all values (71%) mainly due to an underestimation of water (low PA). Omission errors were located mainly along coastlines, water body boundaries and in mountainous areas. In areas where the SAR-WBI was based primarily on data with a spatial resolution of 1000 m, water bodies were either missed, imprecisely delineated or only partially detected in fragments. Most commission errors corresponded to temporary water (e.g. inundated areas, floodplains, deserts and salars) and to a lesser extent to coastlines, irrigated croplands and mountainous areas (Santoro and Wegmuller, 2014).

The second accuracy analysis focused on error-prone areas (Table 2.7). Compared to the accuracy figures of Table 2.6, the PAs and UAs for this stratum were substantially lower (on average, 14% and 21%, respectively).

Table 2.7: Accuracy results, in percent (%), for the error-prone Stratum 3 (1030 samples).

Products	OA	Non-Water			Water		
		PA	UA	F1	PA	UA	F1
	(%)	(%)	(%)	(%)	(%)	(%)	(%)
SAR-WBI	74	90	79	84	23	43	30
GIW v1.0	86	92	90	91	67	72	70
GFC-datamask	89	98	89	93	61	89	73
CCI WB v4.0	89	93	92	93	75	78	77

The trend in OA and the PA of the non-water class in the SAR-WBI and the GIW v1.0 datasets did not differ when restricting the analysis to error-prone areas only (see Tables 2.6 and 2.7). On the contrary, the PA and the F1-score of the water class of the SAR-WBI were substantially lower. This was due to the frequent omission of water in the SAR-WBI; however, since water represented a small proportion of the classes being mapped, the effect of omission was not visible in the statistics derived for the overall assessment.

Similarly, the GFC-datamask and the CCI global map of open water bodies gave identical trends in the results for OA and F1-scores for the class non-water (see Tables 2.6 and 2.7). The GFC-datamask was prone to water omission and the CCI global map of open water bodies to water commission. The underestimation of water in the GFC-datamask (PA of 61%) was exacerbated in error-prone areas that include a high proportion of shorelines, lakes and river banks. The PA of the CCI global map of open water bodies reached 75%, indicating that the large omissions of the GFC-datamask and the GIW v1.0 were effectively compensated for.

The OA obtained with the third accuracy analysis based on the 234 samples corresponding to temporary water was 79%, 89%, 94% and 99% for the SAR-WBI, the GIW v1.0, the CCI global map of open water bodies and the GFC-datamask, respectively. This ranking was in line with the results highlighted in Table 2.6. The GFC-datamask tended to map a minimum water extent and always showed low rates of water commission (high UA). These results will be discussed in the next section.

2.4.3 Assessing total water surface

According to the CCI global map of open water bodies, inland water covers an area of 3.41 million km^2. Following Olofsson et al. (2014a), this area was corrected by weighting the actual area of the land and water classes in each Level-2 stratum by the corresponding UA figures of the accuracy assessment using all samples. The maximal error in this area was calculated by taking

into account the actual error of each class of each Level-2 stratum. This actual error is derived using Equation (2.1) with the actual number of samples within each class of each Level-2. It resulted in an inland water area estimation of 3.17 million km^2 ± 0.24 million km^2.

The CCI global map inland water area is in the range of 3.05–4.57 million km^2 reported by Cao et al. (2014) for a series of global EO products with spatial resolutions from 30 m–1000 m. Estimations provided by (Feng et al., 2016) for the GIW v1.0, by (Carroll et al., 2009) for the MOD44W, by (Yamazaki et al., 2015) for the G3WBM and by (Downing and Cole, 2006) were also in agreement with this range. However, an area of ~5 million km^2 was reported by (Verpoorter et al., 2014b) for the lakes of the GLOWABO product.

2.5 Discussion

This study demonstrated that the combination and consolidation of existing water body products lead to a global map of open water bodies that meets the climate modelers' needs of adequate spatial resolution, maximal spatial extent and completeness along with high accuracy.

The 150-m spatial resolution of the CCI global map of open water bodies was found adequate for contemporary climate models that run at a current horizontal spatial resolution, which is, by far, coarser than 150 m. Global circulation models typically range between 250 and 600 km (IPCC), and regional models provide so-called "HR" simulations at 10–20 km (Flato et al., 2013). Climate modelling using convection-permitting models is now emerging and provides more reliable climate information on regional to local scales (Prein et al., 2015). Those models operate on the kilometer scale up to 0.5 km (Langhans et al., 2012).

According to the survey conducted by (Herold et al., 2010), a resolution finer than 300 m is also of interest for broader LC and "climate-related" communities. In 20% of the answers, the current global standard spatial resolution (300–1000 m) would even be sufficient. Finally, a spatial resolution of 150 m was found to be suitable for communities studying large-scale global dynamics and monitoring of the Earth's surface at 250 m or coarser with satellite data observations like MODIS, Envisat MERIS, PROBA-V and their continuity ensured by S3 (Donlon et al., 2012).

Achieving maximal spatial extent and completeness required up to seven different water bodies and auxiliary products. The fusion of various products with differences in periods of data acquisition and quality can cause inconsistencies in the water body representation, but the high accuracy of the CCI map of open water bodies proved that the methodology adopted overcame this issue. The fusion methodology gave priority to HR and minimum water extent mapping and the consolidation helped remove macroscopic errors and

include recent water bodies. However, one significant drawback of such interactive, systematic, and comprehensive consolidation, achieved through the compilation of various datasets, is the lack of repeatability.

It is expected that the joint and systematic use of S1 every 6–12 days with a 10–20-m spatial resolution (Torres et al., 2012), S2 10-m multispectral data every five days (S2-A and S2-B) (Drusch et al., 2012) and synergies between SAR and optical data (Malenovskỳ et al., 2012; Nizalapur, 2008) will greatly contribute to improving the consistency and allow updating the CCI global map of open water bodies in the future. The Sentinels' high revisit time will provide completeness and reduce manual and time-consuming post-editing by confirming water detection in space and time. A true global extent at 20-m spatial resolution might be achieved as S2 spatial coverage between latitudes 56°South and 84°North (Drusch et al., 2012) could be extended to polar environments with S1 monitoring.

2.5.1 Comparing the capacity of sampling schemes to sample correct and incorrect pixels

In this study, we proposed a rigorous stratified random sampling designed for the quality assessment of a binary classification where one class is marginally distributed. Our analysis revealed that when focusing on sample units in error-prone areas, all products exhibited notably lower accuracy, and the differences between products became significant. It is also interesting to assess the extent to which different sampling designs - whether random, class-based, or 'confidence-based' - represent the correctly and incorrectly classified pixels of the validated product, as it provides insights into the actual precision of accuracy indices. Table 2.8 provides the probability of sampling pixels that are correctly or incorrectly classified as water or land, based on the class distribution, for the three different random sampling schemes. With simple random sampling, there is an equal probability of sampling any pixel on the map. The other two sampling schemes rely on a stratification approach constructed directly from the products themselves, with a specific allocation of samples for each stratum. Following the common practice of class-based stratified sampling schemes, half of the sampling pixels would have been randomly selected inside the water class of the CCI global map of open water bodies, and the other half would fall in the land class. Our proposed sampling scheme used three strata resulting from the combination of independent global water datasets: half of the samples have been selected in the error-prone areas (Stratum 3), while both areas with high confidence in correctly mapping land (Stratum 1) or water (Stratum 2) received one-quarter of the samples.

The probability of capturing incorrectly classified pixels in any of the random sample schemes was low when the OA was large (OA of 99%). Compared with a simple random sampling and a class-based stratified random sampling,

the probability of 3.5% to sample cases of water omissions allowed us to verify a posteriori that the use of a confidence-based stratification improved the precision of the producer accuracy estimation. Indeed, while the class-based stratified sampling allowed sampling more in the marginal class (50%), it further reduced the probability of detecting water omissions (0.1%). The stratification using confidence-based strata increased the probability of sampling the two types of incorrectly classified pixels. The samples' distribution in cases of water omission and commission was dependent on the datasets used in the stratification.

The proposed stratification relied on independent datasets that were not always available. This can be an obstacle for the assessment of individual maps, but in the case of a comparison between products, the area of discrepancy could also be derived from the difference between products. Congalton and Green (2009) also suggested that the rarity of one class could be compensated by strata defined by expert-based knowledge. For instance, in the validation of LCC, they used a buffer surrounding the change mask or LC classes where change was more likely to occur in order to stratify the sampling of a change/no change map.

Table 2.8: Probability, in percent (%), to sample correctly and incorrectly classified pixels depending on the sampling scheme.

Random Sampling Scheme	Land Correct	Water Correct	Water Omission	Water Commission	Water Correct and Incorrect
Simple	96.5	2.8	0.2	0.5	3.3
Class-based stratified	49.9	42.7	0.1	7.3	50
Confidence-based stratified	59.4	33.5	3.5	3.6	37.1

2.5.2 Comparison with the global 3 arc-second water body map

The accuracy of the G3WBM, unavailable at the time of the CCI global map of open water bodies compilation, was evaluated with the same validation reference database used in Section 2.5.1. For the sake of consistency, original classes were grouped as follows: "land", "land (no Landsat observation)", "snow", "wet soil/wet vegetation/lava", "salt marsh" and "temporal flooded area" were merged into one "land" class, while classes "permanent water", "permanent water" (added by SRTM-SWBD) and "ocean (given by external land/sea mask)" as "water". G3WBM global accuracy figures weighted by the

actual surface of the land and water classes and accuracy figures focused on error-prone areas (Table 2.9) are compared to the results of Tables 2.6 and 2.7, respectively.

Table 2.9: G3WBM accuracy values for the global and error-prone area samples (Stratum 3), in percent (%).

	OA	Non-Water			Water		
		PA	UA	F1-score	PA	UA	F1-score
Global	99	100	99	100	77	94	85
Error-prone area only	88	96	90	93	66	82	73

The global assessment revealed that the OAs were not significantly different between the G3WBM and the CCI global map of open water bodies. However, the types of errors were not evenly distributed in each database. The UA of G3WBM was larger than for the CCI global map of open water bodies, while the CCI global map of open water bodies had a larger PA. The CCI water body map minimized the omission errors, while the G3WBM minimized the commission errors. The same conclusion was obtained for the error-prone area, where the CCI map of open water bodies was 1% (not significantly) better. The proportion of correctly classified pixels using the 234 samples related to temporary water was 93%. Class "permanent water added by the SRTM-SWBD" contributed to 16% of these errors.

These results prove that two different methods, one of harmonization and consolidation of existing water bodies and one of the classification of multi-temporal images, produced water body maps with similar high accuracies.

2.5.3 Permanent versus temporary water bodies

According to the FAO LCCS (Di Gregorio, 2005), identified as the most appropriate classification system for LC (Herold et al., 2008), non-perennial, i.e., temporary or seasonal, water corresponds to a surface covered with water during less than three months a year.

In the reference validation database, the use of the historical imagery of Google Earth and the interpretation of the context enabled recording information on temporary water. Yet, a threshold of three months could not strictly be verified due to the lack of historical imagery, regularly spread throughout the year. However, according to the photo-interpretation practices building on the convergence of evidence (Estes and Simonett, 1975; Teng et al., 1997), it was possible to identify water presence at the time of imaging, but also surfaces that can be seasonally flooded according to water availability.

Currently, there is no water body product providing an LCCS-compatible definition of the water status, i.e., temporary or permanent defined on a

yearly. Yet, the water body products, including the SAR-WBI, GIW v1.0 and the GFC-datamask, define water using thresholds on the water detections generated on multitemporal series of images. Differentiating permanent from temporary water bodies could not be achieved in the GIW v1.0 using the GLS data collection for the 2000 epoch only. Based on the 234 validation samples corresponding to temporary water, 11% were mapped as water in the GIW v1.0 (Section 2.4). This issue of water seasonality was already mentioned (Feng et al., 2016), and the area of temporary water included in the GIW v1.0 was evaluated as 0.17 million km^2 (Yamazaki et al., 2015).

Although both the GFC-datamask and the SAR-WBI relied on multitemporal images over several years, the GFC-datamask was more representative of permanent water. The reason is that the GFC-datamask definition of water is based on a stricter threshold on the number of water detections in the image time series. Nevertheless, the GFC-datamask missed water bodies created towards the end of the time interval covered by the Landsat data. These water bodies are permanent but have a minor contribution to the water frequency in the multi-temporal dataset. For the CCI map of open water bodies, the occurrence of temporary water bodies classified as permanent was seldom because of the consolidation steps adopted to minimize temporary water and account for missing water bodies.

2.6 Conclusion

A global map of open water bodies was built within the ESA CCI by combining and consolidating existing nearly global water body and auxiliary datasets. Tailored to the climate modeling community, this map provides a comprehensive land/inland water and ocean classification for any location on Earth's surface at 150-m spatial resolution. An inland water fraction, expressed as a percentage of the 150-m grid cell, is provided as a separate layer for broader use within the LC community. Both layers are freely accessible at: `http://maps.elie.ucl.ac.be/CCI/viewer`.

The inland water area of the CCI global map of open water bodies was estimated at 3.17 million km^2 ± 0.24 million km^2, consistent with the range of 3.05–4.57 million km^2 reported by Cao et al. (2014). Similar estimations were obtained for GIW v1.0 (Feng et al., 2016), MOD44W (Carroll et al., 2009), G3WBM (Yamazaki et al., 2015), and as reported by (Downing and Cole, 2006).

The CCI global map of open water bodies and its constituent inputs underwent extensive validation against an independent reference database of 2110 samples. To better highlight differences among products, we proposed a confidence-based stratified random sampling with a stratification aiming to avoid undersampling rarely occurring map classes, such as "water". This stratification distinguished between high confidence in correctly mapping the land

class (Stratum 1 - 25% of the sample), high confidence in correctly mapping the water class (Stratum 2 - 25% of the sample), and error-prone areas primarily corresponding to shorelines, lakes, and river banks (Stratum 3 - 50% of the sample). Overall accuracy remained consistently high across all products, ranging between 98% and 100% when considering all samples. However, when focusing on sample units targeting error-prone areas, all products exhibited substantially lower accuracy figures. The differences between products became significant in this context, with overall accuracies in the error-prone stratum ranging between 74% and 89%.

Finally, we analyzed the accuracy of the different products in characterizing the temporality of water according to the LCCS definition. The OA obtained based on the 234 samples tagged as temporary water varies from 79% to 99% according to the products, with one of the CCI global maps of open water bodies being 94%. As the frequency of acquisition from EO sensors increases, it is becoming possible to more objectively quantify whether the water detected is truly permanent or temporary. S2 A and B, with their high revisit frequency and global coverage, offer this opportunity at a spatial resolution (10 m) higher than any of the previously described products.

Chapter 3

Quantifying Global Plant Functional Type Composition at the Pixel Level for Climate Models

This chapter is based on the following article:

Harper, K. L., **Lamarche, C.** and Hartley, A., Peylin, P., Ottlé, C., Bastrikov, V., San Martín, R., Bohnenstengel, S. I., Kirches, G., Boettcher, M., Shevchuk, R., Brockmann, C., Defourny, P. A 29-year time series of annual 300-metre resolution plant functional type maps for climate models. *Earth System Science Data Discussions*. 2022. https://doi.org/10.5194/essd-15-1465-2023.

Abstract

The existing medium resolution Land Cover (LC) time series produced in Chapter 1 provides 29 years (1992–2020) of annual LC maps at 300-m resolution, allowing for a detailed study of land change dynamics over the contemporary era. Because models need two-dimensional (2D) parameters rather than 2D LC information, the LC classes must be converted into model-appropriate PFTs to apply this time series to the Earth system and land surface models. The first-generation cross-walking table that was presented with the LC product prescribed pixel-level Plant Functional Types (PFT) fractional compositions that varied by LC class but lacked spatial variability. Here we describe a new ready-to-use data product for climate modelling: spatially explicit annual maps of PFT fractional composition at 300 m resolution for 1992–2020, created by fusing the 300 m medium-resolution LC product with several existing high-resolution datasets using a globally consistent method. In the resulting data product, which has 14 layers for each of the 29 years, pixel values at 300-m resolution indicate the percentage cover (0–100 %) for each of the 14 PFTs, with pixel-level PFT composition exhibiting significant intra-class spatial variability at the global scale.

3.1 Introduction

As shown in Chapter 1, the ESA CCI MR LC dataset provides the longest consistent data record of observed LC, with annual maps from 1992 to 2020 at a spatial resolution of 300 m. It describes the LC in 22 LC classes according to the standard of the UN LCCS (Di Gregorio and Jansen, 2005) and 13 LCC types consistent with the IPCC land categories. However, the use of such a dataset in Earth System models is not straightforward.

The land surface components of global circulation models and global Earth system models play a significant role in quantifying the historical and present-day representations of land use and LCC impacts on climate. Most land surface models (LSMs) parameterize global vegetation processes (e.g., photosynthesis and evapotranspiration) for a reduced set of globally representative and similarly behaving plant types, referred to as PFTs. PFTs can be related to physiognomy and phenology, climate (which defines the geographical ranges in which a plant type can grow and reproduce under natural conditions (Box, 1981; Lavorel et al., 1997), and physiological activity (e.g. C_3/C_4 photosynthetic pathways) (Davidson and Csillag, 2003).

Spectral information acquired by remote sensing techniques does not allow direct mapping of PFTs. However, LC map series derived from satellite EO are a valuable source of physiognomy (life form and leaf type) and phenology information for inferring the spatial distribution of PFTs. EO-derived LC maps must be translated ("cross-walked") into model-specific PFTs, which is typically accomplished using the information provided by the LC class legend (Jung et al., 2006). Differences in LC categories, spatial resolutions, and temporal coverage between various LC products propagate errors to the cross-walked PFT maps and significantly contribute to uncertainties in deriving gross primary production and other climate-relevant variables at the regional scale (Poulter et al., 2011). To reduce uncertainty in model ensembles, Poulter et al. (2015) proposed a standardized cross-walking framework that converts each CCI MR LC class into pre-defined PFT fractions relevant for three leading ESMs (JULES-MOHC, ORCHIDEE-LSCE and JSBACH-MPI) based on expert knowledge and auxiliary data. This reclassification procedure was implemented in a flexible tool to generate other related PFT schemes required by the modelling community.

Hartley et al. (2017) used the same three ESMs to quantify the impact of uncertainties in (1) the LC map and (2) the cross-walking procedure on the spatiotemporal patterns of three important land surface variables: Gross Primary Productivity (GPP), evapotranspiration, and albedo. To disentangle the two sources of uncertainty, the modelling setup translated the plausible uncertainty ranges of the LC and cross-walking components into a common biomass scale. The simulations indicated that the uncertainty of the cross-walking procedure contributed slightly more than the uncertainty of the LC map to the inter-model uncertainty for all three variables.

As a following contribution to the LC ECV, this work aims to reduce the uncertainty in the cross-walking component by adding spatial variability to the PFT composition within a LC class. This work moves beyond fine-tuning the cross-walking approach for specific LC classes and/or regions and, instead, separately quantifies the PFT fractional composition for each 300 m pixel globally for each year in the time series (1992–2020). The new PFT product is generated by fusing the annual CCI MR LC map series with existing HR auxiliary data products that individually characterize one surface type with high accuracy. The resulting 300 m PFT product is a companion time series of continuous field PFT fractions that is consistent with the existing CCI MR LC map series. The global PFT product has an annual resolution, covering 1992–2020, and indicates the specific percentage cover of 14 PFTs for each pixel at 300 m resolution. The set of 14 PFTs represented in the product includes the full set of 13 PFTs initially developed by Poulter et al. (2015) complemented with a new built-up surface type. The full set of PFTs includes bare soil, built, water, snow and ice, natural grasses, managed grasses (i.e., herbaceous cropland), broadleaved deciduous trees, broadleaved evergreen trees, needleleaved deciduous trees, needleleaved evergreen trees, broadleaved deciduous shrubs, broadleaved evergreen shrubs, needleleaved deciduous shrubs, and needleleaved evergreen shrubs. Thus, in this paper, the term "PFT" is applied even to the abiotic surface types to cleanly differentiate between the land types derived from EO data (i.e., LC classes) and the land types required by models (i.e., PFTs).

The following sections describe the auxiliary inputs and method used to quantitatively determine the PFT fractional composition for each 300 m pixel globally, a description of the new PFT data product, and modelling results from the application of the new PFT distribution for the year 2010 to the ORCHIDEE and JULES land surface models.

3.2 Input data

3.2.1 CCI MR LC products (150–300 m)

The CCI MR LC product (Chapter 1) delineates 22 primary classes and 15 additional sub-classes of LC at 300 m resolution (Table 3.1). The maps have global coverage and an annual time step extending from 1992 through 2020, with plans for the continued release of maps for 2021 and future years. The classification system used for the CCI MR LC map series is based on the LCCS of the UN FAO (Di Gregorio and Jansen, 2005). The LCCS defines fundamental criteria, called "classifiers", that can be combined in various proportions to form the legend of a class. For LC classes primarily composed of vegetation, classifiers describe physiognomic and structural characteristics such as Life Form (e.g. tree), Cover (e.g. closed), and Height (e.g. above 5m). A

corresponding legend would be, for example, "tree cover, broadleaved, evergreen, closed (>40%)". Likewise, abiotic classes are characterized by surface aspect classifiers, resulting in a legend such as "consolidated bare areas." The 15 sub-classes, also called "regional classes", are defined only in geographic regions where appropriate training data is available and are those with a numeric classification code that has a final digit of 1, 2, or 3 (Table 3.1). The 22 primary classes and 15 sub-classes are collectively referred to here as simply "classes." For each year of the time series, each 300 m pixel in the dataset is assigned as a single LC class. The change detection algorithm monitors thirteen possible LC transitions through time. For a pixel to register a change in its assigned LC class, the algorithm must identify the change for two consecutive years in the workflow. A lack of change in a pixel's assigned class does not necessarily indicate an absence of change in the land surface over the time series, rather, it indicates that any change that has occurred in the pixel was limited enough in scale or duration that the assigned class did not change. The entire time series and an associated set of quality flags are freely available at `https://maps.elie.ucl.ac.be/CCI/viewer/` (last access April 2024) in GeoTiff and `https://cds.climate.copernicus.eu/cdsapp#!/dataset/satellite-land-cover?tab=overview` (last access April 2024) in netCDF. This CCI PFT product is based on v2.0.8 of the CCI MR LC time series), which includes corrections for the known overestimation of cropland relative to grassland in South America (Chapter 1).

The CCI MR water body product v4.1 (Lamarche et al., 2017) is used to delineate between inland water and ocean. The dataset, consistent with the CCI MR LC maps, designates all pixels at 150 m resolution as either ocean or non-ocean. The latter category encompasses both land areas and inland water bodies. Notably, the North American Great Lakes are classified as inland water rather than ocean. This dataset can be accessed at `http://maps.elie.ucl.ac.be/CCI/viewer/download.php`.

3.2.2 High-resolution auxiliary datasets

Surface water product (30 m)

The Landsat-based surface water product developed by the Joint Research Centre (Pekel et al., 2016) is used to derive the permanent inland water fractions at 300 m resolution (calculation details in Section 3.3). The surface water occurrence layer (obtained at `https://global-surface-water.appspot.com`) indicates the frequency of water occurrence in each 30 m pixel (80°N–60°S) over the period March 1984 to December 2019. The frequency occurrence data is reported as integer values of 1–100%, where a value of 100% occurrence indicates a permanent water surface that existed over the entire analysis, which encompasses all but the most recent year (2020) of the time series of the MR LC product.

Tree canopy cover product (30 m)

A Landsat-based tree canopy cover product (Hansen et al., 2013b) is used to derive the tree cover fractions for 300 m pixels belonging to vegetated classes (except where otherwise noted in Section 3.3). The product (obtained at `https://glad.umd.edu/Potapov/TCC_2010/`) is based on the application of a regression tree model to growing-season Landsat 7 ETM+ data (`https://glad.umd.edu/dataset/global-2010-tree-cover-30-m`). The dataset indicates the maximum tree canopy cover percentage (integer values of 1–100%) at 30 m resolution (80°N–60°S) and is mainly representative of 2010.

Tree canopy height product (30 m)

The global forest canopy height product from Potapov et al. (2021a) is used to derive the fractional covers of trees and shrubs in 300 m pixels classified as shrubland. The 30 m product (obtained at `https://glad.umd.edu/dataset/gedi/`) was created by combining the footprint-level lidar forest height measurements (using the 95th percentile relative height metric) for April–October 2019 from the Global Ecosystem Dynamics Investigation (GEDI) with wall-to-wall Landsat optical data to perform spatiotemporal extrapolation. The resulting dataset indicates the canopy height (0–60 m) at 30 m resolution (52°N–52°S), where canopy heights < 3 m were set to 0 m under the assumption that the pixel lacks woody vegetation.

Built-up product (38 m)

The Landsat-based GHSL dataset produced by the Joint Research Centre (Pesaresi et al., 2013) is used to derive the built-up fraction for 300 m pixels classified as urban LC by the GUF dataset (Esch et al., 2017). The built-up fraction of the PFT dataset is defined as buildings, roads, and man-made structures. The GHSL (alpha version dated November 2014) consists of globally consistent built-up maps for four consecutive years (1975, 1992, 2000, and 2014) at 38 m resolution. Built-up areas include both permanent and temporary above-ground buildings.

3.2.3 Zonation products

In addition, three zonation products are used complementarily to consolidate the assignment of the phenology type (deciduous or evergreen) and leaf type (broadleaved or needleleaved) to shrubs and, in a very small number of pixels, to trees belonging to a class legend of mixed trees. The Köppen-Geiger climate zone product from Beck et al. (2018) divides the Earth's land surface into 30 distinct climate zones at 0.0083° resolution (about 1 km) based on present-day (1980–2016) temperature and precipitation records. Data were obtained at `https://figshare.com/articles/dataset/Present_and_future_K_ppen-`

Geiger_climate_classification_maps_at_1-km_resolution/6396959/2. The landform dataset from Sayre (2014) identifies landforms – surface water, plains, hills, or mountains – at 250 m resolution for 83.6°N–56°S and is derived from a digital elevation model (USGS GMTED2010: Danielson et al. (2011)). The data product was obtained at https://rmgsc.cr.usgs.gov/outgoing/ecosystems/Global/. Finally, world regions follow the definitions used in the Integrated Model to Assess the Global Environment 3.0 (IMAGE03) (Stehfest et al., 2014). The IMAGE03 regional classification framework has been harmonized with the CCI MR LC grid by reconstructing the original dataset using the IMAGE-based list of countries per region (available at https://models.pbl.nl/image/index.php/Region_classification_map) along with country boundaries from the FAO Global Administrative Unit Layers (available at https://data.apps.fao.org/, expanding the list to include Antarctica, Greenland), and additional small islands. The resulting raster dataset divides Earth's surface into 28 regions on the CCI MR LC grid.

3.3 PFT dataset development

The series of PFT distribution maps from 1992 to 2020 was created by integrating a series of auxiliary products with the CCI MR LC map series. These auxiliary datasets, with their higher spatial resolution, are used to compute the PFT fractional covers at a resolution of 300 m.

The CCI MR LC map legend provides a broad description of LC at the 300 m pixel, including the expected vegetation form(s) (tree, shrub, grass) and/or abiotic land type(s) (water, bare area, snow and ice, built-up), an expected usage between natural and cultivated vegetation, and an expected range of fractional cover (e.g. open 15–40%, close to open 15%–40%, etc.). This map legend ensures a standardized definition of the PFT composition and fosters a strong linkage between both map series by maintaining harmonization in instances of inconsistency between the LC product and the auxiliary datasets. The overall approach assumes that the definition of the MR LC class is the basis for harmonizing the four existing HR LC data sets. It proceeds through a systematic sequence of estimating water fraction and tree cover fraction, using tree height to assign life form, and finally deriving phenology. This step-by-step approach is first applied to (1) pixels that did not experience a change in LC classification over the period 1992–2020 (termed "static pixels") and (2) pixels that did experience a change at least once in this period (termed "dynamic pixels").

3.3.1 Static pixels

The PFT fractions of static pixels are treated as temporally invariant for the entire 1992–2020 period. Therefore, any intra-pixel change in the fractions of

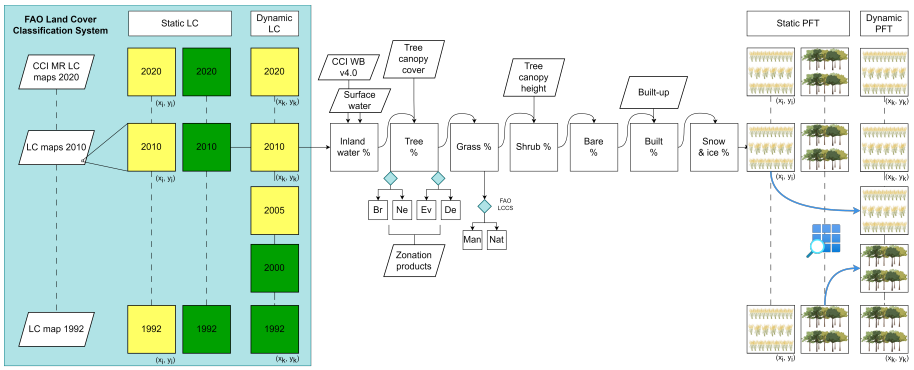

Figure 3.1: Flowchart depicting the creation of the PFT map series for stable and dynamic pixels from the CCI MRLC map series, ensuring legend harmonization, and using high-resolution auxiliary datasets to provide PFT fractions. Large solid colored squares illustrate 300m pixels described by the FAO LCCS categorical legend. Squares on the right-hand side represent the resulting PFT composition per pixel.

a static pixel is not captured in the PFT map series due to a lack of temporally resolved auxiliary inputs extending over the entire time series. Such a change is expected to be limited in scale and/or duration as it did not prompt a change in the MR LC class assignment, underscoring the appropriateness of treating the fractional composition of the static pixels as consistent over time.

General considerations induced by the FAO LCCS and the LC legend

Based on the concepts and definitions of the FAO LCCS (Di Gregorio and Jansen, 2005), only a subset of the 14 PFTs is permitted non-zero fractions for each LC class (Table 3.1). The vegetation thresholds used to define whether pixels are predominantly vegetated or abiotic are also based on the definitions of the CCI MR LC classes. Because the PFT fractional composition is estimated independently for each 300 m pixel of a class, in some cases, an individual pixel can be attributed a zero fractional cover even for a PFT that is allowed non-zero cover for that class. For all pixels, the sum of PFT fractions is 100%.

Table 3.1: Non-zero PFTs fractions permitted per CCI MR LC classes.

Class code	CCI LC Class description	Permitted PFTs fractions
10	Rainfed cropland	Trees, Water, Man grass
11	Rainfed cropland - herbaceous cover	
12	Rainfed cropland - tree or shrub cover	
20	Irrigated or post-flooding cropland	
30	Mosaic: 50 % cropland/ 50 % natural tree, shrub, herbaceous cover	
40	Mosaic: 50 % natural tree, shrub, herbaceous cover/ 50 % cropland	Trees, Water, Nat grass, Man grass
50	15 % BE tree cover	BE trees, Water, Nat grass
60	15 % BD tree cover	
61	40 % BD tree cover	
62	15-40 % BD tree cover	
70	15 % NE tree cover	NE trees, Water, Nat grass
71	40 % NE tree cover	
72	15-40 % NE tree cover	
80	15 % ND tree cover	ND trees, Water, Nat grass
81	40 % ND tree cover	
82	15-40 % ND tree cover	
90	Mixed leaf type (B and N) tree cover	Trees, Water, Nat grass
100	Mosaic: 50 % tree and shrub cover / 50 % herbaceous cover	
110	Mosaic: 50 % herbaceous cover / 50 % tree and shrub cover	
120	Shrubland	Trees, Water, Nat grass, Shrubs
121	Evergreen shrubland	
122	Deciduous shrubland	
130	Grassland	Trees, Water, Nat grass
140	Lichens and mosses	Water, Nat grass

Continued on next page

Table 3.1: Non-zero PFTs fractions permitted per CCI MR LC classes. (Continued)

150	Sparse vegetation: 15 % tree, shrub, herbaceous cover	Trees, Water, Nat grass, Bare soil
151	Sparse vegetation: 15 % tree cover	
152	Sparse vegetation: 15 % shrub cover	
153	Sparse vegetation: 15 % herbaceous cover	
160	Flooded tree cover - fresh or brackish water	Trees, Water, Nat grass
170	Flooded tree cover - saline water	
180	Flooded shrub or herbaceous cover - fresh, saline, or brackish water	Trees, Water, Nat grass, Shrubs
190	Urban areas	Trees, Water, Nat grass, Built
200	Bare areas (total vegetative cover 4%)	Trees, Water, Bare soil
201	Consolidated bare areas	
202	Unconsolidated bare areas	
210	Water body	Trees, Water, Nat grass
220	Permanent snow and ice	Snow and ice

The decision rules used to determine PFT fractions are intended to be widely applicable, while ensuring alignment with the FAO LCCS (Figure 3.2). Following an initial dichotomous phase that categorizes PFTs into primarily vegetated and abiotic areas, a modular-hierarchical phase further classifies vegetation based on water permanency, vegetation fraction, life form, and height. Decision rules aim to be as generic as possible but may vary depending on the information brought by the auxiliary datasets and the thresholds of the ESA CCI MR LC legend. Given the spatial and temporal consistency of the map series, deference is made to the class legend for pixels in which the estimated tree cover fraction derived from the auxiliary datasets disagrees with the class legend. This allows the PFT product to retain the advantages of the CCI MR LC map series while improving the translation of the LC dataset into PFT maps.

Figure 3.3 outlines the sequential steps for calculating the pixel fractional composition of PFTs from the water to the snow/ice fractions. The percentage of the 300 m pixel that is vegetated is calculated as 100% minus the inland water percentage, that is, for all vegetation-containing classes except for the sparse vegetation classes, which have bare soil PFT cover, all non-inland-water area in the 300 m pixel is entirely vegetated (0% bare soil PFT) in the

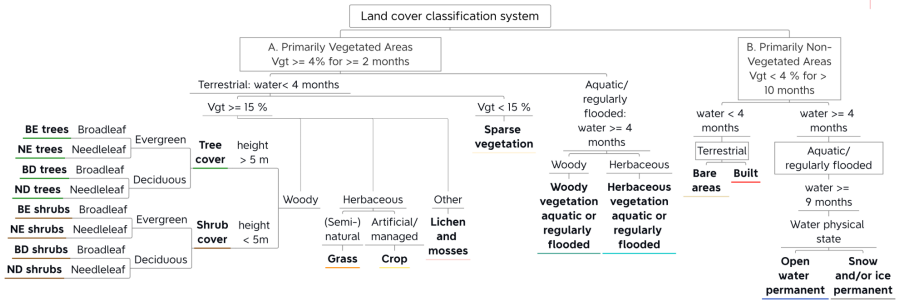

Figure 3.2: Implementation of the FAO land cover classification system to the description of the PFT fractions.

PFT product. Pixels belonging to the shrubland classes can have a mixture of trees, shrubs, and herbaceous cover. For pixels of non-shrubland vegetation-containing classes, the vegetated portion of the pixel is composed of trees and herbaceous cover (i.e., cropland and/or natural grass).

Water fraction

The 30 m water frequency occurrence dataset by Pekel et al. (2016) is used to delineate permanent inland water areas within 300 m pixels, excluding permanent snow and ice regions. Pixels are classified as water if their frequency occurrence exceeds 90%, otherwise as non-water. This binary classification is then used to calculate the percentage of the 300 m pixel occupied by permanent inland water PFT (W_{300}):

$$W_{300} = \frac{n_{w_{30}}}{N_{300}} \times 100$$

where $n_{w_{30}}$ is the count of 30 m pixels classified as permanent inland water within the 300 m pixel, and N_{300} is the total count of 30 m pixels within the 300 m pixel.

Tree cover classes

The percentage of the 300 m pixel that is tree cover is estimated using the 30 m tree cover dataset for 2010 from Hansen et al. (2013b). This Landsat-based dataset provides the percentage of tree canopy cover (integers 1–100%) based on growing season observations. To harmonize the Landsat-based surface water occurrence and tree canopy cover datasets such that the combined tree and water percentages never exceed 100%, the tree cover percentage of the vegetated (non-water) portion of the 300 m pixel ($TC_{veg_{300}}$) is first obtained from

<table>
<tr><th>Class description</th><th>Water %</th><th>Tree%</th><th>Tree type</th><th>Grass%</th><th>Grass type</th><th>Shrub %</th><th>Bare soil%</th><th>Built%</th><th>Snow/ ice%</th></tr>
<tr><td>Rainfed cropland (10 - 12)</td><td rowspan="17">Surface water product</td><td rowspan="4">Tree canopy cover product</td><td rowspan="4">Majority window</td><td rowspan="8">100% - water% - tree%</td><td>LC legend (MAN)</td><td rowspan="8">0%</td><td rowspan="17">0%</td><td rowspan="8">0%</td><td rowspan="17">0%</td></tr>
<tr><td>Irrigated or post-flooding cropland (20)</td></tr>
<tr><td>Mosaic cropland | NAT veg (30 - 40)</td></tr>
<tr><td>Mosaic woody | herbaceous (100% - 110)</td></tr>
<tr><td>Grassland (130)</td><td rowspan="13">LC legend (NAT)</td></tr>
<tr><td>Tree cover BE >15% (50)</td><td rowspan="6">Tree canopy cover product + Method 1</td><td rowspan="3">LC legend</td></tr>
<tr><td>Tree cover BD (60 - 62)</td></tr>
<tr><td>Tree cover NE (70 - 72)</td></tr>
<tr><td>Tree cover ND (80 -82)</td><td rowspan="3">Majority window</td></tr>
<tr><td>Tree cover mixed leaf type</td></tr>
<tr><td>Tree cover - flooded (160 - 170)</td></tr>
<tr><td>Lichens & mosses (140)</td><td>0%</td><td>N/A</td><td>100% - water%</td></tr>
<tr><td>Sparse veg (150 -153)</td><td rowspan="3">Tree canopy cover product + Method 2</td><td rowspan="5">Majority window</td><td>tree% + grass% 4-14%</td></tr>
<tr><td>Shrubland (120 - 122)</td><td rowspan="3">100% - water% - tree% - shrub%</td><td rowspan="3">Tree canopy height product</td></tr>
<tr><td>Shrub or herbaceous - flooded (180)</td><td rowspan="3">Tree canopy cover product</td></tr>
<tr><td>Urban areas (190)</td><td>100% - water% - tree% - built%</td><td>Majority window</td><td>0%</td><td>GHSL/ GUF > 50%</td></tr>
<tr><td>Bare areas (200 - 202)</td><td>0%</td><td>N/A</td><td>0%</td><td>100% - water% - tree% (< 3%)</td><td rowspan="3">0%</td></tr>
<tr><td>Inland water bodies (210)</td><td>0%</td><td rowspan="3">0%</td><td rowspan="3">N/A</td><td>100% - water% - tree%</td><td>NAT</td><td rowspan="3">0%</td><td rowspan="3">0%</td></tr>
<tr><td>Ocean (210)</td><td>100%</td><td rowspan="2">0%</td><td rowspan="2">N/A</td></tr>
<tr><td>Permanent snow & ice (220)</td><td>0%</td><td>100%</td></tr>
</table>

Figure 3.3: Synoptic view of the decision rules applied to derive pixel-level functional type composition by LC class by combining auxiliary datasets and the FAO LCCS used to describe the CCI MR LC classes. For each LC class, a systematic sequence of steps is applied to derive the fraction composition of each pixel from the water % to the snow/ice %. The dashes represent subtractions. See Table 3.1 for more comprehensive class descriptions.

the median of the tree canopy cover fractions of the non-water 30 m pixels ($TC_{NW_{30}}$):

$$TC_{veg_{300}} = \text{median}(TC_{NW_{30}})$$

Then, the tree cover percentage of the entire 300 m pixel is calculated as the product of this value and the non-water fraction of the grid cell:

$$TC_{300} = TC_{veg_{300}} \times (100 - W_{300})$$

For the tree cover classes 50–82, the class legend specifies an expected range for the tree cover percentage defined by TC_{min} and TC_{max} (Table 3.1,

class description column). For the tree cover classes 90, 160, and 170, a tree cover fraction of >15% is implicit from the UN LCCS. To ensure consistency between the CCI MR LC and PFT map series, the resulting tree cover fractions are tested against the class legend. For tree cover class pixels where the estimated tree cover fraction derived from auxiliary datasets disagrees with the class legend, a mean tree cover among all static 300 m pixels of its class $\overline{TC}_{\text{class}}$ is calculated over a geographical window of size ($\Delta\lambda \times \Delta\phi$):

$$\overline{TC}_{\text{class}} = \frac{1}{N_{\text{pix}}} \sum_{i=1}^{N_{\text{pix}}} TC_{300}^{(\Delta\lambda \times \Delta\phi)}$$

Where N_{pix} denotes the total number of pixels within the specified window. This calculation is performed over a geographical window with dimensions of 0.25° longitude ($\Delta\lambda$) × 0.25° latitude ($\Delta\phi$), centered around the pixel of interest. If no static pixels of the class exist within that window size, $\Delta\lambda$ and $\Delta\phi$ are expanded to 0.5°. Close thematic classes with limited pixel representation, such as class 82 and neighboring class 72, are grouped when calculating the window mean for class 82 pixels. Once again, the resulting mean tree cover fraction at the window scale undergoes validation against the class legend. The following rules are applied based on the conditions:

$$TC_{300} = \begin{cases} \overline{TC}_{\text{class}} & \text{if } TC_{\text{min}} \leq \overline{TC}_{\text{class}} \leq TC_{\text{max}} \\ TC_{\text{max}} & \text{if } \overline{TC}_{\text{class}} > TC_{\text{max}} \\ TC_{\text{min}} & \text{if } \overline{TC}_{\text{class}} < TC_{\text{min}} \end{cases}$$

If the 0.5° x 0.5° window does not contain any pixels of the class of interest, either case 2 or case 3 is applied. For pixels that belong to a tree cover class and had TC_{300} defined by $\overline{TC}_{\text{class}}$, the resulting sum of the inland water and tree cover percentages can exceed 100%. In such cases, TC_{300} is calculated as $100\% - W_{300}$. If the resulting $TC_{300} < TC_{\text{min}}$, case 3 is applied and W_{300} is set as the residual area in the pixel ($100\% - TC_{300}$).

For all tree cover class pixels, the grass cover percentage (GC_{300}) is calculated as:

$$GC_{300} = 100\% - TC_{300} - W_{300}$$

and the grass type is assigned as natural grasses. No minimum W_{300} is defined for the flooded tree cover classes.

Cropland classes

For the biotic classes rainfed cropland, irrigated or post-flooding cropland, mosaic of cropland–natural vegetation, mosaic of woody–herbaceous vegetation, and grassland, the tree cover percentage derived from the auxiliary

products is used directly since the legend does not specifically define the expected tree cover, therefore, modification of the PFT fractions based on the class legend is not applied for these classes as it is for some other classes. The percentage of the 300 m pixel that is grass cover is calculated as 100% minus the sum of the inland water and tree cover percentages. The grass type – managed (i.e., crops) or natural – is defined by the class legend. For most mixed classes, the assigned grass type reflects the majority type as indicated by the legend. All grass in the pixel is assigned as managed grass for classes 10, 11, 12, 20, and 30. Pixels belonging to the mosaic of natural–cropland vegetation have a mix of herbaceous crops (up to 49% of the pixel area) and natural grasses (for excess grass cover beyond 49% of the pixel area). All grass cover is assigned as natural grass for all other classes.

In some of the classes in this set, an expected percentage cover is given for total woody vegetation (trees and shrubs) or for the shares of cropland and natural vegetation, where the two categories differentiate by management status rather than life form. In the PFT product, shrub cover is estimated only for the shrubland classes due to a lack of appropriate auxiliary inputs to discriminate between trees and shrubs for all classes, so modification of the life form shares in such pixels based on the legend description may introduce additional bias in the PFT product and is therefore avoided. Management status (cropland vs natural) is assigned in the PFT product only for grasses and is based on the class descriptions, so an independent assessment of the shares by management status is not possible.

Sparse vegetation classes

Pixels belonging to the sparse vegetation classes (codes 150, 151, 152, and 153) can have non-zero fractions of bare soil, trees, natural grass, and inland water. The class definition requires a vegetation fraction of 4–14%. Since shrub cover is not estimated for the sparse vegetation classes, the vegetation component is composed of trees and natural grasses, therefore, the total vegetation fraction is enforced for sparse vegetation pixels, but the resulting life form may differ from that indicated by the legend for the sub-classes with codes 151–153. If the tree cover derived from the auxiliary inputs is $\geq 15\%$, then the tree PFT is reduced to 14% in deference to the legend of the CCI MR LC map series, natural grass PFT is assigned as 0% since tree cover accounts for the maximum total vegetation fraction (trees + grass), and the bare soil PFT percentage is calculated as 100% minus the inland water percentage minus 14% tree PFT. If the tree cover derived from the auxiliary inputs is $< 15\%$, then this input tree percentage value is assigned as the final tree PFT percentage in the pixel and additional legend-consistency steps are applied to assign the grass and bare fractions: (1) if the non-water area of the pixel is 4–14%, then natural grass PFT accounts for the residual portion of the pixel (14% minus tree PFT percentage minus inland water percentage), (2) if the non-water

percentage of the pixel is < 4%, then the natural grass PFT percentage is calculated as 4% minus the tree PFT percentage (since the lower bound on total vegetation is 4%) and the water PFT percentage is scaled down to 96%, or (3) if the non-water percentage of the grid cell exceeds 14%, then the natural grass percentage is calculated as 14% minus the tree PFT percentage (that is, the upper bound of 14% is assumed for total vegetation cover) and the residual pixel area is assigned as bare soil PFT (100% minus water PFT percentage minus 14% vegetation cover).

Shrubland classes

A mixture of tree and shrub woody vegetation types is assigned to pixels of the shrubland classes (codes 120, 121, 122, and 180). The 30 m resolution tree canopy height dataset from Potapov et al. (2021b) is applied to discriminate between shrubs and trees in pixels that are covered by this data product (52°N–52°S). Potapov et al. (2021b) re-assign pixel values of ≤ 2 m to 0 m height. Here, the 30 m resolution pixels are assigned to three broad height classes: 0 m, 3–5 m, and > 5 m. Mean re-sampling to the 300 m resolution of the LC dataset results in pixel values that indicate the percentage cover of the three height classes. The percentage cover of the 3–5 m height class is taken to be the percentage shrub cover in the 300 m pixel and the percentage cover of the > 5 m height class is taken to be the percentage tree cover in the 300 m pixel, recognizing that there may be some bias introduced by 30 m pixels in the input dataset that contain both shrubs and trees. In deference to the class legend, 300 m pixels with shrub cover < 16% are assigned as having 16% shrub cover and those with tree cover > 15% are assigned as having 16% tree cover. For shrubland pixels that occur outside of the extent of the Potapov et al. (2021b) data product (52°N–52°S), the tree cover percentage is assigned according to the tree cover input derived from Hansen et al. (2013b) and the shrub cover percentage is assigned following the most recent version of the global cross-walking table (CWT) (60% shrub cover for classes 120–122 and 40% shrub cover for class 180). For all shrubland pixels, in cases where the sum of water, tree, and shrub cover exceeds 100%, the three PFTs are scaled down proportionally so that the sum is 100% while retaining the legend expectations for the tree and shrub cover. Natural grass cover is assigned as the residual area of the pixel in cases where the sum of water, tree, and shrub cover is < 100%. No minimum water percentage is defined for the flooded shrubland class (code 180).

Urban class

Pixels classified as urban (code 190) can have non-zero fractions of inland water, trees, natural grass, and urban impervious (built-up) PFTs. In the LC classification, pixels are assigned as an urban class when a minimum threshold of

50% built was exceeded based on the GUF dataset (Esch et al., 2017). In the PFT product, the tree and surface water fractions are derived using the same protocol as the one applied to the vegetated classes. The urban impervious fraction is derived from the GHSL dataset (Pesaresi et al., 2013) by aggregating the built-up pixels from the four epochs into a binary built-up / non-built-up distribution at 38 m. Re-sampling to 300 m provides the percentage of the 300 m pixel that is built, introducing local variability which at the global scale ranges from 0–100% built. Only pixels classed as urban by GUF are assigned a non-zero urban impervious fraction in the PFT dataset. Non-urban pixels (i.e., those with less than 50% urban LC according to GUF) are not refined with GHSL data or assigned a percentage built-up. The GHSL appears to capture urban impervious areas more consistently whereas GUF misses road fractions in the built fractions. This is most notable in rural areas and a few selected locations in city centres. If the sum of the urban impervious, tree, and water fractions exceeds 100%, then the urban impervious percentage is retained and the water and tree percentages are scaled down proportionally to a total sum of 100%, otherwise, the residual of the urban impervious, tree, and water percentages is assigned as the natural grass percentage.

Water body class

Waterbody class pixels that are ocean are assigned as 100% water PFT, while those that are inland can additionally have a non-zero cover of tree and natural grass PFTs. The designation of ocean vs. inland at 300 m is determined using the 150 m water body product. The ocean designation is applied to water body class pixels in which all four of the overlapping 150 m pixels of the water body product are classified as the ocean, all other water body class pixels are designated as inland water. The water and tree PFT fractions for inland water body class pixels are assigned using the same 300 m harmonized surface water and tree cover auxiliary inputs that are used for the other classes, however, a minimum of 86% water PFT is enforced following the legend definition for this class. If the sum of the tree fraction and the adjusted water PFT fraction exceeds 100%, then the tree percentage is scaled down as 100% minus the adjusted water PFT percentage. Any residual area is assigned as natural grass PFT.

Bare area classes

The bare area classes (codes 200, 201, and 202) can have up to 3% vegetation cover (by definition of the abiotic class in the FAO LCCS (Di Gregorio and Jansen, 2005)), so bare area pixels can have non-zero fractions of bare soil, tree, and water PFTs. The auxiliary products define the tree and inland water fractions, but tree cover exceeding 3% is scaled down to the class maximum of 3%. Bare soil PFT percentage is calculated as 100% minus the inland water

percentage minus the tree percentage. Pixels of the mosses and lichens class (code 140) can have non-zero fractions of surface water and natural grasses, the latter of which is estimated as 100% minus the inland water percentage.

Permanent snow and ice class

The permanent snow and ice class (code 220) is assigned as 100% snow and ice PFT. All other classes are assigned as 0% snow and ice PFT. Nearly all pixels classified as permanent snow and ice class in the CCI MR LC time series are static pixels, that is, such pixels are snow and ice cover for every year of the LC map series. This is due to a lack of temporally resolved input data available at the global scale to track the evolution of this surface type. Therefore, neither the CCI MR LC classification nor the associated PFT product should be used to track changes in glaciers over time.

Tree fraction leaf type and leaf phenology

For all pixels – of any class – that have a non-zero tree fraction, the total tree fraction is assigned as a single tree type (broadleaved or needleleaved leaf type, deciduous or evergreen phenology). For the tree cover classes coded 50–82, the specific tree type follows the class legend. The vast majority (75%) of pixels with a non-zero tree fraction were assigned a tree type directly using the class legend. For classes where the leaf type and leaf phenology are not indicated in the legend, the specific tree type is assigned by pixel based on the majority tree type in the surrounding $0.25° \times 0.25°$ neighbourhood window, where the majority calculation is performed on static pixels of the tree cover classes with legend-defined tree types. This concerns 24% of pixels with a non-zero tree fraction.

For pixels of the tree cover classes coded 90, 160, and 170 and all other vegetation-containing classes except the shrubland classes, the specific tree type is assigned by pixel based on the majority tree type in the surrounding $0.25° \times 0.25°$ neighbourhood window, where the majority calculation is performed on static pixels of the tree cover classes with legend-defined tree types (classes 50–82). If the $0.25° \times 0.25°$ window does not contain any static pixels of the well-defined tree types, then the window is incrementally expanded by 0.25° in each direction (longitude and latitude) to a maximum window size of $2° \times 2°$ until such a pixel is contained within the search window. The same tree type is assigned to all pixels in a class for the tree cover classes 50–82, while the assigned tree type can vary between pixels within a class for the other classes.

The majority (75%) of pixels with some tree cover were directly assigned a tree type based on the class legend. An additional 24% had their tree type determined using a nearby window measuring 0.25° by 0.25°. Less than 1% were assigned based on a larger window up to 1° by 1° in size, and less than

0.1% used an even larger window up to 2° by 2°. For a small number of pixels where the legend does not specify the leaf type and leaf phenology, and where there are no static pixels representing tree cover classes within the surrounding 2° by 2° window, a climatological approach is applied.

Assigning PFT fraction to the global extent

Most of the auxiliary inputs are based on Landsat images and therefore have an extent of 80°N–60°S. The main processing algorithm for the PFT product, explained above for the static pixels, therefore operates to this extent. Less than 0.5% of the area outside of this extent is composed of pixels belonging to a class other than water bodies (code 210) or permanent snow and ice (code 220). The largest contributors to this small area are the sparse vegetation classes followed by the bare area classes with negligible contributions from shrubland (including flooded shrubland), grassland, and lichens and mosses classes. To extend the PFT product to a global extent, the following assumptions are applied to the pixels north of 80°N and south of 60°S: (1) 100% snow and ice PFT is assigned to pixels of the permanent snow and ice class, (2) 100% water PFT is assigned to pixels of the water body class, (3) 100% bare soil PFT is assigned to pixels of the bare area classes, (4) 100% natural grass PFT is assigned to pixels of the grassland and lichens and mosses classes, (5) 96% bare soil PFT and 4% natural grass PFT (to meet the legend minimum of vegetation cover) are assigned to pixels of the sparse vegetation classes, and (6) 84% natural grass PFT and 16% needleleaved deciduous shrub PFT (matching the legend minimum shrub cover) are assigned to pixels of the shrubland classes. For the shrubland classes, the shrub type of needleleaved deciduous is assigned because the shrubland class pixels needing assignment (north central Russia) occur nearest pixels of needleleaved deciduous shrubs that had shrub type assigned using the standard method.

3.3.2 Pixels experiencing LC change

Dynamic pixels – that is, pixels that have experienced at least one LC class change over the 1992–2020 era – correspond to 5.88% of the ice-free land surface (see Chapter 1). For such pixels, the derived PFT fractions are derived for each of the classes assigned to that pixel over the era. For example, if a pixel changed from forest to cropland, PFT fractions associated with the forest class are estimated and PFT fractions associated with the cropland class are also estimated for the pixel. The method used to assign the PFT fractions depends on the time stamp of the class in relation to the time stamp (2010) of the auxiliary dataset (Hansen et al., 2013b) from which the tree cover fractions are derived. The PFT fraction of a pixel in 2010 was derived using the following class-specific methods described in Section 3.3.1. Any change of class occurring before or after 2010 leads to deriving new PFT fractions as the mean PFT

fractions of all 300 m pixels of the same class pixels within the overlapping 0.25° x 0.25° window centred on the pixel of interest. The input pixels over which the mean is calculated are the 300 m pixels that did not experience LC class change over the 1992–2020 era. If no pixels of the relevant class is within the 0.25° x 0.25° window, then the window is incrementally expanded by 0.25° in both the latitude and longitude directions until at least one pixel of the relevant class is contained in the window. A pixel can experience up to 7 LCCs in the 1992–2020 era (Chapter 1), which leads to deriving new PFT fractions for each new LC class encountered.

3.4 The CCI PFT dataset

The CCI PFT dataset (hereafter called PFT_{local}) provides the percentage cover as discrete values of 0–100% of 14 PFTs at 300 m. The global continuous field maps are produced at an annual resolution, covering the years 1992–2020. The PFT distributions are consistent with the CCI MR LC data product and eliminate the need to use a CWT to translate LC classes into PFTs. The strong coupling maintained with the CCI MRLC map categories ensures spatially consistent harmonization of auxiliary datasets into PFT fractions (Figure 3.4). Additionally, it enables temporally consistent extension of the fractional PFT coverages over the entire time series (1992-2020), despite the lack of auxiliary inputs available throughout the entire period. The 14 PFTs, illustrated in Figure 3.5, encompass (1) permanent inland water bodies, (2) permanent snow and ice cover, (3) bare soil, (4) built-up areas, which include artificial impervious area such as buildings and, frequently but not exhaustively, other paved surfaces such as roads, (5) managed grasses (i.e., herbaceous crops), (6) natural grasses (i.e., non-cultivated herbaceous vegetation), (7) broadleaved deciduous shrubs, (8) broadleaved evergreen shrubs, (9) needleleaved deciduous shrubs, (10) needleleaved evergreen shrubs, (11) broadleaved deciduous trees, (12) broadleaved evergreen trees, (13) needleleaved deciduous trees, and (14) needleleaved evergreen trees. Following the auxiliary inputs, trees are woody vegetation with a height > 5 m, while shrubs are woody vegetation with a height of 3–5 m, inclusive.

Climate models may need products associated with a coarser spatial resolution, over specific areas (e.g., for regional climate models), and/or in another projection. To tackle the variety of requirements, a user tool has been developed that allows users to adjust the products in a way that is suitable to their models. A minimum list of possibilities in terms of spatial resolution and projection has been established and the conversion of CCI-LC classes to other user-defined classes is also foreseen. The CCI PFT product and the user tool are freely available at `maps.elie.ucl.ac.be/CCI/viewer/` and `climate.esa.int/en/projects/land-cover/data/`.

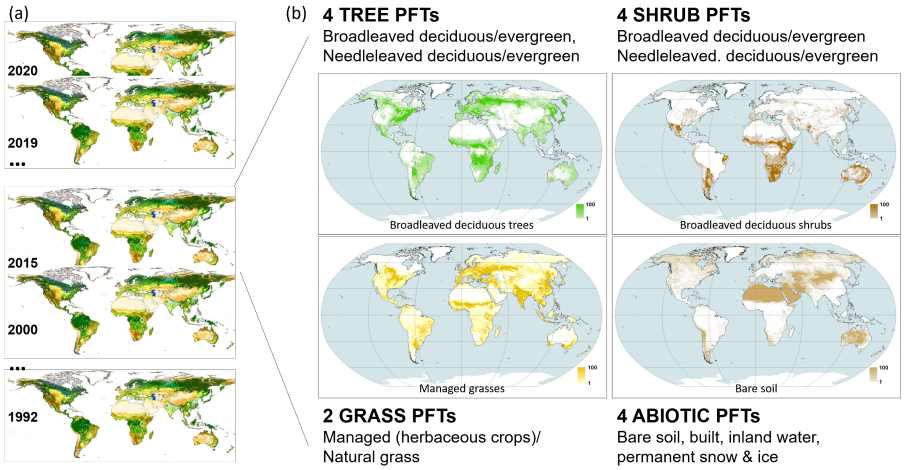

Figure 3.4: For each year within the period, the CCI MRLC map categories (a) ensure both spatial and temporal consistency of the (b) 14 PFT fractions generated (one for each of the 14 PFTs). Data values at a resolution of 300 meters indicate the percentage cover (ranging from 0% to 100%) of the PFT for the given year.

The PFT_{local} dataset indicates that herbaceous vegetation covers 44.8% of the Earth's land surface, with around one-third of that area devoted to herbaceous crops. Tree cover accounts for 21.3% of the land surface, which is much larger than that of shrubs (3.2%). The abiotic surface types cumulatively cover 30.8% of the land surface: 18.4% bare soil, 10.0% snow and ice, 2.1% inland water, and 0.3% built (Figure 3.6).

The PFT_{local} product indicates global areal tree cover of 31.4 million km^2 (Figure 3.5): 45.2% broadleaved evergreen, 24.3% needleleaved evergreen, 23.0% broadleaved deciduous, and 7.5% needleleaved deciduous. The PFT_{local} product indicates 4.7 million km^2 of global shrub cover. The largest contributors to total shrub cover are broadleaved deciduous (44.6%) and needleleaved evergreen shrubs (25.2%). Global grass PFT cover in the PFT_{local} product is 65.7 million km^2, two-thirds of which is natural grass. In the PFT_{local} product, the per-pixel fraction of surface water PFT is estimated for pixels of all classes except the permanent snow and ice class (Table 3.1). The PFT_{local} product indicates around 142, 000 km^2 of water cover globally among pixels of all classes except the water body class. Only two classes – a sparse vegetation sub-class and a needleleaved deciduous tree cover sub-class – have no pixels with inland water cover (Table 3.2), but both classes have extremely limited total areal coverage, each accounting for only a few square kilometres of area globally. Classes with significant water coverage include needleleaved evergreen tree cover (40, 000 km^2 combined), sparse vegetation (20, 000 km^2), lichens and mosses (14, 000 km^2), flooded shrub/herbaceous cover

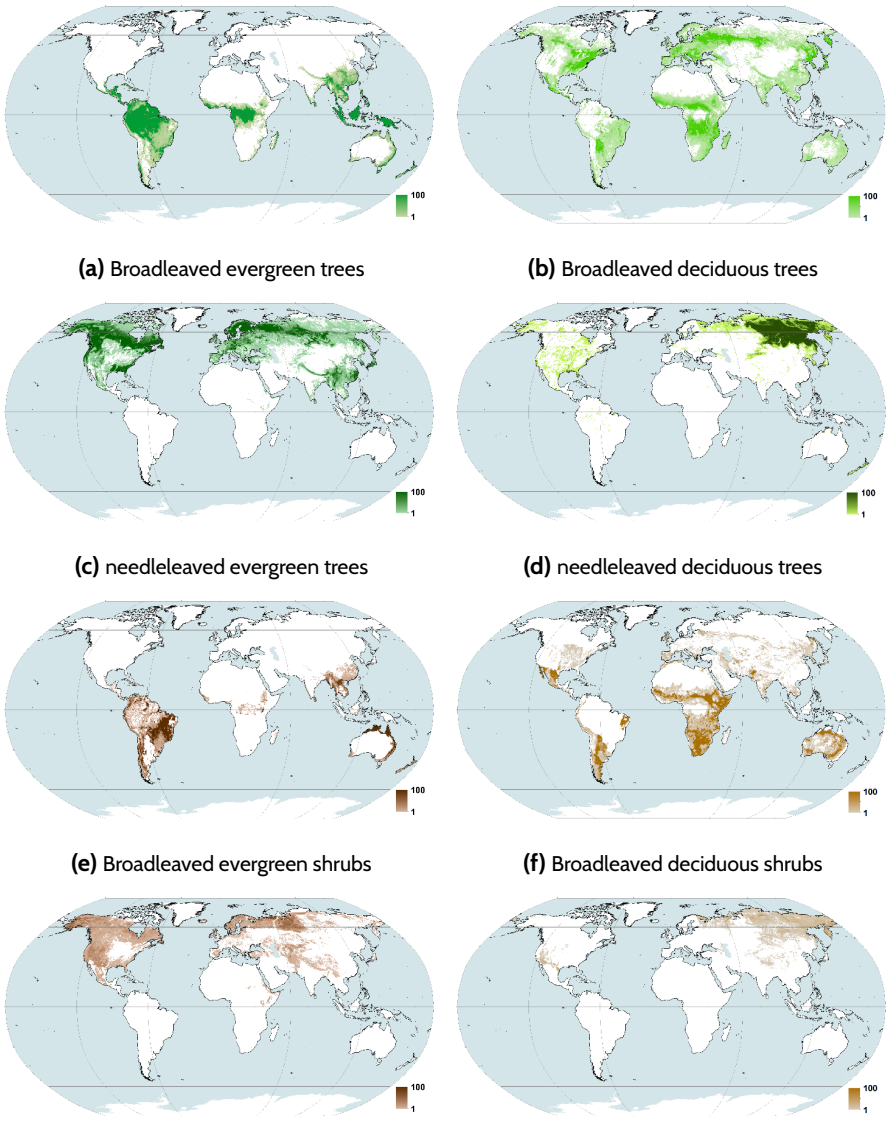

(a) Broadleaved evergreen trees

(b) Broadleaved deciduous trees

(c) needleleaved evergreen trees

(d) needleleaved deciduous trees

(e) Broadleaved evergreen shrubs

(f) Broadleaved deciduous shrubs

(g) needleleaved evergreen shrubs

(h) needleleaved deciduous shrubs

Figure 3.5: (a–h) Percentage cover in 2010 for the 14 PFTs included in the PFT_{local} data product at a spatial resolution of 0.25° × 0.25°.

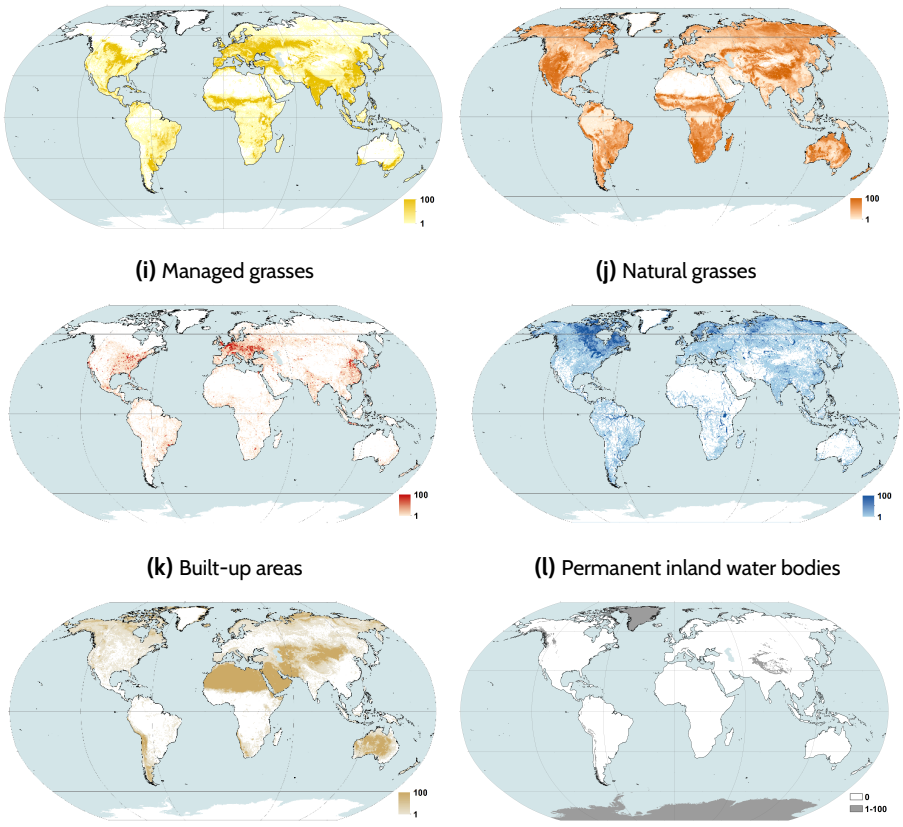

(i) Managed grasses **(j)** Natural grasses

(k) Built-up areas **(l)** Permanent inland water bodies

(m) Bare soil **(n)** Permanent snow and ice cover

Figure 3.5: (a–h) Percentage cover in 2010 for the 14 PFTs included in the PFT_{local} data product at a spatial resolution of 0.25° × 0.25°.

(12, 000 km^2), and bare area (12, 000 km^2). Coverage of water PFT in pixels of the non-water body classes is especially prevalent in the boreal region. Classes with the highest fractional composition of inland water – calculated as the area-weighted mean among all pixels of the class globally (Table 3.3) – include the flooded tree cover (2.3%), the needleleaved evergreen tree cover (1.3%), and the lichens and mosses (0.9%). In the PFT_{local} product, bare soil PFT occurs in the bare area classes and the sparse vegetation classes, accounting for 19.4 million km^2 and 7.6 million km^2 bare soil area, respectively, at the global scale (Table 3.2). The PFT_{local} product suggests 477, 000 km^2 of built area globally (Table 3.2), which corresponds to an area-weighted mean composition of 73.7% built in urban class pixels (Table 3.3). The auxiliary inputs suggest that about 1.6% of urban class pixels have 0% built coverage.

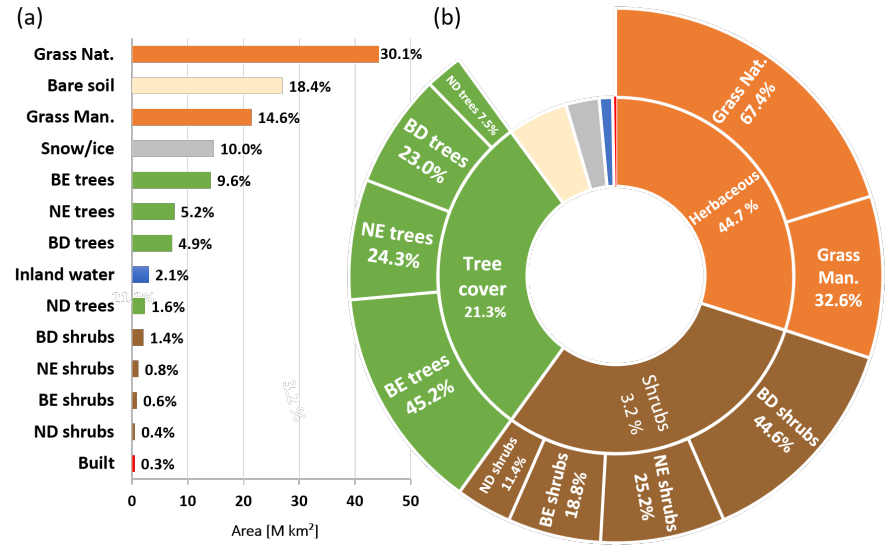

Figure 3.6: (a) Area distribution, in million km², for each PFT of the 2010 PFT$_{local}$ dataset and corresponding proportions (%). (b) Proportion of aggregated PFT types of the 2010 PFT$_{local}$ dataset and the distribution of subtypes.

This suggests a mismatch between the LC classification and the auxiliary inputs for a small number of pixels, which could be related to a mismatch in the time stamp of the auxiliary inputs (2014) relative to the LC dataset. Considering all urban class pixels, 6.2% have built of 0–25%, 7.8% have built fractions of 26–50%, 31.9% have built fractions of 51–75%, and 54.1% have built fractions of 76–100%. As area-weighted means, the non-built portion of urban class pixels is 25.1% natural grass cover, 0.3% inland water, and 0.9% tree cover. The increased spatial heterogeneity in urban class pixels due to the PFT$_{local}$ product is readily apparent in Figure 3.7, which shows the PFT distribution for Amsterdam, the Netherlands. The more realistic characterization of the urban environment in the PFT$_{local}$ product that gives more variability of built coverage within a city should allow a more faithful representation of urban surface fluxes in land-surface models. The permanent snow and ice in PFT$_{local}$ accounts for 14.7 million km^2 of area globally, largely in Greenland and Antarctica, but also in the Arctic and mountainous regions of Asia.

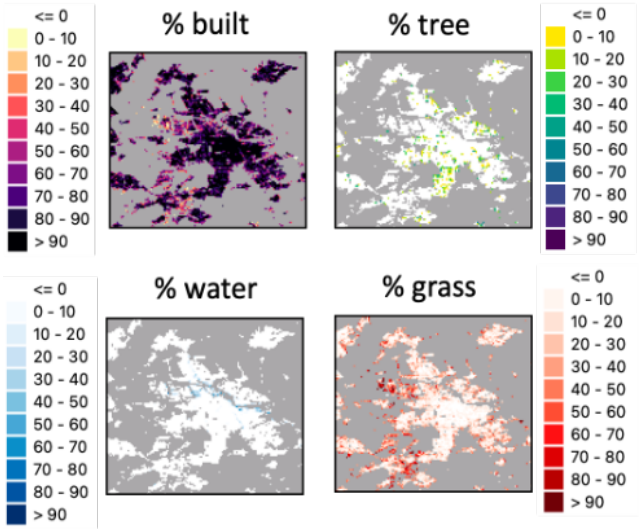

Figure 3.7: Percentage cover in 2010 for the built, total tree, grass, and inland water PFTs in Amsterdam, the Netherlands, in the PFT_{local} product.

3.5 Discussion

3.5.1 Comparison between the CCI PFT dataset fractions (PFT_{local}) and the global CWT table approach (PFT_{global})

Table 3.2 shows the global areal coverage of each PFT by class for 2010 for the PFT_{local} product, and Table A1 shows the equivalent data corresponding to the application of the most recent version of the CCI MR LC global CWT (Lurton et al. (2020), Table B.2) to the v2.0.8 CCI MR LC map for 2010 (hereafter called PFT_{global}). Figure 3.8 shows the areal fraction difference between the PFT_{local} and PFT_{global}. Figure 3.9 provides a spatialized summary of the largest differences between the PFT_{local} and the PFT_{global} products. Figure B.1 complements Table B.1 by illustrating the differences between the PFT_{local} and the PFT_{global} products globally at a spatial resolution of 0.25 x 0.25 degrees. For each class of PFT_{global}, the global CWT specifies the fractional composition of contributing PFTs, in this approach, each pixel of a class is assigned the same fractional PFT composition regardless of its location on Earth. Table 3.3 indicates the percentage PFT composition by class for 2010 for PFT_{local}, calculated as an area-weighted mean taken over all pixels of the class globally.

Tree cover

The PFT_{local} product indicates a global areal tree cover that is 4.6% higher than in the PFT_{global} distribution. Globally, tree coverage is higher in the

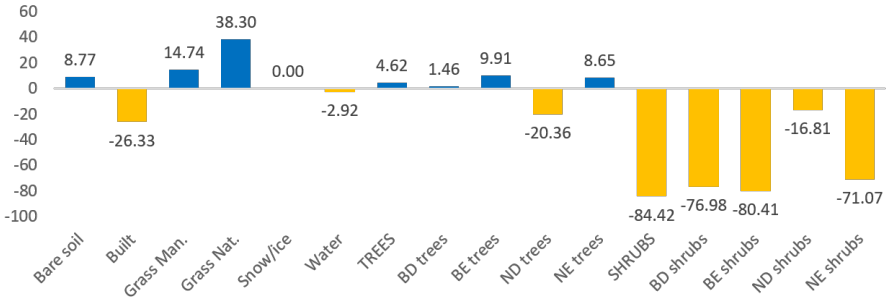

Figure 3.8: Percent difference in areal fraction between PFT$_{local}$ and PFT$_{global}$. Positive values indicate an increase in the areal fraction of PFT$_{local}$ compared to the global fraction.

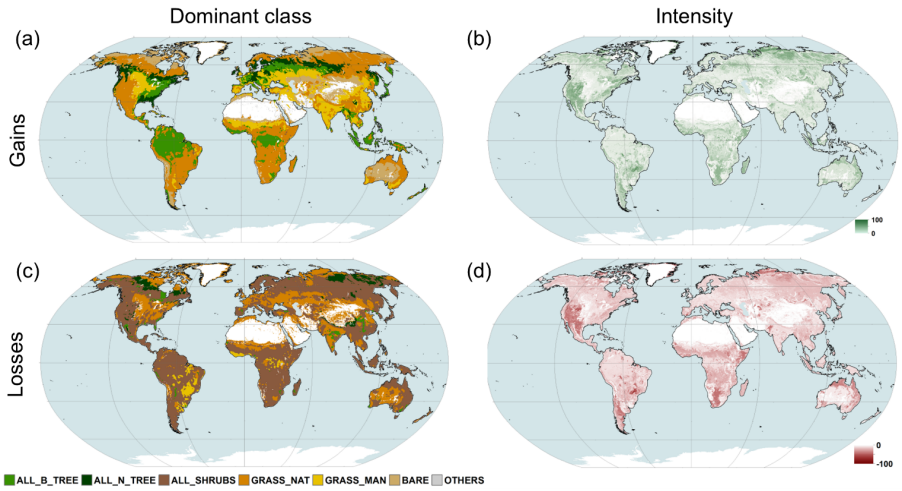

Figure 3.9: PFT with the largest increase (a) and largest loss (c) in coverage within 0.25° x 0.25° pixels in the PFT$_{local}$ dataset compared to the PFT$_{global}$ and corresponding fractions gained (b) and lost (d). White areas remained stable in both PFT datasets.

PFT $_{local}$ product relative to the PFT$_{global}$ distribution for all tree types except needleleaved deciduous trees. Compared to the global CWT, in which every pixel belonging to a given class is assigned the same PFT fractions, the updated method for estimating PFT fractions locally results in greater variability of tree fractions among 300 m pixels within a single class. For example, the global CWT suggests that rainfed cropland pixels are 0% tree cover, but the PFT$_{local}$ product based on auxiliary inputs suggests a much wider range of tree cover at the pixel level, ranging from 0–100% tree cover at the 300 m pixel level. The distribution for Africa is shown in Figure 3.10, where tree crops in the Sahel are readily apparent. Globally, rainfed cropland pixels have

5.1% tree cover on average (Table 3.3). On average, rainfed cropland – tree or shrub cover pixels have 18.4% tree cover. The auxiliary dataset used to derive tree cover for most classes in the PFT_{local} product is based on Landsat 7 images (Hansen et al., 2013b), the artifact associated with the failure of the Landsat 7 Scan Line Corrector (Andréfouët et al., 2003) are visible in the 300 m PFT_{local} dataset in some regions, particularly in west-central Africa.

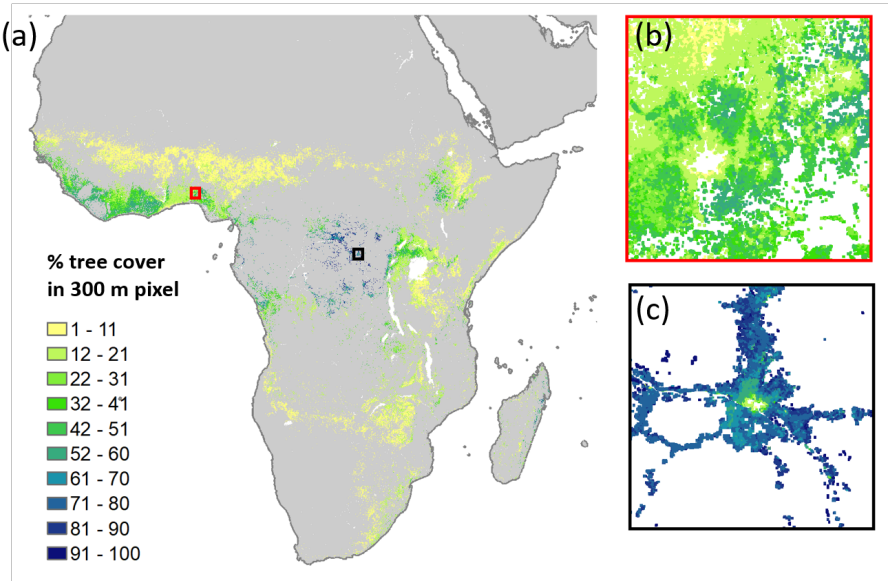

Figure 3.10: Distribution of the tree cover fraction (%) in the rainfed cropland class pixels over (a) Africa, (b) Ibadan (Nigeria), and (c) Kisangani (DRC). Gray pixels belong to other LC classes.

Shrub cover

Shrub cover is 74% lower in the PFT_{local} product than in the PFT_{global} dataset. Some of this difference arises because the PFT_{local} product estimates lower shrub PFT in shrubland class pixels compared to the PFT_{global}dataset, which estimates 8.8 million km^2 of shrub PFT in shrubland classes (Figure 3.11).

The area-weighted mean percentage composition of shrubs in shrubland class pixels is 30.0% for class 120 in the PFT_{local} product, 26.1% for class 121, 34.4% for class 122, and 30.7% for class 180. The CWT suggests 60% shrub cover for classes 120–122 and 40% for class 180. The CWT estimates 0 km^2 of tree PFT cumulatively in these classes compared to 630, 000 km^2 in the PFT_{local} product. The uncertainty associated with the height estimation in the global canopy height product of Potapov et al. (2021b) may contribute to the confusion of shrubs and trees in some cases. Nonetheless, the

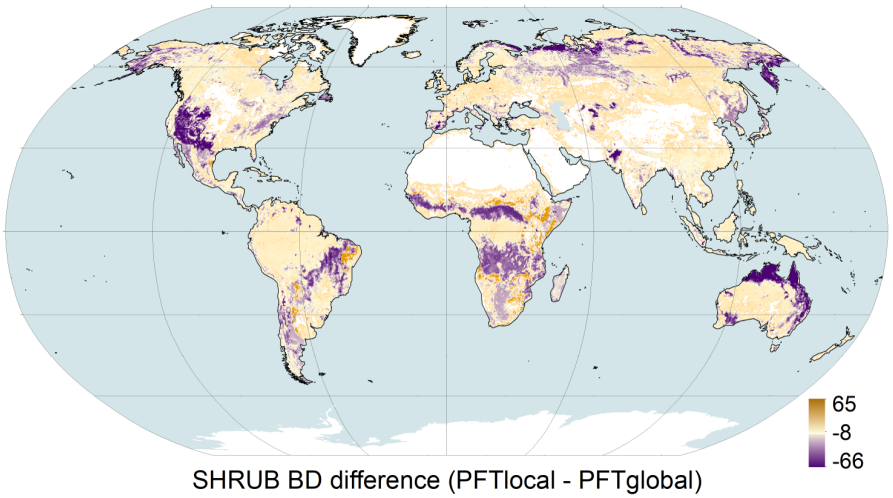

Figure 3.11: Comparison of reduced shrub fraction in the PFT_{local} product, constrained to the shrubland class, against the PFT_{global} fraction.

evidence-based PFT_{local} product indicates a significantly lower estimate for global woody vegetation cover in pixels of the shrubland classes compared to the PFT_{global} dataset, which was largely based on expert knowledge.

The difference in total shrub cover between the PFT_{local} product and the PFT_{global} dataset is partly due to the PFT_{local} product estimating shrub PFTs exclusively within shrubland class pixels due to data limitations for other classes. The CWT estimates 9.5 million km^2 of shrub cover in non-shrubland PFTs, and some of this shrub cover may indeed be missing from the PFT_{local} product. However, given the substantial disparity in the estimates of shrub PFTs in the shrubland class pixels between the PFT_{local} product, which relies on quantitative estimation using auxiliary inputs, and the CWT, which largely relies on expert input, it's conceivable that biases in the CWT contribute to some of the differences observed in the non-shrubland class pixels as well.

Natural and managed grasses

Total grass cover is 29.6% higher in the PFT_{local} product than in the PFT_{global}map (38.3% higher for natural grass and 14.7% higher for managed grass). In the PFT_{local} product algorithm, for the vegetated classes except for sparse vegetation, the entire non-water fraction of the 300 m pixel is assigned as vegetation, typically, water, trees, and other PFTs are estimated based on auxiliary inputs and the CCI MR LC class legend, and then the residual area is assigned as grass cover. Thus, grass vegetation may be assigned in some cases that might otherwise be a temporary bare area.

Water

The PFT_{local} product indicates 3% (91, 000 km^2) lower inland water fractional cover than the PFT_{global} product distribution. While the non-water body classes have a total inland water PFT cover of 142, 000 km^2 in the PFT_{local} product (compared to 0 km^2 from the PFT_{global}), the PFT_{local} product indicates a lower inland water PFT area in the water body class than does the CWT (difference of 233, 000 km^2). The difference in the water body class occurs because the PFT_{local} product allows up to 14% vegetation cover in this class whereas the CWT assumes 100% water PFT. PFTs with significant global coverage in water body class pixels in the PFT_{local} product include natural grasses (183, 000 km^2) and needleleaved evergreen trees (31, 000 km^2) with smaller contributions from the other tree types.

Bare

The global area-weighted mean bare soil percentages are 85.9% in sparse vegetation class pixels and 99.9% in bare area class pixels, which are nearly identical to the compositions suggested by the global CWT (85% for sparse vegetation classes and 100% for bare area classes). Cumulatively for these classes, the PFT_{local} product suggests only 0.2% lower bare soil PFT coverage at the global scale relative to the assumed distribution in the PFT_{global} dataset (difference of 65, 000 km^2). In the PFT_{local} product, the bare area classes contain, in addition to bare soil PFT, inland water PFT (13, 000 km^2) and tree cover (1, 000 km^2).

The PFT_{local} product does not include bare soil PFT in the shrubland classes, while the PFT_{global} dataset assumes 20% bare soil for the non-flooded shrubland classes 120–122. Because the non-flooded shrubland class pixels have such a large extent globally (13.3 million km^2), the PFT_{global} dataset suggests 2.7 million km^2 of additional bare soil in such pixels relative to the PFT product. Differences in the distribution of bare area between the PFT_{local} product and the PFT_{global} are especially pronounced in the U.S. intermountain west, parts of southern and eastern Africa, the northern coast of Australia, and the highlands of Argentina and Brazil, as these are regions with significant shrubland class cover. In the PFT_{local} product, all residual area in the shrubland class pixels that are not assigned as surface water or woody vegetation (trees and/or shrubs) based on the auxiliary input data is assigned as natural grass cover rather than bare soil. Since the PFT_{local} product is built mainly for application to land surface models, the actual presence of grass vegetation vs. bare soil will be determined by the model given simulated or prescribed local climate conditions.

Built fraction

Both the PFT_{local} product and the PFT_{global} assign built fractions only to pixels of the urban class. The presence of a built fraction is not universal in land surface or Earth system models, for example, the current version of the ORCHIDEE land-surface model considers built areas to be 80% bare soil and 20% grasslands. The cross-walking of LC classes to PFTs for the urban class strongly depends on the framework used to calculate surface fluxes in the urban environment and therefore inter-model variation in the global CWT may be stronger for the urban class than for vegetated classes. The global CWT used for this analysis assigns 100% of the urban class as built fraction. For comparison, the JULES land surface model assigns urban class pixels as 75% built and 25% bare soil.

Permanent snow and ice

The PFT_{local} product and PFT_{global} dataset indicate identical coverage for this PFT since both datasets assign 100% snow and ice PFT to the permanent snow and ice class and 0% snow and ice PFT to all other classes.

3.5.2 Evaluation of a land surface model using the CCI PFT dataset

The impact of using the new PFT distributions (PFT_{local}) as a benchmark for JULES-TRIFFID dynamic vegetation is shown in Figure 3.12. When compared to PFT_{global}, JULES-TRIFFID indicates significant over-estimation of tree cover in tropical savannahs, and under-estimation of tree cover in boreal northeast Russia. Additionally, comparison with the global CWT product (PFT_{global}) indicates that JULES-TRIFFID under-estimates shrub cover in tropical savannahs in South America, Africa, and Australia, as well as many semi-arid regions such as western North America. Biases in grass cover are more spatially heterogeneous, but comparison with the global CWT indicates that JULES-TRIFFID strongly overestimates in northeast Russia and northern Australia.

When using the new PFT distributions as a benchmark, many of these biases are reduced, as indicated by green areas in Figure 3.12 (c). In particular, northeast boreal Russia shows reduced biases in tree, shrub, and grass cover. Globally, using the new PFT distributions results in a reduction in biases in shrub cover in JULES-TRIFFID in almost every part of the world, particularly savannahs and semi-arid regions (Figure 3.12 (d)). Whilst no large areas showed a large increase in bias, some areas did show increases in bias of up to 25%, such as tropical forests (10% increase), grass cover in tropical savannahs (15 to 25%) and northern high latitudes (10 to 20%), and bare cover in arid regions (up to 10% increase).

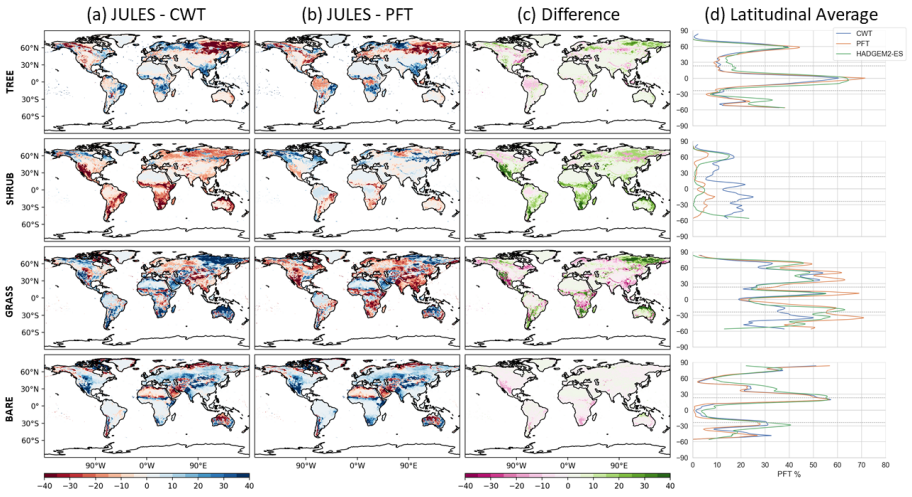

Figure 3.12: Comparison of JULES PFT distributions to both the CWT (PFT_{global}) and PFT (PFT_{local}) products for major vegetation types. Rows show each major surface type (Tree, Shrub, Grass, Bare), whilst rows show (a) JULES vegetation distribution compared to the global CWT, (b) the same compared to new $PFTl_{ocal}$ distributions, (c) the difference between (a) and (b), where green (pink) indicates positive or negative anomalies evaluate closer to 0 (further away from 0) using new PFT_{local} distributions, (d) absolute latitudinal average fractions for each major vegetation type from CWT, PFT, and JULES.

3.6 Conclusion and perspectives

The new PFT product (PFT_{local}) was generated to reduce the cross-walking component of uncertainty by adding spatial variability to the PFT composition within a LC class. This work moved beyond fine-tuning the cross-walking approach for specific LC classes or regions and, instead, separately quantifies the PFT fractional composition for each 300 m pixel globally. The result is a dataset representing the cover fractions of 14 PFTs at 300 m for each year in the 1992–2020 era, consistent with the CCI MR LC map for the corresponding year. The PFT_{local} dataset exhibits intraclass spatial variability in PFT fractional cover at the 300 m pixel level and is complementary to the CCI medium resolution multi-mission LC map series since the derived PFT fractions maintain consistency with the original LC class legend.

The PFT_{local} dataset provides a more faithful representation of PFT distributions because it draws on HR peer-reviewed mapping of specific vegetation classes to refine global assumptions about PFT fractions. In many cases, the global CWT presented a reasonable approximation for estimating PFT fractions within many LC classes as shown by the fractions estimated from the auxiliary products falling close to that suggested by the global CWT. Our re-

sults are supported by a recent study by Marie et al. (2022), which found that rainfed cropland in the Sahel should include tree PFTs corresponding to tree crops (Figure 3.10). Their approach used a map of Above-Ground Biomass (AGB) over Africa (Bouvet et al., 2018) to define local CWTs, leveraging the information from AGB to better delineate the partition between trees and short vegetation PFTs for each ESA LC class. Overall, these efforts highlight the benefits of using additional HR products, like tree cover, AGB, etc. when translating LC into PFT distributions for land surface models. Merging all sources of information into a coherent PFT product remained however a difficult task. This study demonstrated that using the consistent CCI MR LC time series and maintaining deference to the original LCCS class in the combination rules allowed bringing these auxiliary data into consistency.

Production of the PFT_{local} product is dependent on the availability and quality of the auxiliary datasets at a spatial resolution higher than 300 m, this is especially critical for mapping the shrubland class. With the combined information of the phenological attribute of the ESA CCI LC classes, the percentage of tree canopy cover from Hansen et al. (2013b), and the GEDI product (Potapov et al., 2021b), it was possible, for the first time, to map four shrubland classes at the global scale: broadleaved evergreen, broadleaved deciduous, needleleaved evergreen, and needleleaved deciduous. Yet, further research is still needed to improve the estimation of shrubland class pixels north of 52°N (i.e., outside of the extent of the GEDI product). The urban fraction would benefit from separating impervious surfaces from buildings. Finally, the current workflow should further be tested against annual ancillary product updates as operational production of HR datasets will become the norm. It is also expected to find multiple HR datasets for the same class in a given year. The approach outlined in Chapter 2 should be consistently applied to enhance the accuracy of PFT distribution. The proposed methodology is automated so that the PFT dataset will be updated annually as new annual LC maps are produced in C3S.

Table 3.2: Global areal cover (1000 km²) of each PFT by LC class for 2010 in the PFT$_{local}$ product.

Class code	Bare soil	Built	Man. grasses	Nat. grasses	Snow/ ice	Water*	BD trees	BE trees	ND trees	NE trees	BD shrubs	BE shrubs	ND shrubs	NE shrubs
10			7729.7			2.3	175.1	199.5	0.7	36				
11			6774.9			1.5	110.4	112.9	4.1	19.7				
12			155.1			0.1	4.6	29.8		0.6				
20			2415.5			1.2	19	7.4	0.2	1.8				
30			2803			1.1	123.2	467.2	0.8	39				
40			1557.4	1247.9		1.2	195.1	493.2	4.7	65.1				
50				1262.6		4.3		11476.1						
60				2237.9		1.7	3599.6							
61				337		0.2	538.6							
62				2673.9		0.2	1000							
70				2411.4		21.9				4060.4				
71				710.7		18				1720.3				
72				0.7						0.3				
80				2977.6		4	0.1		2143.5					
81				0.7					4.1					
82														
90				441		1.6	674.1	63.7	77.8	918.5				
100				2443.7		2.6	233.8	329.3	43.4	354				
110				977.3		0.5	66.1	26.1	3.5	11.1				
120				7246.3		4	176.3	125.5	3.9	80.7	1746.8	632.9	164.7	724.5
121				142.5			1.6	26.3	5.3	0.6	2.7	31.2	26.8	1.5

Continued on next page

Table 3.2: Global areal cover (1000 km²) of each PFT by LC class for 2010 in the PFT_{local} product. (Continued)

122			1294.6		1.1	41	68.5	10.4	4.2	211	154.6	293.8	86.8
130			13338.8		5.8	144	159	8.5	47.4				
140			1476.9		14.2								
150	7254.8		1157.7		20.4	0.5	1.3	0.6	12				
151													
152	63		8.9		0.2	0.1		0.2	1.1				
153	323.8		52.7		0.1								
160			200.4		2.3	71.7	442.6	27.4	151.4				
170			86.1		5	12.3	110	4.6	0.8				
180			1231.9		11.7	12.7	15.1	5.5	51.8	122.3	56.6	47.7	362.7
190		476.7	162.5		1.9	2.5	1.3	0.2	2.1				
200	19156.9				13.3	0.4		0.2	0.5				
201	108.8				0.3								
202	97.2				0.1								
210			182.6		365991.8	7.2	8.9	3.1	31.3				
220				14694.2									

★ For the water body class (built 210), the water PFT area includes 2, 877, 500 km² of inland water. For all other classes, all water PFT area is inland water.

Table 3.3: Percentage PFT composition by class for 2010 calculated as an area-weighted mean over all pixels of the class globally.

Class code	Bare soil	Built	Man. grasses	Nat. grasses	Snow/ ice	Water*	BD trees	BE trees	ND trees	NE trees	BD shrubs	BE shrubs	ND shrubs	NE shrubs
10			94.9				2.1	2.5		0.4			0	
11			96.5				1.6	1.6	0.1	0.3			0	
12			81.6				2.4	15.7		0.3			0	
20			98.8			0.1	0.8	0.3		0.1			0	
30			81.6				3.6	13.6		1.1			0	
40			43.7	35.0			5.5	13.8	0.1	1.8			0	
50				9.9				90.1					0	
60				38.3			61.6						0	
61				38.5			61.5						0	
62				72.8			27.2						0	
70				37.1		0.3				62.5			0	
71				29.0		0.7				70.2			0	
72				72.6		1.3				26.1			0	
80				58.1		0.1			41.8				0	
81				15.4		0.5			84.1				0	
82				82.9					17.1				0	
90				20.3		0.1	31.0	2.9	3.6	43.3			0	
100				71.7		0.1	6.9	9.7	1.3	10.4			0	
110				90.1			6.1	2.4	0.3	1.0			0	
120				66.4			1.6	1.2		0.7	16.0	5.8	1.5	6.6
121				59.7			0.7	11.0	3.3	0.3	1.1	13.1	11.3	0.6

Continued on next page

Table 3.3: Percentage PFT composition by class for 2010 calculated as an area-weighted mean over all pixels of the class globally. (Continued)

122			59.8	0.1	1.9	3.2	0.5	0.2	9.7	7.1	13.6	4.0
130			97.3		1.1	1.2	0.1	0.3			0	
140			99.1	0.9							0	
150	85.9		13.7	0.2				0.1			0	
151	86.0		14.0								0	
152	85.8		12.1	0.2	0.1		0.3	1.5			0	
153	86.0		14.0								0	
160			22.4	0.3	8.0	49.4	3.1	16.9			0	
170			39.3	2.3	5.6	50.3	2.1	0.4			0	
180			64.2	0.6	0.7	0.8	0.3	2.7	6.4	3.0	2.5	18.9
190		73.7	25.1	0.3	0.4	0.2		0.3			0	
200	99.9			0.1							0	
201	99.7			0.2							0	
202	99.9			0.1							0	
210				99.9								
220			100.0								0	

* For the water body class (code 210), the water PFT percentage includes inland water. The area-weighted mean percentage composition of inland water PFT in water body class pixels is 0.8 %. For all other classes, all water is inland water.

Chapter 4

Pilot Study on Land Cover Categorical Uncertainty

This chapter is intended to evolve into a stand-alone paper:

Lamarche, C., Kirches, G., Quast, R., Boettcher, M., Brockmann, C., Albergel, C. Defourny, P. On the retrieval of categorical LC uncertainty. *In preparation.*

Abstract

Earth Observation (EO) data processing chains, like land cover (LC) classification, inherently involve errors that propagate from raw data acquisition to final products. Accurate uncertainty quantification is crucial for detecting subtle climatic variations among inherent data uncertainty. Metrology principles are increasingly applied to quantify uncertainty at the preprocessing stage. However, clear guidelines for LC categorical uncertainty retrieval are lacking. Current practices primarily assess uncertainty through class area variability and probability vectors. Here, we investigate the impact of preprocessing errors on LC maps using Monte Carlo simulations and Random Forest (RF) classifications. We quantify the effect of the mean compositing technique on uncertainty and introduce three per-pixel indicators (PMax*, Std*, and ERP*) derived from a mean vector of class membership probabilities, along with the most probable LC map*. We show that extending the mean compositing period from 13 to 52 weeks reduces SDR relative uncertainty by 10% to 77%, depending on the study site. The RF contributes to doubling or tripling the LC categorical uncertainty, increasing it from 0.11 to 0.33 depending on the site. LC Map* reduces uncertainty by improving landscape patch compactness, achieving a 52% reduction in isolated pixels. PMax* and ERP* are sensitive to mixed pixels and show lower values in mosaic classes, making them suitable for pixel-level uncertainty assessment. This study provides a foundation for more in-depth categorical uncertainty quantification for LC and the development of new techniques relevant to increasing LC map stability.

4.1 Introduction

Errors and uncertainties occur throughout the remote sensing data processing steps, from the initial acquisition of observations to the final product release (Lunetta et al., 1991; Unwin, 1995; Defourny et al., 2012c). Due to its discrete nature, EO classification overlooks environmental complexities, which further introduces uncertainties in class assignments (Van der Wel et al., 1998). Accurate detection of climatic variations relies on stable, long-term measurements in EO Climate Data Records (CDR) (Merchant et al., 2017; Mittaz et al., 2019; Hollmann et al., 2013). Climate models, which rely on information derived from LC data, are particularly sensitive to uncertainties (Hartley et al., 2017). Errors in LC mapping or inaccurate detection of LC changes can lead to uncertain assessments of surface areas, ultimately resulting in less informed decision-making.

Traditional LC mapping practices have prioritized accuracy quantification through confusion matrices, comparing thematic products to reference data (Stehman, 2009; Congalton, 1991). While uncertainty is often reported based on the variability of class area estimates (Strahler et al., 2006a; Olofsson et al., 2014b), the confusion matrix lacks insight into the spatial structure of uncertainty at the pixel level. However, there has been a growing focus on quantifying uncertainty in machine learning algorithms. Uncertainty is often characterized by probability vectors that indicate the likelihood of each class being the true class (Goodchild et al., 1992). Bayesian classifiers (e.g. maximum likelihood) provide uncertainty estimates through posterior probabilities, while non-probabilistic classifiers (e.g. Random Forest (RF) (Breiman et al., 1984; Breiman, 2001)) rely on maximum class membership after label voting from the various trees. Loosvelt et al. (2012) introduced a methodology to analyze uncertainty in classification using local probabilities of class membership from RFs applied to SAR data. Maximum probability is commonly used as a substitute for uncertainty, despite probability vectors providing a more comprehensive measure (Goodchild et al., 1992; Van der Wel et al., 1998). Information theory indicators like entropy (Shannon, 1948) and the Equivalent Reference Probability (ERP) (Bogaert et al., 2017) address these limitations by considering the unpredictability within the class probability distribution instead of focusing solely on the maximum probability.

In recent years, initiatives have fostered the development and refinement of uncertainty retrieval methods, guided by metrology principles (FIDUCEO, 2023; GCOS, 2022; QA4ECV, 2014; QA4EO, 2013). The Guide to the Expression of Uncertainty in Measurement (GUM) defines "uncertainty" as a parameter characterizing the dispersion of values of a measured quantity (JCGM, 2008). It differs from accuracy, which measures the agreement between a measurement result and the true (unknown) value of the measurand, defined as "the quantity intended to be measured". An "error" is defined as the measured

value minus the true value of the measurand (JCGM, 2008). It often remains unknown since the true value cannot be measured (Merchant et al., 2017).

The principles of metrology are not currently applied operationally to the spatial domain. Typically, only the sensor design specifications are provided. However, advanced uncertainty characterization guidelines exist for S2 surface reflectances (Gorroño et al., 2017). A gap analysis for uncertainty retrieval for Sentinel-3 OLCI was performed by Fahy and Hunt (2021). Principles of metrology have also been applied to historical EO from satellites (Mittaz et al., 2019).

Errors potentially arising at each stage of the processing chain accumulate over time, it is recommended to identify, quantify and propagate these uncertainties through the implementation of an end-to-end uncertainty budget (Merchant et al., 2017). This process of quantifying and propagating uncertainties may rely on analytical methods like the Law of Propagation of Uncertainties or ensemble methods such as Monte Carlo (BIPM et al., 2009). Ensemble methods are particularly useful for non-linear models or when an analytical solution is not possible, such as in neural networks or iterative processes (Fahy et al., 2022). Monte Carlo includes a simultaneous variation of all parameters through repeated random sampling based on the probability density described by the uncertainty (Harris and Cox, 2014).

Although, as outlined above, partial assessments of uncertainty have been made for specific processing steps of the preprocessing and classification steps, the precise quantification and propagation of errors in LC CDRs processing remain largely unexplored. To the knowledge of the authors, no comprehensive end-to-end uncertainty budget for LC CDRs currently exists.

The primary objective of this study is to understand how pre-processing variability impacts the uncertainty of LC classification derived from EO data preprocessing from radiances to mean seasonal surface reflectance composites. Our classification framework maintains consistent parameters and training data throughout multiple classification iterations. We used a RF classifer to quantify the ensemble uncertainty through the overall accuracy standard deviation (i.e. standard uncertainty) and the class area coefficient of variation (known as the relative standard uncertainty). Furthermore, we seek to determine the RF contribution to LC uncertainty by multiple classification iterations maintaining consistent parameters and training data across iterations. To capture the spatial distribution of pre-processing errors on the most probable map of the ensemble, we propose two spatially explicit per-pixel indicators, MaxP* and ERP*, derived from the mean probability vector of the ensemble. Our research further investigates the sensitivity of these indicators to factors like the map legend, class proportions, and the fraction of edge pixels relative to the class area. Finally, we evaluate the impact of the mean compositing technique in reducing uncertainty. This study, thus, provides a comprehensive framework to understand the manifestation of pre-processing

errors in LC uncertainty, ultimately contributing to the enhancement of classification accuracy in EO-based LC mapping.

After introducing the study sites, EO input and auxiliary data, the Method section outlines the processing chain converting radiances to LC maps, with a particular focus on the LC classification scheme and the retrieval of LC uncertainty. This section provides a concise overview of uncertainty retrieval in the preprocessing chain, primarily focusing on the basic principles of the Monte Carlo approach up to the mean compositing step. For comprehensive details, readers are referred to the supplementary materials summarizing the Quast et al. (2024 *in preparation*) approach (Section C). The assessment of LC categorical uncertainty is then presented and discussed.

4.2 Study sites and data

4.2.1 Study sites

Three sites of approximately 24000 km² each were chosen in three different continents to represent diverse geographies in terms of LC classes and spatial patterns (Figure 4.1). The European (EU) site, located in Western Europe, encompasses the eastern part of Belgium as well as parts of Germany and Luxembourg. The landscape is predominantly composed of grasslands, forested areas, and croplands, with unique ecosystems such as the Fagnes wetland. The climate is temperate with a warm summer and marked by the absence of a dry season. The African (AF) site, typical for Sudano-Sahelian region and located in Mali, is characterized by a latitudinal rainfall gradient in an arid hot climate. The landscape patterns here are less compact, and the predominance of mosaics of cropland (mixed pixels) is evident. The fields are small and heterogeneous, with many containing trees in varying proportions. To the South, agriculture is intermixed with shrubby savannah. To the North, the arid climate remains hot but tends to be more desertic, leading to barren and very sporadic vegetation. The South American (SA) site covers a highly contrasting region in southern Paraguay. The majority of the moist tropical forests have been cleared for grasslands. The herbaceous class is often mixed with agriculture or trees to form agricultural or natural mosaic classes.

4.2.2 Satellite imagery

OLCI was selected as it is the most recent dataset integrated into the CCI LC processing chain. The design of Sentinel-3 OLCI is based on MERIS[1]: it records radiances in 21 bands in the visible and near-infrared at spatial resolutions of approximately 300 m and 1.2 km. All granules of Sentinel-3A and -3B OLCI L1B Top-Of-Atmosphere (TOA) measurements from January 2019

[1] source: https://sentinel.esa.int/web/sentinel/missions/sentinel-3/instrument-payload/olci

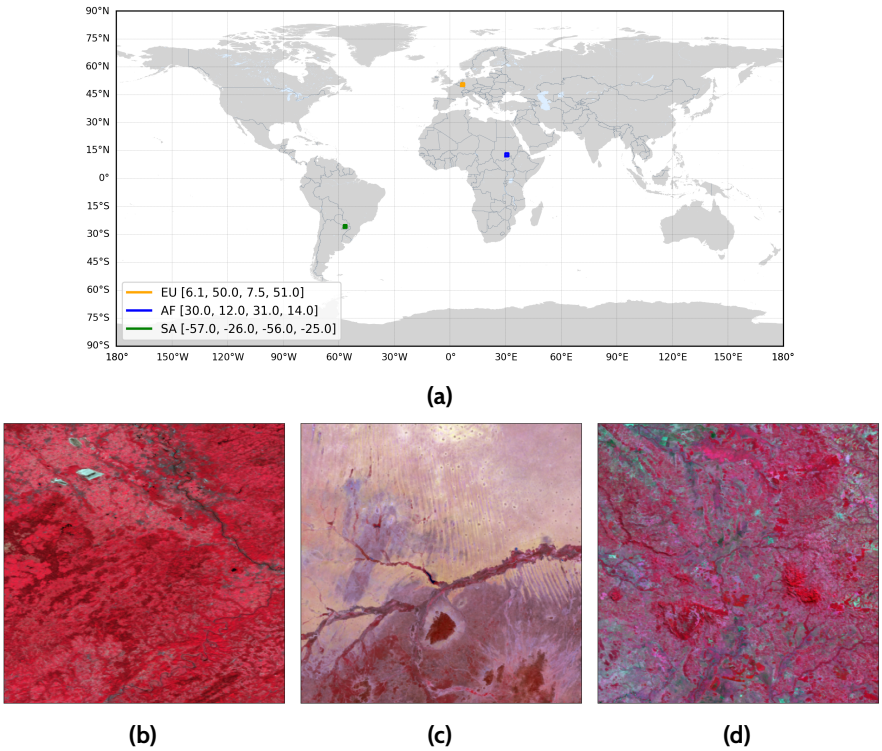

Figure 4.1: (a) Spatial distribution and extents of the 3 study sites. Sentinel-3 OLCI false-color composites for the sites in (a) Europe–EU, (b) Africa–AF, and (c) South America–SA. These are typical infrared false-color composites with 885 nm Near-Infrared (NIR) band in the red channel, 665 nm Red band in the green channel, and 560 nm green band in the blue channel. Composites dates correspond to the first period (see Table 4.1).

to March 2021 were fetched from the EUMETSAT Data Store. The L1B level data are calibrated, ortho-geolocated, and spatially re-gridded TOA radiances at 300 m (Lamquin et al., 2020a). These measurements constitute the primary input for this study, with the measurand being the TOA radiance at the time of each observation in all spectral bands used in the processing chain.

4.2.3 Reference data for the LC classification

The classification training dataset is extracted from two publicly available LC maps with satisfactory accuracy, both from 2020 to match the EO input data period.

WorldCover, based on S2 and S1 data, depicts the LC with spatial details at 10 m with a detailed 11-class legend compatible with the UN FAO

LCCS. The dataset has been independently validated, achieving an OA of 74.4% (Tsendbazar et al., 2021). The dataset is accessible at `https://doi.org/10.5281/zenodo.5571936`. The CCI MR LC LC map for 2020 described the LC at 300m as part of a global series from 1992 to 2020. It provides a thematic detailed legend with 22 primary LC classes and 15 sub-classes following the UN FAO LCCS (Di Gregorio and Jansen, 2005). Only the primary classes were considered and any regional classes were converted to their corresponding primary classes. The CCI MR LC map is reported to have an accuracy of 70.5%, based on a fully independent validation (Defourny et al., 2021). The map can be accessed in GeoTiff format from `https://maps.elie.ucl.ac.be/CCI/viewer/` and in netCDF format from `https://cds.climate.copernicus.eu/cdsapp#!/dataset/satellite-land-cover?tab=overview`.

4.3 Methods

The uncertainty is assessed throughout the CCI LC preprocessing chain converting Sentinel-3 OLCI TOA radiances (CEOS L1B) into Mean Seasonal Composites (MSCs) and ultimately to LC maps (CEOS L3) (Figure 4.2).

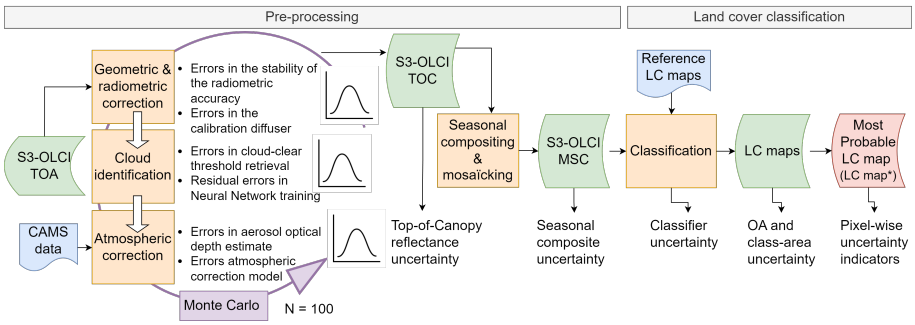

Figure 4.2: Overview of the workflow for the error identification and uncertainty propagation considered in the processing chain split into preprocessing and classification.

Deriving the uncertainty budget begins with assessing the statistical distribution and correlation structure of errors in satellite radiance measurements, atmospheric correction of radiance measurements, and cloud detection.

We distinguish random and systematic uncertainties (Ghent et al., 2019). Random uncertainties, i.e. due to uncorrelated error effects, are defined as "the result of a measurement minus the mean that would result from an infinite number of measurements of the same measurand carried out under repeatability conditions" (JCGM 200, 2008). Pseudo-random uncertainties arise

when measurements appear to fluctuate randomly over large areas or periods but are actually influenced by underlying factors or correlations. Systematic uncertainties, on the other hand, are defined as "the mean that would result from an infinite number of measurements of the same measurand carried out under repeatability conditions minus a true value of the measurand" (JCGM 200, 2008).

The Monte Carlo method enables the propagation of these errors to Mean Seasonal Composites (MSC) of land surface reflectance. In this context, a "MSC variant" is the result of a unique "realization" of a combination of input values derived from the spectrum of uncertainties identified during preprocessing, as further explained in Section 4.3.1. The classification step uses a RF classifier to convert each MSC variant into its corresponding LC map variant (Section 4.3.2). This process starts with the construction of a training dataset from reference LC maps. The uncertainty in categorical LC resulting from the impact of Monte Carlo simulation variations on classification results is evaluated at three levels (Section 4.3.3). We begin by analyzing how the mean compositing strategy influences reflectance uncertainty. Next, variations in overall accuracy (OA) and the coefficient of variation in class areas across LC map variants are assessed to evaluate the non-spatial uncertainty indicators. To further understand the contribution of the RF classifier to the overall uncertainty, we conduct repeated RF classifications for the same variant. Additionally, the ensemble's most probable LC map (LC map*) is introduced alongside three pixel-wise uncertainty indicators: MaxP*, Std*, and ERP*. These indicators are derived from the ensemble mean class membership probability vector at the pixel level.

4.3.1 Preprocessing scheme

During preprocessing, individual TOA surface reflectances are transformed into geolocated bidirectional surface reflectances, corrected for atmospheric and cleared of clouds (Figure 4.3). Steps include geometric and radiometric correction, cloud detection, atmospheric correction (including aerosol retrieval), compositing, and mosaicking. Within the pixel identification algorithm for OLCI, called "IdePix", the cloud detection algorithm classifies different target states including land, water, snow or ice, and various types of clouds (e.g. opaque, semi-transparent clouds, etc.) (Wevers et al., 2022a). The following three error sources have been considered:

1. Errors in calibrated OLCI TOA spectral reflectance, the primary input for preprocessing. The uncertainty for the TOA measurands is assumed to be 0.01, based on the radiometric uncertainty reported in the S3 instrument specifications and mission requirements (ESA, 2023; Donlon, 2011).

2. Errors in estimating the atmospheric state where the most significant error source is the estimation of total Aerosol Optical Depth (AOD). In comparison to this primary source of error, other potential sources like errors in estimating total atmospheric ozone, water vapour mass column densities, and errors in calculating illumination and viewing geometry are considered minor (Lewis et al., 2013; Vermote and Kotchenova, 2008a).

3. Errors in cloud detection, where cloud omission errors result in excessively bright seasonal composites, while cloud commission errors may lead to incomplete or unrepresentative MSCs.

Monte Carlo simulations

The Monte Carlo method simultaneously varies radiometric data, auxiliary input data, and different processing parameters using repeated random sampling. As the measurand can be considered strictly positive, this involves sampling random values for each parameter from a lognormal probability density function (Fox, 2010). To address errors that impact all measurements similarly, errors in all measurements were assumed to be correlated with a correlation coefficient of r = 0.5. In other words, half of the total error variance arises from uncorrelated random noise, while the other half stems from a common random source (e.g., calibration error, total AOD error). Detailed quantitative assessments of radiometric, AOD uncertainty, atmospheric model uncertainties, and cloud detection, including error correlation structures, are extensively discussed in Quast et al. (2024 *in preparation*). The uncertainty of each preprocessing step is then determined by computing the standard deviation of the model output (Woolliams et al., 2014).

Seasonal compositing

Surface bidirectional reflectances are averaged into multispectral seasonal composites using the mean compositing technique (Vancutsem et al., 2007). Among multiple observations available on a single day, the surface reflectance spectrum with the highest NDVI, calculated as $\frac{\text{NIR885nm}-\text{Red665nm}}{\text{NIR885nm}+\text{Red665nm}}$, was selected. Only daily spectra falling within the seasonal standard deviation interval of NDVI were included in the seasonal mean calculation to minimize errors arising from factors such as clouds and cloud shadows.

Seasons and bands (blue: 490 nm; green: 560 nm; red: 665 nm; and near-infrared: 885 nm) were chosen according to the CCI MR LC algorithm, tailored to each site's specific location. Table 4.1 details season starts and duration for each site. In regions like SA, characterized by high cloud cover and tropical forests with less pronounced vegetation phenology, the compositing period extends up to 52 weeks. This duration aims to maximize the likelihood

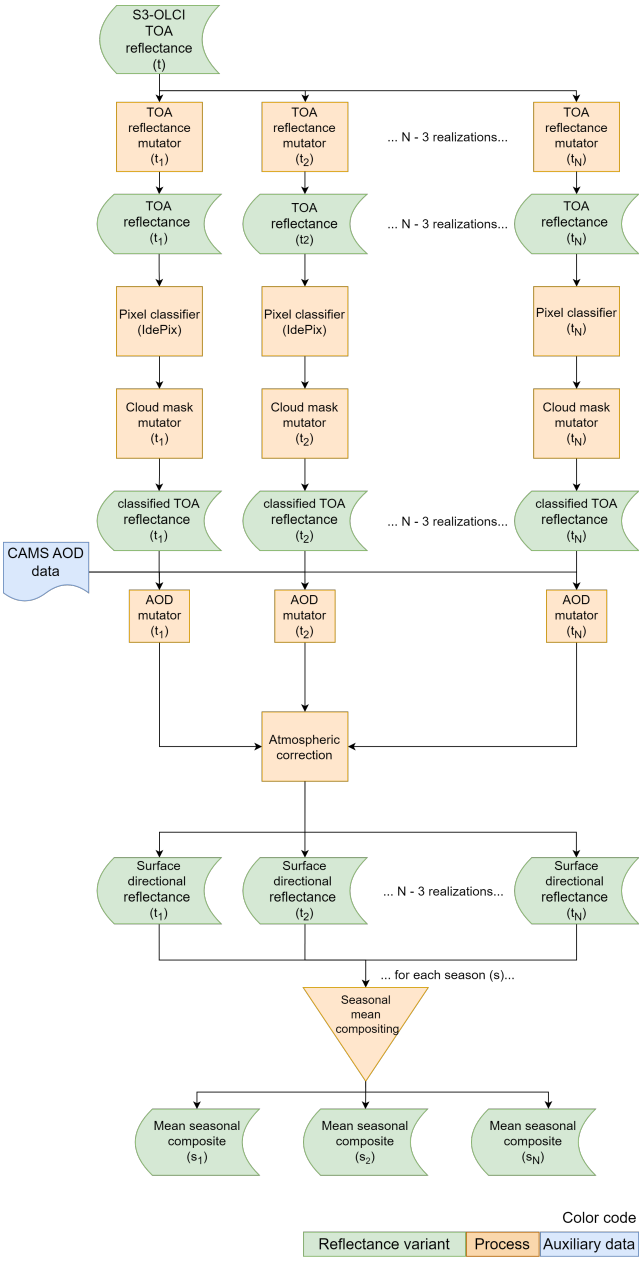

Figure 4.3: Monte Carlo simulations applied to the preprocessing stage, which converts TOA reflectance to surface directional reflectance. Simulations involve randomizing reflectance measurements, cloud detection, and atmospheric correction.

of including clear observations in the composite. Figures 4.4 and 4.5 illustrate resulting Monte Carlo variants of composite surface reflectance in the blue and the near-infrared.

Table 4.1: Seasons selected for seasonal compositing

	Season 1		Season 2	
Site	Start (dd/mm/yyyy)	Duration (weeks)	Start (dd/mm/yyyy)	Duration (weeks)
AF	16/07/2020	7	01/10/2020	13
EU	04/06/2020	13	03/09/2020	13
SA	02/04/2020	13	01/01/2020	52

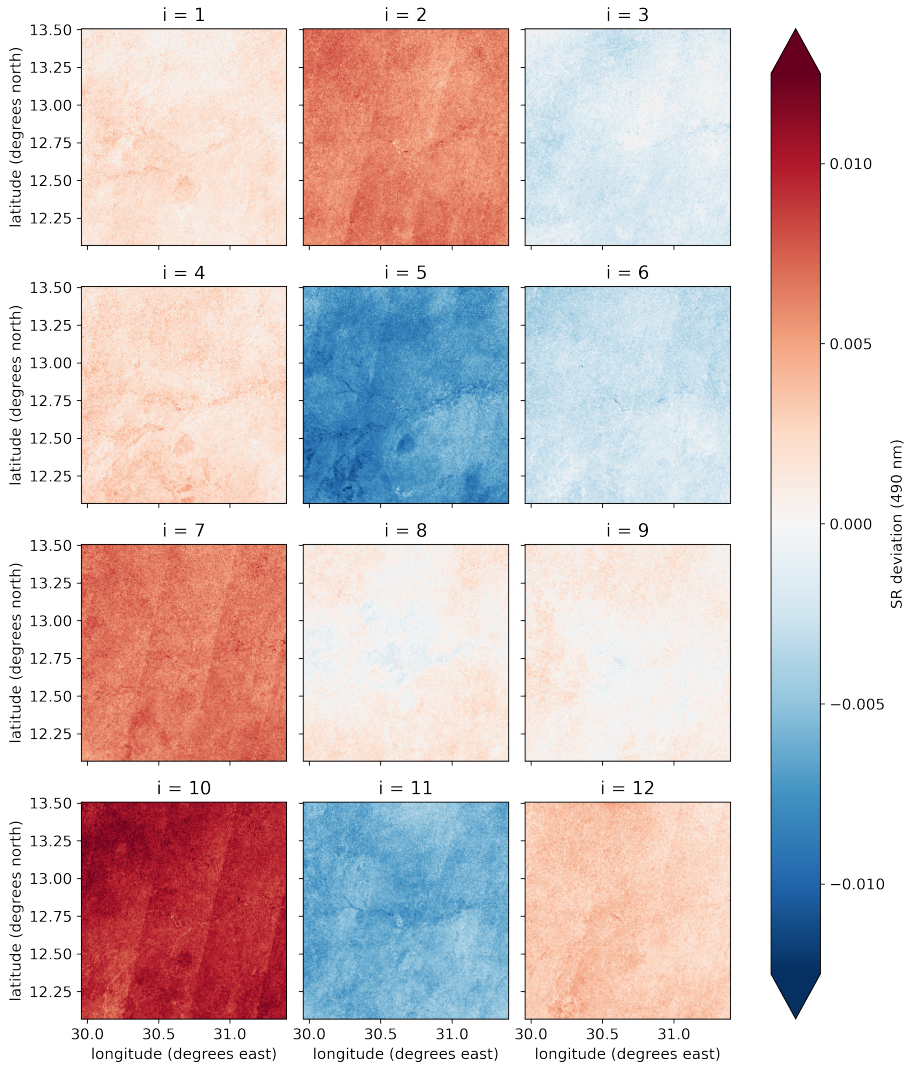

Figure 4.4: Example of twelve Monte Carlo variants of 490 nm surface reflectance (SR) for the African site (52 week composite). Colours indicate the deviation of a variant from the pixel-wise ensemble mean (Quast et al., 2024 *in preparation*).

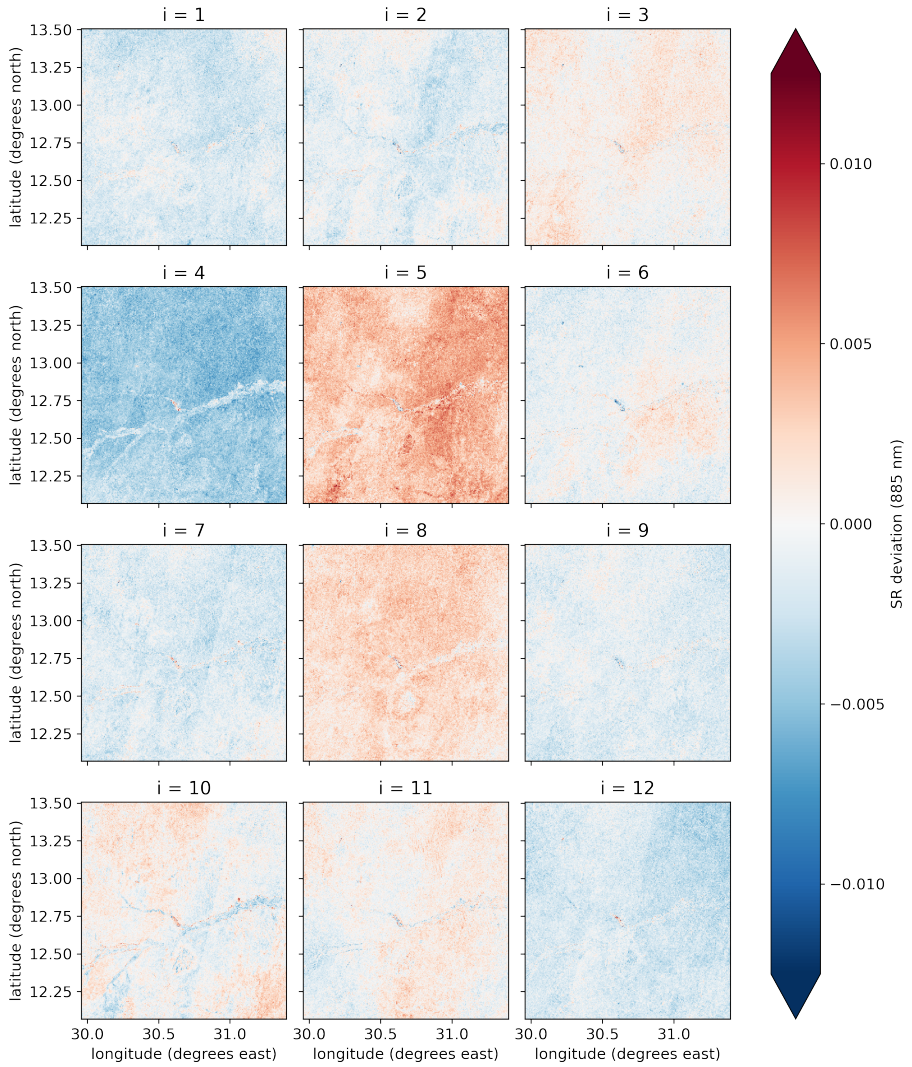

Figure 4.5: Example of Monte Carlo variants of 885 nm surface reflectance (SR) for the African site (52 week composite). Colours indicate the deviation of a variant from the pixel-wise ensemble mean (Quast et al., 2024 *in preparation*).

4.3.2 LC classification scheme

Reference dataset preparation

WorldCover 2020 (Zanaga et al., 2022) was chosen due to its high spatial accuracy, ensuring reference samples with maximum purity and accuracy. However, the classification proposed here aims to evaluate the detailed legend of the CCI MR LC, which comprises over 22 classes, at a resolution of 300m. To handle this complexity while leveraging the benefits of information at higher spatial resolution for more accurate class descriptions, attributes based on leaf type, leaf seasonality, flooding characteristics, or the mixed character of the mosaic classes from the CCI MR LC map 2020 were assigned to the 10 classes from WorldCover. These assignments were made in areas where compatible LC categories were defined by the aggregated legend detailed in Table A.4.

To mitigate potential misclassifications that could arise at the edges of LC patches, a conservative erosion method was applied (Radoux et al., 2014). Homogeneous LC patches larger than 3x3 OLCI pixels were not fully eroded, preserving weakly represented classes (e.g., water bodies, urban areas) for subsequent training.

Classifier description

Independent RF classifiers as coded in scikit-learn (Pedregosa et al., 2011) were calibrated to classify the 100 MSC variants. The RF classifier is a non-parametric ensemble classifier consisting of multiple decision trees. It uses bootstrapping of the input features with replacements to avoid overfitting and determines the output class based on a majority vote from the individual trees (Breiman, 2001). The RF classifier outperforms most classical classifiers in terms of accuracy, feature selection sensitivity, training speed, and stability (Belgiu and Drăgu, 2016). RF benefits also include the need for minimal user-defined parameters and robustness to noise (Rodriguez-Galiano et al., 2012; Pal, 2005).

For each site, 5,000 random samples per class are deliberately chosen to minimize reference uncertainty. If a class has fewer than 5,000 samples, all available points are included in the sampling process. However, this does not encompass the entire class area in the training database, as areas of disagreement or those resulting from the erosion method were excluded. The only variability introduced among the MSC variant classifications is the randomness in feature sampling during the search for the best split at each node. The training database was partitioned using a test size ratio of 0.2, resulting in the allocation of 80% of the data for the training set and 20% for the testing set. Model performance is evaluated using OA computed from the test set, with the number of samples in the test set referred to as support. In our case, with 5,000 samples per class, this is approximately 1,000 samples or less

if the reference class is smaller. As an initial step in the study, we systematically explored different RF classification configurations by testing varying numbers of trees (100, 200, and 500) and random split variables (2, 3, or 5) to optimize performance. Models using 100 trees and 2 random split variables consistently achieved satisfactory OA, exceeding 80% across all sites, and were consequently implemented.

4.3.3 Uncertainty in the classification scheme

The retrieval of LC map uncertainty follows the steps illustrated in Figure 4.6.

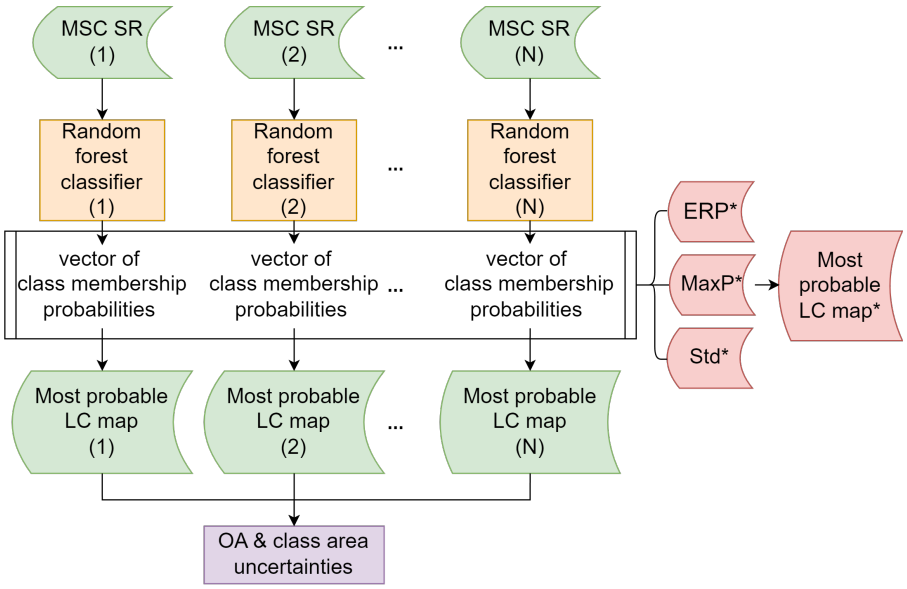

Figure 4.6: Uncertainty retrieval at the classification stage. Variability in OA and class areas among variants serve as non-spatially explicit uncertainty indicators. Pixel-wise uncertainty indicators (ERP*, MaxP*, and Std*) are derived from the mean class membership probability vector of the ensemble. The most probable LC map in the ensemble is derived from MaxP*.

The preprocessing generated a set of N MSCs for each pixel, represented as $MSC_{ij}^{n} \quad (n = 1,\ldots,N)$. For each pixel in each MSC, MSC_{ij}^{n}, the RF classifier produces a vector of class membership probabilities where k denotes the class index in the vector $(k = 1,\ldots,K)$ (Loosvelt et al., 2012). These probabilities are determined by the proportion of trees assigning each class to the total number of trees in the classifier (here: 100 trees).

$$\mathbf{p}_{ij}^{n} = \begin{pmatrix} p_{ij,1}^{n} & \cdots & p_{ij,k}^{n} & \cdots & p_{ij,K}^{n} \end{pmatrix} \qquad n = 1,\ldots,N; \quad k = 1,\ldots,K \tag{4.1}$$

$$\sum_{k=1}^{K} p_{ij,k}^{n} = 1 \qquad n = 1,\ldots,N$$

Selecting the class k_{ij}^{*} corresponding to the maximum probability in the vector of class membership probabilities $\mathbf{p}_{ij}$ makes it straightforward to derive the most probable LC map per MSC variant.

$$p_{ij,k^{*}}^{n} = \max_{k=1,\ldots,K} p_{ij,k}^{n} \tag{4.2}$$

From this information, both non-spatially and spatially explicit indicators of LC categorical uncertainty can be derived.

Non-spatially explicit LC maps uncertainty

Map accuracy and precise class area estimation are of critical concern for users. To address this, we propose two non-spatial uncertainty indicators: the average OA with its standard deviation, and the coefficient of variation for class surfaces, which highlights variation among ensemble members relative to the average class area.

RF contribution to uncertainty

The LC uncertainty is influenced by variations in both MSC variants and the RF model and its parameters. We hypothesized that the training dataset had minimal impact, selecting a high number of training samples per class, and applying the same training set to each MSC classification. To understand the specific contribution of the RF classifier, 30 RF classification repetitions were independently executed for each MSC variants, following the classification setup detailed in 4.3.2.

The uncertainty of the entire processing chain is computed as the standard deviation of the mean OA from 30 x 100 classifications (Figure 4.7). To isolate the contribution of the RF, we first calculate the mean OA for each RF ensemble, yielding one mean OA per MSC variant. The standard deviation of these 100 means represents the reduced uncertainty due to RF ensembling. By comparing this standard deviation to that of the entire processing chain, we quantify the variability introduced by the RF classifiers to the total uncertainty.

Pixel-wise LC uncertainty and ensemble most probable LC map

A vector of mean class membership probabilities is computed per pixel across the N MSC variants (Eq. 1.3). It indicates the likelihood of each class being the correct classification for each pixel. From it, two indicators of uncertainty are being considered per pixel (i, j): MaxP*, representing the maximum of

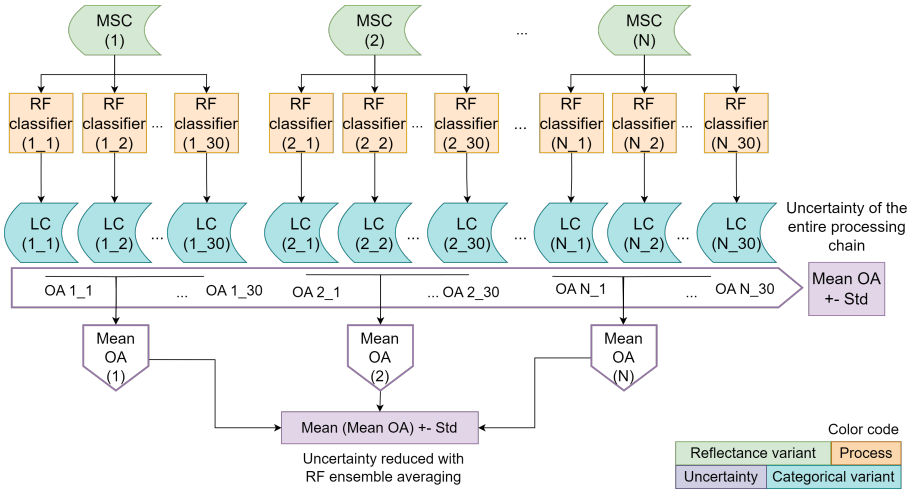

Figure 4.7: Quantification of the RF classifier contribution to the LC accuracy calculated from 30 repeated classifications per MSC variant.

the mean probability vector, and the ERP* (Bogaert et al., 2017). Selecting the class k^*_{ij} corresponding to the maximum mean probability in this vector (MaxP*, $\hat{\mathbf{p}}_{ij}$) directly yields the most probable LC map of the ensemble, referred to as LC map*. The associated standard deviation is also computed (Std*).

$$\hat{p}_{ij,k} = \frac{1}{N}\sum_{n=1}^{N} p^n_{ij,k} \quad k = 1,\ldots,K \tag{4.3}$$

$$\sum_{k=1}^{K} \hat{p}_{ij,k} = 1$$

$$\sigma_{ij,k} = \sqrt{\frac{1}{N}\sum_{n=1}^{N}\left(p^n_{ij,k} - \hat{p}_{ij,k}\right)^2} \quad k = 1,\ldots,K \tag{4.4}$$

$$\hat{p}_{ij,k^*} = \max_{k=1,\ldots,K} \hat{p}_{ij,k} \tag{4.5}$$

To provide additional insights beyond MaxP*, the ERP* was also computed as it combines the probability distribution across the entire vector of class membership into a single synthetic value (see Eq. 22 and 12 in Bogaert et al. (2017), with $E[D(k\|k^*)]$ being the expected difference of information when observing a class k being different of the most probable class $k*$). The ERP ranges from 0 to 1. Lower ERP values indicate higher uncertainty in the classifier's

assignment of LC labels. It is positively correlated with accuracy and provides a comprehensive representation of classification uncertainty (Waldner et al., 2017).

$$\begin{aligned} E[D(k\|k^*)]_{ij} &= \sum_{k=1;k\neq k^*}^{K} \left[\frac{\hat{p}_{ij,k}}{1-\hat{p}_{ij,k^*}} \ln\left(\frac{\hat{p}_{ij,k^*}}{\hat{p}_{ij,k}}\right)\right] \\ &= \ln\left(\hat{p}_{ij,k^*}\right) - \frac{1}{1-\hat{p}_{ij,k^*}} \sum_{k=1;k\neq k^*}^{K} \left(\hat{p}_{ij,k} \ln\left(\hat{p}_{ij,k}\right)\right) \end{aligned} \tag{4.6}$$

$$ERP^*_{ij} = \frac{exp\left(E[D(k\|k^*)]_{ij}\right)}{exp\left(E[D(k\|k^*)]_{ij}\right) + K - 1} \tag{4.7}$$

We investigate whether the LC map*, derived from averaging class membership probabilities across multiple MSC variants, effectively reduces classification uncertainty. We make the hypothesis that a successful LC map* should significantly decrease the proportion of mixed pixels. Previous research suggests that higher classification errors occur near textured areas or patch boundaries (Edwards and Lowell, 1996; Plourde and Congalton, 2003). Mixed pixels are common in fragmented landscapes where different LC coexist, indicating higher uncertainty (Canters, 1997). To test this, we use a connectivity index to assess local class homogeneity within a 3x3 pixel window, with values ranging from 1 (an isolated pixel) to 9 (a pixel surrounded by same-class pixels). Comparing this index across LC variants and in LC map* allows us to evaluate whether reductions in mixed pixels correlate with the effectiveness of the LC map* in reducing classification uncertainties. We use the index to estimate how sensitive pixel-wise LC uncertainty is to uncertainty.

4.4 Results and discussion

4.4.1 Seasonal compositing strategy impact on reflectance uncertainty

Figure 4.8(a) compares the relative standard uncertainties of the seasonal land surface reflectance for the 52-week MSC per site and band. Table C.1 in the Annex summarizes the ranges specifically. Longer wavelengths (560 nm, 665 nm, and 885 nm) exhibit lower relative standard uncertainty compared to the 490 nm waveband. This pattern persists across all sites and compositing periods (Figures 4.8(b) and 4.8(c)). The relative standard uncertainties of the seasonal land surface reflectance range from up to 11% in the blue (490 nm) to less than 1% in the NIR (885 nm). The highest uncertainty in the blue can be attributed to significant atmospheric interference in the visible spectrum, leading to less accurate atmospheric correction, especially in the blue (Vermote and Kotchenova, 2008b).

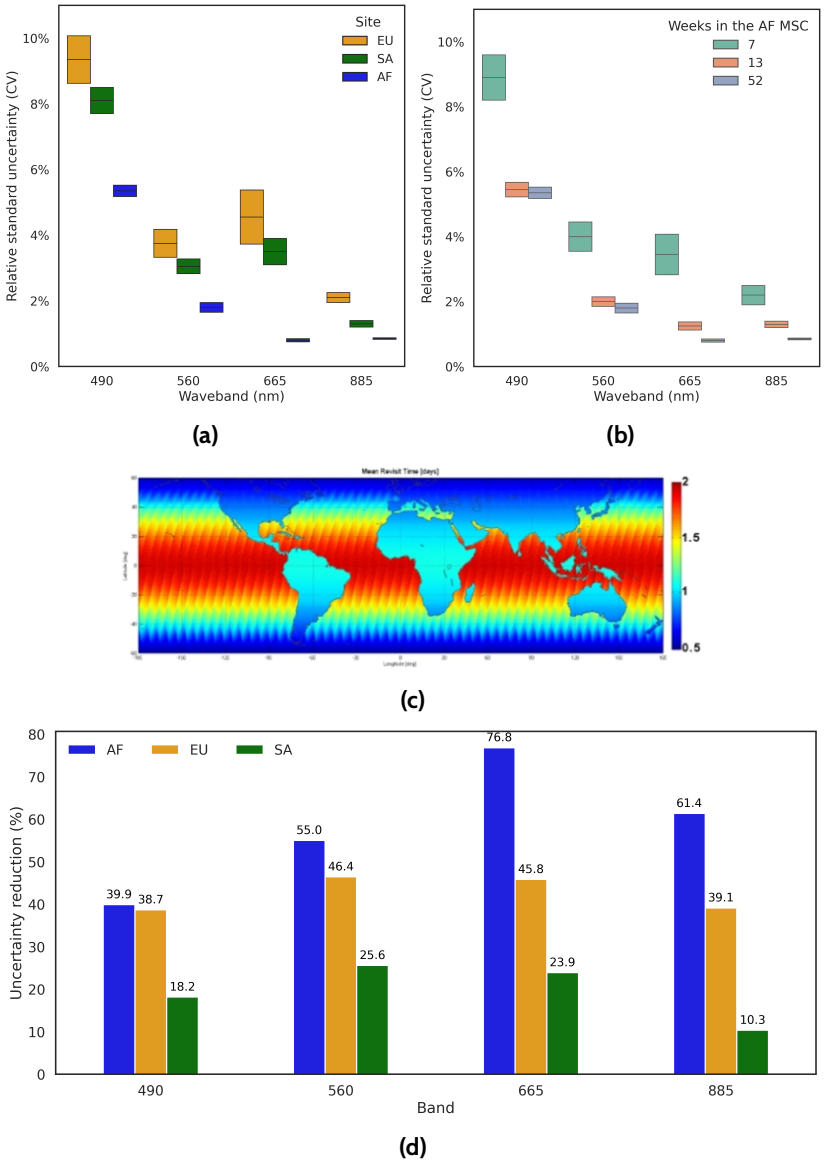

Figure 4.8: (a) Box plot depicting the relative uncertainty distribution of seasonal land surface reflectance across sites for the 52-week MSC duration. (b) Box plot of the relative uncertainty distribution of seasonal land surface reflectance across wavebands for Africa, according to the season duration (weeks). (c) OLCI mean revisit time with two satellites: 2 days at the equator (red) and less than 0.5 days at high latitudes (blue) (`https://sentinels.copernicus.eu/web/sentinel/user-guides/sentinel-3-olci`). (d) Bar plots expressing the reduction in uncertainty as a percentage, per band, as the composite period changes from 7 weeks for the Africa site and 13 weeks for the Europe and South America sites to 52 weeks.

The European site exhibits the highest relative standard uncertainties (CV%) across wavebands. This region also has the broadest interquartile ranges compared to Africa and South America. The variability in surface reflectance can be attributed to the maximum NDVI selection criterion during the mean compositing process. This criterion prioritizes Monte Carlo variants with higher NIR or lower red band reflectance when multiple spectra are available on a given day. The radiometric uncertainty in the NIR band, possibly amplified by the radiometric model, could increase the seasonal variance in surface reflectance (Quast et al., 2024 *in preparation*). This effect is more pronounced in regions where the selection criterion is frequently applied. This includes higher latitudes like Europe and to a lesser extent in South America (Figure 4.8(d)). In contrast, in Africa, the criterion is rarely applied due to the equatorial repeat cycles of OLCI-A and OLCI-B, which dictate the measurement frequency.

Figure 4.8(b) shows that, for the African site and all wavebands, there is a significant reduction in relative standard uncertainty when extending the compositing period from 7 weeks to longer periods (13 and 52 weeks). Extending the compositing period improves data reliability. It was indeed clear that increasing the number of valid and cloud-free observations using the mean compositing technique (Vancutsem et al., 2007) reduces uncorrelated random uncertainty. The reduction in uncertainty from 7 to 13 weeks is more pronounced than from 13 to 52 weeks. This pattern is evident across all wavebands, indicating that additional data beyond 13 weeks offers limited benefits in further reducing uncertainty. This residual uncertainty approaches correlated uncertainty as the number of observations increases in the mean. Figure 4.8(d) quantifies the average decrease in relative uncertainty in percent, per band, as the composite period transitions from 7 to 52 weeks (AF site) and 13 to 52 weeks (EU and SA sites).

4.4.2 Non-spatially-explicit LC uncertainty

The RF algorithm classified 100 MSC variants, with specifications detailed in Table 4.1, resulting in 100 LC maps for each site. From these maps, two non-spatial uncertainty indicators were quantified: the standard deviation of OA and the relative uncertainty of the class surfaces.

The RF model achieved OAs of approximately 80% for the EU and SA sites and up to 86% for the AF site, with standard deviations ranging from 0.33 (EU and AF sites) to 0.4% (SA site), as indicated in Table 4.2. Across sites, the RF classifier demonstrates consistent performance, as reflected in similar ranges for precision, recall, and F1-scores. The well-balanced precision and recall confirm that the variability in accuracy stems from a random pattern rather than systematic bias.

Tables C.2, C.3, and C.4 in Appendix C provide detailed accuracy metrics per site and LC class. Urban areas and water bodies often achieve F1-scores

above 94% due to their distinct spectral signatures. Urban materials and water exhibit unique spectral responses, allowing for high discrimination from natural and terrestrial classes, respectively (Herold et al., 2003; Gao, 1996). Contrary to initial expectations, there is no clear link between class accuracy and mosaic classes. While mosaic classes do not always exhibit the lowest F1-scores, the 'Mosaic tree and shrub (>50%) / herbaceous cover' class notably has the lowest F1-scores, specifically 55% in SA and 53% in EU sites, respectively. Conversely, the "Mosaic tree and shrub (50%) / herbaceous cover (50%)" class in the AF region achieves an F1-score of 86%, but with a higher variability (standard deviation of 0.05) due to its limited presence in the reference map, supported by fewer than 30 samples.

Table 4.2: Mean overall accuracy (percentage) computed from 100 land cover maps obtained for each study site using a RF applied on the 100 variants of mean seasonal composites. The standard deviation indicates the impact of the processing chain set-up of 100 classifications on land cover map uncertainty.

Site	OA (mean ± std)
EU	80.45 ± 0.33
AF	86.09 ± 0.33
SA	81.31 ± 0.40

We also assessed LC uncertainty using the class area coefficients of variation (CV). Factors contributing to class area uncertainty include the separability of spectral signatures compared to other classes, the definitions within the class legend, inherent class heterogeneity, spatial fragmentation, and class dominance within the area. To explore the impact of class fragmentation on uncertainty, we calculated an "edge density" indicator for each class, which quantifies the edge pixel surface relative to the overall class area. The average of these edge density indicators was computed per site and per class over the 100 LC map variants. The influence of class fragmentation on uncertainty varies significantly by site with a strong correlation in the AF site (R^2=0.85), moderate in the SA site (R^2=0.70), and a weak correlation in the EU site (R^2=0.39) (Figure 4.9(a)). In contrast, relative uncertainty is significantly influenced by low mean class dominance (below 5%)—the proportion of a class relative to the total site area (Figure 4.9(b)). Below this threshold, there is a sharp increase in the CV, reaching up to 27%. Diversity in CV for classes with similar dominance underscores the complexity introduced by multiple interconnected factors, such as the number of samples in the training set and discriminant spectral signatures. Further examination of class types confirms that legend descriptions have minimal impact on CVs, as evidenced by mosaic classes exhibiting similar CVs to other classes (see Figure 4.9(c)).

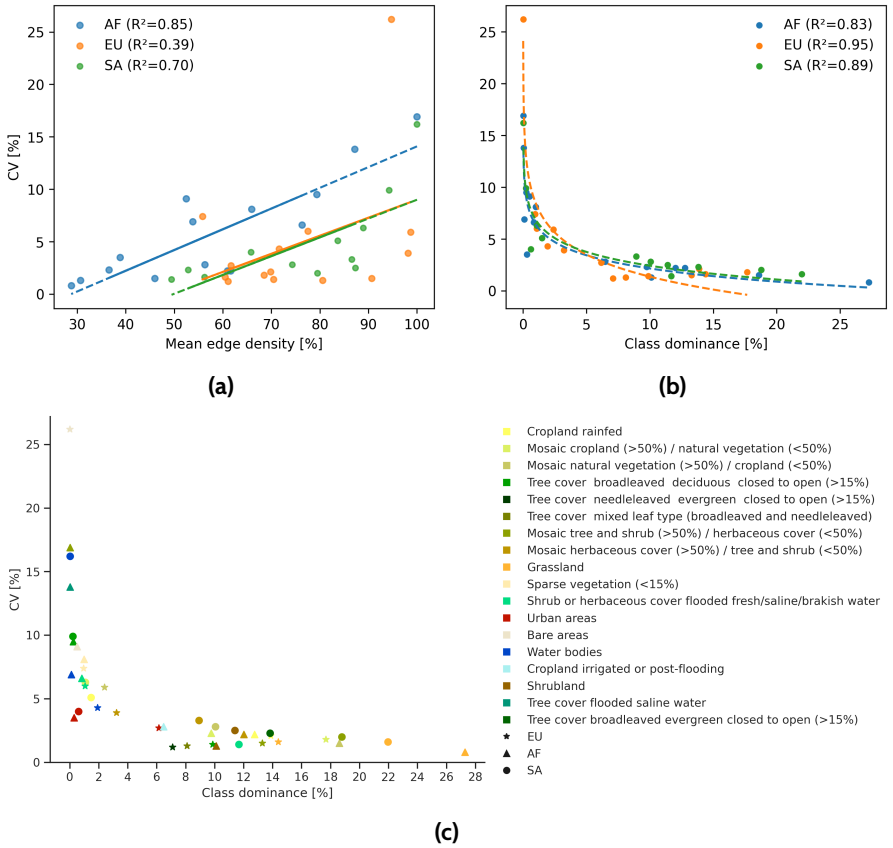

Figure 4.9: Per-site relationship between class area uncertainty (CV) and (a) the mean edge density per class, and (b) the class area dominance. (c) Relationship between class area uncertainty and class dominance per LC categories.

4.4.3 RF uncertainty contribution to LC map uncertainty

To assess the contribution of uncertainty stemming from the RF classifier, 30 repetitions of the RF process were conducted for each MSC variant. The RF setup, including the training set and hyperparameters (number of trees, number of split variables, etc.), is identical to that used in the previous experiment. The observed variability arises from the random selection of features and training data subsets, used to mitigate overfitting. The distributions obtained from the 3000 LC map OA are plotted in Figure 4.10(a), with the OA values and standard deviations summarized in Table 4.3. The two setups exhibit nearly identical performance in terms of accuracy and variability (Table 4.2 vs Table 4.3). The current setup of 3000 classifications primarily aims

to estimate the RF contribution to uncertainty, rather than to provide more precise accuracy estimates.

Table 4.3: Mean overall accuracy (percentage) computed from an ensemble of 30 RF applied on 100 land cover maps obtained for each study site using 100 variants of mean seasonal composites. The standard deviation indicates the impact of the entire processing chain made of 3000 classifications on land cover map uncertainty.

Site	OA (mean ± std)
EU	80.38 ± 0.33
AF	86.10 ± 0.31
SA	81.29 ± 0.39

Table 4.4 summarizes the mean OA and standard deviations computed from an ensemble of 30 RF applied on 100 land cover maps. Mitigating the variability of the RF contribution results in a significant reduction in standard deviations, almost by 3 for both the EU and AF sites (3 and 2.8 times, respectively) and by 2 for the SA site (Figure 4.10(b)). In other words, the random component inherent in the RF algorithm increases the uncertainty of the MSC alone by 200% for the EU and AF sites, and by 100% for the SA site.

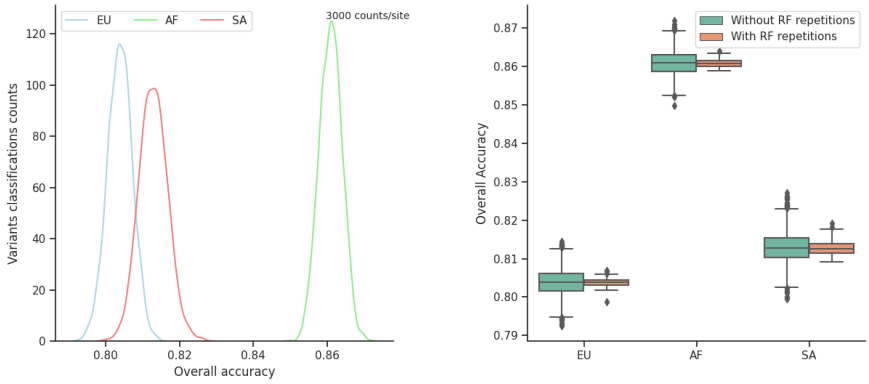

(a) **(b)**

Figure 4.10: (a) Probability density functions of OA per site, combining the Monte Carlo randomization process and RF contribution to uncertainty. Each distribution represents 100 x 30 classifications. (b) Box plot comparing OA with and without mitigating the RF contribution to uncertainty. The lower and upper boundaries of the box represent the 25th and 75th percentiles, respectively, with the line inside being the median. Error lines depict the 10th and 90th percentiles, while diamonds highlight data outside this range.

Table 4.4: Mean overall accuracy (percentage) computed from an ensemble of 30 RF applied on 100 land cover maps obtained for each study site using 100 variants of mean seasonal composites. The contribution of the RF random component to uncertainty is expressed in comparison to OA std across the entire processing chain (see Table 4.3).

Site	OA (mean ± std)	Reduction factor
EU	80.38 ± 0.11	3.0
AF	86.10 ± 0.11	2.8
SA	81.29 ± 0.20	2.0

4.4.4 LC map* and pixel-wise uncertainty indicators

The 100 LC map variants allow us to compute the average vector of class membership probabilities and derive the most probable LC map of the ensemble (LC map*) from the most probable class of the average vector of class membership probabilities. The 100 LC map variants allow us to compute the mean vector of class membership probabilities and derive the most probable LC map of the ensemble (LC map*) by selecting the most likely class from this mean vector. Additionally, three per-pixel indicators of uncertainty were derived from the mean vector of class membership probabilities: the maximum of the mean probability vector (MaxP*), its standard deviation (Std*), and the ERP* (Figure 4.11).

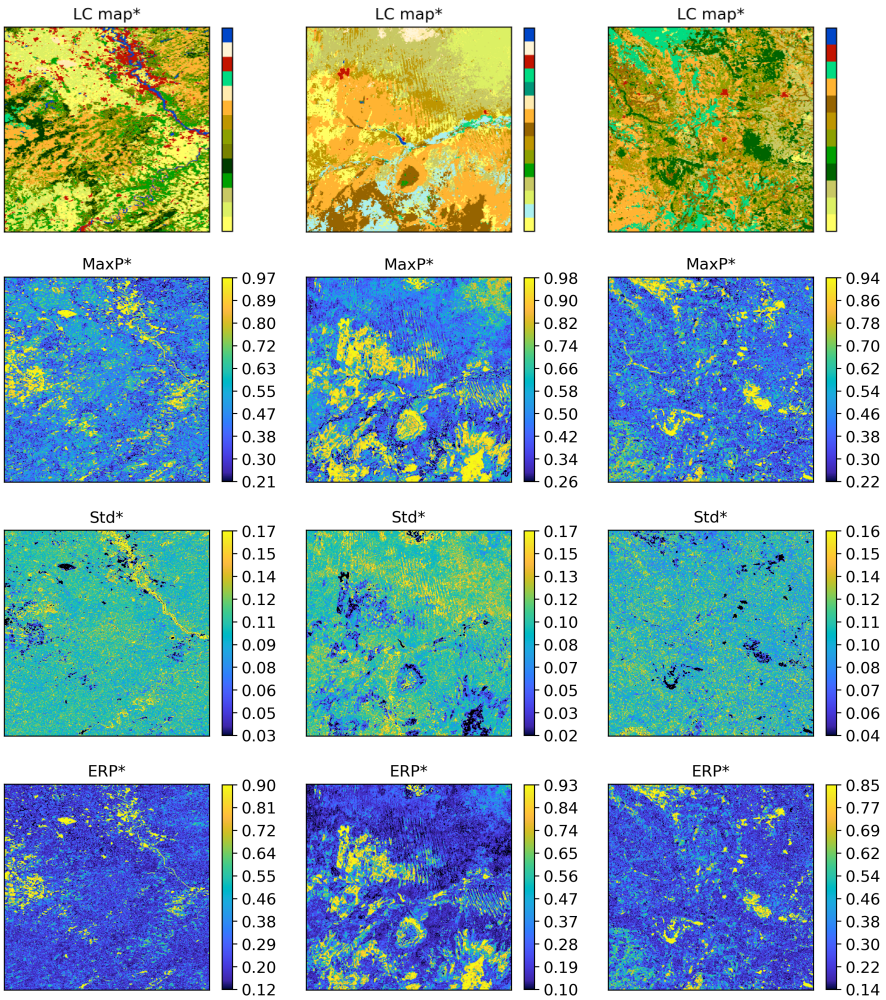

Figure 4.11: (a) EU, (b) AF, and (c) SA. From top to bottom: most probable LC map of the Monte Carlo ensemble (LC map*) determined by the LC class with the maximum probability (legend in Table A.3), the maximum probability (MaxP*), standard deviation (Std*), and the equivalent reference probability (ERP*). All variables are derived from the average vector of class membership probabilities of the Monte Carlo ensemble.

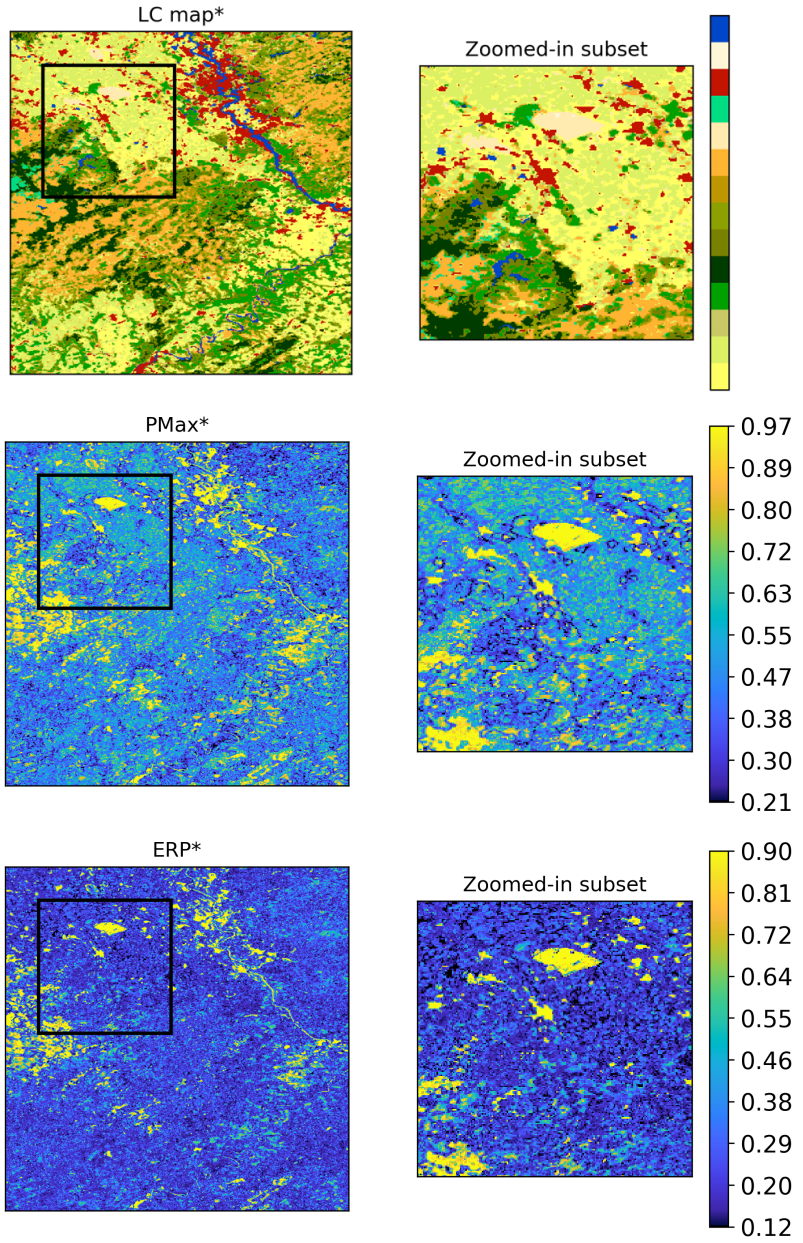

Figure 4.12: EU site. More detailed illustration of the spatially explicit uncertainty LC map*, MaxP*, and ERP* indicators.

LC map* depicts realistic and spatially consistent LC patterns, with minimal salt-and-pepper effects compared to other LC map variants (Figures 4.13(a)–4.13(b)). Consequently, there is no need to apply arbitrary spatial filtering to LC map*.

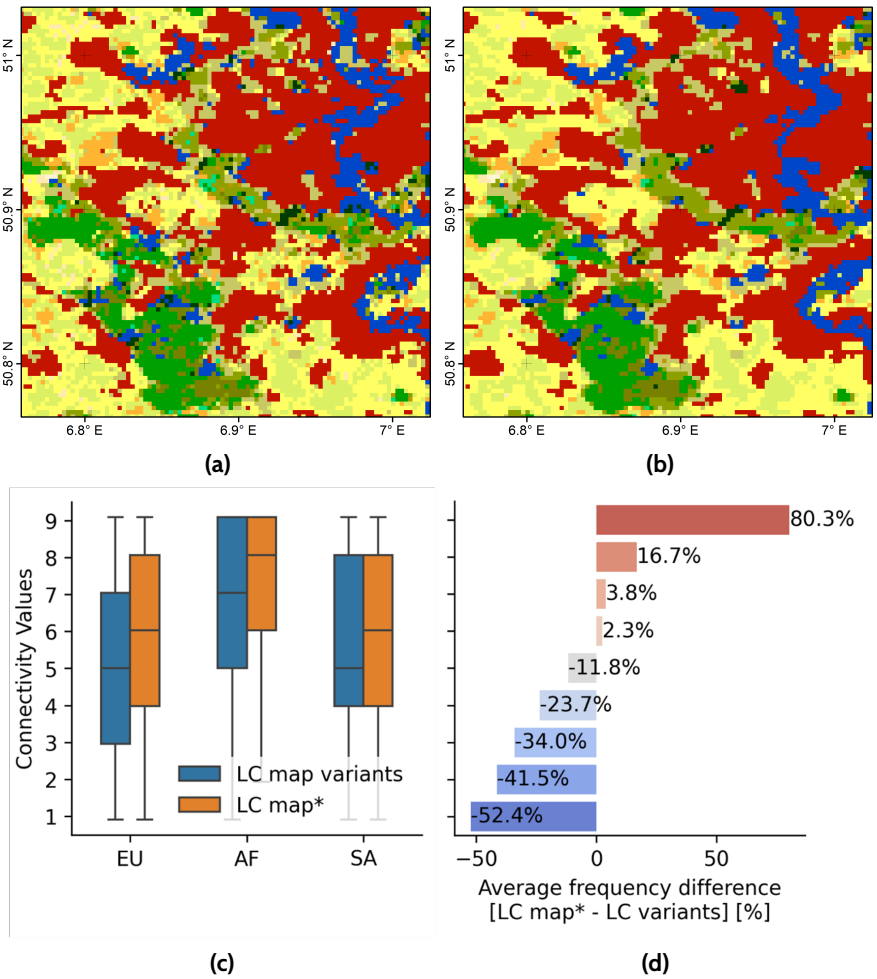

Figure 4.13: Zoomed-in section of the EU site illustrates (a) Salt-and-pepper effect of a randomly selected LC variant compared to (b) the more compact class patches in the LC map*. (c) Comparison of connectivity value distributions between LC map variants and LC map* across EU, AF, and SA sites. (d) Percentage difference in average frequency of connectivity values between LC map* and all variants across sites. Negative values indicate lower average frequency in LC map*.

Connectivity values, the number of similar pixel classes among the 3x3 pixel window, reveal that LC maps* systematically exhibit higher median connectivity compared to LC map variants, indicating greater spatial consistency and reduced classification uncertainty (Figure 4.13(c)). The index differs across the EU, AF, and SA regions. AF exhibits a higher degree of homogeneity compared to other sites, as evidenced by its higher median values. This homogeneity may contribute to the enhanced OA observed at this site, already presented in Table 4.4. The LC map* achieves a noteworthy reduction in uncertainty. Specifically, it results in an 80% increase in the frequency of contiguous and similarly classified pixels, along with a 52% reduction in the presence of isolated pixels, as shown in Figure 4.13(d). This confirms that the proposed methodology, which derives LC classification from mean probability vectors of class membership, effectively reduces the spatial impact of the classification uncertainty.

4.4.5 Pixel-wise uncertainty indicators

Areas with homogeneous LC patches, such as sparse vegetation, forests, and urban regions, exhibit high MaxP*, indicating high stability among variants (Figures 4.11 and 4.12, see Section C.3 in the Annex for similar illustrations on the AF and SA sites). MaxP* gradually decreases at LC patch edges, illustrating the decreasing uncertainty gradient towards border pixels. This is especially evident in linear landscape features like rivers. The central riverbed displays high certainty, as it predominantly consists of a single LC type—water. However, the banks exhibit lower MaxP*, confirming increased uncertainty when the recorded reflectance no longer corresponds to a pure or single LC type but instead reflects a mix of different LC types. Beyond the pixel size, the Point Spread Function (PSF) of the measurement instrument increases this uncertainty. The PSF spreads the recorded signal over several pixels, particularly affecting those near the edges of distinct LC types (Huang et al., 2002).
The cropland area displays intermediate MaxP*, with clusters showing both higher and lower values. This variation can be attributed to the diversity of crop type signatures, which collectively form the cropland class. This spatial consistency gives confidence in the reliability of the indicator to reflect the uncertainty of classification at the pixel level.
The ERP* behaves similarly to MaxP*, showing high values in stable areas of bare and urban (EU site), grassland and shrubland large patches (AF site), and dense evergreen forest (SA site).
Both ERP* and MaxP* indicate higher certainty with higher values. However, ERP* demonstrates a broader range of values and consistently remains lower than MaxP*. This behavior is expected due to the construction of ERP, where lower values prevail, influenced by the higher number of classes in the legend, typically ranging from 12 to 15 depending on the site.

Std* provides the degree of confidence in MaxP*, with lower values suggesting higher certainty in the selection of a LC class. It logically shows low values when MaxP* is high. However, Std* appears less useful because its low contrast indicates less sensitivity to variations in landscape patterns.
Figure 4.14 presents boxplots illustrating how the distributions of MaxP* and ERP* vary with edge pixels, as represented by the connectivity indicator. The decrease in MaxP* and ERP* values with lower connectivity (indicating more edge pixels) demonstrates their sensitivity to areas with higher uncertainty, confirming their effectiveness for uncertainty quantification. The Std* remains relatively constant across connectivity values and sites, appearing less informative.

Figure 4.15 compares the data distribution and variability of MaxP*, ERP*, and Std* across LC classes for the EU site, representative of all sites. Both indicators tend to show reduced values for mosaic classes, such as Mosaic natural vegetation with cropland, Natural mosaic with a majority of trees and shrubs, and Natural mosaic with a majority of grassland. This tendency highlights another interesting feature of these indicators for uncertainty quantification.

In the RF ensemble runs, a key challenge is establishing the minimum number of repetitions necessary to accurately estimate the overall accuracy, the class areas and pixel-wise uncertainty via Monte Carlo simulations. As the number of runs increases, the precision of estimates—such as the mean and variance—improves, as both estimators of uncertainty are inversely proportional to the number of realizations. To address this, an experimental approach would involve repeating the Monte Carlo method with an increasing number of iterations until the coefficient of variation of the measurand falls below a certain threshold or becomes stable.

4.4.6 Comparison against LC maps of majority

A common method for assessing uncertainty in LC classification is to identify the class with the highest frequency as the most likely and use this frequency as an uncertainty indicator. Santoro et al. (2015a) used this approach for mapping water bodies, which does not require calculating a class membership probability vector. This method has several advantages. It is computationally efficient, as processing time is reduced by only considering the class with the maximum probability for each variant. Additionally, storage demands are lower for categorical information compared to float data, such as class membership vectors.

While LC Map* and LC Map Maj show a 98% agreement for the EU site (see Table C.5 in Annex section C.3), a closer comparison reveals differences in uncertainty quantification. Figure 4.12 illustrates spatial uncertainty indicators from the mean class membership probability vector, while Figure 4.16 shows those from the map variant frequency. The focus is on the EU site, with consistent findings across other sites.

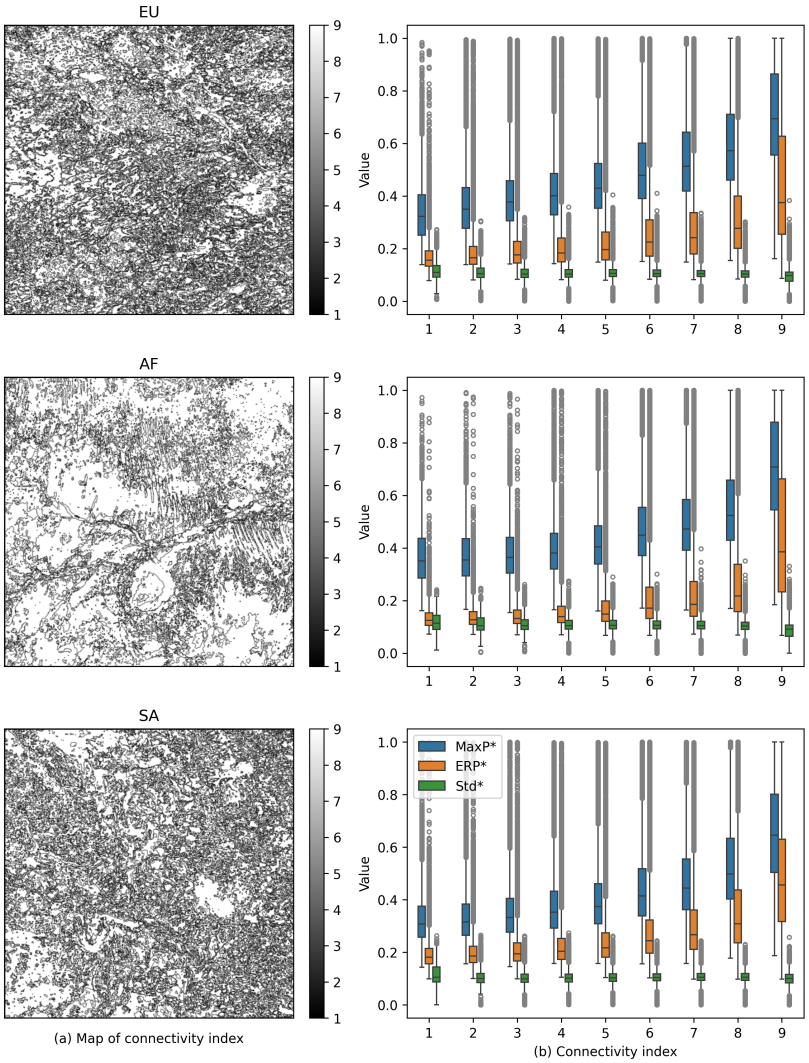

Figure 4.14: (a) Connectivity index maps per site, where a value of 1 denotes an isolated pixel of a class, while 9 indicates a pixel entirely surrounded by pixels of the same class. (b) Boxplot displaying the distribution of MaxP*, ERP* and Std* values per connectivity value.

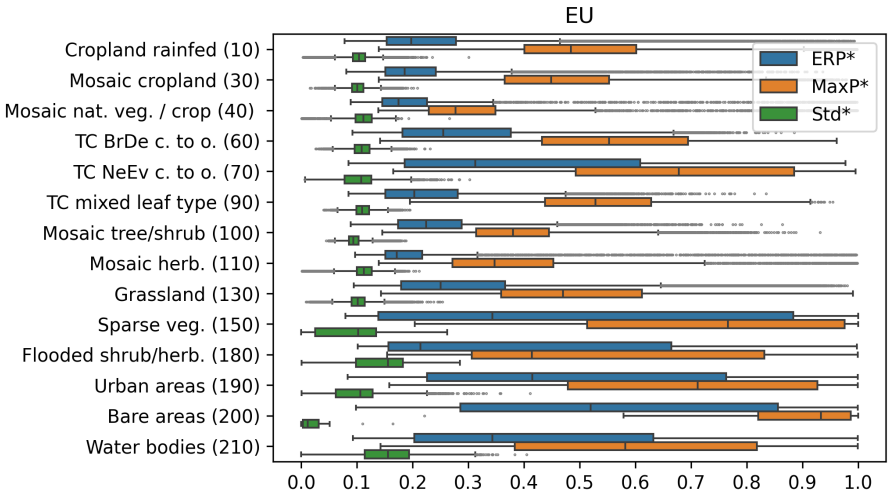

Figure 4.15: EU site. Distribution of ERP*, MaxP* and Std* indicators across LC classes. nat. veg.: natural vegetation, TC: tree cover, Br: broadleaved, De: deciduous, Ne: needleleaved, Ev: evergreen, c. to o.: close to open, herb.: herbaceous cover.

,

MaxFreq demonstrates a 20% narrower range and tends to saturate at higher values. Areas with a maximum frequency of 1 often coincide with those identified by MaxP*, but they appear more numerous and spatially dilated. This method also leads to a salt-and-pepper effect, characterized by sharp contrasts between adjacent pixels and within homogeneous class patches. This suggests that relying solely on the class frequency for uncertainty quantification may oversimplify the representation of complex landscapes and overlook subtle variations in pixel classification uncertainty.

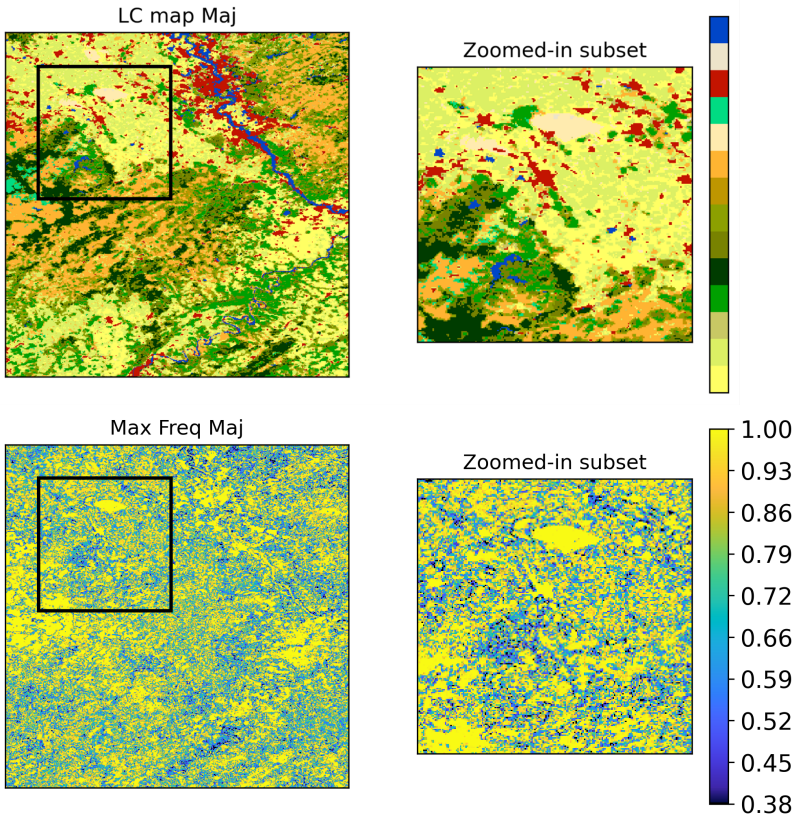

Figure 4.16: EU site. Illustration of a most probable LC map (top) derived from the maximum frequency of LC variants (bottom).

4.5 Conclusions

Uncertainty quantification in categorical variables, such as LC, poses significant challenges due to the lack of clear guidelines. This study extends previous research that introduced and propagated errors from radiances to mean seasonal composite variants using a Monte Carlo approach (Quast et al., 2024 *in preparation*). We investigated the impact of these errors on LC classification across three study sites.

We first demonstrated that increasing the mean compositing period from 13 to 52 weeks reduces SDR relative uncertainty by 10% to 46% at the EU and SA sites, and up to 77% at the AF site. However, using a maximum NDVI selection criterion when multiple observations are available on a single day, common at higher latitudes, counterbalances these positive effects. Therefore, we recommend treating all observations equally, regardless of the acquisition day, in the mean compositing process.

For applications requiring higher monitoring frequencies, such as crop type discrimination, compositing uncertainty can be reduced by implementing features like a weighted mean based on the temporal distance to the central date of the compositing period or weights related to AOD thickness and distance to clouds (ESA, 2024b). These findings emphasize the importance of the mean compositing technique in reducing uncertainty in surface reflectance data. They also highlight the critical need for operational satellite missions to achieve high revisit frequencies, ensuring sufficient valid and cloud-free observations in the compositing period for accurate estimation of mean surface reflectance. This approach acknowledges the current limitations of atmospheric and Bidirectional Reflectance Distribution Function (BRDF) correction models.

When we classified the 100 MSC variants with an RF model, we found that processing uncertainty had a minimal impact on the relative uncertainty (CV) of class surfaces, remaining below 3% for classes covering over 5% of the total site area. Mosaic classes did not show higher uncertainty levels. However, in small classes with inadequate representation in the training dataset, surface relative uncertainty could reach up to 27%. This implies that insufficient sample sizes in the training data contribute more to uncertainty than processing chain uncertainty.

The whole processing chain uncertainty (OA standard deviation from 30 RF x 100 MSC variants) ranges from 0.31% to 0.39%, depending on the site. Errors had minimal impact on uncertainty, largely thanks to the mean compositing technique and likely due the RF classifier's adaptability to noise. We showed that mitigating the RF classifier uncertainty reduced uncertainty at the SA site by 2 and by 3 at the EU and AF sites. Conducting an ensemble of RF classifier runs per variant is thus highly recommended to reduce uncertainty.

LC Map*, derived from the most probable class of a mean vector of class membership probabilities, effectively reduces uncertainty by improving the compactness of landscape patches, achieving a 52% reduction in isolated pixels.

We proposed three key indicators of pixel-wise uncertainty derived from the mean class membership probability vector: the maximum mean probability (MaxP*), its standard deviation (Std*), and the mean Equivalent Reference Probability (ERP*). They were evaluated against mixed pixels, representing local heterogeneity and thus uncertainty, and against various LC classes. While Std* showed low information content, MaxP*, ERP* demonstrated high sensitivity to mixed pixels and lower values in mosaic classes, making them well-suited indicators for pixel-level uncertainty assessment. Relying solely on the class frequency for uncertainty quantification, as based on visual inspection, may oversimplify the representation of complex landscapes and overlook subtle variations in pixel classification uncertainty.

To establish an overall uncertainty budget, all errors in the classification process contributing to uncertainty should be considered. For instance, the impact of reference uncertainty on classification could be explored by generating reference variants through random permutation of some reference pixels, with the magnitude determined by reported map accuracy. Alternatively, sampling the training set proportional to class area, instead of uniform sampling per class as implemented here, could be tested.

This thorough investigation into the sources of uncertainty in producing categorical maps, like LC from EO measurements, not only paves the way for accurate uncertainty quantification but also reveals that the widely-used RF classifier is a significant contributor to this uncertainty. Using classification ensembles and deriving maps from the most probable class in a mean vector of class membership probabilities could significantly reduce uncertainty in LC mapping.

Conclusions and perspectives

Summary of the principal contributions

Long-term, accurate, and consistent Essential Climate Variable data records, including land cover and land cover change map series, are crucial for monitoring and understanding land cover transitions, which are influenced by climate change and, in turn, impact the physical climate system. The ESA Climate Change Initiative Land Cover provides global, annual, consistent land use and land cover change data spanning up to 29 years at 300 m resolution, with a detailed legend. This series, created using data from five different satellite streams, offers a unique opportunity for comprehensive, data-driven land accounting over a long period, enabling detailed quantification of global land cover dynamics for the first time.

However, despite these significant advancements in global land cover mapping, the improvements are not systematically reflected in the land cover information used as input in climate models. Several intermediate steps, such as converting land cover classifications to types compatible with climate models, are needed to make the data ready for use, thereby introducing uncertainty.

In this regard, the numerous EO-derived products could be instrumental in reducing this uncertainty. However, their considerable number has created the challenge of determining their accuracy and highlighted the need for better methods to compare and select among them. While international guidelines for validating individual products are well-established, they have yet to address map product benchmarking specifically.

Uncertainty quantification therefore appears as a critical aspect in the processing of EO data into useful land cover observations. Yet, proper uncertainty is not systematically provided with reflectance data, and error propagation in the processing chain is traditionally ignored. Currently, there is no clear guideline for categorical uncertainty quantification for land cover.

The overall objective of this thesis was therefore to develop methods for globally refining land cover mapping consistently in time and characterize its associated uncertainty. It is achieved by taking advantage of multiple satellite

missions and integrating various Earth Observation products. This overarching objective was divided into four questions, which serve as the framework for this section. Following the principal contributions, potential directions for improvement are explored.

What do harmonized satellite data streams tell us about the global LC transformations over the past ~30 years?

Chapter 1 provided a multifaceted view of how our planet is experiencing land use land cover change. It highlighted the importance of using annual time steps in pixel-based observation approaches for monitoring land cover change, compared to inventory-based reporting.

The 300-meter spatially explicit CCI LC dataset with the original legend converted to the six IPCC Agriculture, Forestry, and Other Land Uses categories reveals that over 5.88% (7.78 Mkm² over 29 years) of the global ice-free land surface experienced land cover change once between 1992 and 2020. Additionally, 0.47% of the global ice-free land surface experienced more than one change during the same period, bringing the cumulative land change to 6.35% (8.4 Mkm²).

This rate is three times more dynamic than the net change suggested by global-scale national statistics. Indeed, the annual time step of the ESA CCI LC provides access to the gross rate of land cover change by quantifying swap changes that would otherwise remain hidden. In contrast, comparing the CCI maps from 1992 to 2020 globally reveals a net change of only 2.18% (2.88 Mkm²) of the global ice-free land surface. The disparity between the gross (0.22%/year) and net (0.075%/year) annual average land use land cover change rates emphasizes the dynamic nature of land cover transitions.

The quantification of the main change patterns per land cover category showed that land cover change is predominantly anthropogenic, illustrated by significant expansions in croplands, settlements, and grasslands. Agriculture and urban expansion are the main drivers, with urban areas more than doubling (133% increase). Urban growth accounts for 23% of cropland loss. Despite a modest net increase of 2.56% in agricultural areas since 1992, the agricultural landscape is highly dynamic, with 14% of the 1992 agricultural area having changed. In particular, 60% of the cropland loss and gains are actually due to swapping with forest.

On the other hand, 7% of semi-natural land cover categories have been affected by change. Among these, 6% of the global forest area experienced land cover changes during this period, with 60% of the loss due to agricultural conversion. Wetlands have shrunk by 4% since 1992, 85% of them due to conversion into forests. High swapping rates (above 75%) indicate a failure to preserve the biological diversity and resilience of these natural ecosystems. Forests and wetlands are particularly affected, as they need persistence over

time for their development and sustainability. Finally, bare areas are the most stable category, with 96% of their 1992 area remaining unchanged. The water category shows a very balanced dynamic over the entire period, with a relative net change close to 0 (0.39%), and a slight expansion likely reflecting dam constructions.

The analysis of spatial distribution revealed that 40% of land cover change occurred in Asia, 20% each in South America and Africa, and the remaining 20% in the rest of the world. Indonesia showed the simplest transitions, mainly between forest and cropland while South Africa and China were significantly impacted by urban expansion. In Central Asia, water is dramatically converted to bare soil due to the Aral Sea water being used for irrigation.

The study concludes by quantifying the impact of biodiversity conservation on land cover change rates over the last three decades. Protected areas, now covering over 14% of terrestrial land, have significantly reduced anthropogenic land cover conversions. The legal protection status of these areas has halved such conversions by 2020, indicating effective mitigation of human-induced changes.

How to evaluate and compare the performance of existing similar LC products, enabling better-informed product selection?

To account for the diversity of datasets mapping the same class, the chapter introduced stratified sampling based on areas of classification agreement and disagreement between maps (land agreement, water agreement, and error-prone strata). This method enables the comparison and selection of the optimal binary product, in line with validation guidelines that recommend stratified random sampling. This confidence-based design was tested in a case study comparing four land/water masks.

Considering the 2110 samples across all strata, all products showed very high overall accuracies (from 98% to 100%) due to the dominance of the land class globally compared to the marginal water class. However, focusing on error-prone areas revealed significant differences between products. Overall accuracy dropped to between 74% and 89%, compared to 98% to 99% in traditional sampling, and F1-scores ranged from 30% to 77%, compared to 71% to 89%.

Our analysis quantified how different sampling designs—random, class-based, or confidence-based—capture correctly and incorrectly classified pixels, impacting the precision of accuracy indices. With high overall accuracy (99%), random sampling schemes had a low probability of detecting incorrectly classified pixels. In contrast, confidence-based stratification improved producer accuracy estimation by increasing the probability (3.5%) of sampling water omission cases. Class-based stratified sampling, while sampling more in the marginal class (50%), reduced the probability of detecting water

omissions (0.1%). Confidence-based stratification increased the likelihood of sampling both types of classification errors, with the distribution of samples in water omission and commission cases dependent on the datasets used for stratification.

The proposed confidence-based stratified sampling method thus improves the reliability and representativeness of data sampling. Unlike traditional benchmarking approaches that solely compare products, this method incorporates reference data, enabling the identification of the optimal product.

This study also led to the compilation of a new global land mask, differentiating between inland water and oceans. The benchmarking approach was tested on this new product which was adopted within the CCI programme.

How can we provide a spatially explicit quantification of PFT compositions using harmonized datasets at multiple scales?

In Chapter 3, we created annual global maps of 14 Plant Functional Types (PFTs) at a 300-meter resolution for 1992-2020. Our objective was to refine the generic global PFT composition defined by a cross-walking table for each climate model to a spatially explicit quantification of PFTs at this fine scale.

By harmonizing independent high spatial resolution datasets at the 300 m scale and utilizing the seasonality and leaf type information from the LC map dataset presented in Chapter 1, we successfully generated detailed annual maps describing the percentage cover (0-100%) of 14 PFTs: broadleaved evergreen trees, broadleaved deciduous trees, needleleaved evergreen trees, needleleaved deciduous trees, broadleaved evergreen shrubs, broadleaved deciduous shrubs, needleleaved evergreen shrubs, needleleaved deciduous shrubs, natural grasses, herbaceous cropland (i.e., managed grasses), built, water, bare areas, and snow and ice. This dataset revealed a significant variability of PFT distributions for a given LC class across the regions.

Maintaining the synergies between the datasets developed in Chapter 1 and the PFT work in Chapter 3 was the cornerstone of the harmonization approach. The quantitative assessment of PFT fractions helped us view the LC classes defined broadly in the previous chapter with a more detailed landscape composition. This level of detail proved valuable for classes known to introduce uncertainty in land surface and Earth system models, such as the LCCS-based mosaic classes. For non-mosaic classes, we now have a more detailed understanding of the landscape composition, such as the fraction of trees in cropland areas, which can indicate the agriculture intensification level as purely agricultural classes tend to be less natural. Additionally, we explored the diversity of PFT composition in urban areas, considering the fractions of built areas, trees, water, and grass. This valuable information is highly relevant for climate change mitigation and adaptation, as the presence of trees in cities is known to mitigate temperatures by reducing the urban heat island effect.

Although the PFT fraction was explicitly derived for the year 2010, we exploited the temporal dimension of the LC map series to estimate PFT proportions in areas where LC changes were identified.

However, this study has limitations. The PFT dataset lacks information on the spatial distribution of landscape features within 300 m pixels, which significantly affects land surface parameters like roughness. Another consideration is that when a LCC occurs at the 300 m pixel level in the categorical maps, the pixel adopts the PFT fractions of the surrounding pixels with the class corresponding to the post-change class. This lacks the details needed to accurately reflect a change in proportions.

On the estimation of LC categorical uncertainty

In the absence of established guidelines on retrieving categorical LC uncertainty, Chapter 4 explored the impact of errors within an EO observation preprocessing chain on LC maps. This study builds on previous work where Monte Carlo simulations were used to propagate preprocessing errors into a series of 100 mean seasonal composite variants.

The mean compositing technique proved successful in reducing the surface directional reflectance relative uncertainty by 10 to 77%, depending on the study site, with the compositing period extending from 13 to 52 weeks. However, this positive effect is mitigated by the use of an NDVI selection criterion when multiple observations are available on a single day, a situation common at higher latitudes.

The set-up of 100 land cover classifications shows that LC maps can be mapped with a mean OA of ~80% (EU, SA) and up to 86% (AF). OA uncertainty remains low, ranging between 0.3% (EU, AF) and 0.4% (SA), indicating the minimal impact of processing uncertainty. Class surface uncertainty is generally low, below 5%, but can exceed 15% for poorly characterized classes with low support, i.e. the number of actual occurrences of the class in the training set.

The proposed methodology, which derives LC map*, the most probable map of the ensemble from mean probability vectors, effectively reduces the spatial impact of classification uncertainty. Using LC map* results in an 80% increase in the frequency of contiguous and similarly classified pixels, along with a 52% reduction in the presence of isolated pixels.

The values of pixel-wise uncertainty indicators, MaxP* and ERP*, decrease as the number of edge pixels increases in LC map*, reflecting higher uncertainty. The sensitivity of MaxP* and ERP* to areas with higher uncertainty is confirmed, while Std* remains relatively constant and appears less informative across different connectivity values and sites. Both MaxP* and ERP* indicators reflect higher uncertainties for mosaic classes, highlighting their effectiveness for uncertainty quantification.

The uncertainty was also quantified for the 3000 classification set-up of the 30 RF models applied to 100 variants of mean seasonal composites. The uncertainty of the entire processing chain was estimated to range between 0.33 and 0.39. This setup exhibits nearly identical performance in terms of accuracy and variability as the set-up of 100 land cover classifications. The uncertainty reduction with RF ensemble averaging indicates that the RF contributes to doubling or tripling the LC categorical uncertainty.

Perspectives

Opportunities to further reduce uncertainties in global LC mapping

Improvements in satellite technology, advanced classification algorithms, and enhanced data accessibility provide opportunities to improve global land cover class description and spatial resolution. This progress enables more accurate high-resolution assessment of terrestrial carbon budgets and land surface and carbon models, at a scale suitable for decision-making.

Ongoing initiatives for high-resolution LC and LCC mapping are still not globally available (ESA, 2024a), nor are they delivered at a 10 m spatial resolution (Potapov et al., 2022). However, the long-term data from Landsat (30 m resolution, 16-day revisit cycle) and Sentinel-2 (10 m resolution, 5-day revisit cycle) provide an opportunity to reassess our approach from Chapter 1. By decoupling stable LC mapping from LCC detection, we can generate a global long-term series of LC maps at a 10 m scale, with change detection at 30 m, ensuring consistency over time and space.

While 30 m pixels may not be pure (Friedl et al., 2022; Potapov et al., 2022), the 10 m scale is ideal for mapping individual LC elements and directly addresses mosaic and mixed-pixel issues discussed in Chapter 3 and Chapter 4. The commercial Planet constellation, with its 3-5 m resolution and daily coverage, offers an excellent reference for photo interpretation, training, and validation, even though it is not globally accessible. Additionally, Planet-derived products, for instance, capable of mapping individual trees (Skole et al., 2021; Brandt et al., 2024), would be valuable for training and comparison with the PFT map series.

The LC classification approach introduced in Chapter 1 combined ISODATA and maximum likelihood classifiers due to global data scarcity. However, these methods are now outdated. Non-parametric classifiers like Support Vector Machines (SVM), decision trees, and RF have proven to be more efficient and accurate (Thanh Noi and Kappas, 2017). Among these, RF is widely used for large-scale land cover classification (Belgiu and Drăgu, 2016).

The growing availability of data has led to increased interest in deep learning for LC classification and change detection (Zhang et al., 2016; Sefrin et al., 2020; Karra et al., 2021). Despite achieving high accuracy, deep learning

methods face challenges such as the "black-box" problem, which refers to their lack of interpretability, hindering broader adoption (Montavon et al., 2018; Campos-Taberner et al., 2020). Additionally, deep learning requires substantial training data and is computationally expensive (LeCun et al., 2018; Tyagi and Rekha, 2020).

LCC detection algorithms have also advanced with the availability of dense EO time series, particularly from Landsat data. Zhu (2017) highlight two widely-used per-pixel LCC algorithms worth investigating to improve the ESA CCI LC maps. BFAST/BFAST-Monitor can estimate the timing, magnitude, and direction of changes by detecting breaks in NDVI time series (Verbesselt et al., 2010, 2012). CCDC/COLD detects changes by identifying anomalies in multispectral Landsat time series (Zhu and Woodcock, 2014; Zhu et al., 2020). Both methods have been successfully applied across various LC classes (DeVries et al., 2015; Reiche et al., 2015; Fang et al., 2018; Chen et al., 2014). However, challenges remain in filtering detected perturbations that do not align with our LCC legend (see Chapter 1) and in accurately attributing post-change LC classes.

Exploiting synergies

Mapping LC and its dynamics at HR is facilitated by consistent EO data records with valid cloud-free observations over time. In Chapter 1, we ensured consistency by standardizing reflectance pre-processing across five sensor archives and decoupling stable area mapping from change detection. To deal with data scarcity, we used the mean compositing strategy and selected sensors with higher revisiting frequencies, although this meant sacrificing resolution for LCC detection. Beyond post-hoc consistency methods (Bogaert et al., 2022; Abercrombie and Friedl, 2016), satellite synergies offer a promising avenue for improving LC and LCC detection upstream of the processing chain. Virtual constellations of satellite sensors aim to overcome limitations in individual sensors' spatial, temporal, and spectral capabilities (Wulder et al., 2015). Multi-mission multispectral datasets, provided as Analysis Ready Data (ARD), are now accessible (Lewis et al., 2018; Siqueira et al., 2019). Harmonized or fused Landsat and Sentinel-2 data offer consistent near-daily reflectance observations at 30-m and 10-m resolutions (Claverie et al., 2018; Saunier et al., 2022). Additionally, sensor-agnostic, consistent 3 m spatial resolution time series can automatically generated in four spectral bands by integrating Sentinel-2, Landsat, and MODIS/VIIRS with Planet data (Planet, 2018).

Opportunities for synergies extend beyond surface reflectance levels. Chapter 3 introduced a 300-m pixel-wise representation of PFTs globally. This representation categorized PFTs based on life forms (e.g., tree, shrub) and traits such as leaf type (*broadleaved* vs. *needleleaved*) and plant phenol-

ogy (e.g., *evergreen* vs. *deciduous*, *annual* vs. *perennial*). However, to comprehensively address climate change impacts on carbon uptake and storage, PFT mapping should encompass a broader range of plant traits beyond categorical growth forms such as leaf nitrogen content, biomass, Leaf Area Index, and C3/C4 photosynthetic pathways. Moreno-Martínez et al. (2018) exploited machine learning techniques, MODIS and Landsat imagery along with measured trait and climate data, to produce high-resolution global maps of leaf traits. Integrating narrow-band hyperspectral data with high spatial and temporal multispectral data offers opportunities for large-scale plant traits mapping (Guanter et al., 2019). While historically limited by airborne sensors, recent spaceborne missions like EnMAP (Foerster et al., 2008) and PRISMA (Loizzo et al., 2018) now provide more regular and comprehensive hyperspectral data over larger areas (Transon et al., 2018). Upcoming ESA Biomass, dedicated to tracking forest structure change in biomass, and FLEX, providing fluorescence data, indicative of photosynthetic activity (Quegan et al., 2019; Coppo et al., 2017) will also be instrumental in reducing uncertainties beyond mapping LC category. In-situ data, available in quantity, quality, and appropriate scales of inference (König et al., 2019) offer opportunities for in-situ plant trait upscaling to larger scales but existing ones still lack completeness and representativeness (Kattge et al., 2020; Asner et al., 2003).

The big data era: challenges and opportunities

The availability of EO data from sources such as Landsat (Woodcock et al., 2008), Sentinel collections (EU Directive No 1159/2013), and Planet (through Norway's international climate and forest initiative) has significantly boosted the development of standardized products, such as global LC mapping (Wulder et al., 2012). These advancements led to the creation of long-term, single-class maps at 30 meters resolution (Pekel et al., 2016; Hansen et al., 2013a; Pesaresi et al., 2016; Esch et al., 2017), as well as multi-class global LC map series at the same resolution (Friedl et al., 2022; Hansen et al., 2022; Potapov et al., 2022) and 10-meter single multi-class global LC maps (Karra et al., 2021; Zanaga et al., 2021, 2022; Brown et al., 2022).

In this era of big data, traditional on-site data storage and processing setups have become obsolete. The shift to online processing using Earth Observation Data Cubes (EODCs) has enhanced storage, organization, management, and interaction with analysis-ready data (ARD) (Baumann et al., 2019; Dwyer et al., 2018). Platforms such as Google Earth Engine, Digital Earth Australia, and the Copernicus data space ecosystem exemplify innovative approaches to data interaction (Gorelick et al., 2017; Tamiminia et al., 2020; Dhu et al., 2017; Musial et al., 2024). For example, the ODC platform of Digital Earth Australia has been used to generate yearly LC maps and detect changes across Australia using Landsat and Sentinel-1/2 data (Lucas et al., 2019).

To maximize the potential of big data to improve our understanding of climate change and support action, the concept of Digital Twin Earth (DTE) has emerged. This dynamic digital replica of our planet aims at accurately mirroring Earth's behavior, seamlessly integrating EO data, in-situ measurements, and artificial intelligence. DTE will enable us to monitor past and present Earth system states, predict their evolution, and assess potential outcomes under different scenarios.

The "V" quintet—Volume (exceeding petabyte scale since 2019), Variety (diverse data types), Velocity (rapid data processing), Veracity (precise data uncertainty management), and Value (extracting valuable insights)—summarizes the challenges and opportunities of EO big data (Guo et al., 2017). To effectively manage these challenges, FAIR principles have emerged as a guiding framework, promoting data Findability, Accessibility, Interoperability, and Reuse (Jacobsen et al., 2020).

While the enthusiasm surrounding big data is understandable, uncertainty exists at every phase of big data processing, including problems of database scalability, the use of various data types (unstructured, incomplete or noisy data) and their conversion between formats. The growing complexity of processing chains complicates the retrieval of accuracy and trust in big data analytics (Hariri et al., 2019). In addition, it should not overshadow the importance of small data—experimental or intentionally collected human-scale studies focused on causation (Faraway and Augustin, 2018; Kattge et al., 2020). An undisputable example is in-situ or reference data, which, although time-consuming and costly to acquire, is essential for ensuring data accuracy and therefore should receive adequate funding (Saha and Srivastava, 2014; Kattge et al., 2020).

Most importantly, it is essential to remember that scientists have recognized anthropogenic climate change unequivocally and have intensively studied it since the 1980s, well before the advent of big data. We now possess substantial evidence of its severe impacts and the necessary mitigation measures (Santos et al., 2022). The challenge is unmistakably clear: we must urgently turn the era of big data into an era of big action.

Chapter 5

Appendix

Appendices

A The CCI MR LC processing chain

A.1 Data

A multisensor archive

Level 1 (L1) EO data at 300 m to 1 km from five missions acquired between 1992 and 2020 underwent uniform processing treatments to mitigate inter-sensor discrepancies for subsequent land cover classifications.

AVHRR LTDR 1 km The National Oceanic and Atmospheric Administration (NOAA) advanced very high-resolution radiometer (AVHRR) provides extended global daily observations from 1981 to 2002, among which is the 1 km Long-Term Data Record (LTDR) v4 HRPT and LAC (1992-1999). We used the three available surface reflectances channels (Kiddwell, 1998).

ENVISAT - MERIS Full (300 m) and reduced (1 km) resolutions were acquired every five days for the 2003 - 2012 period. Level 1B data Top-Of-Atmosphere (TOA) radiances are provided in 15 channels with quality flags (Bicheron et al., 2011). The full archive of MERIS was used as input to the baseline classification.

SPOT VGT P. The Vegetation instruments 1 and 2 aboard SPOT 4 and 5 sensors extend global daily TOA acquisitions at 1 km from 1999 to 2013. Four surface reflectance channels (Blue, Red, NIR, and SWIR) are available with quality flags (Dierckx et al., 2015).

PROBA-V. The Project for On-Board Autonomy Vegetation (PROBA-V) was designed to be a gap-filler mission between SPOT-VGT and Sentinel-3. It shares similar spectral bands SPOT-VGT centred on the Blue, Red, NIR, and SWIR channels. All global TOA daily synthesis at 333 m and 1 km spatial resolutions were used from 2013 to 2019 (Dierckx et al., 2014).

Sentinel-3 OLCI. The SENTINEL-3 Ocean and Land Colour Instrument (OLCI) is based on the imaging design of the Envisat's MERIS instrument (`https://sentinel.esa.int/web/sentinel/missions/sentinel-3/instrument-payload/olci`). OLCI acquires data in 21 bands in the visible and near-infrared regions at spatial resolutions of approximately 300 m and 1.2 km. All L1b

TOA measurements (calibrated, ortho-geolocated and spatially re-gridded TOA radiances) were used at both spatial resolutions for 2020 and 2021.

Auxiliary data

A critical auxiliary dataset in the classification chain is a global reference LC layer. It is compiled at 20 m spatial resolution after preparatory transformations and according to specific merging rules from up to 52 existing regional and global land cover products selected for being the most accurate, thematically rich, up-to-date, and with a legend compatible with the LCCS of the FAO (Defourny et al., 2017b). This reference LC layer serves as a training and labelling layer in the supervised and unsupervised classification modules.

Prior to running the pre-processing and classification modules, the world is partitioned into 22 strata based on ecological and remote sensing criteria. The stratification serves two purposes: (1) reducing the variability in land surface reflectance within the dataset to enhance classification efficiency, and (2) enabling regional customization of algorithm parameters to account for regional landscape characteristics (e.g. vegetation seasonality and cloud coverage). Essentially, each module of the full processing chain is executed independently for each stratum using tailored parameters. This approach affords a high level of control and flexibility in achieving a globally valid classification process that addresses the regional heterogeneity of land cover characteristics.

A.2 Pre-processing: from L1b to seasonal composites

A key asset in fostering the spatiotemporal consistency of the final LC maps lies in designing a standard automated pre-processing chain that converts L1b images to seasonal composites. The pre-processing chain includes the following steps: (1) a geometric correction aimed at ensuring sufficient geolocation, (2) spectral and radiometric corrections, (3) a pixel state identification and cloud screening, (4) atmospheric and BRDF corrections, and (5) tile formatting to standard global projected 7-day surface reflectance composites.

The geometric correction aimed at ensuring that the geolocation accuracy remains better than 70 Root Mean Square (RMS). The ESA Accurate MERIS Ortho Rectified Geo-location Operational Software v4.0 (AMORGOS) was applied to improve MERIS FR geolocation and alignment with the MERIS RR. The AVHRR HRPT L1b relative pixel geolocation accuracy at the nadir was estimated to be ± one pixel in flat areas. Substantial deviations were detected in regions with mountainous terrain and off-nadir imaging, resulting in the removal of approximately 700 edge pixels on either side of the swath. Despite this precaution, the geometric accuracy failed to meet the original geolocation criteria. The geometric correction was not applied to SPOT VGT P, PROBA-V and S3-OLCI data because they met the geometric accuracy requirements.

The MERIS spectral and radiometric L1b calibrations achieved accuracies of 0.1 nm and 0.2 nm, respectively. A radiometric equalization reduced detector-to-detector and camera-to-camera systematic radiometric differences of the MERIS the L1b products. Minor variations of the spectral wavelength of each image pixel called the "smile effect", were also corrected. The spectral and radiometric calibration provided by data suppliers were applied to SPOT-VGT and PROBA-V. A spectral correction function retrieved equivalent SPOT VGT P measurements to apply similar PROBA-V and SPOT-VGT P processing chains (Dierckx et al., 2015). AVHRR was calibrated in the visible and infrared channels after (Kiddwell, 1998). The consistency of TOA reflectance values of AVHRR, SPOT-VGT P and MERIS RR has been assessed over the CEOS Land-Net sites and other stable areas (Ph1 PVASRv2.0, 2012). Anomalous AVHRR products were discarded.

Pixel states must be distinguished because particular processing steps are associated with each surface type. The IdePix framework was applied to identify pixel states among land, clear sky water, totally cloudy, snow/ice, and semi-transparent clouds. Pixel state classifications rely on decision trees, probabilistic combinations of calculated features or neural networks. This generic framework is easily transferrable among sensors as shown in (Lewis et al., 2013; Wevers et al., 2022b).

The atmospheric correction, including corrections for the absorption and scattering effects of atmospheric gases, air molecules (Rayleigh scattering), and aerosol particles, is detailed in (Defourny et al., 2017b). The resulting L3 top-of-canopy daily reflectances were finally composited to standard 7-day syntheses using the Mean Compositing technique (Vancutsem et al., 2007) as BRDF correction and compositing method. The final pre-processing steps consist of reprojecting to a Plate-Carrée grid and mosaicking tiles to global L3 products.

A.3 Land cover and land cover change legends

Table A.1: Types of LCC detected at 1km. Note that changes in the settlement class are detected in a separate processing chain.

Change Type	Description
Forest Loss	To crops, shrubs, grasses, sparse vegetation, wetlands and bare areas
Forest Gain	From crops, shrubs, grasses, sparse vegetation, wetlands and bare areas
Cropland Loss	To crops classes to grasses, sparse vegetation and bare areas
Cropland Gain	From grasses, sparse vegetation and bare areas
Grassland Loss	To sparse vegetation and bare areas, and from sparse vegetation to bare areas
Grassland Gain	From sparse vegetation and bare areas to grasses, and from bare areas to sparse vegetation
Shrubland Loss	From shrubs to crops, grasses, sparse vegetation and bare areas
Shrubland Gain	From crops, grasses, sparse vegetation and bare areas to shrub
Wetland Loss	To wetland to crops, grasses, shrubs, sparse vegetation and bare areas
Wetland Gain	From crops, grasses, shrubs, sparse vegetation and bare areas to wetland
Water Loss	To crops, forests, grasses, shrubs, sparse vegetation, wetland and bare areas
Water Gain	From crops, forests, grasses, shrubs, sparse vegetation, wetland and bare areas

Table A.3: LCCS legend of the CCI MR LC product

Code	Label	Color
10	Cropland, rainfed	
11	Herbaceous cover	
12	Tree or shrub cover	
20	Cropland, irrigated or post-flooding	
30	Mosaic cropland (>50%) / natural vegetation (tree, shrub, herbaceous cover) (<50%)	
40	Mosaic natural vegetation (tree, shrub, herbaceous cover) (>50%) / cropland (<50%)	
50	Tree cover, broadleaved, evergreen, closed to open (>15%)	
60	Tree cover, broadleaved, deciduous, closed to open (>15%)	
61	Tree cover, broadleaved, deciduous, closed (>40%)	
62	Tree cover, broadleaved, deciduous, open (15-40%)	
70	Tree cover, needleleaved, evergreen, closed to open (>15%)	
71	Tree cover, needleleaved, evergreen, closed (>40%)	
72	Tree cover, needleleaved, evergreen, open (15-40%)	
80	Tree cover, needleleaved, deciduous, closed to open (>15%)	
81	Tree cover, needleleaved, deciduous, closed (>40%)	
82	Tree cover, needleleaved, deciduous, open (15-40%)	
90	Tree cover, mixed leaf type (broadleaved and needleleaved)	
100	Mosaic tree and shrub (>50%) / herbaceous cover (<50%)	
110	Mosaic herbaceous cover (>50%) / tree and shrub (<50%)	
120	Shrubland	
121	Shrubland evergreen	
122	Shrubland deciduous	
130	Grassland	
140	Lichens and mosses	
150	Sparse vegetation (tree, shrub, herbaceous cover) (<15%)	
151	Sparse tree (<15%)	
152	Sparse shrub (<15%)	
153	Sparse herbaceous cover (<15%)	
160	Tree cover, flooded, fresh or brackish water	
170	Tree cover, flooded, saline water	
180	Shrub or herbaceous cover, flooded, fresh/saline/brackish water	
190	Urban areas	
200	Bare areas	
201	Consolidated bare areas	
202	Unconsolidated bare areas	
210	Water bodies	
220	Permanent snow and ice	

Table A.4: Correspondence between LCCS codes of the CCI LC class aggregation used to assess thematic discrepancies between the classifications of the seasonal composite ensemble mean and realizations. See table A.3 for the labels associated with the LCCS codes.

IPCC groups	LCCS codes	Color
Cropland	10–12, 20, 30, 40	
Forest	50, 60–62, 70–72, 80–82, 90, 100, 160, 170	
Grassland	110, 130	
Wetland	180	
Settlement	190	
Shrubland	120–122	
Lichens and mosses	140	
Sparse vegetation	150–153	
Bare areas	200–202	
Water	210	

B Complementary information about the CCI PFT dataset description

Tree fraction leaf type and leaf phenology

For a small number of pixels where the legend does not specify the leaf type and leaf phenology, and where there are no static pixels representing tree cover classes within the surrounding 2° by 2° window, a climatological approach is applied.

This approach uses three auxiliary inputs: (1) the present-day Köppen-Geiger climate zone map from Beck et al. (2018), downscaled from 1 km resolution to the 300 m CCI MR LC grid using mode resampling, (2) the map of world regions derived for use with the IMAGE03 model, expanded to include Greenland, Antarctica, and additional small islands, and (3) the landform map from Sayre (2014), resampled from 250 m resolution to the 300 m CCI MR LC grid using mode resampling. The nearest neighbour analysis is used to gap-fill missing data at 300 m resolution for each of the three auxiliary inputs. Pixels requiring data are those with < 100% water PFT cover in the PFT product. Pixels that are designated as surface water in the landform dataset and have < 100% water PFT cover in the PFT product are additionally filled with one of the terrestrial landforms (plains, hills, and mountains). Missing data generally occur along coastlines due to mismatches in the land-sea masks of the auxiliary datasets and the CCI MR LC data. The gap-filled datasets are combined to create a dataset of 1,531 unique combinations of landforms, regions, and climate zone. For each of the unique combinations, the areal cover of each of the tree cover classes with well-defined tree types (codes 50–82) is calculated using static pixels of those classes, and the majority of tree type by area is identified for each unique combination. There are very few static pixels of the type-defined tree cover classes in the Middle East and Sahara regions, so the dominant tree type in these regions is set as broadleaved deciduous. For pixels in which the tree type – broadleaved or needleleaved, deciduous or evergreen – cannot be assigned based on the neighbourhood window, the majority tree type of the pixel's unique zone is assigned. This method is also applied to assign the types of both shrubs and trees in all shrubland class pixels. Thus, there may be inconsistencies between the shrub type indicated by the class legend and that assigned using this biogeographical approach.

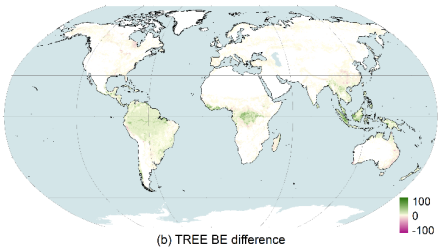

(a) Broadleaved evergreen trees difference

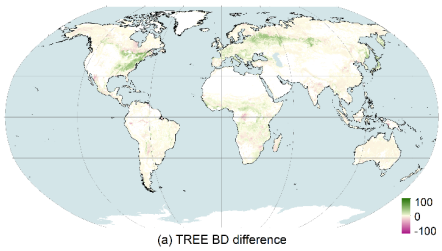

(b) Broadleaved deciduous trees difference

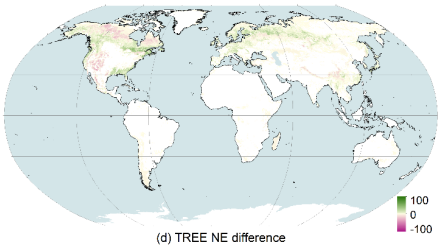

(c) needleleaved evergreen trees difference

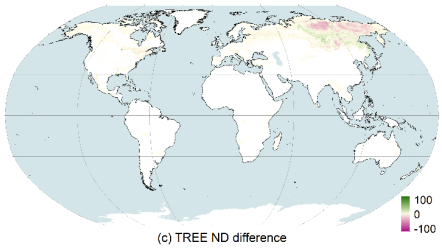

(d) needleleaved deciduous trees difference

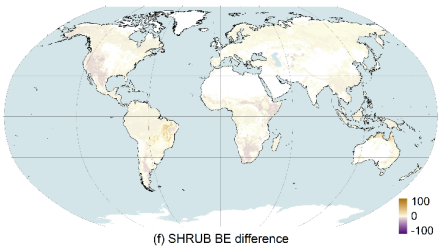

(e) Broadleaved evergreen shrubs difference

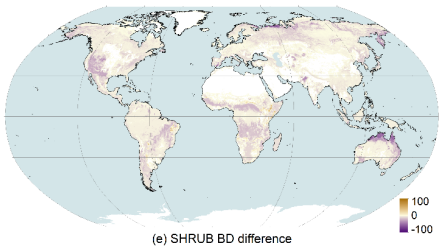

(f) Broadleaved deciduous shrubs difference

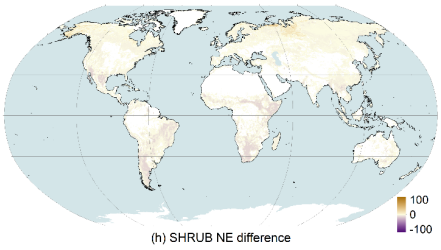

(g) needleleaved evergreen shrubs difference

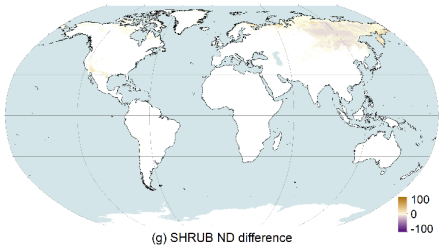

(h) needleleaved deciduous shrubs difference

Figure B.1: (a–h) Absolute differences (percentage of pixel) between the 2010 PFT_{local} dataset and corresponding PFT_{global} maps (i.e., applying the global cross-walking scheme) for the 14 PFT types. The spatial resolution is 0.25 x 0.25 degrees.

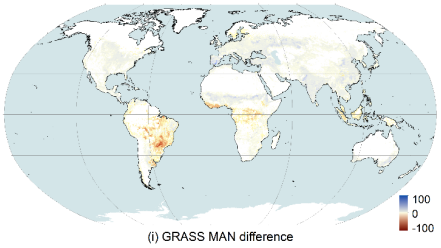

(i) Managed grasses difference

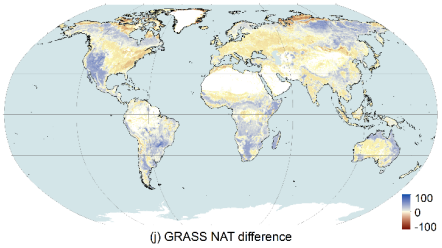

(j) Natural grasses difference

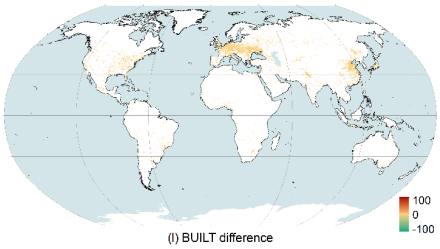

(k) Built-up areas difference

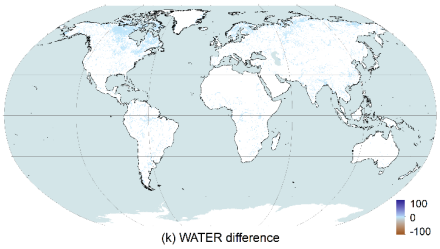

(l) Permanent inland water bodies difference

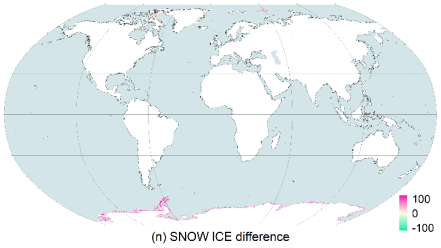

(m) Bare soil difference

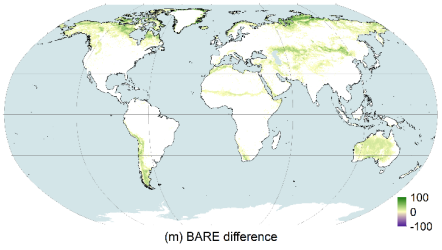

(n) Permanent snow and ice cover difference

Figure B.1: (a–h) Absolute differences (percentage of pixel) between the 2010 PFT$_{local}$ dataset and corresponding PFT$_{global}$ maps (i.e., applying the global cross-walking scheme) for the 14 PFT types. The spatial resolution is 0.25 x 0.25 degrees.

Table B.1: Global areal cover (1000 km²) of each PFT by land cover class for 2010 based on the most recent version of the global CWT applied to v2.0.8 of the CCI MR LC map.

Class code	Bare soil	Built	Man. grasses	Nat. grasses	Snow/ ice	Water*	BD trees	BE trees	ND trees	NE trees	BD shrubs	BE shrubs	ND shrubs	NE shrubs
10			7328.9	814.3										
11			6321.2	702.4										
12			57.1								133.2			
20			2200.6	244.5										
30			2060.5	515.1			171.7	171.7			171.7	171.7		171.7
40			712.9	1069.4			267.4	267.4			534.7	356.5		356.5
50								11468.7			637.1	637.1		
60				1751.8			2919.6				1167.9			
61				131.4			613.1				131.4			
62				1653.3			1103.3				918.5			
70				974						4545.6	324.7	324.7		324.7
71				367.4						1714.4	122.5	122.5		122.5
72				0.5						0.3				0.3
80				1537.6					2562.6		128.1	128.1	640.7	128.1
81				0.7					3.4		0.2	0.2		0.2
82														
90				544.2			653		217.7	435.3	108.8	108.8		108.8
100				1362.7			681.4	340.7	170.3	170.3	340.7	170.3		170.3
110				650.8			108.5	54.2		54.2	108.5	54.2		54.2
120	2181.1			2181.1							2181.1	2181.1		2181.1

Continued on next page

Table B.1: Global areal cover (1000 km²) of each PFT by land cover class for 2010 based on the most recent version of the global CWT applied to v2.0.8 of the CCI MR LC map. (Continued)

121	47.7		47.7						71.6	71.6
122	433.2		433.2				1299.7			
130			13703.6							
140			1491							
150	7180.2		422.4	253.4	84.5	84.5	253.4	84.5		84.5
151										
152	62.4		3.7				4.4	1.5		1.5
153	320.1		56.5							
160			224	335.9	335.9					
170					164.1			54.7		
180			1150.8				479.5			287.7
190		647.1								
200	19170.2									
201	109.1									
202	97.3									
210				366225						

★ For the water body class (code 210), the water PFT area includes 3,110,600 km² of inland water.

Table B.2: Percentage PFT composition by class based on the most recent update to the global cross-walking table.

Class code	Bare soil	Built	Man. grasses	Nat. grasses	Snow/ ice	Water	BD trees	BE trees	ND trees	NE trees	BD shrubs	BE shrubs	ND shrubs	NE shrubs
10			90	10										
11			90	10										
12			30								70			
20			90	10										
30			60	15			5	5			5	5		5
40			20	30			7.5	7.5			15	10		10
50								90			5	5		
60				30			50				20			
61				15			70				15			
62				45			30				25			
70				15						70	5	5		5
71				15						70	5	5		5
72				45						30				25
80				30					50		2.5	2.5	12.5	2.5
81				15					70		5	5		5
82				45					30				25	
90				25			30		10	20	5	5		5
100				40			20	10	5	5	10	5		5
110				60			20	10	5	5	10	5		5
120	20			20							20	20		20
121	20			20								30		30

Continued on next page

Table B.2: Percentage PFT composition by class based on the most recent update to the global cross-walking table. (Continued)

122	20		20					60			
130			100								
140			100								
150	85		5		3	1		1	3	1	1
151	85		5		2		2	6			
152	85		5						6	2	2
153	85		15								
160			25		37.5	37.5					
170						75				25	
180			60						25		15
190		100									
200	100										
201	100										
202	100										
210				100							
220				100							

Table B.3: Default land cover to plant functional type cross-walking table from (Poulter et al., 2015).

Code	UN LCCS Land Cover Class Description	Trees				Shrubs				Grasses		Non-vegetated		
		Br Ev	Br De	Ne Ev	Ne De	Br Ev	Br De	Ne Ev	Ne De	Nat Gr	Crops	Bare Soil	Water	Snow/ Ice
10	Cropland, rainfed										100			
11	Herbaceous cover										100			
12	Tree or shrub cover						50				50			
20	Cropland, irrigated or post-flooding										100			
30	Mosaic cropland (50 %) / natural vegetation (tree, shrub, herbaceous cover) (50 %)	5	5			5	5	5		15	60			
40	Mosaic natural vegetation (tree, shrub, herbaceous cover) (50 %) / cropland (50 %)	5	5			7.5	10	7.5		25	40			
50	Tree cover, broadleaved, evergreen, closed to open (15 %)	90				5	5							
60	Tree cover, broadleaved, deciduous, closed to open (15 %)		70				15			15				
61	Tree cover, broadleaved, deciduous, closed (40 %)		70				15			15				
62	Tree cover, broadleaved, deciduous, open (15-40 %)		30				25			35		10		
70	Tree cover, needleleaved, evergreen, closed to open (15 %)			70		5	5	5		15				
71	Tree cover, needleleaved, evergreen, closed (40 %)			70		5	5	5		15				

Continued on next page

Table B.3: Default land cover to plant functional type cross-walking table from (Poulter et al., 2015). (Continued)

72	Tree cover, needleleaved, evergreen, open (15-40 %)			30			5	5		30	30
80	Tree cover, needleleaved, deciduous, closed to open (15 %)				70	5	5	5	0	15	
81	Tree cover, needleleaved, deciduous, closed (40 %)				70	5	5	5		15	
82	Tree cover, needleleaved, deciduous, open (15-40 %)				30		5	5	0	30	30
90	Tree cover, mixed leaf type (broadleaved and needleleaved)		30	20	10	5	5	5		15	10
100	Mosaic tree and shrub (50 %) / herbaceous cover (50 %)	10	20	5	5	5	10	5		40	
110	Mosaic herbaceous cover (50 %) / tree and shrub (50 %)	5	10	5		5	10	5		60	
120	Shrubland					20	20	20		20	20
121	Shrubland evergreen					30		30		20	20
122	Shrubland deciduous						60			20	20
130	Grassland									60	40
140	Lichens and mosses									60	40
150	Sparse vegetation (tree, shrub, herbaceous cover) (15 %)	1	3	1		1	3	1		5	85
151	Sparse tree (15 %)		2	6	2					5	85
152	Sparse shrub (15 %)					2	6	2		5	85
153	Sparse herbaceous cover (15 %)									15	85

Continued on next page

Table B.3: Default land cover to plant functional type cross-walking table from (Poulter et al., 2015). (Continued)

160	Tree cover, flooded, fresh or brakish water	30	30					20		20		
170	Tree cover, flooded, saline water	60			20					20		
180	Shrub or herbaceous cover, flooded,		5	10		10	5	40		30		
190	Urban areas		2.5	2.5				15	75	5		
200	Bare areas								100			
201	Consolidated bare areas								100			
202	Unconsolidated bare areas								100			
210	Water bodies									100		
220	Permanent snow and ice											100

C Supplementary materials to Ch4. LC uncertainty

C.1 Uncertainty analysis

The uncertainty analysis focuses on a measurement equation (or function), using the term "measurement equation" (or "function") in a general sense. Some measurement functions can be specified by relatively simple equations, other measurement functions constitute complex algorithms. Typically, some input quantities are directly determined (by, e.g., measurement, model parameters, or data analysis) while others are determined through their measurement function of other input quantities. Thus, there is a hierarchical aspect to uncertainty analysis.

Uncertainty analysis diagrams

To help organise an equation-centred analysis of uncertainty Mittaz et al. (2019) have developed a graphical representation (Figure C.1). The measurement equation is centrally placed in the uncertainty analysis diagram. For each term of the measurement function, the origin of uncertainties is identified. Along the branches of the diagram, sensitivity matrices quantify the

Table C.1: Relative standard uncertainty of pixel-wise seasonal land surface reflectance. The table lists the interquartile ranges $(Q1, Q3)$ of pixel-wise relative standard uncertainties (Quast et al., 2024 *in preparation*).

Wave-band (nm)	Season duration (weeks)	Relative standard uncertainty Africa Q_1 – Q_3	Europe Q_1 – Q_3	S. Am. Q_1 – Q_3
490	7	0.075 – 0.103	–	–
560	7	0.031 – 0.049	–	–
665	7	0.022 – 0.047	–	–
885	7	0.016 – 0.028	–	–
490	13	0.050 – 0.059	0.080 – 0.110	–
560	13	0.017 – 0.023	0.038 – 0.054	–
665	13	0.010 – 0.015	0.038 – 0.070	–
885	13	0.011 – 0.015	0.019 – 0.028	–
490	13	–	0.125 – 0.180	0.087 – 0.111
560	13	–	0.054 – 0.086	0.035 – 0.047
665	13	–	0.054 – 0.114	0.035 – 0.057
885	13	–	0.028 – 0.041	0.012 – 0.017
490	52	0.050 – 0.057	0.079 – 0.108	0.073 – 0.089
560	52	0.015 – 0.021	0.029 – 0.046	0.026 – 0.035
665	52	0.007 – 0.009	0.029 – 0.062	0.027 – 0.043
885	52	0.008 – 0.009	0.018 – 0.024	0.011 – 0.015

sensitivity of a term to errors in other terms. The endpoints of the diagram identify sources of error considered (Mittaz et al., 2019). The template diagram uses matrix-vector form to express measurement functions and calculation equations to reflect the uncertainty analysis of spectral quantities. The colour of paths in the uncertainty analysis diagram discerns different sources of error at the end of different branches. Thus, the correlation of errors associated with different quantities (which result from the same error source) becomes evident. The diagram template also illustrates the law of propagation of uncertainty, demonstrating how to traverse a path (and thus propagate uncertainty from end to center), combine different paths from the same error source, and aggregate all paths from all considered error sources. Figure C.2 presents the uncertainty analysis diagrams for the processing from TOA reflectances. Equations are written in (spectral) vector form and all basic arithmetic operations apply element-wise.

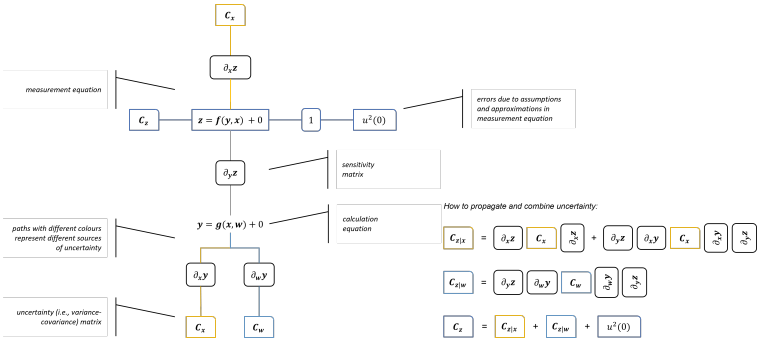

Figure C.1: Uncertainty analysis diagram template

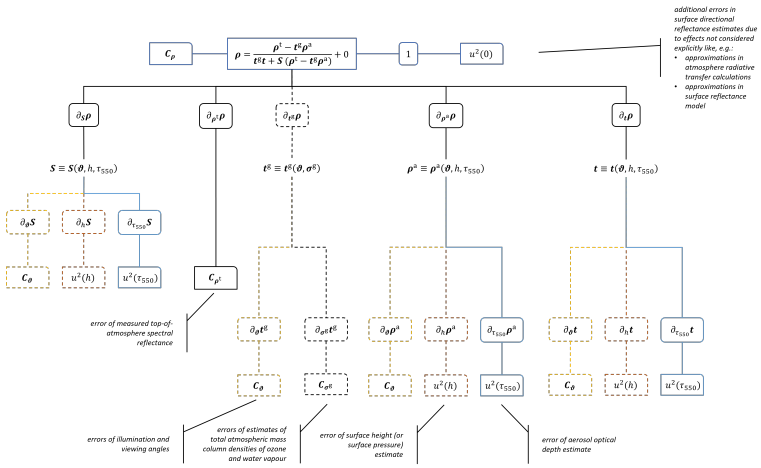

Figure C.2: Uncertainty analysis diagram for the processing from TOA reflectance ρ^t to surface directional reflectance ρ. Dashed lines indicate minor sources of error not considered in this study.

Monte Carlo simulations

We created an ensemble of $N = 100$ variants of surface directional reflectance by mutating radiometric measurements of TOA reflectance and the cloud detection and atmospheric correction algorithms. Figures C.3 and C.4 illustrate the mutation. Each label $i \in \{1, \ldots, N\}$ denotes a variant. Each variant i comprises a specific realization of radiometry, clouds discovered or omitted, and aerosol optical depth (AOD).

Monte Carlo simulations were conducted in a deterministic manner and produced the same realizations when repeated. Several random number (Harase and Kimoto, 2018; O'Neill, 2014) and Sobol sequence (Joe and Kuo, 2003, 2008) generators were used to generate Monte Carlo variants obeying certain rules. In particular, each variant i consistently displayed varying common and random mutations per granule in the TOA spectral reflectance granules, cloud detection results, and global maps of aerosol optical depth.

C.2 Methodology for retrieving preprocessing uncertainty

Auxiliary data for the preprocessing

Reanalysis maps of total aerosol optical depth (AOD) at 550 nm, total atmospheric mass column densities of ozone (GTCO3) and water vapour (TCWV) were obtained from Copernicus Atmosphere Monitoring Service (CAMS) Data Store with global coverage (0.75°) for all days (12:00 UTC) from January 2019 to March 2021.

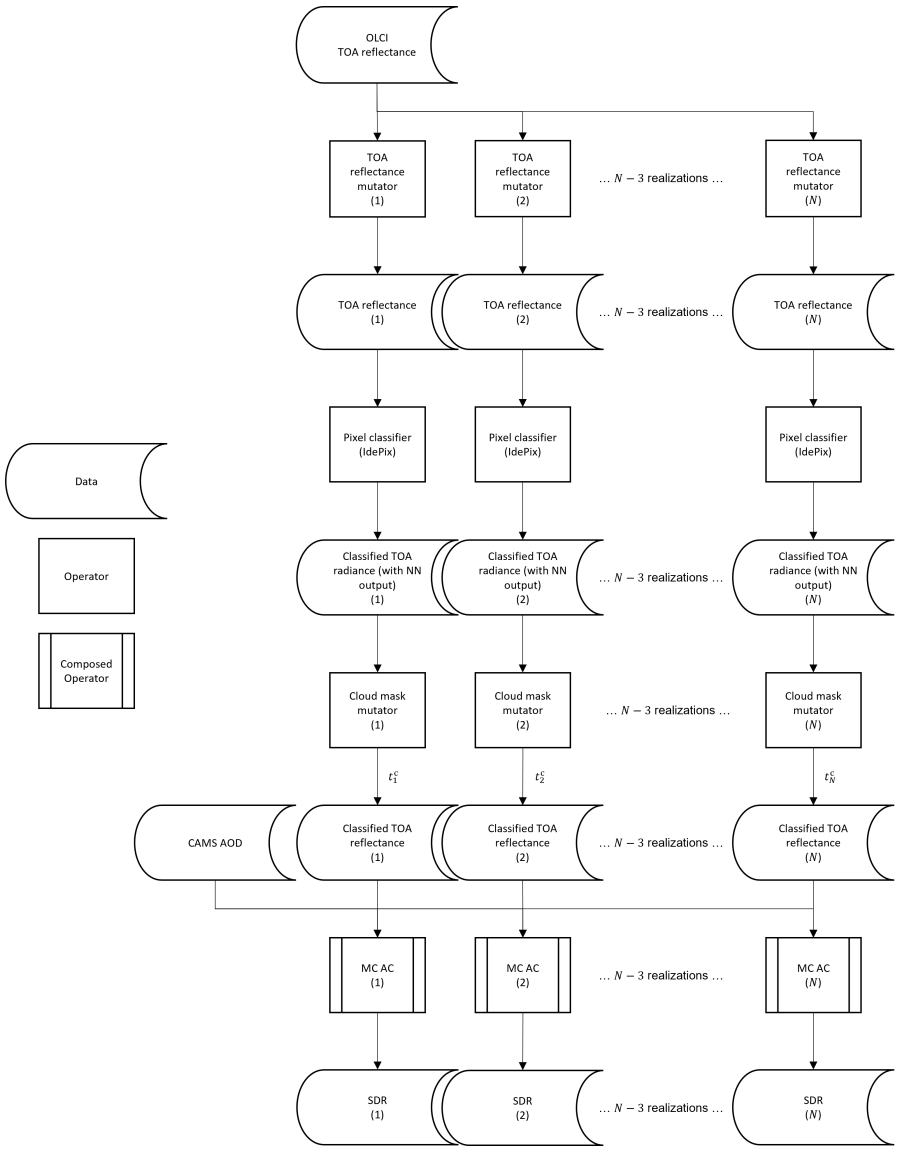

Figure C.3: Monte Carlo processing of TOA reflectance to surface directional reflectance (SDR) randomizing reflectance measurements, cloud detection, and atmospheric correction.

Sentinel-3 OLCI L1B uncertainty

The OLCI L1B product provides images of calibrated TOA spectral reflectance $\rho_\lambda^{\mathrm{t}}$ for 21 spectral bands of wavelengths between 400 nm and 1020 nm

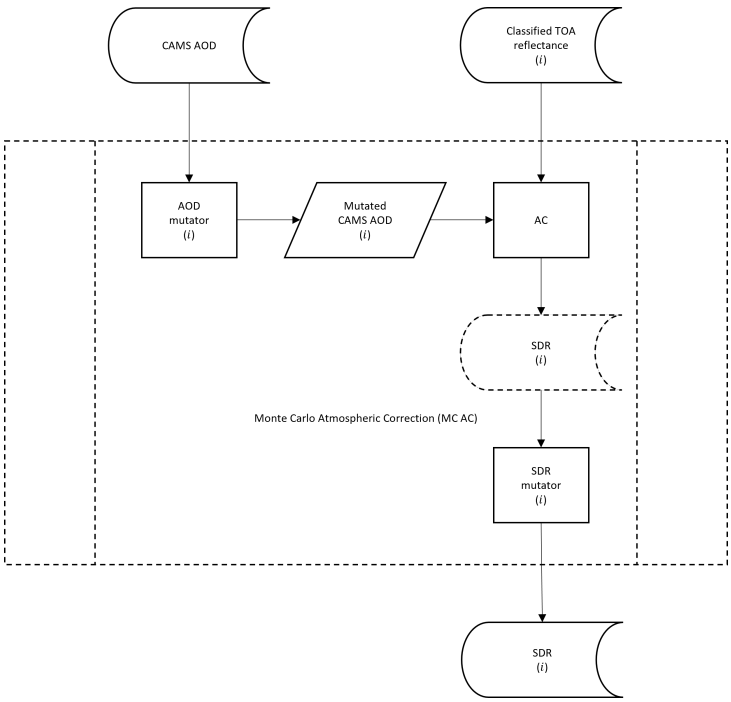

Figure C.4: Monte Carlo atmospheric correction randomizing estimates of aerosol optical depth (AOD).

through coefficients f_λ and Sun zenith angle ϑ^s to transform images of TOA spectral radiance L^t_λ into respective reflectance, i.e.,

$$\rho^\mathrm{t}_\lambda = \frac{\pi L^\mathrm{t}_\lambda}{f_\lambda \cos \vartheta^\mathrm{s}} \tag{1}$$

Since the instrument was calibrated in terms of TOA spectral reflectance the transformation is purely numerical and does not induce any uncertainty.

The OLCI L1B product does not include quantitative estimates of spectral radiometric uncertainty ρ^t_λ per image pixel. The specification of the OLCI instrument states: The radiometric accuracy is less than 2% with reference to the sun for the 400 nm to 900 nm wavelengths and less than 5% with reference to the sun for wavelengths beyond 900 nm; the stability for radiometric accuracy over each orbit is 0.1%; and the relative accuracy for the calibration diffuser Bidirectional Reflectance Distribution Function (BRDF) is 0.5% (ESA, 2023). In the tentative interpretation of this specification, we attribute an uncertainty of

$$u(\rho^\mathrm{t}_\lambda) = 0.01\, \rho^\mathrm{t}_\lambda \tag{2}$$

to the measured TOA spectral reflectance ρ_λ^t. That is to say, the error in measurements of ρ_λ^t is less than 1% of the measured value for about 68% of all measurements, less than 2% of the measured value for 95% of all measurements, and less than 3% of the measured value for almost all measurements, assuming a normal distribution of measurement errors. To take into account that the error of the calibration diffuser BRDF affects all measurements of ρ_λ^t in a common manner we assume that the errors in all measurements of ρ_λ^t are correlated with a correlation coefficient of $r = 0.5$, i.e., half of the error variance is due to random noise and the other half is due to a common calibration error. Assessing errors of Sentinel-3A and -3B OLCI has been an ongoing activity of the ESA Mission Performance Centre (e.g. Lamquin et al., 2020a,b) but per pixel assessments have not been available for public use. Nevertheless, OLCI L1B products including per pixel uncertainty $u(\rho_\lambda^t)$ can be expected for the future.

In order to generate Monte Carlo variant i of a sequence of n measured values $(\rho_\lambda^t)_1, \ldots, (\rho_\lambda^t)_n$ we generate a sequence of $n+1$ random numbers $\zeta_0^{(i)}, \zeta_1^{(i)}, \ldots, \zeta_n^{(i)}$ drawn from a standard normal distribution (except for $\zeta_0^{(i)}$ we make new draws for each waveband λ). From these $n+1$ numbers, we generate a sequence of n correlated random numbers $v_1^{(i)}, \ldots, v_n^{(i)}$ by means of the linear transformation

$$\begin{pmatrix} v_1^{(i)} \\ \vdots \\ v_n^{(i)} \end{pmatrix} = \begin{pmatrix} \sqrt{r} & \sqrt{1-r} & & \\ \vdots & & \ddots & \\ \sqrt{r} & & & \sqrt{1-r} \end{pmatrix} \begin{pmatrix} \zeta_0^{(i)} \\ \zeta_1^{(i)} \\ \vdots \\ \zeta_n^{(i)} \end{pmatrix} \tag{3}$$

The measurand can be considered strictly positive, i.e., $\rho_\lambda^t \in (0, \infty)$. Following the recommendation given in the GUM (JCGM, 2008) we attribute the lognormal probability density function to the measurand, since among all real-valued distributions with support $(0, \infty)$ and with expectation $E(x)$ and variance $u^2(x)$ the lognormal distribution

$$f(x; \mu, \sigma) = \frac{1}{\sigma x \sqrt{2\pi}} \exp\left(-\frac{(\ln x - \mu)^2}{2\sigma^2}\right) \tag{4}$$

with

$$\mu = \ln(E(x)) - \frac{\sigma^2}{2}, \quad \sigma^2 = \ln\left(1 + \frac{u^2(x)}{(E(x))^2}\right) \tag{5}$$

as the maximum entropy. The recipe to generate a random sample $(\rho_\lambda^t)_j^{(i)}$ from a lognormal distribution with expectation $(\rho_\lambda^t)_j$ and variance $u^2((\rho_\lambda^t)_j)$ is first

to compute μ and σ from expectation and variance using Eq. (5). Secondly, it is to take the random sample $v_j^{(i)}$ generated by Eq. (3).

$$(\rho_\lambda^{\mathrm{t}})_j^{(i)} = \exp\left(\mu + \sigma v_j^{(i)}\right) \tag{6}$$

The resulting sequence $(\rho_\lambda^{\mathrm{t}})_1^{(i)},\ldots,(\rho_\lambda^{\mathrm{t}})_n^{(i)}$ is a Monte Carlo variant of the measured values $(\rho_\lambda^{\mathrm{t}})_1,\ldots,(\rho_\lambda^{\mathrm{t}})_n$ with the desired properties. Figure C.5 depicts examples of generated variants. Consistently positive (reddish) or negative (blueish) reflectance difference images reflect the common calibration error. Spatially correlated smaller differences (whitish) are due to darker surfaces. The remaining variability is due to random noise.

Aerosol optical depth uncertainty

The CAMS maps do not include information on the uncertainty attributed to the assimilated parameters. Based on AeroCom validation reports (AeroCom) against AOD values measured at AERONET stations in 2020, we attribute an uncertainty of $u(\tau_5 50) = 0.08$ to the assimilated AOD and assume a global error correlation coefficient of $r = 0.5$, i.e., half of the error variance is due to pure random errors and the other half is due to common data assimilation errors. Like reflectance described in the previous subsection, total aerosol optical depth can be considered a strictly positive measurand, i.e., $\tau_5 50 \in (0, \infty)$. In the laboratory, air may be ultra clean and free from aerosols, but under non-laboratory situations there always is some aerosol. Like in the previous subsection, we attribute the lognormal probability density function to the measurand and generate Monte Carlo variants using the recipe given above.

Figures C.6 and C.7 show examples of generated AOD variants co-registered (bi-cubic interpolation) with OLCI L1B images. All sites include four coarse (0.75°) grid cells.

Cloud detection uncertainty

Cloud detection is embedded within the IdePix algorithm, which identifies the target states as land, water, snow or ice, opaque clouds, and semi-transparent or sub-pixel clouds (Wevers et al., 2022a). The main cloud test applies a threshold value t^{c} to the output of a trained artificial neural network, which separates cloudy-sky from clear-sky conditions. Based on the IdePix training and verification dataset, we calculated confusion matrices as a function of the threshold value, and corresponding probabilities of false cloud omission and false cloud discovery to assess cloud detection errors. The threshold value itself was attributed to the binomial probability distribution of achieving m successes (i.e, true cloud discoveries and true cloud omissions) in n trials, given the maximum success probability (i.e., accuracy)

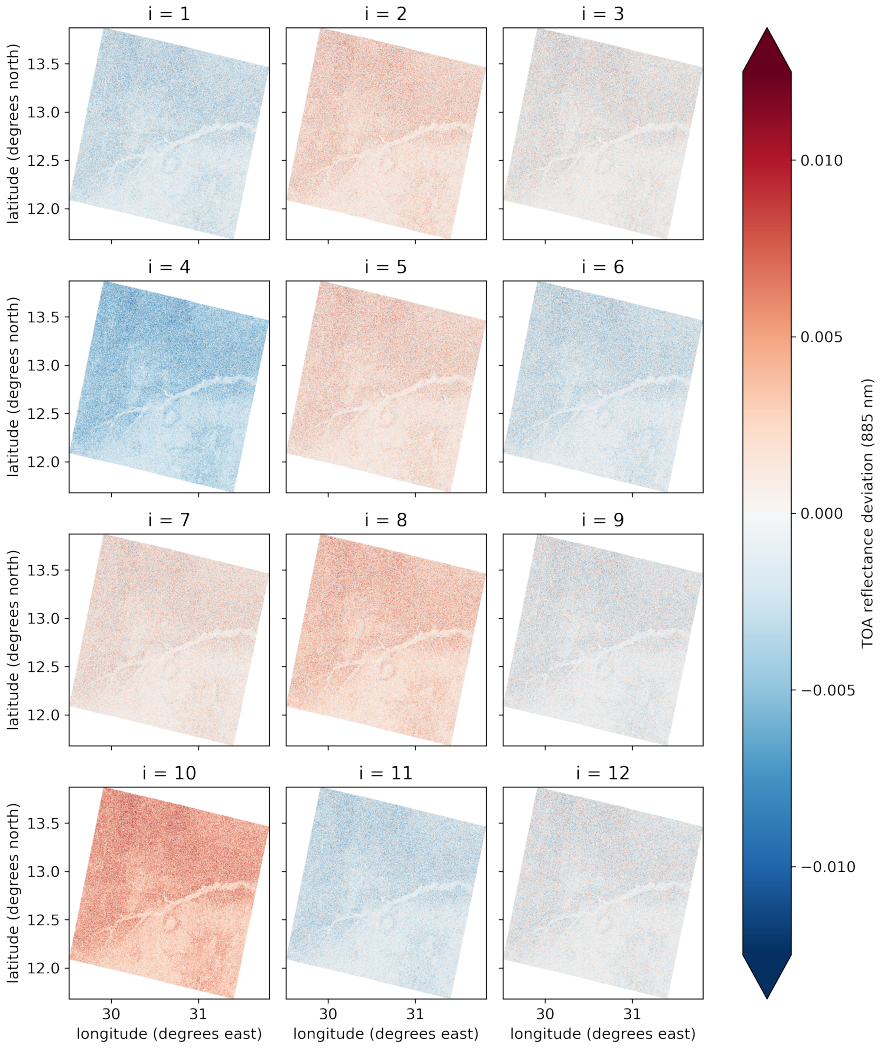

Figure C.5: Example of Monte Carlo variants of 885 nm TOA reflectance for the African site. The colour indicates the deviation from the ensemble mean TOA reflectances. (Based on Sentinel-3A OLCI L1B EFR granule 2020-05-28; cycle 058, relative orbit 363, frame 2700).

of $P(t^c = 3.7) = 0.87$ the cloud test was able to achieve. Figure C.8 illustrates the calculated probability distributions.

For each Monte Carlo variant i of the cloud detection algorithm, a different threshold value $(t^c)^{(i)}$ was drawn from the probability distribution of t^c. Then

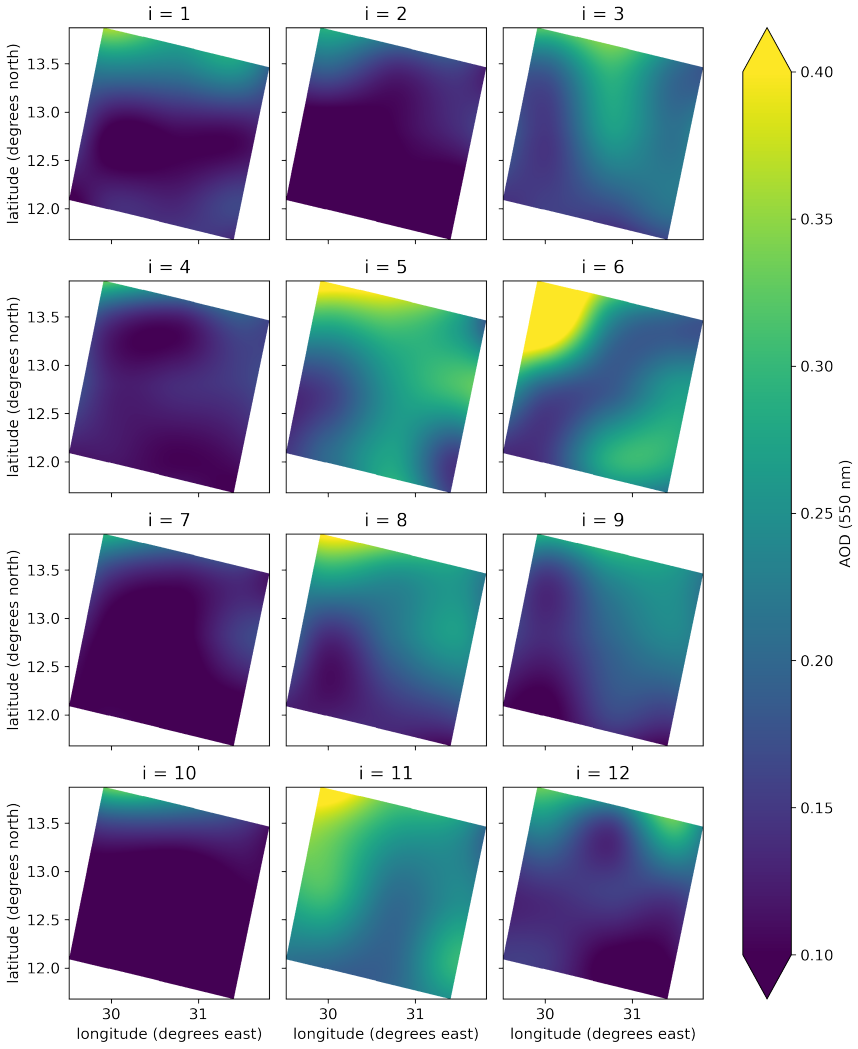

Figure C.6: Examples of Monte Carlo variants of total aerosol optical depth (AOD) for the African site. (Based on CAMS total aerosol optical depth data; co-registered with Sentinel-3A OLCI L1B EFR granule 2020-05-28; cycle 058, relative orbit 363, frame 2700).

cloud test results were mutated randomly according to false cloud omission (clear-to-cloud mutation) and false cloud discovery (cloud-to-clear mutation) probabilities for the drawn value $(t^c)^{(i)}$.

Cases of false cloud omission were nevertheless mitigated in the seasonal compositing through multi-temporal analysis, whereas cases of false cloud

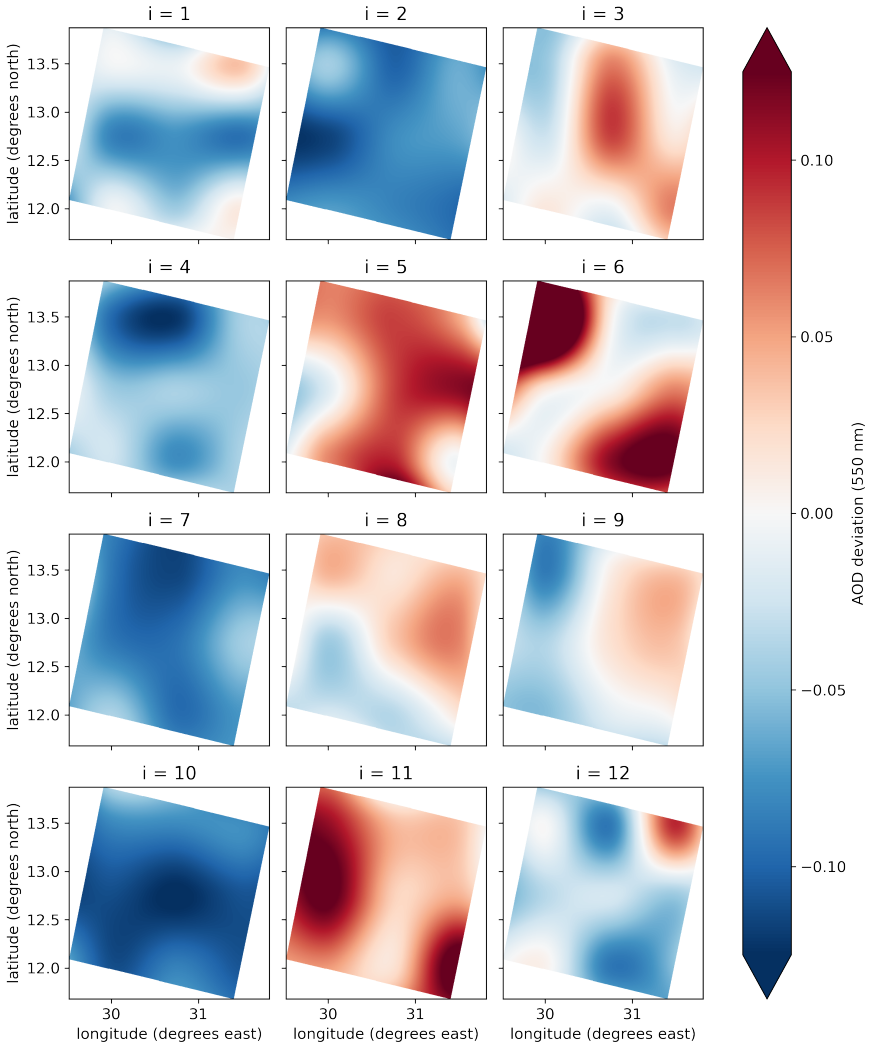

Figure C.7: Examples of Monte Carlo variants of total aerosol optical depth (AOD) for the African site. The colour indicates the deviation from the ensemble mean AOD. (Based on CAMS total aerosol optical depth data; co-registered with Sentinel-3A OLCI L1B EFR granule 2020-05-28; cycle 058, relative orbit 363, frame 2700).

discovery (as cases of true cloud discovery) were removed from the set of observations.

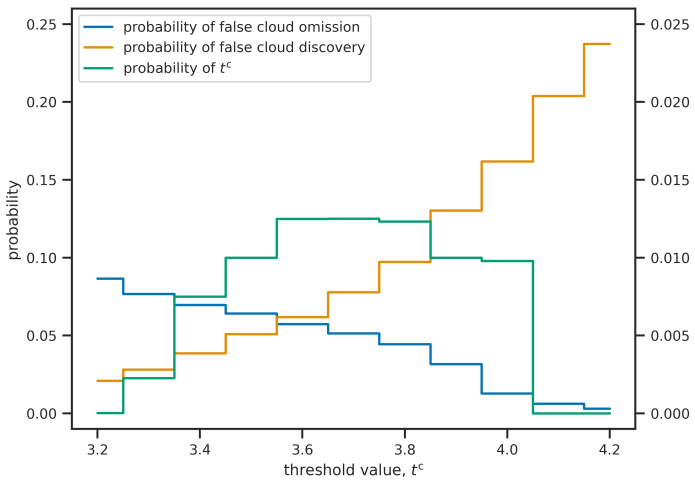

Figure C.8: Probabilities of false cloud omission and false cloud discovery over land surface as a function of the threshold value t^c. The graph of the probability distribution of the threshold value (green) refers to the axis on the right-hand side.

Atmospheric correction

The atmospheric correction used by ESA CCI MR LC is based on the algorithms originally designed for Envisat MERIS. Adaptation for OLCI was feasible due to the shared set of 15 spectral wavebands between both sensors, along with their similar spectral response functions and comparable on-ground resolution. The MERIS algorithm employs a numerical inversion of radiative transfer equations to estimate total AOD at 550 nm (continental aerosols) over dark targets in an image, and subsequent gap filling. Deviations of total AOD estimated by the MERIS algorithm from measurements of AERONET stations (Lewis et al., 2013) are higher than the deviation between CAMS AOD reanalysis and AERONET measurements usually reported by AeroCom (AeroCom). Since our study considers relatively small site areas, which would not always include enough dark targets, we decided to adopt the estimates of total AOD from CAMS instead (see Section C.2).

For a given waveband λ and a given atmospheric profile, the relationship between TOA reflectance $\rho_\lambda^{\mathrm{t}}$ and surface directional reflectance ρ_λ is approximated by

$$\rho_\lambda^{\mathrm{t}} = t_\lambda^{\mathrm{g}} \left(\rho_\lambda^{\mathrm{a}} + \frac{t_\lambda \rho_\lambda}{1 - S_\lambda \rho_\lambda} \right) \tag{7}$$

where t_λ^{g} denotes the total (i.e., Sun to ground and ground to sensor) atmospheric transmittance due to absorption by ozone and water vapour, t_λ

denotes the total atmospheric transmittance apart from absorption, $\rho_\lambda^{\mathrm{a}}$ denotes the atmospheric scattering term, and S_λ denotes the atmospheric bi-hemispherical albedo. Inversion of this relation yields

$$\rho_\lambda = \frac{\rho_\lambda^{\mathrm{t}} - t_\lambda^{\mathrm{g}} \rho_\lambda^{\mathrm{a}}}{t_\lambda^{\mathrm{g}} t_\lambda + S_\lambda \left(\rho_\lambda^{\mathrm{t}} - t_\lambda^{\mathrm{g}} \rho_\lambda^{\mathrm{a}}\right)}. \tag{8}$$

Transmittance t_λ, atmospheric scattering term $\rho_\lambda^{\mathrm{a}}$, and atmospheric bi-hemispherical albedo S_λ were calculated using the matrix operator code MOMO (Doppler et al., 2014; Fischer and Grassl, 1984; Hollstein and Fischer, 2012) and stored into look-up tables as functions of waveband, viewing and illumination angles $\boldsymbol{\vartheta}$, surface elevation h, and total aerosol optical depth τ_{550}. The atmospheric absorption term was calculated using the Second Simulation of a Satellite Signal in the Solar Spectrum - Vector (6SV) code (Kotchenova and Vermote, 2007; Kotchenova et al., 2008, 2006; Vermote et al., 1997) and stored into a look-up table as a function of waveband, $\boldsymbol{\vartheta}$, and total atmospheric column mass densities of ozone and water vapour $\boldsymbol{\sigma}^{\mathrm{g}} = (\sigma^{\mathrm{O_3}}, \sigma^{\mathrm{H_2O}})$.

With a known atmospheric profile, the atmospheric radiative transfer codes enable precise calculation of atmospheric terms with a relative precision better than 0.01 (Fischer and Grassl, 1984; Kotchenova et al., 2006). To reflect the calculation error in our Monte Carlo simulations we attribute a lognormal probability density function with a standard deviation of $u(\rho_\lambda) = 0.01\rho_\lambda$ to the measurand and generate Monte Carlo variants using the recipe given in Section C.2. Figures C.9 and C.10 depict examples of generated surface directional reflectance variants for the blue and the near-infrared, respectively. A comparison of Figure C.9 and Figure C.7 illustrates the strong anti-correlation of the variation of surface directional reflectance with the variation of total aerosol optical depth. In the near-infrared, which is less sensitive to aerosol optical depth, the variation of surface directional reflectance (Figure C.5) is correlated with the variation of TOA reflectance (Figure C.10).

C.3 Complementary results to land cover uncertainty

The most probable land cover map and pixel-wise uncertainty indicators

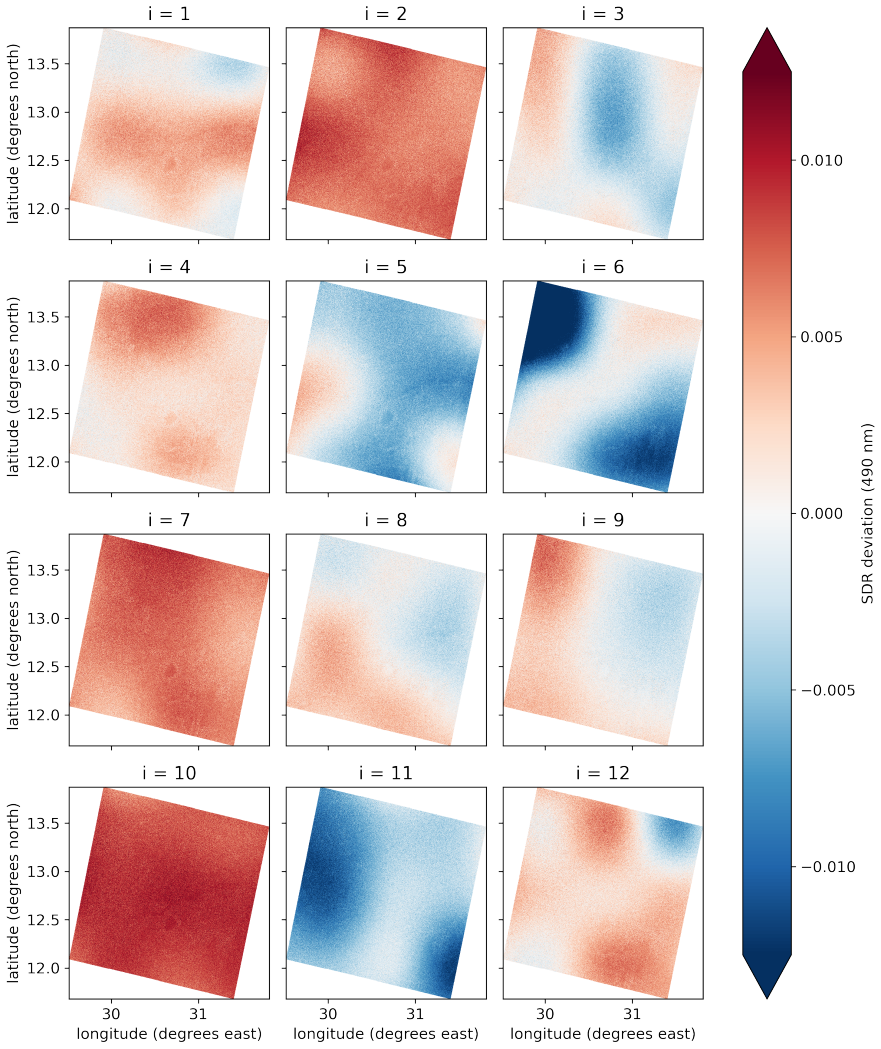

Figure C.9: Examples of Monte Carlo variants of 490 nm surface directional reflectance (SDR) for the African site. The colour indicates the deviation from the ensemble mean SDR. (Based on Sentinel-3A OLCI L1B EFR granule 2020-05-28; cycle 058, relative orbit 363, frame 2700).

Comparison to the maximum frequency uncertainty

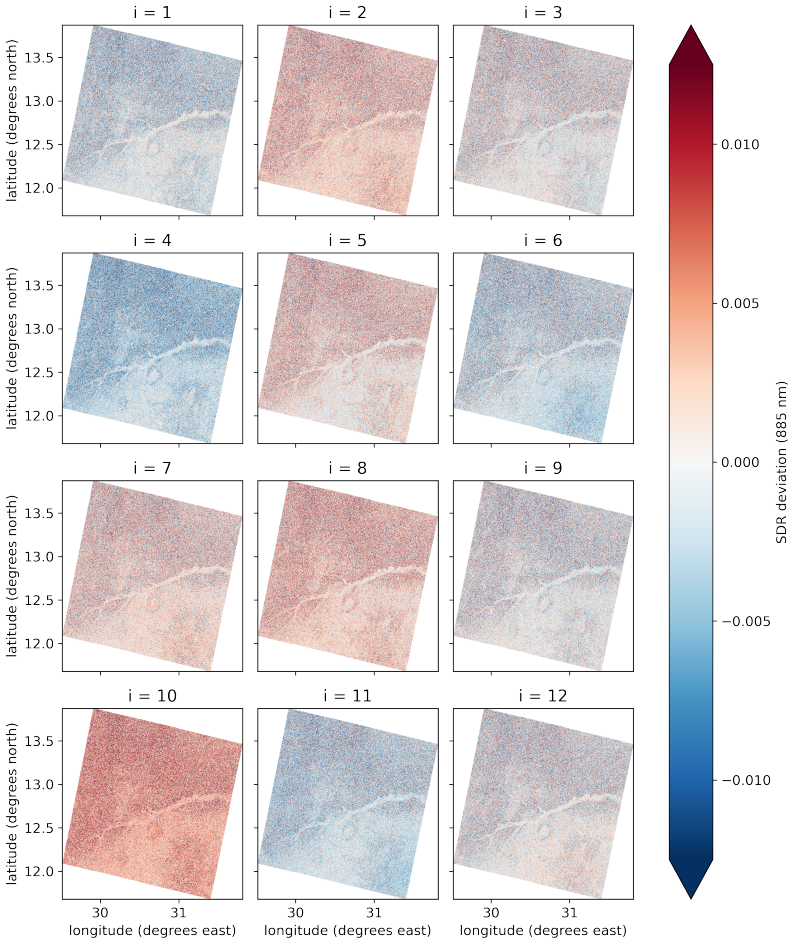

Figure C.10: Examples of Monte Carlo variants of 885 nm surface directional reflectance (SDR) for the African site. The colour indicates the deviation from the ensemble mean SDR. (Based on Sentinel-3A OLCI L1B EFR granule 2020-05-28; cycle 058, relative orbit 363, frame 2700).

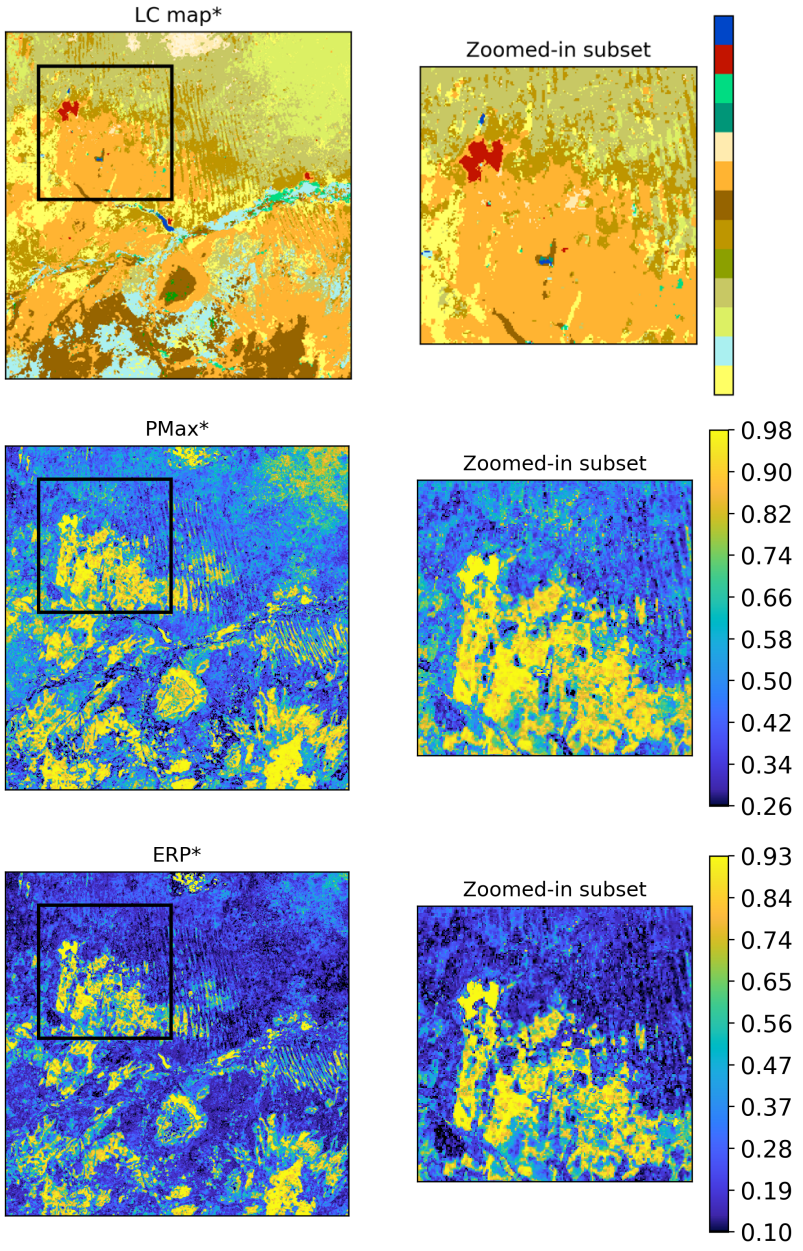

Figure C.11: AF site. More detailed illustration of the spatially explicit uncertainty LC map*, PMax*, and ERP* indicators.

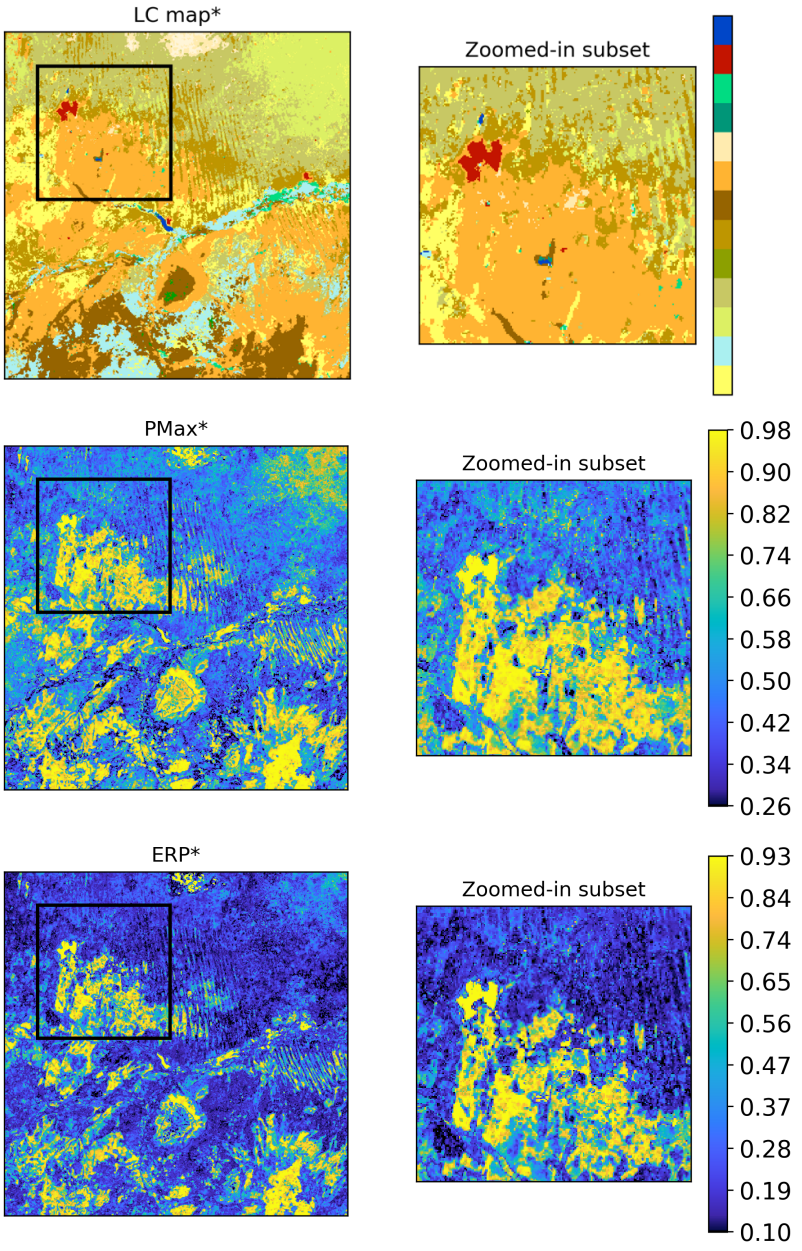

Figure C.12: SA site. More detailed illustration of the spatially explicit uncertainty LC map*, PMax*, and ERP* indicators.

Table C.2: EU site. RF model accuracy per site and per class, with f1-score, precision, recall, and support as mean ± std, for the 100 variants of mean seasonal composites.

Class	F1-score	Precision	Recall	Support
Bare areas	0.98 ± 0.003	0.97 ± 0.005	0.99 ± 0.002	673 ± 22
Sparse vegetation (15%)	0.98 ± 0.003	0.99 ± 0.004	0.97 ± 0.005	1011 ± 28
Water bodies	0.96 ± 0.005	0.95 ± 0.007	0.98 ± 0.005	1007 ± 24
Shrub or herbaceous cover flooded	0.96 ± 0.004	0.95 ± 0.006	0.97 ± 0.005	999 ± 24
Urban areas	0.94 ± 0.006	0.96 ± 0.006	0.91 ± 0.009	1002 ± 32
Mosaic natural vegetation (50%) / cropland (50%)	0.92 ± 0.007	0.92 ± 0.009	0.92 ± 0.008	995 ± 27
Mosaic herbaceous cover (50%) / tree and shrub (50%)	0.88 ± 0.009	0.86 ± 0.013	0.9 ± 0.01	1003 ± 21
Cropland rainfed	0.77 ± 0.009	0.79 ± 0.013	0.75 ± 0.014	992 ± 26
Tree cover needleleaved evergreen closed to open (15%)	0.74 ± 0.011	0.77 ± 0.013	0.72 ± 0.016	992 ± 31
Grassland	0.7 ± 0.01	0.72 ± 0.016	0.69 ± 0.013	992 ± 25
Mosaic cropland (50%) / natural vegetation (50%)	0.69 ± 0.009	0.67 ± 0.014	0.71 ± 0.012	996 ± 28
Tree cover broadleaved deciduous closed to open (15%)	0.64 ± 0.01	0.66 ± 0.015	0.62 ± 0.016	1015 ± 30
Tree cover mixed leaf type (broadleaved and needleleaved)	0.61 ± 0.008	0.6 ± 0.015	0.63 ± 0.009	998 ± 24
Mosaic tree and shrub (50%) / herbaceous cover (50%)	0.53 ± 0.011	0.51 ± 0.016	0.55 ± 0.011	1001 ± 24.0

Table C.3: AF site. RF model accuracy per site and per class, with f1-score, precision, recall, and support as mean ± std, for the 100 variants of mean seasonal composites.

Class	F1-score	Precision	Recall	Support
Water bodies	1 ± 0.002	1 ± 0.001	0.99 ± 0.003	1000 ± 26
Tree cover flooded saline water	0.99 ± 0.005	0.98 ± 0.008	1 ± 0.003	287 ± 14
Urban areas	0.99 ± 0.001	1 ± 0.001	0.99 ± 0.003	1000 ± 33
Shrub or herbaceous cover flooded	0.98 ± 0.003	0.97 ± 0.005	0.99 ± 0.003	996 ± 27
Bare areas	0.97 ± 0.004	0.98 ± 0.005	0.95 ± 0.007	995 ± 29
Sparse vegetation (15%)	0.96 ± 0.004	0.94 ± 0.007	0.98 ± 0.005	995 ± 27
Shrubland	0.96 ± 0.004	0.94 ± 0.008	0.97 ± 0.004	1005 ± 26
Tree cover broadleaved deciduous closed to open (15%)	0.95 ± 0.009	0.96 ± 0.012	0.94 ± 0.012	360 ± 17
Cropland irrigated or post-flooding	0.88 ± 0.006	0.84 ± 0.01	0.93 ± 0.006	1006 ± 24
Mosaic tree and shrub (50%) / herbaceous cover (50%)	0.86 ± 0.051	0.85 ± 0.074	0.88 ± 0.058	28 ± 5
Grassland	0.84 ± 0.009	0.84 ± 0.013	0.84 ± 0.011	1000 ± 29
Mosaic herbaceous cover (50%) / tree and shrub (50%)	0.76 ± 0.01	0.73 ± 0.014	0.78 ± 0.016	997 ± 23
Mosaic cropland (50%) / natural vegetation (50%)	0.73 ± 0.01	0.71 ± 0.014	0.75 ± 0.013	1009 ± 21
Mosaic natural vegetation (50%) / cropland (50%)	0.65 ± 0.013	0.64 ± 0.017	0.65 ± 0.014	997 ± 29
Cropland rainfed	0.54 ± 0.015	0.66 ± 0.022	0.46 ± 0.015	1002 ± 30.0

Table C.4: SA site. RF model accuracy per site and per class, with f1-score, precision, recall, and support as mean ± std, for the 100 variants of mean seasonal composites.

Class	F1-score	Precision	Recall	Support
Water bodies	1 ± 0.0	1 ± 0.0	1 ± 0.001	992 ± 35
Urban areas	0.99 ± 0.002	0.99 ± 0.005	0.99 ± 0.003	1000 ± 30
Tree cover broadleaved deciduous closed to open (15%)	0.99 ± 0.002	0.99 ± 0.003	0.99 ± 0.003	1004 ± 25
Cropland rainfed	0.91 ± 0.007	0.92 ± 0.01	0.9 ± 0.01	1000 ± 22
Mosaic cropland (50%) / natural vegetation (50%)	0.88 ± 0.008	0.94 ± 0.008	0.83 ± 0.012	997 ± 27
Mosaic herbaceous cover (50%) / tree and shrub (50%)	0.83 ± 0.01	0.77 ± 0.014	0.9 ± 0.011	997 ± 30
Shrub or herbaceous cover flooded	0.83 ± 0.008	0.82 ± 0.012	0.83 ± 0.01	999 ± 25
Tree cover broadleaved evergreen closed to open (15%)	0.74 ± 0.009	0.74 ± 0.013	0.73 ± 0.013	1013 ± 30
Mosaic natural vegetation (50%) / cropland (50%)	0.73 ± 0.009	0.75 ± 0.013	0.72 ± 0.011	997 ± 20
Grassland	0.66 ± 0.01	0.67 ± 0.012	0.66 ± 0.014	1001 ± 21
Shrubland	0.65 ± 0.011	0.68 ± 0.014	0.63 ± 0.016	1005 ± 20
Mosaic tree and shrub (50%) / herbaceous cover (50%)	0.55 ± 0.008	0.53 ± 0.015	0.58 ± 0.012	997 ± 30.0

Table C.5: Matrice of overall agreement between LC map* and LC map Maj

		LC map Maj															
		1	3	4	6	7	9	1	11	13	15	18	19	2	21	Sum	PA
LC map*	1	34964	449	113	1	1		12	4	29	37	1	57		5	35673	98.1
	3	646	48867	85	22		2	45	49	271	9	1	8		6	52	97.7
	4	4	18	5285	2	3		17	6	9		1	23		18	5422	97.5
	6	6	2	1	25957	8	122	24	1	13		34	1		3	2646	98.3
	7	1		5	1	18517	131	121	3	2		1			23	18814	98.4
	9			1	124	138	211	127	1	2		3			6	2152	98.1
	1	24	78	64	159	67	13	37791	93	71		29	16		9	3854	98.2
	11		21	1	1			171	5756	98			1		4	662	95.0
	13	21	337	38	15	3	3	97	197	3959	1	27	9		7	4345	98.1
	15	31	3	1							1867		1			193	98.1
	18		1		38	1	1	17		19		1755				1832	95.8
	19	78		73		1				1	6		16463		38	1666	98.8
	2													19		19	1.0
	21	9	1	3	1	14	8	23	1	5			22		548	5162	97.8
	Sum	3582	49795	576	2633	18753	2147	38661	6111	411	192	1861	1661	19	5167	268324	
	UA	97.6	98.1	92.6	98.6	98.7	98.3	97.8	94.2	98.7	97.2	94.3	99.2	1.0	97.7		98.1
	F1	97.8	97.9	95.0	98.4	98.6	98.2	98.0	94.6	98.4	97.7	95.4	99.0	1.0	97.7		OA

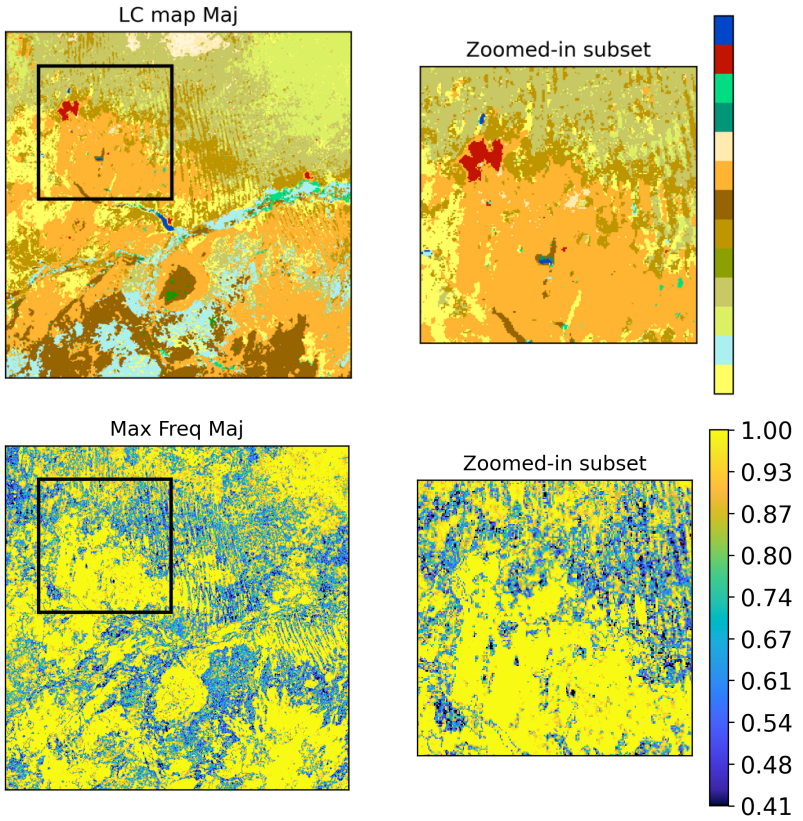

Figure C.13: AF site. Illustration of spatially explicit uncertainty indicators derived from the frequency of LC variants.

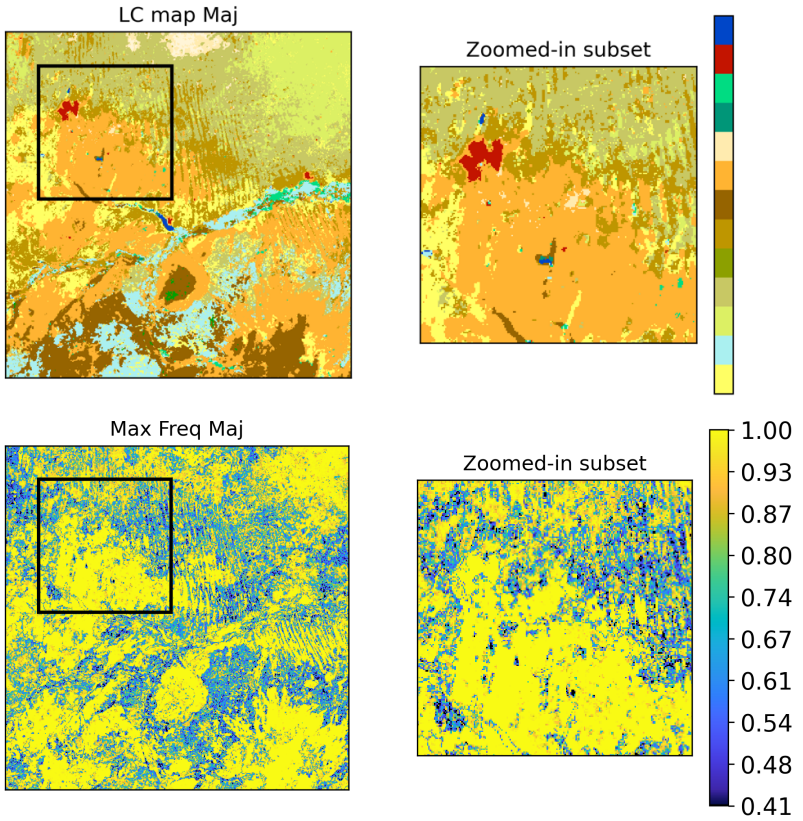

Figure C.14: SA site. Illustration of spatially explicit uncertainty indicators derived from the frequency of LC variants.

Bibliography

Abercrombie, S.P., Friedl, M.A., 2016. Improving the Consistency of Multitemporal Land Cover Maps Using a Hidden Markov Model. IEEE Trans. Geosci. Remote Sens. 54, 703–713. doi:10.1109/TGRS.2015.2463689.

AeroCom, . Cams84 - aerocom evaluation. AeroCom. URL: https://aerocom-classic.met.no/cgi-bin/surfobs_annualrs.pl.

Andréfouët, S., Bindschadler, R., Brown De Colstoun, E.C., Choate, M., Chomentowski, W., Christopherson, J., Doorn, B., Hall, D.K., Holifield, C., Howard, S., Kranenburg, C., Lee, S., Masek, J.B., Moran, M., Mueller-Karger, F., Ohlen, D., Palandro, D., Price, J., Qi, J., Reed, B.C., Samek, J., Scaramuzza, P., Skole, D., Schott, J., Storey, J., Thome, K., Torres-Pulliza, D., Vogelmann, J., Williams, D.L., Woodcock, C., Wylie, B., 2003. Preliminary Assessment of the Value of Landsat 7 ETM+ Data following Scan Line Corrector Malfunction. Science (80-.). , 1–86.

Arino, O., Bicheron, P., Achard, F., Latham, J., Witt, R., Weber, J.L., 2008. GlobCover: The most detailed portrait of Earth. Eur. Sp. Agency Bull. 2008, 24–31.

Arneth, A., Denton, F., Agus, F., Elbehri, A., Erb, K., Elasha, B.O., Rahimi, M., Rounsevell, M., Spence, A., Valentini, R., 2019. Chapter 1: Framing and context. Clim. Chang. L. an IPCC Spec. Rep. Clim. Chang. Desertif. L. Degrad. Sustain. L. Manag. food Secur. Greenh. gas fluxes Terr. Ecosyst. [P.R. Shukla, J. Skea, E. Calvo Buendia, V. Masson-Delmot , 77–129.

Asner, G.P., Scurlock, J.M., A. Hicke, J., 2003. Global synthesis of leaf area index observations: implications for ecological and remote sensing studies. Global ecology and biogeography 12, 191–205.

Augspurger, C.K., 2013. Reconstructing patterns of temperature, phenology, and frost damage over 124 years: spring damage risk is increasing. Ecology 94, 41–50.

Ballantyne, A.P., Andres, R., Houghton, R., Stocker, B.D., Wanninkhof, R., Anderegg, W., Cooper, L.A., DeGrandpre, M., Tans, P.P., Miller, J.B., Alden, C., White, J.W., 2015. Audit of the global carbon budget: Estimate errors and their impact on uptake uncertainty. Biogeosciences 12, 2565–2584. doi:10.5194/bg-12-2565-2015.

Bartholomé, E., Belward, A.S., 2005. GLC2000: a new approach to global land cover mapping from Earth observation data. Int. J. Remote Sens. 26, 1959–1977. doi:10.1080/01431160412331291297.

Bastos, A., Hartung, K., Nützel, T.B., Nabel, J.E., Houghton, R.A., Pongratz, J., 2021. Comparison of uncertainties in land-use change fluxes from bookkeeping model parameterisation. Earth Syst. Dyn. 12, 745–762. doi:10.5194/esd-12-745-2021.

Bastos, A., O'Sullivan, M., Ciais, P., Makowski, D., Sitch, S., Friedlingstein, P., Chevallier, F., Rödenbeck, C., Pongratz, J., Luijkx, I.T., Patra, P.K., Peylin, P., Canadell, J.G., Lauerwald, R., Li, W., Smith, N.E., Peters, W., Goll, D.S., Jain, A.K., Kato, E., Lienert, S., Lombardozzi, D.L., Haverd, V., Nabel, J.E., Poulter, B., Tian, H., Walker, A.P., Zaehle, S., 2020. Sources of Uncertainty in Regional and Global Terrestrial CO2 Exchange Estimates. Global Biogeochem. Cycles 34, 1–21. doi:10.1029/2019GB006393.

Bates, B., Kundzewicz, Z.W., Wu, S., Palutikof, J., 2008. climate change and Water: technical Paper vi. Intergovernmental Panel on Climate Change (IPCC).

Baumann, P., Misev, D., Merticariu, V., Huu, B.P., 2019. Datacubes: Towards space/time analysis-ready data. Service-Oriented Mapping: Changing Paradigm in Map Production and Geoinformation Management , 269–299.

Beck, H.E., Zimmermann, N.E., McVicar, T.R., Vergopolan, N., Berg, A., Wood, E.F., 2018. Present and future köppen-geiger climate classification maps at 1-km resolution. Scientific data 5, 1–12.

Belgiu, M., Drăgu, L., 2016. Random forest in remote sensing: A review of applications and future directions. ISPRS J. Photogramm. Remote Sens. 114, 24–31. doi:10.1016/j.isprsjprs.2016.01.011.

Bicheron, P., Amberg, V., Bourg, L., Petit, D., Huc, M., Miras, B., Brockmann, C., Hagolle, O., Delwart, S., Ranéra, F., Leroy, M., Arino, O., 2011. Geolocation assessment of MERIS GlobCover orthorectified products. IEEE Trans. Geosci. Remote Sens. 49, 2972–2982. doi:10.1109/TGRS.2011.2122337.

Bindoff, N.L., Stott, P.A., AchutaRao, K.M., Allen, M.R., Gillett, N., Gutzler, D., Hansingo, K., Hegerl, G., Hu, Y., Jain, S., et al., 2014. Detection and attribution of climate change: from global to regional.

BIPM, I., IFCC, I., ISO, I., IUPAP, O., 2009. Evaluation of measurement data -an introduction to the guide to the expression of uncertainty in measurement and related documents. JCGM 104, 1–104.

Bogaert, P., Lamarche, C., Defourny, P., 2022. Hidden Markov Models for Annual Land Cover Mapping-Increasing Temporal Consistency and Completeness. IEEE Trans. Geosci. Remote Sens. 60. doi:10.1109/TGRS.2021.3123738.

Bogaert, P., Waldner, F., Defourny, P., 2017. An information-based criterion to measure pixel-level thematic uncertainty in land cover classifications.

Stoch. Environ. Res. Risk Assess. 31, 2297–2312. doi:10.1007/s00477-016-1310-y.

Bojinski, S., Verstraete, M., Peterson, T.C., Richter, C., Simmons, A., Zemp, M., 2014. The concept of essential climate variables in support of climate research, applications, and policy. Bull. Am. Meteorol. Soc. 95, 1431–1443. doi:10.1175/BAMS-D-13-00047.1.

Bonan, G.B., 2008. Forests and climate change: Forcings, feedbacks, and the climate benefits of forests. Science (80-.). 320, 1444–1449. doi:10.1126/science.1155121.

Bontemps, S., Defourny, P., Bogaert, E.V., Kalogirou, V., Perez, J.R., 2011. GLOBCOVER 2009 Products Description and Validation Report. ESA Bull. 136, 53. doi:10013/epic.39884.d016.

Bontemps, S., Herold, M., Kooistra, L., Van Groenestijn, A., Hartley, A., Arino, O., Moreau, I., Defourny, P., Others, 2012. Revisiting land cover observation to address the needs of the climate modeling community. Biogeosciences 9, 2145–2157.

Bouvet, A., Mermoz, S., Le Toan, T., Villard, L., Mathieu, R., Naidoo, L., Asner, G.P., 2018. An above-ground biomass map of African savannahs and woodlands at 25 m resolution derived from ALOS PALSAR. Remote Sens. Environ. 206, 156–173. doi:10.1016/j.rse.2017.12.030.

Box, E.O., 1981. Predicting physiognomic vegetation types with climate variables. Vegetatio 45, 127–139. doi:10.1007/BF00119222.

Box, E.O., 1996. Plant functional types and climate at the global scale. J. Veg. Sci. 7, 309–320. doi:10.2307/3236274.

Bradstock, R.A., Cohn, J.S., Gill, A.M., Bedward, M., Lucas, C., 2009. Prediction of the probability of large fires in the Sydney region of south-eastern Australia using fire weather. Int. J. Wildl. Fire 18, 932–943.

Brandt, M., Gominski, D., Reiner, F., Kariryaa, A., Guthula, V.B., Ciais, P., Tong, X., Zhang, W., Govindarajulu, D., Ortiz-Gonzalo, D., et al., 2024. Severe decline in large farmland trees in india over the past decade. Nature Sustainability , 1–9.

Breiman, L., 2001. Random forests. Machine learning 45, 5–32.

Breiman, L., Friedman, J., Olshen, R., Stone, C., 1984. Classification and Regression Trees. Routledge. doi:https://doi.org/10.1201/9781315139470.

Brovkin, V., Claussen, M., Driesschaert, E., Fichefet, T., Kicklighter, D., Loutre, M.F., Matthews, H.D., Ramankutty, N., Schaeffer, M., Sokolov, A., 2006. Biogeophysical effects of historical land cover changes simulated by six Earth system models of intermediate complexity. Clim. Dyn. 26, 587–600. doi:10.1007/s00382-005-0092-6.

Brown, C.F., Brumby, S.P., Guzder-Williams, B., Birch, T., Hyde, S.B., Mazzariello, J., Czerwinski, W., Pasquarella, V.J., Haertel, R., Ilyushchenko, S., et al., 2022. Dynamic world, near real-time global 10 m land use land cover mapping. Scientific Data 9, 251.

Buchhorn, M., Lesiv, M., Tsendbazar, N.E., Herold, M., Bertels, L., Smets, B., 2020a. Copernicus global land cover layers-collection 2. Remote Sens. 12, 1–14. doi:10.3390/rs12061044.

Buchhorn, M., Smets, B., Bertels, L., Roo, B.D., Lesiv, M., Tsendbazar, N.E., Herold, M., Fritz, S., 2020b. Copernicus Global Land Service: Land Cover 100m: collection 3: epoch 2015: Globe. doi:10.5281/zenodo.3939038.

Burini, A., Fox, N., Chander, G., Goryl, P., 2010. The CEOS Cal/Val Portal: a new instrument for the cal/val community, in: Sensors, Syst. Next-Generation Satell. XIV, International Society for Optics and Photonics. p. 782622.

Cai, X., McKinney, D.C., Rosegrant, M.W., 2003. Sustainability analysis for irrigation water management in the Aral Sea region. Agric. Syst. 76, 1043–1066. doi:10.1016/S0308-521X(02)00028-8.

Callendar, G.S., 1938. The artificial production of carbon dioxide and its influence on temperature. Q. J. R. Meteorol. Soc. 64, 223–240.

Campos-Taberner, M., García-Haro, F.J., Martínez, B., Izquierdo-Verdiguier, E., Atzberger, C., Camps-Valls, G., Gilabert, M.A., 2020. Understanding deep learning in land use classification based on sentinel-2 time series. Scientific reports 10, 17188.

Canters, F., 1997. Evaluating the uncertainty of area estimates derived from fuuy land-cover classification. Photogramm. Eng. Remote Sens 63, 403–414.

Cao, X., Chen, J., Chen, L.J., Liao, A.P., Sun, F.D., Li, Y., Li, L., Lin, Z.H., Pang, Z.G., Chen, J., He, C.Y., Peng, S., 2014. Preliminary analysis of spatiotemporal pattern of global land surface water. Sci. China Earth Sci. 57, 2330–2339. doi:10.1007/s11430-014-4929-x.

Carroll, M.L., Townshend, J.R., DiMiceli, C.M., Noojipady, P., Sohlberg, R.A., 2009. A new global raster water mask at 250 m resolution. Int. J. Digit. Earth 2, 291–308.

CEOS, 2024. Working Group on Calibration & Validation. URL: https://ceos.org/ourwork/workinggroups/wgcv/.

Chen, J., Chen, J., Liao, A., Cao, X., Chen, L., Chen, X., He, C., Han, G., Peng, S., Lu, M., Others, 2015a. Global land cover mapping at 30m resolution: A POK-based operational approach. ISPRS J. Photogramm. Remote Sens. 103, 7–27.

Chen, L., Michishita, R., Xu, B., 2014. Abrupt spatiotemporal land and water changes and their potential drivers in poyang lake, 2000–2012. ISPRS journal of photogrammetry and remote sensing 98, 85–93.

Chen, X., Liang, S., Cao, Y., He, T., Wang, D., 2015b. Observed contrast changes in snow cover phenology in northern middle and high latitudes from 2001-2014. Sci. Rep. 5, 1–9. doi:10.1038/srep16820.

Claverie, M., Ju, J., Masek, J.G., Dungan, J.L., Vermote, E.F., Roger, J.C., Skakun, S.V., Justice, C., 2018. The harmonized landsat and sentinel-2 surface reflectance data set. Remote sensing of environment 219, 145–161.

Congalton, R., Green, K., 2009. Assessing the Accuracy of Remotely Sensed Data: Principles and Practices. Mapping Science Series, CRC Press/Taylor & Francis. URL: https://books.google.be/books?id=FKssAQAAMAAJ.

Congalton, R.G., 1988. A comparison of sampling schemes used in generating error matrices for assessing the accuracy of maps generated from remotely sensed data. Photogrammetric engineering and remote sensing .

Congalton, R.G., 1991. A review of assessing the accuracy of classifications of remotely sensed data. Remote Sens. Environ. 37, 35–46.

Congalton, R.G., Green, K., 2019. Assessing the accuracy of remotely sensed data: principles and practices. CRC press.

Connor, R., 2015. The United Nations world water development report 2015: water for a sustainable world. volume 1. UNESCO Publishing.

Coppo, P., Taiti, A., Pettinato, L., Francois, M., Taccola, M., Drusch, M., 2017. Fluorescence imaging spectrometer (floris) for esa flex mission. Remote Sensing 9, 649.

Dale, V.H., 1997. The relationship between land-use change and climate change. Ecol. Appl. 7, 753–769. doi:10.1890/1051-0761(1997)007[0753:TRBLUC]2.0.CO;2.

Danielson, J.J., Gesch, D.B., et al., 2011. Global multi-resolution terrain elevation data 2010 (gmted2010) .

Davidson, A., Csillag, F., 2003. A comparison of three approaches for predicting c4 species cover of northern mixed grass prairie. Remote Sensing of Environment 86, 70–82.

Dee, D.P., Uppala, S.M., Simmons, A.J., Berrisford, P., Poli, P., Kobayashi, S., Andrae, U., Balmaseda, M.A., Balsamo, G., Bauer, P., Bechtold, P., Beljaars, A.C.M., van de Berg, L., Bidlot, J., Bormann, N., Delsol, C., Dragani, R., Fuentes, M., Geer, A.J., Haimberger, L., Healy, S.B., Hersbach, H., Hólm, E.V., Isaksen, L., Kållberg, P., Köhler, M., Matricardi, M., Mcnally, A.P., Monge-Sanz, B.M., Morcrette, J.J., Park, B.K., Peubey, C., de Rosnay, P., Tavolato, C., Thépaut, J.N., Vitart, F., 2011. The ERA-Interim reanalysis: Configuration and performance of the data assimilation system. Q. J. R. Meteorol. Soc. 137, 553–597. doi:10.1002/qj.828.

Defourny, P., Bicheron, P., Brockman, C., Bontemps, S., Van Bogaert, E., Vancutsem, C., Pekel, J.F., Huc, M., Henry, C.C., Ranera, F., Others, 2009. The first 300 m global land cover map for 2005 using ENVISAT MERIS time series: A product of the GlobCover system, in: 33rd Int. Symp. Remote Sens. Environ.

Defourny, P., Bontemps, S., 2012. Revisiting land-cover mapping concepts. Remote Sensing of Land Use and Land Cover: Principles and Applications , 49–63.

Defourny, P., Lamarche, C., Bontemps, S., De Maet, T., Van Bogaert, E., Moreau, I., Brockmann, C., Boettcher, M., Kirches, G., Wevers, J., Santoro, M., Ramoino, F., Arino, O., 2017a. Land

Cover CCI Product User Guide Version 2.0. Technical Report. ESA, UCLouvain-Geomatics(Belgium). URL: http://maps.elie.ucl.ac.be/CCI/viewer/download/ESACCI-LC-Ph2-PUGv2_2.0.pdf.

Defourny, P., Lamarche, C., Bontemps, S., De Maet, T., Van Bogaert, E., Radoux, J., Moreau, I., Ramoino, F., Arino, O., 2017b. Land Cover CCI Algorithm Theoretical Basis Document. Part III. Classification. 1.2. Technical Report. UCLouvain. URL: https://www.esa-landcover-cci.org/?q=webfm_send/139.

Defourny, P., Lamarche, C., Marissiaux, Q., 2021. Copernicus Climate Change Service Product Quality Assessment Report. ICDR Land Cover 2016-2020. Technical Report. ECMWF, UCLouvain. URL: https://datastore.copernicus-climate.eu/documents/satellite-land-cover/D5.2.2{_}PQAR{_}ICDR{_}LC{_}v2.1.x{_}PRODUCTS{_}v1.0.pdf.

Defourny, P., Mayaux, P., Herold, M., Bontemps, S., 2012a. Global land-cover map validation experiences: toward the characterization of quantitative uncertainty. Remote Sens. L. Use L. Cover Princ. Appl. .

Defourny, P., Mayaux, P., Herold, M., Bontemps, S., 2012b. Global Land Cover Map Validation Experiences: Toward the Characterization of Quantitative Uncertainty, in: "Remote Sensing of Land Use and Land Cover : Principles and Applications". Taylor and Francis, pp. 207–223. URL: http://dial.uclouvain.be/handle/boreal:114555.

Defourny, P., Mayaux, P., Herold, M., Bontemps, S., 2012c. Global Land Cover Map Validation Experiences: Toward the Characterization of Quantitative Uncertainty. Taylor and Francis.

Defourny, P., Vancutsem, C., Bicheron, C., Brockmann, C., Nino, F., Schouten, L., Leroy, M., 2007. GlobCover: A 300M Global Land Cover Product for 2005 Using ENVISAT MERIS Time Series. Proc. ISPRS Comm. VII Mid-Term Symp. , 8–11.

Derksen, C., Brown, R., 2012. Spring snow cover extent reductions in the 2008-2012 period exceeding climate model projections. Geophys. Res. Lett. 39, 1–6. doi:10.1029/2012GL053387.

DeVries, B., Decuyper, M., Verbesselt, J., Zeileis, A., Herold, M., Joseph, S., 2015. Tracking disturbance-regrowth dynamics in tropical forests using structural change detection and landsat time series. Remote Sensing of Environment 169, 320–334.

Dhu, T., Dunn, B., Lewis, B., Lymburner, L., Mueller, N., Telfer, E., Lewis, A., McIntyre, A., Minchin, S., Phillips, C., 2017. Digital earth australia–unlocking new value from earth observation data. Big Earth Data 1, 64–74.

Di Gregorio, A., 2005. Land cover classification system: classification concepts and user manual: LCCS. 8, Food & Agriculture Org.

Di Gregorio, A., Jansen, L., 2005. Land Cover Classification System (LCCS): Classification Concepts and User Manual. volume 53. Food & Agriculture Org. arXiv:arXiv:1011.1669v3.

Díaz, S.M., Settele, J., Brond\'\izio, E., Ngo, H., Guèze, M., Agard, J., Arneth, A., Balvanera, P., Brauman, K., Butchart, S., Others, 2019. The global assessment report on biodiversity and ecosystem services: Summary for policy makers .

Dierckx, W., Sterckx, S., Benhadj, I., Livens, S., Duhoux, G., Van Achteren, T., Francois, M., Mellab, K., Saint, G., 2014. PROBA-V mission for global vegetation monitoring: standard products and image quality. Int. J. Remote Sens. 35, 2589–2614.

Dierckx, W., Swinnen, E., Kempeneers, P., 2015. Validation of spectral continuity between PROBA-V and SPOT-VEGETATION global daily datasets. Int. Arch. Photogramm. Remote Sens. Spat. Inf. Sci. - ISPRS Arch. 40, 1155–1162. doi:10.5194/isprsarchives-XL-7-W3-1155-2015.

Donchyts, G., Baart, F., Winsemius, H., Gorelick, N., Kwadijk, J., Van De Giesen, N., 2016. Earth's surface water change over the past 30 years. Nat. Clim. Chang. 6, 810–813. doi:10.1038/nclimate3111.

Donlon, C., 2011. Sentinel-3 Mission Requirements Traceability Document (MRTD). Technical Report EOP-SM/2184/CD-cd. ESA. URL: https://sentinel.esa.int/documents/247904/1848151/Sentinel-3-Mission-Requirements-Traceability.

Donlon, C., Berruti, B., Buongiorno, a., Ferreira, M.H., Féménias, P., Frerick, J., Goryl, P., Klein, U., Laur, H., Mavrocordatos, C., Nieke, J., Rebhan, H., Seitz, B., Stroede, J., Sciarra, R., 2012. The Global Monitoring for Environment and Security (GMES) Sentinel-3 mission. Remote Sensing of Environment 120, 37–57. doi:10.1016/j.rse.2011.07.024.

Doppler, L., Preusker, R., Bennartz, R., Fischer, J., 2014. k-bin and k-ir: k-distribution methods without correlation approximation for non-fixed instrument response function and extension to the thermal infrared—applications to satellite remote sensing. Journal of Quantitative Spectroscopy and Radiative Transfer 133, 382–395. doi:https://doi.org/10.1016/j.jqsrt.2013.09.001.

Downing, J.A., Cole, J.J., 2006. The global abundance and size distribution of lakes , ponds , and impoundments 51, 2388–2397.

Drusch, M., Del Bello, U., Carlier, S., Colin, O., Fernandez, V., Gascon, F., Hoersch, B., Isola, C., Laberinti, P., Martimort, P., et al., 2012. Sentinel-2: Esa's optical high-resolution mission for gmes operational services. Remote Sensing of Environment 120, 25–36.

Duveiller, G., Baret, F., Defourny, P., 2011. Crop specific green area index retrieval from modis data at regional scale by controlling pixel-target adequacy. Remote Sensing of Environment 115, 2686–2701.

Dwyer, J.L., Roy, D.P., Sauer, B., Jenkerson, C.B., Zhang, H.K., Lymburner, L., 2018. Analysis ready data: enabling analysis of the landsat archive. Remote Sensing 10, 1363.

Edwards, G., Lowell, K.E., 1996. Modeling uncertainty in photointerpreted

boundaries. Photogrammetric Engineering and Remote Sensing 62, 377–390.

Erb, K.H., Gaube, V., Krausmann, F., Plutzar, C., Bondeau, A., Haberl, H., 2007. A comprehensive global 5 min resolution land-use data set for the year 2000 consistent with national census data. J. Land Use Sci. 2, 191–224. doi:10.1080/17474230701622981.

ESA, 2023. Specifications - Sentinel-3 OLCI Technical Guide - Sentinel Online. URL: https://sentinel.esa.int/web/sentinel/technical-guides/sentinel-3-olci/olci-instrument/specifications. accessed 2023-06-23.

ESA, 2024a. ESA-CCI HRLC. URL: https://climate.esa.int/en/projects/high-resolution-land-cover/.

ESA, 2024b. SEN4STAT. URL: https://www.esa-sen4stat.org/.

Esch, T., Heldens, W., Hirner, A., Keil, M., Marconcini, M., Roth, A., Zeidler, J., Dech, S., Strano, E., 2017. Breaking new ground in mapping human settlements from space - The Global Urban Footprint. ISPRS J. Photogramm. Remote Sens. 134, 30–42. doi:10.1016/j.isprsjprs.2017.10.012, arXiv:1706.04862.

Estes, J.E., Simonett, D.S., 1975. Fundamentals of image interpretation. Man. Remote Sens. 1, 869–1076.

Europa-Technologies, 2014. Europa technologies global insight. URL: https://www.europa.uk.com/map-data/global-map-data/global-insight/.

Fahy, J., Fox, N., Gardiner, T., Green, P., Hunt, S., Mittaz, J., Mota, B., De Vis, P., Woolliams, E., 2022. Metrological Approach for Eo General Guidance on a Metrological Approach To Fundamental Data Records (Fdr), Thematic Data Products (Tdps) and Fiducial Reference Measurements (Frms)-Executive Summary , 1–13URL: https://qa4eo.org/docs/1{_}Executive{_}Summary.pdf.

Fahy, J.S., Hunt, S.E., 2021. Uncertainty analysis for sentinel-3 olci radiance observations, in: 2021 IEEE International Geoscience and Remote Sensing Symposium IGARSS, IEEE. pp. 8150–8153.

Fang, X., Zhu, Q., Ren, L., Chen, H., Wang, K., Peng, C., 2018. Large-scale detection of vegetation dynamics and their potential drivers using modis images and bfast: A case study in quebec, canada. Remote Sensing of Environment 206, 391–402.

FAO, 2017. FAOSTAT Agri-Environmental Indicators, Land Cover. Technical Report. URL: https://fenixservices.fao.org/faostat/static/documents/LC/LC_e.pdf.

FAO, 2021a. FAO. URL: http://www.fao.org/faostat/en/{#}data/RL.

FAO, 2021b. Land use statistics and indicators Global, regional and country trends. Technical Report. FAO. Rome. URL: https://www.fao.org/3/cb6033en/cb6033en.pdf.

FAO, JRC, SDSU, UCL, 2009. The 2010 Global Forest Resources Assessment Remote Sensing Survey: an outline of the objectives, data, methods and approach. For. Resour. Assess. Work. Pap. 155, 10.

Faraway, J.J., Augustin, N.H., 2018. When small data beats big data. Statistics & Probability Letters 136, 142–145.

Farr, T.G., Rosen, P.A., Caro, E., Crippen, R., Duren, R., Hensley, S., Kobrick, M., Paller, M., Rodriguez, E., Roth, L., et al., 2007. The shuttle radar topography mission. Reviews of geophysics 45.

Feddema, J., Oleson, K., Bonan, G., Mearns, L., Washington, W., Meehl, G., Nychka, D., 2005. A comparison of a GCM response to historical anthropogenic land cover change and model sensitivity to uncertainty in present-day land cover representations. Clim. Dyn. 25, 581–609. doi:10.1007/s00382-005-0038-z.

Feng, M., Sexton, J.O., Channan, S., Townshend, J.R., 2016. A global, high-resolution (30-m) inland water body dataset for 2000: First results of a topographic–spectral classification algorithm. International Journal of Digital Earth 9, 113–133.

FIDUCEO, 2023. Fidelity and Uncertainty in Climate Data Records from Earth Observations. URL: https://research.reading.ac.uk/fiduceo/.

Fischer, J., Grassl, H., 1984. Radiative transfer in an atmosphere–ocean system: an azimuthally dependent matrix-operator approach. Appl. Opt. 23, 1032–1039. doi:10.1364/AO.23.001032.

Fisher, R.A., Koven, C.D., 2020. Perspectives on the Future of Land Surface Models and the Challenges of Representing Complex Terrestrial Systems. J. Adv. Model. Earth Syst. 12. doi:10.1029/2018MS001453.

Flato, G., Marotzke, J., Abiodun, B., Braconnot, P., Chou, S.C., Collins, W.J., Cox, P., Driouech, F., Emori, S., Eyring, V., Forest, C., Gleckler, P., Guilyardi, E., Jakob, C., Kattsov, V., Reason, C., Rummukaines, M., 2013. Evaluation of Climate Models. In: Climate Change 2013: The Physical Science Basis. Contribution of Working Group I to the Fifth Assessment Report of the Intergovernmental Panel on Climate Change, in: (WMO), W.M.O., (UNEP), U.N.E.P. (Eds.), Climate Change 2013. Cambridge University Press, pp. 741–866. doi:10.1017/CBO9781107415324.020.

Foerster, K.P., et al., 2008. Environmental mapping and analysis program (enmap)-recent advances and status, in: IGARSS 2008-2008 IEEE International Geoscience and Remote Sensing Symposium, IEEE. pp. IV–109.

Foley, J.A., DeFries, R., Asner, G.P., Barford, C., Bonan, G., Carpenter, S.R., Chapin, F.S., Coe, M.T., Daily, G.C., Gibbs, H.K., Helkowski, J.H., Holloway, T., Howard, E.A., Kucharik, C.J., Monfreda, C., Patz, J.A., Prentice, I.C., Ramankutty, N., Snyder, P.K., 2005. Global consequences of land use. Sci. (80-.). 309, 570–574. doi:10.1126/science.1111772.

Foody, G.M., 2004. Thematic map comparison: Evaluating the statistical significance of differences in classification accuracy. Photogramm. Eng. Remote Sensing 70, 627–633. doi:10.14358/PERS.70.5.627.

Fox, A., Herbert, D., Fretwell, P., Fleming, A., . Scar antarctic digital database v 6.0 .

Fox, N., 2010. A guide to expression of uncertainty of measurements. Technical Report QA4EO-QAEO-GEN-DQK-006. QA4EO. URL: https://qa4eo.org/docs/QA4EO-QAEO-GEN-DQK-006_v4.0.pdf.

Friedl, M.A., McIver, D.K., Hodges, J.C.F., Zhang, X.Y., Muchoney, D., Strahler, A.H., Woodcock, C.E., Gopal, S., Schneider, A., Cooper, A., Others, 2002. Global land cover mapping from MODIS: algorithms and early results. Remote Sens. Environ. 83, 287–302.

Friedl, M.A., Sulla-Menashe, D., Tan, B., Schneider, A., Ramankutty, N., Sibley, A., Huang, X., 2010. MODIS Collection 5 global land cover: Algorithm refinements and characterization of new datasets. Remote Sens. Environ. 114, 168–182.

Friedl, M.A., Woodcock, C.E., Olofsson, P., Zhu, Z., Loveland, T., Stanimirova, R., Arevalo, P., Bullock, E., Hu, K.T., Zhang, Y., Turlej, K., Tarrio, K., McAvoy, K., Gorelick, N., Wang, J.A., Barber, C.P., Souza, C., 2022. Medium Spatial Resolution Mapping of Global Land Cover and Land Cover Change Across Multiple Decades From Landsat. Front. Remote Sens. 3, 1–15. doi:10.3389/frsen.2022.894571.

Friedlingstein, P., Jones, M.W., Sullivan, M.O., Andrew, R.M., Bakker, D.C.E., Hauck, J., Quéré, C.L., Peters, G.P., Peters, W., 2022. Global Carbon Budget 2021. Earth Syst. Sci. Data 14, 1917–2005. URL: https://doi.org/10.5194/essd-14-1917-2022.

Fritz, S., See, L., 2008. Identifying and quantifying uncertainty and spatial disagreement in the comparison of global land cover for different applications. Global Change Biology 14, 1057–1075.

Fuchs, R., Schulp, C.J., Hengeveld, G.M., Verburg, P.H., Clevers, J.G., Schelhaas, M.J., Herold, M., 2016. Assessing the influence of historic net and gross land changes on the carbon fluxes of Europe. Glob. Chang. Biol. 22, 2526–2539. doi:10.1111/gcb.13191.

Fyson, C.L., Jeffery, M.L., 2019. Ambiguity in the Land Use Component of Mitigation Contributions Toward the Paris Agreement Goals. Earth's Futur. 7, 873–891. doi:10.1029/2019EF001190.

Galatowitsch, S.M., 2018. Natural and Anthropogenic Drivers of Wetland Change. Springer Netherlands, Dordrecht. pp. 359–367. doi:10.1007/978-94-007-4001-3_217.

Gao, B.C., 1996. Ndwi—a normalized difference water index for remote sensing of vegetation liquid water from space. Remote sensing of environment 58, 257–266.

GCOS, 2006. Satellite-based products for climate. Supplemental details to the satellite-based component of the. WMO 107, 90. URL: http://ams.confex.com/ams/87ANNUAL/techprogram/paper_117467.htm.

GCOS, 2022. The 2022 gcos ecvs requirements (gcos 245) , 244URL: https://library.wmo.int/index.php?lvl=notice_display{&}id=22135{#}.Y0bua3bMKUk.

van der Geest, K., de Sherbinin, A., Kienberger, S., Zommers, Z., Sitati, A., Roberts, E., James, R., 2019. The Impacts of Climate Change on Ecosys-

tem Services and Resulting Losses and Damages to People and Society. Springer International Publishing, Cham. pp. 221–236. doi:10.1007/978-3-319-72026-5_9.

GEO, 2013. The geoss water strategy, from observations to decision, executive summary and full report.

Ghent, D., Veal, K., Trent, T., Dodd, E., Sembhi, H., Remedios, J., 2019. A new approach to defining uncertainties for modis land surface temperature. Remote Sensing 11. doi:10.3390/rs11091021.

Giri, C., Ochieng, E., Tieszen, L.L., Zhu, Z., Singh, A., Loveland, T., Masek, J., Duke, N., 2011. Status and distribution of mangrove forests of the world using earth observation satellite data. Glob. Ecol. Biogeogr. 20, 154–159. doi:10.1111/j.1466-8238.2010.00584.x.

GLIMS, . Randolph Glacier Inventory. URL: http://www.glims.org/RGI/.

Gong, P., Liu, H., Zhang, M., Li, C., Wang, J., Huang, H., Clinton, N., Ji, L., Li, W., Bai, Y., Chen, B., Xu, B., Zhu, Z., Yuan, C., Ping Suen, H., Guo, J., Xu, N., Li, W., Zhao, Y., Yang, J., Yu, C., Wang, X., Fu, H., Yu, L., Dronova, I., Hui, F., Cheng, X., Shi, X., Xiao, F., Liu, Q., Song, L., 2019. Stable classification with limited sample: transferring a 30-m resolution sample set collected in 2015 to mapping 10-m resolution global land cover in 2017. Sci. Bull. 64, 370–373. doi:10.1016/j.scib.2019.03.002.

Gong, P., Wang, J., Yu, L., Zhao, Y., Zhao, Y., Liang, L., Niu, Z., Huang, X., Fu, H., Liu, S., Others, 2013. Finer resolution observation and monitoring of global land cover: First mapping results with Landsat TM and ETM+ data. Int. J. Remote Sens. 34, 2607–2654.

Goodchild, M.F., Guoqing, S., Ren, Y.S., 1992. Development and test of an error model for categorical data. Int. J. Geogr. Inf. Syst. 6, 87–104. doi:10.1080/02693799208901898.

Gorelick, N., Hancher, M., Dixon, M., Ilyushchenko, S., Thau, D., Moore, R., 2017. Google earth engine: Planetary-scale geospatial analysis for everyone. Remote sensing of Environment 202, 18–27.

Gorroño, J., Fomferra, N., Peters, M., Gascon, F., Underwood, C.I., Fox, N.P., Kirches, G., Brockmann, C., 2017. A radiometric uncertainty tool for the sentinel 2 mission. Remote Sens. 9, 1–25. doi:10.3390/rs9020178.

Gregorio, A.D., 2016. Land Cover Classification System. October. URL: http://www.fao.org/docrep/003/x0596e/x0596e00.htm.

Guanter, L., Brell, M., Chan, J.C.W., Giardino, C., Gomez-Dans, J., Mielke, C., Morsdorf, F., Segl, K., Yokoya, N., 2019. Synergies of spaceborne imaging spectroscopy with other remote sensing approaches. Surveys in Geophysics 40, 657–687.

Guo, H., Liu, Z., Jiang, H., Wang, C., Liu, J., Liang, D., 2017. Big earth data: A new challenge and opportunity for digital earth's development. International Journal of Digital Earth 10, 1–12.

Hansen, M.C., Potapov, P.V., Moore, R., Hancher, M., Turubanova, S., Tyukavina, A., Thau, D., Stehman, S., Goetz, S., Loveland, T., et al., 2013a. High-

resolution global maps of 21st-century forest cover change. Science 342, 850–853.

Hansen, M.C., Potapov, P.V., Moore, R., Hancher, M., Turubanova, S.A., Tyukavina, A., Thau, D., Stehman, S.V., Goetz, S.J., Loveland, T.R., Kommareddy, A., Egorov, A., Chini, L., Justice, C.O., Townshend, J.R., 2013b. High-resolution global maps of 21st-century forest cover change. Science (80-.). 342, 850–853. doi:10.1126/science.1244693.

Hansen, M.C., Potapov, P.V., Pickens, A.H., Tyukavina, A., Hernandez-Serna, A., Zalles, V., Turubanova, S., Kommareddy, I., Stehman, S.V., Song, X.P., Kommareddy, A., 2022. Global land use extent and dispersion within natural land cover using Landsat data. Environ. Res. Lett. 17. doi:10.1088/1748-9326/ac46ec.

Harase, S., Kimoto, T., 2018. Implementing 64-bit maximally equidistributed f2-linear generators with mersenne prime period. ACM Trans. Math. Softw. 44. doi:10.1145/3159444.

Hariri, R.H., Fredericks, E.M., Bowers, K.M., 2019. Uncertainty in big data analytics: survey, opportunities, and challenges. Journal of Big data 6, 1–16.

Harris, P., Cox, M., 2014. On a monte carlo method for measurement uncertainty evaluation and its implementation. Metrologia 51, S176.

Hartley, A.J., MacBean, N., Georgievski, G., Bontemps, S., 2017. Uncertainty in plant functional type distributions and its impact on land surface models. Remote Sens. Environ. 203, 71–89. doi:10.1016/j.rse.2017.07.037.

Haščič, I., Mackie, A., 2018. Land Cover Change and Conversions: Methodology and Results for OECD and G20 Countries. OECD Green Growth Pap. 2018, 60. doi:10.1787/72A9E331-EN.

Hawkins, E., Frame, D., Harrington, L., Joshi, M., King, A., Rojas, M., Sutton, R., 2020. Observed Emergence of the Climate Change Signal: From the Familiar to the Unknown. Geophys. Res. Lett. 47. doi:10.1029/2019GL086259.

Hegglin, M.I., Bastos, A., Bovensmann, H., Buchwitz, M., Fawcett, D., Ghent, D., Kulk, G., Sathyendranath, S., Shepherd, T.G., Quegan, S., Röthlisberger, R., Briggs, S., Buontempo, C., Cazenave, A., Chuvieco, E., Ciais, P., Crisp, D., Engelen, R., Fadnavis, S., Herold, M., Horwath, M., Jonsson, O., Kpaka, G., Merchant, C.J., Mielke, C., Nagler, T., Paul, F., Popp, T., Quaife, T., Rayner, N.A., Robert, C., Schröder, M., Sitch, S., Venturini, S., van der Schalie, R., van der Vliet, M., Wigneron, J.P., Woolway, R.I., 2022. Space-based Earth observation in support of the UNFCCC Paris Agreement. Front. Environ. Sci. 10, 1–23. doi:10.3389/fenvs.2022.941490.

Herold, M., 2009. Assessment of the status of the development of the standards for the terrestrial essential climate variables - ECV-T9: Land cover. GTOS-64. Glob. Terr. Obs. Syst. 10, 36. URL: http://www.fao.org/gtos/doc/ECVs/T09/T09.pdf.

Herold, M., Di Gregorio, A., 2012. Evaluating land-cover legends using the

UN land-cover classification system, in: Giri, C. (Ed.), Remote Sens. L. Use L. Cover Princ. Appl.. CRC Press, South Dakota. chapter 6, p. 477.

Herold, M., Gardner, M.E., Noronha, V., Roberts, D.A., 2003. Spectrometry and hyperspectral remote sensing of urban road infrastructure. Online Journal of Space Communication 2, 9.

Herold, M., van Groenestijn, A., Kooistra, L., Kalogirou, V., Arino, O., 2010. User Requirements Document of the Land Cover CCI project. Technical Report.

Herold, M., Hubald, R., Di Gregorio, A., 2009. Translating and evaluating land cover legends using the un land cover classification system (lccs). GOGC-GOLD Report 43.

Herold, M., Mayaux, P., Woodcock, C., Baccini, A., Schmullius, C., 2008. Some challenges in global land cover mapping: An assessment of agreement and accuracy in existing 1 km datasets. Remote Sensing of Environment 112, 2538–2556.

Hersbach, H., Bell, B., Berrisford, P., Hirahara, S., Horányi, A., Muñoz-Sabater, J., Nicolas, J., Peubey, C., Radu, R., Schepers, D., Simmons, A., Soci, C., Abdalla, S., Abellan, X., Balsamo, G., Bechtold, P., Biavati, G., Bidlot, J., Bonavita, M., De Chiara, G., Dahlgren, P., Dee, D., Diamantakis, M., Dragani, R., Flemming, J., Forbes, R., Fuentes, M., Geer, A., Haimberger, L., Healy, S., Hogan, R.J., Hólm, E., Janisková, M., Keeley, S., Laloyaux, P., Lopez, P., Lupu, C., Radnoti, G., de Rosnay, P., Rozum, I., Vamborg, F., Villaume, S., Thépaut, J.N., 2020. The ERA5 global reanalysis. Q. J. R. Meteorol. Soc. 146, 1999–2049. doi:10.1002/qj.3803.

Hibbard, K., Janetos, A., Van Vuuren, D.P., Pongratz, J., Rose, S.K., Betts, R., Herold, M., Feddema, J.J., 2010. Research priorities in land use and land-cover change for the Earth system and integrated assessment modelling. Int. J. Climatol. 30, 2118–2128. doi:10.1002/joc.2150.

Hollmann, R., Merchant, C.J., Saunders, R., Downy, C., Buchwitz, M., Cazenave, A., Chuvieco, E., Defourny, P., de Leeuw, G., Forsberg, R., Holzer-Popp, T., Paul, F., Sandven, S., Sathyendranath, S., van Roozendael, M., Wagner, W., 2013. The ESA Climate Change Initiative: Satellite Data Records for Essential Climate Variables. Bull. Am. Meteorol. Soc. 94, 1541–1552. doi:10.1175/BAMS-D-11-00254.1.

Hollstein, A., Fischer, J., 2012. Radiative transfer solutions for coupled atmosphere ocean systems using the matrix operator technique. Journal of Quantitative Spectroscopy and Radiative Transfer 113, 536–548. doi:https://doi.org/10.1016/j.jqsrt.2012.01.010.

Houghton, R.A., 2005. Aboveground forest biomass and the global carbon balance. Glob. Chang. Biol. 11, 945–958. doi:10.1111/j.1365-2486.2005.00955.x.

Houghton, R.A., House, J.I., Pongratz, J., Van Der Werf, G.R., Defries, R.S., Hansen, M.C., Le Quéré, C., Ramankutty, N., 2012. Carbon emissions

from land use and land-cover change. Biogeosciences 9, 5125–5142. doi:10.5194/bg-9-5125-2012.

Houghton, R.A., Nassikas, A.A., 2017. Global and regional fluxes of carbon from land use and land cover change 1850-2015. Global Biogeochem. Cycles 31, 456–472. doi:10.1002/2016GB005546.

Hua, T., Zhao, W., Liu, Y., Wang, S., Yang, S., 2018. Spatial consistency assessments for global land-cover datasets: A comparison among GLC2000, CCI LC, MCD12, GLOBCOVER and GLCNMO. Remote Sens. 10. doi:10.3390/rs10111846.

Huang, C., Townshend, J.R.G., Liang, S., Kalluri, S.N.V., DeFries, R.S., 2002. Impact of sensor's point spread function on land cover characterization: Assessment and deconvolution. Remote Sens. Environ. 80, 203–212. doi:10.1016/S0034-4257(01)00298-X.

Iannini, L., Molijn, R., Mousivand, A., Hanssen, R., Lamparelli, R., 2016. A HMM-based approach for historic and up-to-date land cover mapping through Landsat time-series in the state of Sao Paulo, Brazil. Int. Geosci. Remote Sens. Symp. 2016-Novem, 5457–5460. doi:10.1109/IGARSS.2016.7730421.

IPCC, . Technical Guidelines, Fact Sheets and other Supporting Material. URL: http://www.ipcc-data.org/guidelines/.

IPCC, 2014. IPCC Fifth Assessment Synthesis Report-Climate Change 2014 Synthesis Report. IPCC Fifth Assess. Synth. Report-Climate Chang. 2014 Synth. Rep. .

IPCC, 2021. Regional fact sheet - Introduction. Clim. Chang. 2021 Phys. Sci. basis IPCC Work. Gr. I Sixth Assess. Rep. , 2URL: https://www.ipcc.ch/report/ar6/wg1/downloads/factsheets/IPCC_AR6_WGI_Regional_Fact_Sheet_Introduction.pdf.

IPCC, 2022. Climate Change 2022: Mitigation of Climate Change. Working Group III Contribution to the Sixth Assessment Report of the Intergovernmental Panel on Climate Change. Technical Report. Cambridge University Press. In Press. URL: https://www.ipcc.ch/report/ar6/wg3/downloads/report/IPCC_AR6_WGIII_FullReport.pdf.

Jacobsen, A., de Miranda Azevedo, R., Juty, N., Batista, D., Coles, S., Cornet, R., Courtot, M., Crosas, M., Dumontier, M., Evelo, C.T., et al., 2020. Fair principles: interpretations and implementation considerations.

JCGM, 2008. Evaluation of measurement data — Supplement 1 to the "Guide to the expression of uncertainty in measurement" — Propagation of distributions using a Monte Carlo method. Joint Committee for Guides in Metrology (BIPM and IEC and IFCC and ILAC and ISO and IUPAC and IUPAP and OIML), JCGM 101:2008. URL: https://www.bipm.org/documents/20126/2071204/JCGM_101_2008_E.pdf/325dcaad-c15a-407c-1105-8b7f322d651c.

JCGM, 2008. JCGM 101:2008 Supplement 1 - Propagation of distributions using a Monte Carlo method. Technical Report. JCGM.

JCGM 200, 2008. JCGM 200 : 2008 International vocabulary of metrology — Basic and general concepts and associated terms (VIM) Vocabulaire international de métrologie — Concepts fondamentaux et généraux et termes associés (VIM). Int. Organ. Stand. Geneva ISBN 3, 104. doi:10.1016/0263-2241(85)90006-5.

Jeong, S.J., Medvigy, D., Shevliakova, E., Malyshev, S., 2012. Uncertainties in terrestrial carbon budgets related to spring phenology. J. Geophys. Res. Biogeosciences 117, 1–17. doi:10.1029/2011JG001868.

Joe, S., Kuo, F.Y., 2003. Remark on algorithm 659: Implementing sobol's quasirandom sequence generator. ACM Trans. Math. Softw. 29, 49–57. doi:10.1145/641876.641879.

Joe, S., Kuo, F.Y., 2008. Constructing sobol sequences with better two-dimensional projections. SIAM Journal on Scientific Computing 30, 2635–2654. doi:10.1137/070709359, arXiv:https://doi.org/10.1137/070709359.

Jung, M., Henkel, K., Herold, M., Churkina, G., 2006. Exploiting synergies of global land cover products for carbon cycle modeling. Remote Sens. Environ. 101, 534–553. doi:10.1016/j.rse.2006.01.020.

Karra, K., Kontgis, C., Statman-Weil, Z., Mazzariello, J.C., Mathis, M., Brumby, S.P., 2021. Global land use/land cover with Sentinel 2 and deep learning, in: 2021 IEEE Int. Geosci. Remote Sens. Symp. IGARSS, IEEE. pp. 4704–4707.

Kattge, J., Bönisch, G., Díaz, S., Lavorel, S., Prentice, I.C., Leadley, P., Tautenhahn, S., Werner, G.D., Aakala, T., Abedi, M., Acosta, A.T., Adamidis, G.C., Adamson, K., Aiba, M., Albert, C.H., Alcántara, J.M., Alcázar C, C., Aleixo, I., Ali, H., Amiaud, B., Ammer, C., Amoroso, M.M., Anand, M., Anderson, C., Anten, N., Antos, J., Apgaua, D.M.G., Ashman, T.L., Asmara, D.H., Asner, G.P., Aspinwall, M., Atkin, O., Aubin, I., Baastrup-Spohr, L., Bahalkeh, K., Bahn, M., Baker, T., Baker, W.J., Bakker, J.P., Baldocchi, D., Baltzer, J., Banerjee, A., Baranger, A., Barlow, J., Barneche, D.R., Baruch, Z., Bastianelli, D., Battles, J., Bauerle, W., Bauters, M., Bazzato, E., Beckmann, M., Beeckman, H., Beierkuhnlein, C., Bekker, R., Belfry, G., Belluau, M., Beloiu, M., Benavides, R., Benomar, L., Berdugo-Lattke, M.L., Berenguer, E., Bergamin, R., Bergmann, J., Bergmann Carlucci, M., Berner, L., Bernhardt-Römermann, M., Bigler, C., Bjorkman, A.D., Blackman, C., Blanco, C., Blonder, B., Blumenthal, D., Bocanegra-González, K.T., Boeckx, P., Bohlman, S., Böhning-Gaese, K., Boisvert-Marsh, L., Bond, W., Bond-Lamberty, B., Boom, A., Boonman, C.C., Bordin, K., Boughton, E.H., Boukili, V., Bowman, D.M., Bravo, S., Brendel, M.R., Broadley, M.R., Brown, K.A., Bruelheide, H., Brumnich, F., Bruun, H.H., Bruy, D., Buchanan, S.W., Bucher, S.F., Buchmann, N., Buitenwerf, R., Bunker, D.E., Bürger, J., Burrascano, S., Burslem, D.F., Butterfield, B.J., Byun, C., Marques, M., Scalon, M.C., Caccianiga, M., Cadotte, M., Cailleret, M., Camac, J., Camarero, J.J.,

Campany, C., Campetella, G., Campos, J.A., Cano-Arboleda, L., Canullo, R., Carbognani, M., Carvalho, F., Casanoves, F., Castagneyrol, B., Catford, J.A., Cavender-Bares, J., Cerabolini, B.E., Cervellini, M., Chacón-Madrigal, E., Chapin, K., Chapin, F.S., Chelli, S., Chen, S.C., Chen, A., Cherubini, P., Chianucci, F., Choat, B., Chung, K.S., Chytrý, M., Ciccarelli, D., Coll, L., Collins, C.G., Conti, L., Coomes, D., Cornelissen, J.H., Cornwell, W.K., Corona, P., Coyea, M., Craine, J., Craven, D., Cromsigt, J.P., Csecserits, A., Cufar, K., Cuntz, M., da Silva, A.C., Dahlin, K.M., Dainese, M., Dalke, I., Dalle Fratte, M., Dang-Le, A.T., Danihelka, J., Dannoura, M., Dawson, S., de Beer, A.J., De Frutos, A., De Long, J.R., Dechant, B., Delagrange, S., Delpierre, N., Derroire, G., Dias, A.S., Diaz-Toribio, M.H., Dimitrakopoulos, P.G., Dobrowolski, M., Doktor, D., Dřevojan, P., Dong, N., Dransfield, J., Dressler, S., Duarte, L., Ducouret, E., Dullinger, S., Durka, W., Duursma, R., Dymova, O., E-Vojtkó, A., Eckstein, R.L., Ejtehadi, H., Elser, J., Emilio, T., Engemann, K., Erfanian, M.B., Erfmeier, A., Esquivel-Muelbert, A., Esser, G., Estiarte, M., Domingues, T.F., Fagan, W.F., Fagúndez, J., Falster, D.S., Fan, Y., Fang, J., Farris, E., Fazlioglu, F., Feng, Y., Fernandez-Mendez, F., Ferrara, C., Ferreira, J., Fidelis, A., Finegan, B., Firn, J., Flowers, T.J., Flynn, D.F., Fontana, V., Forey, E., Forgiarini, C., François, L., Frangipani, M., Frank, D., Frenette-Dussault, C., Freschet, G.T., Fry, E.L., Fyllas, N.M., Mazzochini, G.G., Gachet, S., Gallagher, R., Ganade, G., Ganga, F., García-Palacios, P., Gargaglione, V., Garnier, E., Garrido, J.L., de Gasper, A.L., Gea-Izquierdo, G., Gibson, D., Gillison, A.N., Giroldo, A., Glasenhardt, M.C., Gleason, S., Gliesch, M., Goldberg, E., Göldel, B., Gonzalez-Akre, E., Gonzalez-Andujar, J.L., González-Melo, A., González-Robles, A., Graae, B.J., Granda, E., Graves, S., Green, W.A., Gregor, T., Gross, N., Guerin, G.R., Günther, A., Gutiérrez, A.G., Haddock, L., Haines, A., Hall, J., Hambuckers, A., Han, W., Harrison, S.P., Hattingh, W., Hawes, J.E., He, T., He, P., Heberling, J.M., Helm, A., Hempel, S., Hentschel, J., Hérault, B., Hereş, A.M., Herz, K., Heuertz, M., Hickler, T., Hietz, P., Higuchi, P., Hipp, A.L., Hirons, A., Hock, M., Hogan, J.A., Holl, K., Honnay, O., Hornstein, D., Hou, E., Hough-Snee, N., Hovstad, K.A., Ichie, T., Igić, B., Illa, E., Isaac, M., Ishihara, M., Ivanov, L., Ivanova, L., Iversen, C.M., Izquierdo, J., Jackson, R.B., Jackson, B., Jactel, H., Jagodzinski, A.M., Jandt, U., Jansen, S., Jenkins, T., Jentsch, A., Jespersen, J.R.P., Jiang, G.F., Johansen, J.L., Johnson, D., Jokela, E.J., Joly, C.A., Jordan, G.J., Joseph, G.S., Junaedi, D., Junker, R.R., Justes, E., Kabzems, R., Kane, J., Kaplan, Z., Kattenborn, T., Kavelenova, L., Kearsley, E., Kempel, A., Kenzo, T., Kerkhoff, A., Khalil, M.I., Kinlock, N.L., Kissling, W.D., Kitajima, K., Kitzberger, T., Kjøller, R., Klein, T., Kleyer, M., Klimešová, J., Klipel, J., Kloeppel, B., Klotz, S., Knops, J.M., Kohyama, T., Koike, F., Kollmann, J., Komac, B., Komatsu, K., König, C., Kraft, N.J., Kramer, K., Kreft, H., Kühn, I., Kumarathunge, D., Kuppler, J., Kurokawa, H., Kurosawa, Y., Kuyah, S., Laclau, J.P., Lafleur, B., Lallai, E., Lamb, E.,

Lamprecht, A., Larkin, D.J., Laughlin, D., Le Bagousse-Pinguet, Y., le Maire, G., le Roux, P.C., le Roux, E., Lee, T., Lens, F., Lewis, S.L., Lhotsky, B., Li, Y., Li, X., Lichstein, J.W., Liebergesell, M., Lim, J.Y., Lin, Y.S., Linares, J.C., Liu, C., Liu, D., Liu, U., Livingstone, S., Llusià, J., Lohbeck, M., López-García, Á., Lopez-Gonzalez, G., Lososová, Z., Louault, F., Lukács, B.A., Lukeš, P., Luo, Y., Lussu, M., Ma, S., Maciel Rabelo Pereira, C., Mack, M., Maire, V., Mäkelä, A., Mäkinen, H., Malhado, A.C.M., Mallik, A., Manning, P., Manzoni, S., Marchetti, Z., Marchino, L., Marcilio-Silva, V., Marcon, E., Marignani, M., Markesteijn, L., Martin, A., Martínez-Garza, C., Martínez-Vilalta, J., Mašková, T., Mason, K., Mason, N., Massad, T.J., Masse, J., Mayrose, I., McCarthy, J., McCormack, M.L., McCulloh, K., McFadden, I.R., McGill, B.J., McPartland, M.Y., Medeiros, J.S., Medlyn, B., Meerts, P., Mehrabi, Z., Meir, P., Melo, F.P., Mencuccini, M., Meredieu, C., Messier, J., Mészáros, I., Metsaranta, J., Michaletz, S.T., Michelaki, C., Migalina, S., Milla, R., Miller, J.E., Minden, V., Ming, R., Mokany, K., Moles, A.T., Molnár, A., Molofsky, J., Molz, M., Montgomery, R.A., Monty, A., Moravcová, L., Moreno-Martínez, A., Moretti, M., Mori, A.S., Mori, S., Morris, D., Morrison, J., Mucina, L., Mueller, S., Muir, C.D., Müller, S.C., Munoz, F., Myers-Smith, I.H., Myster, R.W., Nagano, M., Naidu, S., Narayanan, A., Natesan, B., Negoita, L., Nelson, A.S., Neuschulz, E.L., Ni, J., Niedrist, G., Nieto, J., Niinemets, Ü., Nolan, R., Nottebrock, H., Nouvellon, Y., Novakovskiy, A., Nystuen, K.O., O'Grady, A., O'Hara, K., O'Reilly-Nugent, A., Oakley, S., Oberhuber, W., Ohtsuka, T., Oliveira, R., Öllerer, K., Olson, M.E., Onipchenko, V., Onoda, Y., Onstein, R.E., Ordonez, J.C., Osada, N., Ostonen, I., Ottaviani, G., Otto, S., Overbeck, G.E., Ozinga, W.A., Pahl, A.T., Paine, C.E., Pakeman, R.J., Papageorgiou, A.C., Parfionova, E., Pärtel, M., Patacca, M., Paula, S., Paule, J., Pauli, H., Pausas, J.G., Peco, B., Penuelas, J., Perea, A., Peri, P.L., Petisco-Souza, A.C., Petraglia, A., Petritan, A.M., Phillips, O.L., Pierce, S., Pillar, V.D., Pisek, J., Pomogaybin, A., Poorter, H., Portsmuth, A., Poschlod, P., Potvin, C., Pounds, D., Powell, A.S., Power, S.A., Prinzing, A., Puglielli, G., Pyšek, P., Raevel, V., Rammig, A., Ransijn, J., Ray, C.A., Reich, P.B., Reichstein, M., Reid, D.E., Réjou-Méchain, M., de Dios, V.R., Ribeiro, S., Richardson, S., Riibak, K., Rillig, M.C., Riviera, F., Robert, E.M., Roberts, S., Robroek, B., Roddy, A., Rodrigues, A.V., Rogers, A., Rollinson, E., Rolo, V., Römermann, C., Ronzhina, D., Roscher, C., Rosell, J.A., Rosenfield, M.F., Rossi, C., Roy, D.B., Royer-Tardif, S., Rüger, N., Ruiz-Peinado, R., Rumpf, S.B., Rusch, G.M., Ryo, M., Sack, L., Saldaña, A., Salgado-Negret, B., Salguero-Gomez, R., Santa-Regina, I., Santacruz-García, A.C., Santos, J., Sardans, J., Schamp, B., Scherer-Lorenzen, M., Schleuning, M., Schmid, B., Schmidt, M., Schmitt, S., Schneider, J.V., Schowanek, S.D., Schrader, J., Schrodt, F., Schuldt, B., Schurr, F., Selaya Garvizu, G., Semchenko, M., Seymour, C., Sfair, J.C., Sharpe, J.M., Sheppard, C.S., Sheremetiev, S., Shiodera, S., Shipley, B., Shovon, T.A., Siebenkäs, A., Sierra, C., Silva, V., Silva, M.,

Sitzia, T., Sjöman, H., Slot, M., Smith, N.G., Sodhi, D., Soltis, P., Soltis, D., Somers, B., Sonnier, G., Sørensen, M.V., Sosinski, E.E., Soudzilovskaia, N.A., Souza, A.F., Spasojevic, M., Sperandii, M.G., Stan, A.B., Stegen, J., Steinbauer, K., Stephan, J.G., Sterck, F., Stojanovic, D.B., Strydom, T., Suarez, M.L., Svenning, J.C., Svitková, I., Svitok, M., Svoboda, M., Swaine, E., Swenson, N., Tabarelli, M., Takagi, K., Tappeiner, U., Tarifa, R., Tauugourdeau, S., Tavsanoglu, C., te Beest, M., Tedersoo, L., Thiffault, N., Thom, D., Thomas, E., Thompson, K., Thornton, P.E., Thuiller, W., Tichý, L., Tissue, D., Tjoelker, M.G., Tng, D.Y.P., Tobias, J., Török, P., Tarin, T., Torres-Ruiz, J.M., Tóthmérész, B., Treurnicht, M., Trivellone, V., Trolliet, F., Trotsiuk, V., Tsakalos, J.L., Tsiripidis, I., Tysklind, N., Umehara, T., Usoltsev, V., Vadeboncoeur, M., Vaezi, J., Valladares, F., Vamosi, J., van Bodegom, P.M., van Breugel, M., Van Cleemput, E., van de Weg, M., van der Merwe, S., van der Plas, F., van der Sande, M.T., van Kleunen, M., Van Meerbeek, K., Vanderwel, M., Vanselow, K.A., Vårhammar, A., Varone, L., Vasquez Valderrama, M.Y., Vassilev, K., Vellend, M., Veneklaas, E.J., Verbeeck, H., Verheyen, K., Vibrans, A., Vieira, I., Villacís, J., Violle, C., Vivek, P., Wagner, K., Waldram, M., Waldron, A., Walker, A.P., Waller, M., Walther, G., Wang, H., Wang, F., Wang, W., Watkins, H., Watkins, J., Weber, U., Weedon, J.T., Wei, L., Weigelt, P., Weiher, E., Wells, A.W., Wellstein, C., Wenk, E., Westoby, M., Westwood, A., White, P.J., Whitten, M., Williams, M., Winkler, D.E., Winter, K., Womack, C., Wright, I.J., Wright, S.J., Wright, J., Pinho, B.X., Ximenes, F., Yamada, T., Yamaji, K., Yanai, R., Yankov, N., Yguel, B., Zanini, K.J., Zanne, A.E., Zelený, D., Zhao, Y.P., Zheng, J., Zheng, J., Ziemińska, K., Zirbel, C.R., Zizka, G., Zo-Bi, I.C., Zotz, G., Wirth, C., 2020. TRY plant trait database - enhanced coverage and open access. Glob. Chang. Biol. 26, 119–188. doi:10.1111/gcb.14904.

Kiddwell, K., 1998. Noaa polar orbiter data user's guide (tiros-n, noaa-6, noaa-7, noaa-8, noaa-9, noaa-10, noaa-11, noaa-12, noaa-13 and noaa-14) november 1998 revision. NOAA/NESDIS/NCDC .

Klein, I., Dietz, A., Gessner, U., Dech, S., Kuenzer, C., 2015. Results of the Global WaterPack: A novel product to assess inland water body dynamics on a daily basis. Remote Sens. Lett. 6, 78–87. doi:10.1080/2150704X.2014.1002945.

König, C., Weigelt, P., Schrader, J., Taylor, A., Kattge, J., Kreft, H., 2019. Biodiversity data integration—the significance of data resolution and domain. PLoS biology 17, e3000183.

Kotchenova, S.Y., Vermote, E.F., 2007. Validation of a vector version of the 6s radiative transfer code for atmospheric correction of satellite data. part ii. homogeneous lambertian and anisotropic surfaces. Appl. Opt. 46, 4455–4464. doi:10.1364/AO.46.004455.

Kotchenova, S.Y., Vermote, E.F., Levy, R., Lyapustin, A., 2008. Radiative transfer codes for atmospheric correction and aerosol retrieval: intercomparison study. Appl. Opt. 47, 2215–2226. doi:10.1364/AO.47.002215.

Kotchenova, S.Y., Vermote, E.F., Matarrese, R., Frank J. Klemm, J., 2006. Validation of a vector version of the 6s radiative transfer code for atmospheric correction of satellite data. part i: Path radiance. Appl. Opt. 45, 6762–6774. doi:10.1364/AO.45.006762.

Krausmann, F., Langthaler, E., 2019. Food regimes and their trade links: A socio-ecological perspective. Ecological Economics 160, 87–95. doi:https://doi.org/10.1016/j.ecolecon.2019.02.011.

Lacaze, R., Smets, B., Baret, F., Weiss, M., Ramon, D., Montersleet, B., Wandrebeck, L., Calvet, J.C., Roujean, J.L., Camacho, F., 2015. OPERATIONAL 333m BIOPHYSICAL PRODUCTS OF THE COPERNICUS GLOBAL LAND SERVICE FOR AGRICULTURE MONITORING. ISPRS - International Archives of the Photogrammetry, Remote Sensing and Spatial Information Sciences XL-7/W3, 53–56. doi:10.5194/isprsarchives-XL-7-W3-53-2015.

Lamarche, C., Santoro, M., Bontemps, S., D'Andrimont, R., Radoux, J., Giustarini, L., Brockmann, C., Wevers, J., Defourny, P., Arino, O., 2017. Compilation and validation of sar and optical data products for a complete and global map of inland/ocean water tailored to the climate modeling community. Remote Sens. 9. doi:10.3390/rs9010036.

Lamquin, N., Clerc, S., Bourg, L., Donlon, C., 2020a. Olci a/b tandem phase analysis, part 1: Level 1 homogenisation and harmonisation. Remote Sensing 12. doi:10.3390/rs12111804.

Lamquin, N., Déru, A., Clerc, S., Bourg, L., Donlon, C., 2020b. Olci a/b tandem phase analysis, part 2: Benefits of sensors harmonisation for level 2 products. Remote Sensing 12. doi:10.3390/rs12172702.

Langhans, W., Schmidli, J., Schär, C., 2012. Bulk convergence of cloud-resolving simulations of moist convection over complex terrain. Journal of the Atmospheric Sciences 69, 2207–2228.

Latham, J., Cumani, R., Rosati, I., Bloise, M., 2014. Global land cover SHARE (GLC-SHARE). Food Agric. Organ. United Nations , 1–39.

Lavorel, S., McIntyre, S., Landsberg, J., Forbes, T., 1997. Plant functional classifications: from general groups to specific groups based on response to disturbance. Trends in Ecology & Evolution 12, 474–478.

LeCun, Y., Bengio, Y., Hinton, G., 2018. Deep learning. nature. Nature 521.

Lehner, B., Döll, P., 2004. Development and validation of a global database of lakes, reservoirs and wetlands. Journal of Hydrology 296, 1–22.

Leonard, O., Pinnock, S., Muller, J.P., Kennedy, T., Lewis, P., Kharbouche, S., North, P., Fisher, J., Preusker, R., Brockmann, C., Krämer, U., Danne, O., Fomferra, N., 2013. GlobAlbedo Algorithm Theoretical Basis Document , 1–313.

Lewis, A., Lacey, J., Mecklenburg, S., Ross, J., Siqueira, A., Killough, B., Szantoi, Z., Tadono, T., Rosenavist, A., Goryl, P., et al., 2018. Ceos analysis ready data for land (card4l) overview, in: IGARSS 2018-2018 IEEE International Geoscience and Remote Sensing Symposium, IEEE. pp. 7407–7410.

Lewis, P., Muller, J., Lopez, G., Shane, N., Kharbouche, S., Fisher, D., Brockmann, C., Danne, O., O, K., Heckel, A., North, P., L., G., 2013. Globalbedo algorithm theoretical basis document. URL: http://www.globalbedo.org/docs/GlobAlbedo_Albedo_ATBD_V4.12.pdf.

Li, W., Macbean, N., Ciais, P., Defourny, P., Lamarche, C., Bontemps, S., Houghton, R.A., Peng, S., 2018. Gross and net land cover changes in the main plant functional types derived from the annual ESA CCI land cover maps (1992-2015). Earth Syst. Sci. Data 10, 219–234. doi:10.5194/essd-10-219-2018.

van Lierop, P., Lindquist, E., Sathyapala, S., Franceschini, G., 2015. Global forest area disturbance from fire, insect pests, diseases and severe weather events. For. Ecol. Manage. 352, 78–88. doi:10.1016/j.foreco.2015.06.010.

Liu, H., Gong, P., Wang, J., Clinton, N., Bai, Y., Liang, S., 2020. Annual dynamics of global land cover and its long-term changes from 1982 to 2015. Earth Syst. Sci. Data 12, 1217–1243. doi:10.5194/essd-12-1217-2020.

Liu, S., Bond-Lamberty, B., Boysen, L.R., Ford, J.D., Fox, A., Gallo, K., Hatfield, J., Henebry, G.M., Huntington, T.G., Liu, Z., Lovelan, T.R., Norby, R.J., Soh, T., Steiner, A.L., Yuan, W., Zhang, Z., Zhao, S., 2017. Grand challenges in understanding the interplay of climate and land changes. Earth Interact. 21, 1–43. doi:10.1175/EI-D-16-0012.1.

Liu, X., Yu, L., Li, W., Peng, D., Zhong, L., Li, L., Xin, Q., Lu, H., Yu, C., Gong, P., 2018. Comparison of country-level cropland areas between ESA-CCI land cover maps and FAOSTAT data. Int. J. Remote Sens. 39, 6631–6645. doi:10.1080/01431161.2018.1465613.

Lobell, D.B., Schlenker, W., Costa-Roberts, J., 2011. Climate trends and global crop production since 1980. Science 333, 616–620.

Loizzo, R., Guarini, R., Longo, F., Scopa, T., Formaro, R., Facchinetti, C., Varacalli, G., 2018. Prisma: The italian hyperspectral mission, in: IGARSS 2018-2018 IEEE International Geoscience and Remote Sensing Symposium, IEEE. pp. 175–178.

Loosvelt, L., Peters, J., Skriver, H., Lievens, H., Van Coillie, F.M., De Baets, B., Verhoest, N.E., 2012. Random Forests as a tool for estimating uncertainty at pixel-level in SAR image classification. Int. J. Appl. Earth Obs. Geoinf. 19, 173–184. doi:10.1016/j.jag.2012.05.011.

Loveland, T.R., Belward, A.S., 1997. The international geosphere biosphere programme data and information system global land cover data set (DISCover). Acta Astronaut. 41, 681–689. doi:10.1016/S0094-5765(98)00050-2.

Lucas, R., Mueller, N., Siggins, A., Owers, C., Clewley, D., Bunting, P., Kooymans, C., Tissott, B., Lewis, B., Lymburner, L., et al., 2019. Land cover mapping using digital earth australia. Data 4, 143.

Lunetta, R.S., Congalton, R.G., Fenstermaker, L.K., Jensen, J.R., McGwire, K.C., Tinney, L.R., 1991. Remote sensing and geographic information system data integration: error sources and

research issues. Photogramm. Eng. Remote Sens. 57, 677 – 687. URL: https://www.scopus.com/inward/record.uri?eid=2-s2.0-0026358101{&}partnerID=40{&}md5=0b1112da2cf117a249d9ea5e1382a2b5.

Lurton, T., Balkanski, Y., Bastrikov, V., Bekki, S., Bopp, L., Braconnot, P., Brockmann, P., Cadule, P., Contoux, C., Cozic, A., Cugnet, D., Dufresne, J.L., Éthé, C., Foujols, M.A., Ghattas, J., Hauglustaine, D., Hu, R.M., Kageyama, M., Khodri, M., Lebas, N., Levavasseur, G., Marchand, M., Ottlé, C., Peylin, P., Sima, A., Szopa, S., Thiéblemont, R., Vuichard, N., Boucher, O., 2020. Implementation of the CMIP6 Forcing Data in the IPSL-CM6A-LR Model. J. Adv. Model. Earth Syst. 12, 1–22. doi:10.1029/2019MS001940.

Luyssaert, S., Jammet, M., Stoy, P.C., Estel, S., Pongratz, J., Ceschia, E., Churkina, G., Don, A., Erb, K., Ferlicoq, M., Gielen, B., Grünwald, T., Houghton, R.A., Klumpp, K., Knohl, A., Kolb, T., Kuemmerle, T., Laurila, T., Lohila, A., Loustau, D., McGrath, M.J., Meyfroidt, P., Moors, E.J., Naudts, K., Novick, K., Otto, J., Pilegaard, K., Pio, C.A., Rambal, S., Rebmann, C., Ryder, J., Suyker, A.E., Varlagin, A., Wattenbach, M., Dolman, A.J., 2014. Land management and land-cover change have impacts of similar magnitude on surface temperature. Nat. Clim. Chang. 4, 389–393. doi:10.1038/nclimate2196.

Mahmood, R., Pielke, R.A., Hubbard, K.G., Niyogi, D., Dirmeyer, P.A., Mcalpine, C., Carleton, A.M., Hale, R., Gameda, S., Beltrán-Przekurat, A., Baker, B., Mcnider, R., Legates, D.R., Shepherd, M., Du, J., Blanken, P.D., Frauenfeld, O.W., Nair, U.S., Fall, S., 2014. Land cover changes and their biogeophysical effects on climate. Int. J. Climatol. 34, 929–953. doi:10.1002/joc.3736.

Malenovskỳ, Z., Rott, H., Cihlar, J., Schaepman, M.E., García-Santos, G., Fernandes, R., Berger, M., 2012. Sentinels for science: Potential of sentinel-1,-2, and-3 missions for scientific observations of ocean, cryosphere, and land. Remote Sensing of Environment 120, 91–101.

Mann, M.E., Bradley, R.S., Hughes, M.K., 1999. Northern hemisphere temperatures during the past millennium: Inferences, uncertainties, and limitations. Geophys. Res. Lett. 26, 759–762. doi:10.1029/1999GL900070.

Mann, M.E., Bradley, R.S., Hughes, M.K., 2004. Correction: Corrigendum: Global-scale temperature patterns and climate forcing over the past six centuries. Nature 430, 105–105. doi:10.1038/nature02478.

Marie, G., Luyssaert, B.S., Dardel, C., Le Toan, T., Bouvet, A., Mermoz, S., Villard, L., Bastrikov, V., Peylin, P., 2022. Constraining a land cover map with satellite-based aboveground biomass estimates over Africa. Geosci. Model Dev. 15, 2599–2617. doi:10.5194/gmd-15-2599-2022.

Masson-Delmotte, V., Zhai, P., Pörtner, H.O., Roberts, D., Skea, J., Shukla, P.R., Others, 2022. Global Warming of 1.5° C: IPCC Special Report on Impacts of Global Warming of 1.5° C above Pre-industrial Levels in Context of Strengthening Response to Climate Change, Sustainable Development, and Efforts to Eradicate Poverty. Cambridge University Press.

McConnell, W., Moran, E.F., et al., 2002. Meeting in the middle: the challenge of meso-level integration. Land Use Policy 19, 99–101.

McGlynn, E., Li, S., F. Berger, M., Amend, M., L. Harper, K., 2022. Addressing uncertainty and bias in land use, land use change, and forestry greenhouse gas inventories. Clim. Change 170, 1–25. doi:10.1007/s10584-021-03254-2.

McNemar, Q., 1947. Note on the sampling error of the difference between correlated proportions or percentages. Psychometrika 12, 153–157.

Merchant, C.J., Paul, F., Popp, T., Ablain, M., Bontemps, S., Defourny, P., Hollmann, R., Lavergne, T., Laeng, A., De Leeuw, G., Mittaz, J., Poulsen, C., Povey, A.C., Reuter, M., Sathyendranath, S., Sandven, S., Sofieva, V.F., Wagner, W., 2017. Uncertainty information in climate data records from Earth observation. Earth Syst. Sci. Data 9, 511–527. doi:10.5194/essd-9-511-2017.

Micklin, P., 2010. The past, present, and future Aral Sea. Lakes Reserv. Res. Manag. 15, 193–213. doi:10.1111/j.1440-1770.2010.00437.x.

Millennium Assessment Ecosystem, 2005. Ecosystems and human well-being: wetlands and water. Synthesis. World resources institute, Washington, DC, USA. URL: http://biblioteca.cehum.org/bitstream/123456789/143/1/MillenniumEcosystemAssessment.ECOSYSTEMSANDHUMANWELL-BEINGWETLANDSANDWATERSynthesi.pdf.

Mittaz, J., Merchant, C.J., Woolliams, E.R., 2019. Applying principles of metrology to historical Earth observations from satellites. Metrologia 56. doi:10.1088/1681-7575/ab1705.

Montavon, G., Samek, W., Müller, K.R., 2018. Methods for interpreting and understanding deep neural networks. Digit. Signal Process. A Rev. J. 73, 1–15. doi:10.1016/j.dsp.2017.10.011, arXiv:1706.07979.

Moreau, I., 2016. Evidencing land cover dynamics and tropical forest seasonality: the benefit of 13 years of daily global observations. PhD thesis. Technical Report. UCLouvain.

Moreno-Martínez, Á., Camps-Valls, G., Kattge, J., Robinson, N., Reichstein, M., van Bodegom, P., Kramer, K., Cornelissen, J.H.C., Reich, P., Bahn, M., et al., 2018. A methodology to derive global maps of leaf traits using remote sensing and climate data. Remote sensing of environment 218, 69–88.

Mousivand, A., Arsanjani, J.J., 2019. Insights on the historical and emerging global land cover changes: The case of ESA-CCI-LC datasets. Appl. Geogr. 106, 82–92. doi:10.1016/j.apgeog.2019.03.010.

Musial, J., Leszczenski, J., Bojanowski, J., Milcinski, G., Vrecko, A., Clarijs, D., Dries, J., Marquard, U., 2024. Overview of the Copernicus Data Space Ecosystem APIs. Technical Report. Copernicus Meetings.

Nabuurs, G.J., Mrabet, R., Hatab, A.A., Bustamante, M., Clark, H., Havl\'\ik, P., House, J.I., Mbow, C., Ninan, K.N., Popp, A., Others, 2022. Agriculture, Forestry and Other Land Uses (AFOLU) .

Nizalapur, V., 2008. Land cover classification using multi-source data fusion of envisat-asar and irs p6 liss-iii satellite data: A case study over tropical most deciduous forested regions of karnataka, india. The International

Archives of the Photogrammetry, Remote Sensing and Spatial Information Science .

Nowosad, J., Stepinski, T.F., Netzel, P., 2019. Global assessment and mapping of changes in mesoscale landscapes: 1992-2015. Int. J. Appl. Earth Obs. Geoinf. 78, 332–340. doi:10.1016/j.jag.2018.09.013.

Olofsson, P., Foody, G.M., Herold, M., Stehman, S.V., Woodcock, C.E., Wulder, M.A., 2014a. Good practices for estimating area and assessing accuracy of land change. Remote Sensing of Environment 148, 42 – 57. doi:http://dx.doi.org/10.1016/j.rse.2014.02.015.

Olofsson, P., Foody, G.M., Herold, M., Stehman, S.V., Woodcock, C.E., Wulder, M.A., 2014b. Good practices for estimating area and assessing accuracy of land change. Remote Sens. Environ. 148, 42–57.

Olofsson, P., Foody, G.M., Stehman, S.V., Woodcock, C.E., 2013. Making better use of accuracy data in land change studies: Estimating accuracy and area and quantifying uncertainty using stratified estimation. Remote Sens. Environ. 129, 122–131. doi:10.1016/j.rse.2012.10.031.

O'Neill, M.E., 2014. PCG: A Family of Simple Fast Space-Efficient Statistically Good Algorithms for Random Number Generation. Technical Report HMC-CS-2014-0905. Harvey Mudd College. Claremont, CA.

Pachauri, R., Meyer, L., 2014. Climate Change 2014: Synthesis Report. Contribution of Working Groups I, II and III to the Fifth Assessment Report of the Intergovernmental Panel on Climate Change.

Pal, M., 2005. Random forest classifier for remote sensing classification. Int. J. Remote Sens. 26, 217–222. doi:10.1080/01431160412331269698.

Parmesan, C., Yohe, G., 2003. A globally coherent fingerprint of climate change impacts across natural systems. Nature 421, 37–42. doi:10.1038/nature01286.

Pedregosa, F., Varoquaux, G., Gramfort, A., Michel, V., Thirion, B., Grisel, O., Blondel, M., Prettenhofer, P., Weiss, R., Dubourg, V., et al., 2011. Scikit-learn: Machine learning in python. the Journal of machine Learning research 12, 2825–2830.

Pekel, J.F., Cottam, A., Gorelick, N., Belward, A.S., 2016. High-resolution mapping of global surface water and its long-term changes. Nature 540, 418–422. doi:10.1038/nature20584.

Perugini, L., Pellis, G., Grassi, G., Ciais, P., Dolman, H., House, J.I., Peters, G.P., Smith, P., Günther, D., Peylin, P., 2021. Emerging reporting and verification needs under the Paris Agreement: How can the research community effectively contribute? Environ. Sci. Policy 122, 116–126. doi:10.1016/j.envsci.2021.04.012.

Pesaresi, M., Ehrlich, D., Ferri, S., Florczyk, A.J., Freire, S., Halkia, M., Julea, A., Kemper, T., Soille, P., Syrris, V., 2016. Operating procedure for the production of the Global Human Settlement Layer from Landsat data of the epochs 1975, 1990, 2000, and 2014. doi:10.2788/253582.

Pesaresi, M., Huadong, G., Blaes, X., Ehrlich, D., Ferri, S., Gueguen, L., Halkia, M., Kauffmann, M., Kemper, T., Lu, L., Marin-Herrera, M.A., Ouzounis, G.K., Scavazzon, M., Soille, P., Syrris, V., Zanchetta, L., 2013. A global human settlement layer from optical HR/VHR RS data: Concept and first results. volume 6. doi:10.1109/JSTARS.2013.2271445.

Pfeffer, W.T., Arendt, A.A., Bliss, A., Bolch, T., Cogley, J.G., Gardner, A.S., Hagen, J.O., Hock, R., Kaser, G., Kienholz, C., Miles, E.S., Moholdt, G., Mölg, N., Paul, F., Radić, V., Rastner, P., Raup, B.H., Rich, J., Sharp, M.J., Andreassen, L.M., Bajracharya, S., Barrand, N.E., Beedle, M.J., Berthier, E., Bhambri, R., Brown, I., Burgess, D.O., Burgess, E.W., Cawkwell, F., Chinn, T., Copland, L., Cullen, N.J., Davies, B., De Angelis, H., Fountain, A.G., Frey, H., Giffen, B.A., Glasser, N.F., Gurney, S.D., Hagg, W., Hall, D.K., Haritashya, U.K., Hartmann, G., Herreid, S., Howat, I., Jiskoot, H., Khromova, T.E., Klein, A., Kohler, J., König, M., Kriegel, D., Kutuzov, S., Lavrentiev, I., Le Bris, R., Li, X., Manley, W.F., Mayer, C., Menounos, B., Mercer, A., Mool, P., Negrete, A., Nosenko, G., Nuth, C., Osmonov, A., Pettersson, R., Racoviteanu, A., Ranzi, R., Sarikaya, M.A., Schneider, C., Sigurdsson, O., Sirguey, P., Stokes, C.R., Wheate, R., Wolken, G.J., Wu, L.Z., Wyatt, F.R., 2014. The randolph glacier inventory: A globally complete inventory of glaciers. J. Glaciol. 60, 537–552. doi:10.3189/2014JoG13J176.

Pielke, R.A., 2005. Land use and climate change. Science (80-.). 310, 1625–1626. doi:10.1126/science.1120529.

Pielke, R.A., Pitman, A., Niyogi, D., Mahmood, R., McAlpine, C., Hossain, F., Goldewijk, K.K., Nair, U., Betts, R., Fall, S., Reichstein, M., Kabat, P., de Noblet, N., 2011. Land use/land cover changes and climate: Modeling analysis and observational evidence. Wiley Interdiscip. Rev. Clim. Chang. 2, 828–850. doi:10.1002/wcc.144.

Pitman, A.J., De Noblet-Ducoudré, N., Cruz, F.T., Davin, E.L., Bonan, G.B., Brovkin, V., Claussen, M., Delire, C., Ganzeveld, L., Gayler, V., Van Den Hurk, B.J., Lawrence, P.J., Van Der Molen, M.K., Müller, C., Reick, C.H., Seneviratne, S.I., Strengen, B.J., Voldoire, A., 2009. Uncertainties in climate responses to past land cover change: First results from the LUCID intercomparison study. Geophys. Res. Lett. 36, 1–6. doi:10.1029/2009GL039076.

Planet, T.P.F., 2018. Planet fusion monitoring technical specification.

Plourde, L., Congalton, R.G., 2003. Sampling method and sample placement: How do they affect the accuracy of remotely sensed maps? Photogramm. Eng. Remote Sensing 69, 289–297. doi:10.14358/PERS.69.3.289.

Pongratz, J., Reick, C.H., Houghton, R.A., House, J.I., 2014. Terminology as a key uncertainty in net land use and land cover change carbon flux estimates. Earth Syst. Dyn. 5, 177–195. doi:10.5194/esd-5-177-2014.

Pongratz, J., Schwingshackl, C., Bultan, S., Obermeier, W., Havermann, F., Guo, S., 2021. Land Use Effects on Climate: Current State, Recent Progress, and Emerging Topics. Curr. Clim. Chang. Reports 7, 99–120. doi:10.1007/s40641-021-00178-y.

Pontius, R.G., Shusas, E., McEachern, M., 2004. Detecting important categorical land changes while accounting for persistence. Agric. Ecosyst. Environ. 101, 251–268. doi:10.1016/j.agee.2003.09.008.

Pörtner, H.O., Roberts, D.C., Masson-Delmotte, V., Zhai, P., Tignor, M., Poloczanska, E., Weyer, N., 2019. The ocean and cryosphere in a changing climate. IPCC Spec. Rep. Ocean Cryosph. a Chang. Clim. 1155.

Potapov, P., Hansen, M.C., Pickens, A., Hernandez-Serna, A., Tyukavina, A., Turubanova, S., Zalles, V., Li, X., Khan, A., Stolle, F., Harris, N., Song, X.P., Baggett, A., Kommareddy, I., Kommareddy, A., 2022. The Global 2000-2020 Land Cover and Land Use Change Dataset Derived From the Landsat Archive: First Results. Front. Remote Sens. 3, 1–22. doi:10.3389/frsen.2022.856903.

Potapov, P., Li, X., Hernandez-Serna, A., Tyukavina, A., Hansen, M.C., Kommareddy, A., Pickens, A., Turubanova, S., Tang, H., Silva, C.E., Armston, J., Dubayah, R., Blair, J.B., Hofton, M., 2021a. Mapping global forest canopy height through integration of GEDI and Landsat data. Remote Sens. Environ. 253, 112165. doi:10.1016/j.rse.2020.112165.

Potapov, P., Turubanova, S., Hansen, M.C., Tyukavina, A., Zalles, V., Khan, A., Song, X.P., Pickens, A., Shen, Q., Cortez, J., 2021b. Global maps of cropland extent and change show accelerated cropland expansion in the twenty-first century. Nat. Food doi:10.1038/s43016-021-00429-z.

Potapov, P.V., Turubanova, S.A., Hansen, M.C., Adusei, B., Broich, M., Altstatt, A., Mane, L., Justice, C.O., 2012. Quantifying forest cover loss in Democratic Republic of the Congo, 2000-2010, with Landsat ETM+ data. Remote Sens. Environ. 122, 106–116. doi:10.1016/j.rse.2011.08.027.

Poulter, B., Ciais, P., Hodson, E., Lischke, H., Maignan, F., Plummer, S., Zimmermann, N.E., 2011. Plant functional type mapping for earth system models. Geosci. Model Dev. 4, 993–1010. doi:10.5194/gmd-4-993-2011.

Poulter, B., MacBean, N., Hartley, A., Khlystova, I., Arino, O., Betts, R., Bontemps, S., Boettcher, M., Brockmann, C., Defourny, P., Hagemann, S., Herold, M., Kirches, G., Lamarche, C., Lederer, D., Ottlé, C., Peters, M., Peylin, P., 2015. Plant functional type classification for earth system models: results from the European Space Agency's Land Cover Climate Change Initiative. Geosci. Model Dev. 8, 2315–2328. doi:10.5194/gmd-8-2315-2015.

Pouzols, F.M., Toivonen, T., Minin, E.D., Kukkala, A.S., Kullberg, P., Kuustera, J., Lehtomaki, J., Tenkanen, H., Verburg, P.H., Moilanen, A., 2014. Global protected area expansion is compromised by projected land-use and parochialism. Nature 516, 383–386. doi:10.1038/nature14032.

Prein, A.F., Langhans, W., Fosser, G., Ferrone, A., Ban, N., Goergen, K., Keller, M., Tölle, M., Gutjahr, O., Feser, F., et al., 2015. A review on regional convection-permitting climate modeling: Demonstrations, prospects, and challenges. Reviews of geophysics 53, 323–361.

QA4ECV, 2014. Quality Assurance for Essential Climate Variables. URL: http://www.qa4ecv.eu/.

QA4EO, 2013. Quality Assurance framework for Earth Observation. URL: https://qa4eo.org/.

Quast, R., Kirches, G., Lamarche, C., Boettcher, M., Brockmann, C., Albergel, C., Defourny, P., 2024 *in preparation*). Uncertainty budget for ESA CCI Land Cover: Quantitative variables. Part 1. , 81.

Quegan, S., Le Toan, T., Chave, J., Dall, J., Exbrayat, J.F., Minh, D.H.T., Lomas, M., D'alessandro, M.M., Paillou, P., Papathanassiou, K., et al., 2019. The european space agency biomass mission: Measuring forest above-ground biomass from space. Remote Sensing of Environment 227, 44–60.

Radoux, J., Lamarche, C., Van Bogaert, E., Bontemps, S., Brockmann, C., Defourny, P., 2014. Automated Training Sample Extraction for Global Land Cover Mapping. Remote Sens. 6, 3965–3987.

Raffa, K.F., Aukema, B.H., Bentz, B.J., Carroll, A.L., Hicke, J.A., Turner, M.G., Romme, W.H., 2008. Cross-scale drivers of natural disturbances prone to anthropogenic amplification: The dynamics of bark beetle eruptions. Bioscience 58, 501–517. doi:10.1641/B580607.

Ramsar, 1971. Convention on Wetlands of International Importance especially as Waterfowl Habitat. URL: https://www.ramsar.org/sites/default/files/documents/library/current_convention_text_e.pdf.

Reiche, J., Verbesselt, J., Hoekman, D., Herold, M., 2015. Fusing landsat and sar time series to detect deforestation in the tropics. Remote Sensing of Environment 156, 276–293.

Richardson, D., Black, A.S., Irving, D., Matear, R.J., Monselesan, D.P., Risbey, J.S., Squire, D.T., Tozer, C.R., 2022. Global increase in wildfire potential from compound fire weather and drought. npj Clim. Atmos. Sci. 5. doi:10.1038/s41612-022-00248-4.

Rodriguez-Galiano, V.F., Ghimire, B., Rogan, J., Chica-Olmo, M., Rigol-Sanchez, J.P., 2012. An assessment of the effectiveness of a random forest classifier for land-cover classification. ISPRS J. Photogramm. Remote Sens. 67, 93–104. doi:10.1016/j.isprsjprs.2011.11.002.

Rosenzweig, C., Karoly, D., Vicarelli, M., Neofotis, P., Wu, Q., Casassa, G., Menzel, A., Root, T.L., Estrella, N., Seguin, B., Tryjanowski, P., Liu, C., Rawlins, S., Imeson, A., 2008. Attributing physical and biological impacts to anthropogenic climate change. Nature 453, 353–357. doi:10.1038/nature06937.

Saha, B., Srivastava, D., 2014. Data quality: The other face of big data, in: 2014 IEEE 30th international conference on data engineering, IEEE. pp. 1294–1297.

Santoro, M., Wegmuller, U., 2014. Multi-temporal synthetic aperture radar metrics applied to map open water bodies. Sel. Top. Appl. Earth Obs. Remote Sensing, IEEE J. 7, 3225–3238.

Santoro, M., Wegmüller, U., Lamarche, C., Bontemps, S., Defourny, P., Arino, O., 2015a. Strengths and weaknesses of multi-year Envisat ASAR backscatter measurements to map permanent open water bodies at global scale. Remote Sens. Environ. 171, 185–201. doi:10.1016/j.rse.2015.10.031.

Santoro, M., Wegmüller, U., Lamarche, C., Bontemps, S., Defourny, P., Arino, O., 2015b. Strengths and weaknesses of multi-year envisat {ASAR} backscatter measurements to map permanent open water bodies at global scale. Remote Sensing of Environment 171, 185 – 201. doi:http://dx.doi.org/10.1016/j.rse.2015.10.031.

Santos, F.D., Ferreira, P.L., Pedersen, J.S.T., 2022. The climate change challenge: A review of the barriers and solutions to deliver a paris solution. Climate 10, 75.

Saunier, S., Pflug, B., Lobos, I.M., Franch, B., Louis, J., De Los Reyes, R., Debaecker, V., Cadau, E.G., Boccia, V., Gascon, F., et al., 2022. Sen2like: Paving the way towards harmonization and fusion of optical data. Remote Sensing 14, 3855.

Sayre, R., 2014. A New Map of Global Ecological Land Units — An Ecophysiographic Stratification Approach. A New Map Glob. Ecol. L. Units — An Ecophysiographic Stratif. Approach , 25.

Sefrin, O., Riese, F.M., Keller, S., 2020. Deep learning for land cover change detection. Remote Sensing 13, 78.

Seleiman, M.F., Al-Suhaibani, N., Ali, N., Akmal, M., Alotaibi, M., Refay, Y., Dindaroglu, T., Abdul-Wajid, H.H., Battaglia, M.L., 2021. Drought stress impacts on plants and different approaches to alleviate its adverse effects. Plants 10, 259.

Shannon, C.E., 1948. The mathematical theory of communication. Bell System Technical Journal , 549–558.

Silva Junior, C.H., Pessôa, A.C., Carvalho, N.S., Reis, J.B., Anderson, L.O., Aragão, L.E., 2021. The Brazilian Amazon deforestation rate in 2020 is the greatest of the decade. Nat. Ecol. Evol. 5, 144–145. doi:10.1038/s41559-020-01368-x.

Simmons, A., Fellous, J.L., Ramaswamy, V., Trenberth, K., Asrar, G., Balmaseda, M., Burrows, J.P., Ciais, P., Drinkwater, M., Friedlingstein, P., Gobron, N., Guilyardi, E., Halpern, D., Heimann, M., Johannessen, J., Levelt, P.F., Lopez-Baeza, E., Penner, J., Scholes, R., Shepherd, T., 2016. Observation and integrated Earth-system science: A roadmap for 2016-2025. Adv. Sp. Res. 57, 2037–2103. doi:10.1016/j.asr.2016.03.008.

Siqueira, A., Lewis, A., Thankappan, M., Szantoi, Z., Goryl, P., Labahn, S., Ross, J., Hosford, S., Mecklenburg, S., Tadono, T., et al., 2019. Ceos analysis ready data for land–an overview on the current and future work, in: IGARSS 2019-2019 IEEE International Geoscience and Remote Sensing Symposium, IEEE. pp. 5536–5537.

Skole, D.L., Mbow, C., Mugabowindekwe, M., Brandt, M.S., Samek, J.H., 2021. Trees outside of forests as natural climate solutions. Nature Climate Change 11, 1013–1016.

Slater, J.A., Garvey, G., Johnston, C., Haase, J., Heady, B., Kroenung, G., Little, J., 2006. The srtm data "finishing" process and products. Photogrammetric Engineering & Remote Sensing 72, 237–247.

Smith, P., Clark, H., Dong, H., Elsiddig, E.A., Haberl, H., Harper, R., House, J., Jafari, M., Masera, O., Mbow, C., Others, 2014. Agriculture, forestry and other land use (AFOLU) .

Snow, N., (US), I.D.C., Haran, T., 2005. MODIS mosaic of Antarctica (MOA) image map. National Snow and Ice Data Center.

Solomon, S., Qin, D., Manning, M., Averyt, K., Marquis, M., 2007. Climate change 2007-the physical science basis: Working group I contribution to the fourth assessment report of the IPCC. volume 4. Cambridge university press.

Song, X.P., Hansen, M.C., Stehman, S.V., Potapov, P.V., Tyukavina, A., Vermote, E.F., Townshend, J.R., 2018a. Global land change from 1982 to 2016. Nature 560, 639–643. doi:10.1038/s41586-018-0411-9.

Song, X.P., Hansen, M.C., Stehman, S.V., Potapov, P.V., Tyukavina, A., Vermote, E.F., Townshend, J.R., 2018b. Global land change from 1982 to 2016. Nature 560, 639–643. doi:10.1038/s41586-018-0411-9.

Stadelman, W., 1994. Contaminants of liquid egg products, in: Microbiology of the Avian Egg. Springer, pp. 139–151.

Stehfest, E., van Vuuren, D., Kram, T., Bouwman, L., Alkemade, R., Bakkenes, M., Biemans, H., Bouwman, A., den Elzen, M., Janse, J., Lucas, P., van Minnen, J., Müller, C., Prins, A.G., 2014. Integrated Assessment of Global Environmental Change with IMAGE 3.0. Model description and policy applications. URL: https://dspace.library.uu.nl/bitstream/handle/1874/308545/PBL_2014_Integrated_Assessment_of_Global_Environmental_Change_with_IMAGE_30_735.pdf?sequence=1.

Stehman, S.V., 2009. Sampling designs for accuracy assessment of land cover. Int. J. Remote Sens. 30, 5243–5272. doi:10.1080/01431160903131000.

Strahler, A.H., Boschetti, L., Foody, G.M., Friedl, M.A., Hansen, M.C., Herold, M., Mayaux, P., Morisette, J.T., Stehman, S.V., Woodcock, C.E., 2006a. 2006_Strahler et al._Unknown.pdf .

Strahler, A.H., Boschetti, L., Foody, G.M., Friedl, M.A., Hansen, M.C., Herold, M., Mayaux, P., Morisette, J.T., Stehman, S.V., Woodcock, C.E., 2006b. Global land cover validation: Recommendations for evaluation and accuracy assessment of global land cover maps. European Communities, Luxembourg 51.

Sulla-Menashe, D., Friedl, M.A., 2018. User Guide to Collection 6 MODIS Land Cover (MCD12Q1 and MCD12C1) Product. Usgs , 1–18URL: https://doi.org/10.5067/MODIS/MCD12Q1.006.

Sulla-Menashe, D., Gray, J.M., Abercrombie, S.P., Friedl, M.A., 2019. Hierarchical mapping of annual global land cover 2001 to present: The MODIS Collection 6 Land Cover product. Remote Sens. Environ. 222, 183–194. doi:10.1016/j.rse.2018.12.013.

Tamiminia, H., Salehi, B., Mahdianpari, M., Quackenbush, L., Adeli, S., Brisco, B., 2020. Google earth engine for geo-big data applications: A meta-

analysis and systematic review. ISPRS journal of photogrammetry and remote sensing 164, 152–170.

Teng, W., Loew, E., Ross, D., Zsilinsky, V., Lo, C., Philipson, W., Philpot, W., Morain, S., 1997. Fundamentals of photographic interpretation. Manual of photographic interpretation , 49–113.

Thanh Noi, P., Kappas, M., 2017. Comparison of random forest, k-nearest neighbor, and support vector machine classifiers for land cover classification using sentinel-2 imagery. Sensors 18, 18.

Torres, R., Snoeij, P., Geudtner, D., Bibby, D., Davidson, M., Attema, E., Potin, P., Rommen, B., Floury, N., Brown, M., et al., 2012. Gmes sentinel-1 mission. Remote Sensing of Environment 120, 9–24.

Transon, J., d'Andrimont, R., Maugnard, A., Defourny, P., 2018. Survey of hyperspectral earth observation applications from space in the sentinel-2 context. Remote Sensing 10, 157.

Tsendbazar, N., de Bruin, S., Mora, B., Schouten, L., Herold, M., 2016. Comparative assessment of thematic accuracy of GLC maps for specific applications using existing reference data. Int. J. Appl. Earth Obs. Geoinf. 44, 124–135. doi:10.1016/j.jag.2015.08.009.

Tsendbazar, N., Li, L., Koopman, M., Carter, S., Herold, M., Georgieva, I., Lesiv, M., 2021. Product validation report (d12-pvr) v 1.1 .

Turner, B.L., Moss, R.H., Skole, D.L., 1993. Relating land use and global land-cover change. Technical Report 24.

Tyagi, A.K., Rekha, G., 2020. Challenges of applying deep learning in real-world applications, in: Challenges and applications for implementing machine learning in computer vision. IGI Global, pp. 92–118.

UNEP-WCMC, 2019. User Manual for the World Database on Protected Areas and world database on other effective area-based conservation measures: 1.6. URL: https://wdpa.s3-eu-west-1.amazonaws.com/WDPA_Manual/English/WDPA_WDOECM_Manual_1_6.pdfhttps://www.protectedplanet.net/en/thematic-areas/wdpa?tab=WDPA.

UNFCCC, 2015. Decision 1/CP.21. Adoption of the Paris Agreement. FCCC/CP/2015/10/Add.1. URL: https://unfccc.int/resource/docs/2015/cop21/eng/10a01.pdf{#}page=2.

Unterberger, C., Brunner, L., Nabernegg, S., Steininger, K.W., Steiner, A.K., Stabentheiner, E., Monschein, S., Truhetz, H., 2018. Spring frost risk for regional apple production under a warmer climate. PloS one 13, e0200201.

Unwin, D.J., 1995. Geographical information systems and the problem of 'error and uncertainty'. Prog. Hum. Geogr. 19, 549–558. doi:10.1177/030913259501900408.

Urban, M.C., 2015. Accelerating extinction risk from climate change. Science (80-.). 348, 571–573.

US DMA, 1991. US Defense Mapping Agency– (DIGITAL LANDMASS BLANKING (DLMB) DATA PROGRAM -MILITARY SPECIFICATION. Technical Report June.

Van Asselen, S., Verburg, P.H., Vermaat, J.E., Janse, J.H., 2013. Drivers of wetland conversion: A global meta-analysis. PLoS One 8, 1–13. doi:10.1371/journal.pone.0081292.

Van der Wel, F.J., Van der Gaag, L.C., Gorte, B.G., 1998. Visual exploration of uncertainty in remote-sensing classification. Comput. Geosci. 24, 335–343. doi:10.1016/S0098-3004(97)00120-9.

Vancutsem, C., Bicheron, P., Cayrol, P., Defourny, P., 2007. An assessment of three candidate compositing methods for global MERIS time series. Can. J. Remote Sens. 33, 492–502. doi:10.5589/m07-056.

Venter, O., Sanderson, E.W., Magrach, A., Allan, J.R., Beher, J., Jones, K.R., Possingham, H.P., Laurance, W.F., Wood, P., Fekete, B.M., Levy, M.A., Watson, J.E., 2016. Sixteen years of change in the global terrestrial human footprint and implications for biodiversity conservation. Nat. Commun. 7, 1–11. doi:10.1038/ncomms12558.

Venter, Z.S., Barton, D.N., Chakraborty, T., Simensen, T., Singh, G., 2022. Global 10 m Land Use Land Cover Datasets: A Comparison of Dynamic World, World Cover and Esri Land Cover. Remote Sens. 14. doi:10.3390/rs14164101.

Verbesselt, J., Hyndman, R., Zeileis, A., Culvenor, D., 2010. Phenological change detection while accounting for abrupt and gradual trends in satellite image time series. Remote Sens. Environ. 114, 2970–2980. doi:10.1016/j.rse.2010.08.003.

Verbesselt, J., Zeileis, A., Herold, M., 2012. Near real-time disturbance detection using satellite image time series. Remote Sensing of Environment 123, 98–108.

Vermote, E., Tanre, D., Deuze, J., Herman, M., Morcette, J.J., 1997. Second simulation of the satellite signal in the solar spectrum, 6s: an overview. IEEE Transactions on Geoscience and Remote Sensing 35, 675–686. doi:10.1109/36.581987.

Vermote, E.F., Kotchenova, S., 2008a. Atmospheric correction for the monitoring of land surfaces. Journal of Geophysical Research: Atmospheres 113. doi:https://doi.org/10.1029/2007JD009662.

Vermote, E.F., Kotchenova, S., 2008b. Atmospheric correction for the monitoring of land surfaces. Journal of Geophysical Research: Atmospheres 113.

Verpoorter, C., Kutser, T., Seekell, D.A., Tranvik, L.J., 2014a. A global inventory of lakes based on high-resolution satellite imagery. Geophys. Res. Lett. 41, 6396–6402. doi:10.1002/2014GL060641.

Verpoorter, C., Kutser, T., Seekell, D.A., Tranvik, L.J., 2014b. A global inventory of lakes based on high-resolution satellite imagery. Geophysical Research Letters 41, 6396–6402.

van Vliet, J., 2019. Direct and indirect loss of natural area from urban expansion. Nat. Sustain. 2, 755–763. doi:10.1038/s41893-019-0340-0.

Waldner, F., Hansen, M.C., Potapov, P.V., Löw, F., Newby, T., Ferreira, S., Defourny, P., 2017. National-scale cropland mapping based on spectral-

temporal features and outdated land cover information. PLoS One 12, 1–24. doi:10.1371/journal.pone.0181911.

Wessel, P., Smith, W.H., 1996. A global, self-consistent, hierarchical, high-resolution shoreline. J. geophys. Res 101, 8741–8743.

Westerling A L, Hidalgo H G, Cayan D R, Swetnam T W, 2006. Warming and earlier spring increase western U.S. forest wildfire activity. Science (80-.). 313, 940–943.

Wevers, J., Müller, D., Kirches, G., Quast, R., Brockmann, C., 2022a. IdePix for Sentinel-3 OLCI Algorithm Theoretical Basis Document. doi:10.5281/zenodo.6517333.

Wevers, J., Müller, D., Kirches, G., Quast, R., Brockmann, C., 2022b. IdePix for Sentinel-3 OLCI Algorithm Theoretical Basis Document. doi:10.5281/zenodo.6517333.

Winkler, K., Fuchs, R., Rounsevell, M., Herold, M., 2021. Global land use changes are four times greater than previously estimated. Nat. Commun. 12, 1–10. doi:10.1038/s41467-021-22702-2.

Woodcock, C.E., Allen, R., Anderson, M., Belward, A., Bindschadler, R., Cohen, W., Gao, F., Goward, S.N., Helder, D., Helmer, E., et al., 2008. Free access to landsat imagery. Science 320, 1011–1011.

Woolliams, E., Hueni, A., Gorroño, J., 2014. Intermediate uncertainty analysis for earth observation (instrument calibration module): Training course textbook .

Wulder, M.A., Belward, A., Cohen, W.B., 2012. and open access to imagery : A history with Landsat and future including Sentinel-2 Value of MSRI to National programs , Feb—-47.

Wulder, M.A., Hilker, T., White, J.C., Coops, N.C., Masek, J.G., Pflugmacher, D., Crevier, Y., 2015. Virtual constellations for global terrestrial monitoring. Remote Sensing of Environment 170, 62–76.

Yamazaki, D., Trigg, M.A., Ikeshima, D., 2015. Development of a global ~90m water body map using multi-temporal Landsat images. Remote Sens. Environ. 171, 337–351. doi:10.1016/j.rse.2015.10.014.

Yang, Y., Xiao, P., Feng, X., Li, H., 2017. Accuracy assessment of seven global land cover datasets over China. ISPRS J. Photogramm. Remote Sens. 125, 156–173. doi:10.1016/j.isprsjprs.2017.01.016.

Zanaga, D., Van De Kerchove, R., Daems, D., De Keersmaecker, W., Brockmann, C., Kirches, G., Wevers, J., Cartus, O., Santoro, M., Fritz, S., Others, 2022. ESA WorldCover 10 m 2021 v200 .

Zanaga, D., Van De Kerchove, R., De Keersmaecker, W., Souverijns, N., Brockmann, C., Quast, R., Wevers, J., Grosu, A., Paccini, A., Vergnaud, S., Cartus, O., Santoro, M., Fritz, S., Georgieva, I., Lesiv, M., Carter, S., Herold, M., Li, L., Tsendbazar, N., Ramoino, F., Arino, O., 2021. ESA WorldCover 10 m 2020 v100 .

Zhang, C., Dong, J., Ge, Q., 2022. Mapping 20 years of irrigated croplands

in China using MODIS and statistics and existing irrigation products. Sci. Data 9, 1–12. doi:10.1038/s41597-022-01522-z.

Zhang, L., Zhang, L., Du, B., 2016. Deep learning for remote sensing data: A technical tutorial on the state of the art. IEEE Geoscience and remote sensing magazine 4, 22–40.

Zhu, Z., 2017. Change detection using landsat time series: A review of frequencies, preprocessing, algorithms, and applications. ISPRS J. Photogramm. Remote Sens. 130, 370–384. doi:10.1016/j.isprsjprs.2017.06.013.

Zhu, Z., Woodcock, C.E., 2014. Continuous change detection and classification of land cover using all available Landsat data. Remote Sens. Environ. 144, 152–171. doi:10.1016/j.rse.2014.01.011.

Zhu, Z., Zhang, J., Yang, Z., Aljaddani, A.H., Cohen, W.B., Qiu, S., Zhou, C., 2020. Continuous monitoring of land disturbance based on landsat time series. Remote Sensing of Environment 238, 111116.

List of publications

Peer reviewed articles

Defourny, P., **Lamarche, C.**, Brockmann, C., Boettcher, M., Bontemps, S., De Maet, T., Duveiller, G., Hartley, A., Kirches, G., Moreau, I., Peylin, P.,Ottlé, C., Radoux, J., Van Bogaert, E., Ramoino, F., Albergel, C., Arino, O. 29 years of consistent land use observation from harmonized satellite streams reveal annual changes for every pixel on Earth. *Under revision.*

Harper, K. L., **Lamarche, C.** and Hartley, A., Peylin, P., Ottlé, C., Bastrikov, V., San Martín, R., Bohnenstengel, S. I., Kirches, G., Boettcher, M., Shevchuk, R., Brockmann, C., Defourny, P. A 29-year time series of annual 300-metre resolution plant functional type maps for climate models. *Earth System Science Data Discussions*. 2022. https://doi.org/10.5194/essd-15-1465-2023.

Bogaert, P., **Lamarche, C.**, Defourny, P. (2021). Hidden Markov Models for Annual Land Cover Mapping—Increasing Temporal Consistency and Completeness. *IEEE Transactions on Geoscience and Remote Sensing*, 60, 1-14.

Wang, Libo; Bartlett, Paul; Pouliot, Darren; Chan, Ed; **Lamarche, Céline**; Wulder, Michael A.; Defourny, Pierre; Brady, Mike. Comparison and Assessment of Regional and Global Land Cover Datasets for Use in CLASS over Canada. In: *Remote Sensing*, Vol. 11, no.19, p. 2286 (2019). doi:10.3390/rs11192286.

Li, Wei; MacBean, Natasha; Ciais, Philippe; Defourny, Pierre; **Lamarche, Céline**; Bontemps, Sophie; Houghton, Richard A.; Peng, Shushi. Gross and net land cover changes in the main plant functional types derived from the annual ESA CCI land cover maps (1992-2015). In: *Earth System Science Data*, Vol. 10, p. 219-234 (2018). doi:10.5194/essd-10-219-2018. http://hdl.handle.net/2078.1/194772.

Lamarche, Céline; Santoro, Maurizio; Bontemps, Sophie; d'Andrimont, Raphaël; Radoux, Julien; Giustarini, Laura; Brockmann, Carsten; Wevers, Jan; Defourny, Pierre; Arino, Olivier. Compilation and Validation

of SAR and Optical Data Products for a Complete and Global Map of Inland/Ocean Water Tailored to the Climate Modeling Community. In: *Remote Sensing*, Vol. 9, no.1, p. 36 (2017). doi:10.3390/rs9010036. http://hdl.handle.net/2078.1/183960.

Waldner, François; Fritz, Steffen; **Lamarche, Céline**; Bontemps, Sophie; Defourny, Pierre. A Unified Cropland Layer at 250 m for Global Agriculture Monitoring. In: *Data*, Vol.1 (1), no.3, p. 1-13 (2016). doi:10.3390/data1010003. http://hdl.handle.net/2078.1/172928.

Radoux, Julien; Chomé, Guillaume; Jacques, Damien Christophe; Waldner, François; Bellemans, Nicolas; Matton, Nicolas; **Lamarche, Céline**; d'Andrimont, Raphaël; Defourny, Pierre. Sentinel-2's Potential for Sub-Pixel Landscape Feature Detection. In: *Remote Sensing*, Vol. 8, no.6, p. 488 (2016). doi:10.3390/rs8060488. http://hdl.handle.net/2078.1/174665.

Poulter, Ben; MacBean, Natasha; Hartley, Andrew; Khlystova, Iryna; Arino, Olivier; Betts, Richard; Bontemps, Sophie; Boettcher, Martin; Brockmann, Carsten; Defourny, Pierre; Hagemann, Stefan; Herold, Martin; Kirches, Grit; **Lamarche, Céline**; Lederer, Dimitri; Ottlé, Catherine; Peters, Marco; Peylin, Philippe. Plant functional type classification for earth system models: results from the European Space Agency's Land Cover Climate Change Initiative. In: *Geoscientific Model Development*, Vol. 8, no.C550-C551, p. 2315-2328 (2015). doi:10.5194/gmd-8-2315-2015. http://hdl.handle.net/2078.1/166340.

Santoro, Maurizio; Wegmüller, Urs; **Lamarche, Céline**; Bontemps, Sophie; Defourny, Pierre; Arino, Olivier. Strengths and weaknesses of multi-year Envisat ASAR backscatter measurements to map permanent open water bodies at the global scale. In: *Remote Sensing of Environment*, Vol. 171, p. 185-201 (2015). doi:10.1016/j.rse.2015.10.031. http://hdl.handle.net/2078.1/173259.

Radoux, Julien; **Lamarche, Céline**; Van Bogaert, Eric; Bontemps, Sophie; Brockmann, Carsten; Defourny, Pierre. Automated Training Sample Extraction for Global Land Cover Mapping. In: *Remote Sensing*, Vol. 6, no.5, p. 3965-3987 (2014). doi:10.3390/rs6053965. http://hdl.handle.net/2078.1/143085.

Conferences, as a speaker

Lamarche, C., Harper, K., Hartley, A., Peylin, P., Ottlé, C., Bastrikov, V., ... & Defourny, P. (2023). A 29-year time series of annual 300-metre resolution plant functional type maps for climate models (No. EGU23-16740). Copernicus Meetings.

Céline Lamarche, Kandice L. Harper, Andrew J. Hartley, P. Peylin, Catherine Ottle, et al.. Spatially explicit vegetation fractions to improve climate model simulation: A 29-year time series of annual Plant Functional Type (PFT) fraction maps through the fusion of the CCI MRLC 300 m land cover dataset and existing high-resolution data products. LPVE23 Symposium, LPVE; ESA, Jun 2023, Frascati (Rome), Italy. ⟨hal-04264760⟩

C. Lamarche, S. Bontemps, Q. Marissiaux, P. Defourny and O. Arino, "Towards a Multi-Level Sampling Scheme for Land Cover and Land Cover Change Validation. Lessons Learned from the Land Cover Climate Change Initiative," 2021 IEEE International Geoscience and Remote Sensing Symposium IGARSS, Brussels, Belgium, 2021, pp. 1986-1989, doi: 10.1109/IGARSS47720.2021.9553898.

Bontemps, S., Bellemans, N., Defourny, P., Koetz, B., & **Lamarche, C.** (2018). Validation of the ESA Sen2-Agri cropland and crop type products: lessons learnt from local to national scale experiments. In AGU Fall Meeting 2018. AGU.

Defourny, P., **Lamarche, C.**, & Bontemps, S. (2018). Consistent 1992-2015 global land cover time series at 300 m thanks to a state-of-the-art reprocessing of multi-mission archives. In AGU Fall Meeting 2018. AGU.

Lamarche, Céline; Bontemps, S., Boettcher, M., Brockmann, C., Kirches, G., **Lamarche, C.**, Radoux, J., ... & Defourny, P. (2017). Africa land cover mapping at 10 m with Sentinel 2: current achievements of the land cover component of the ESA Climate Change Initiative. The 37th International Symposium on Remote Sensing of Environment (Tshwane, South Africa, 08–12/05/2017).

Lamarche, Céline; Bontemps, S., Boettcher, M., Brockmann, C., Kirches, G., **Lamarche, C.**, Radoux, J., ... & Defourny, P. (2017). Towards a decametric global land cover map with Sentinel-2. Africa as a feasibility study. World-Cover 2017 conference. Frascati (Rome), Italy, 14–16/03/2017.

Lamarche, Céline; Santoro, Maurizio; Bontemps, Sophie; d'Andrimont, Raphaël; Giustarini, Laura; Brockmann, Carsten; Militzer, Jan; Defourny, Pierre; Arino, Olivier. (2016). A global map of open water bodies and coastlines at 150 m based on synergies between SAR and optical datasets. Living Planet Symposium 2016 (Prague, Czech Republik, 09–13/05/2016). In: Proceedings of Living Planet Symposium 2016. 978-92-9221-305-3.

Defourny, Pierre; Bontemps, Sophie; **Lamarche, Celine**; Brockmann, Carsten; Achard, Frédéric; Boettcher, Martin; De Maet, Thomas; Gamba, Paolo; Hagemann, Stephan. (2016). The Land Cover component of the ESA

Climate Change Initiative. Extending the series of global land cover maps to 2015 with PROBA-V: current achievements. PROBA-V Symposium (Gent, Belgium, 26–28/01/2016).

Lamarche, Céline; Bontemps, Sophie; Rousseau, Corentin; De Maet, Thomas; Verhegghen, Astrid; Radoux, Julien; Van Bogaert, Eric; Arino, Olivier; Defourny, Pierre. (2014). CCI-LC seasonality product. Characterizing the reference dynamics of the land surface. The 4th International Symposium on Recent Advances in Quantitative Remote Sensing: RAQRS'IV (Torrent, Valencia-Spain, 22–26/09/2014).

Lamarche, Céline; Defourny, Pierre; Tomaszewska, M.; Dabrowska-Zielinska, K. (2012). Object-based automatic change detection in forested areas of Poland between 2000 and 2006 using NDVI times series at moderate resolution. EGU General Assembly 2012.